



**This electronic thesis or dissertation has been
downloaded from Explore Bristol Research,
<http://research-information.bristol.ac.uk>**

Author:

Ariu, Giampaolo

Title:

Functionalised Graded Composites for Induction Processing in Manufacture

General rights

Access to the thesis is subject to the Creative Commons Attribution - NonCommercial-No Derivatives 4.0 International Public License. A copy of this may be found at <https://creativecommons.org/licenses/by-nc-nd/4.0/legalcode>. This license sets out your rights and the restrictions that apply to your access to the thesis so it is important you read this before proceeding.

Take down policy

Some pages of this thesis may have been removed for copyright restrictions prior to having it been deposited in Explore Bristol Research. However, if you have discovered material within the thesis that you consider to be unlawful e.g. breaches of copyright (either yours or that of a third party) or any other law, including but not limited to those relating to patent, trademark, confidentiality, data protection, obscenity, defamation, libel, then please contact collections-metadata@bristol.ac.uk and include the following information in your message:

- Your contact details
- Bibliographic details for the item, including a URL
- An outline nature of the complaint

Your claim will be investigated and, where appropriate, the item in question will be removed from public view as soon as possible.

Functionalised Graded Composites for Induction Processing in Manufacture



Giampaolo Ariu

A dissertation submitted to the University of Bristol in accordance with the requirements for award of the degree of Doctor of Philosophy (PhD) in the Faculty of Engineering, School of Civil, Aerospace and Mechanical Engineering.

September 2018

Word count: 54,403

Abstract

This project focuses on investigating several methods, such as magnetic positioning and liquid resin printing, to introduce and position carbon nanotubes (CNTs) in a viscous medium. The combination of magnetic manipulation through static magnetic field and liquid resin printing represents an unprecedented approach that could be used in composite manufacture, specifically for patch repair applications of composite materials. The possibility of spatially positioning the CNTs in a tailored and accurately controlled fashion is a focal point of the presented project. The main advantages of the proposed approach are the local CNT positioning and heat dissipation tailoring by conductive networks within the part. More precisely, the generation of such conductive pathways through spatial additive positioning can be used to trigger inductive heating by alternated magnetic field. Homogeneous heat distribution within the inductively sensitive region could be aided by the inhomogeneity of the magnetic field.

CNTs were metal functionalised through chemistry-based electroless plating. Metal-plated CNT positioning through static magnetic field was achieved both in epoxy resin and within glass fabric. The CNT positioning within fabric was assessed by introducing the CNTs within fabric through liquid resin printing. The CNT positioning was characterised within fabric by elemental analysis of selected fracture surfaces across the patch by assessing the metal particle distribution. Metal-plated CNTs affected the preform resin cure kinetics. The effect of grading the electrical conductivity within the patch by spatially locating the nanotubes was assessed through numerical inductive modelling. Homogeneous spatial distribution of CNTs provided uniform heat dissipation within the patch by means of eddy current generation. Enhancement of dielectric properties of the resin matrix by synergetic effect of dielectric particles and CNTs can be combined with eddy currents to aid and better control the cure process. Further experimental work on inductive heating for patch repair represents the next step of this investigation.

Dedication and Acknowledgements

The present dissertation for the award of the degree of Doctor of Philosophy (PhD) has been carried out from January 2015 to September 2018. The experimental tests and numerical analyses have been conducted at the University of Bristol.

The work has been done with the precious help and support of the people working at the department. I would like to thank directly them, particularly my supervisors Dr Dmitry Ivanov and Prof. Ian Hamerton, for being always available for improving my practical and theoretical knowledge, giving me their guidance during the entire project. I would also like to thank my friends and family, my parents and my brothers who, although distant geographically, were always morally present to support me throughout this experience.

The authors would like to acknowledge support from Rolls-Royce plc, particularly Mr Paul Williams and Ms. Bhrami Jegatheeswaram Pillai, through the Composites University Technology Centre (UTC) at the University of Bristol, and from the Engineering and Physical Sciences Research Council (EPSRC) through the Centre for Doctoral Training in Advanced Composites at the University of Bristol (Grant no. EP/L016028/1). The authors would also like to acknowledge Dr. Jacopo Ciambella from the “Sapienza” University of Rome and the Wolfson Centre of Magnetism at the Cardiff University for the valuable technical assistance during the initial and concluding stages of the project.

Author's Declaration

I declare that the work in this dissertation was carried out in accordance with the requirements of the University's Regulations and Code of Practice for Research Degree Programmes and that it has not been submitted for any other academic award. Except where indicated by specific reference in the text, the work is the candidate's own work. Work done in collaboration with, or with the assistance of, others, is indicated as such. Any views expressed in the dissertation are those of the author.

SIGNED: DATE:.....

Table of Contents

Table of Tables	XIV
Table of Figures.....	XVI
List of Abbreviations	XXIV
1. Introduction	1
1.1 Aim of the study	2
1.2 Research objectives.....	3
1.3 Repair of aerospace components: problems and solutions	4
1.3.1 Repair patches: manufacturing, geometry	4
1.3.2 Functionalising additives.....	5
1.3.3 Alignment and positioning of additives	6
1.4 Structure of the thesis	7
1.5 List of publications and conferences	8
1.5.1 Publications	8
1.5.2 Conference presentation	8
2. Literature Review	9
2.1 Electrical percolation threshold theories.....	10
2.2 Conductivity of CNT resins	11
2.3 Manufacturing of electrically conductive composites	12
2.4 Functionalisation of CNTs.....	15
2.4.1 Physical functionalisation.....	15
2.4.2 Chemical functionalisation	15
2.5 Nano-filler alignment	18
2.5.1 Electric field alignment	19
2.5.2 Magnetic field alignment.....	26
2.5.3 Ultrasonic alignment	31
2.6 Induction heating	34
2.6.1 Eddy currents.....	34

2.6.2 Joule heating	36
2.6.3 Introduction on induction heating	38
2.6.4 Inductive heating parameters	39
2.6.5 Induction heating literature	41
2.7 Dielectric heating	47
2.8 Summary and outlook	52
3. Manufacturing of functionalised additives and functionalised resins	54
3.1 Functionalisation of CNT additives	54
3.1.1 Materials.....	55
3.1.2 Methods.....	55
3.1.2.1 Chemical approach	56
3.1.2.2 Physical approach.....	57
3.2 Characterisation of functionalised CNT	58
3.2.1 Microstructural analysis of metal particles on MWCNTs	59
3.3 Manufacturing of functionalised matrices	61
3.3.1 Rheological properties of the epoxy-MWCNT blends	61
3.3.2 Cure kinetics characterization of the epoxy-MWCNT blends.....	63
3.3.3 Determining the magnetic susceptibility of the blends	65
3.4. Conclusions.....	67
4. Magnetic alignment and placement of functionalised additives within epoxy resin	69
4.1. Assessment of non-uniform DC magnetic field.....	69
4.1.1 Non-uniform DC field assessment: numerical model specification	70
4.2 Magnetic alignment and placement of functionalised particles in DC field	72
4.2.1. Analytical assessment of CNT motion.....	74
4.2.2. Analytical assessment of CNT orientation.....	76
4.3 Experimental demonstration of particle placement.....	80
4.3.1 Magnetic DC set-up	80
4.3.2 Implementation of experiments	81

4.3.3	Experimental analysis.....	82
4.4	Conclusions.....	88
5.	Functionalised repair patches with graded properties	90
5.1	Materials	90
5.2	Liquid resin printing: sample preparation and procedure.....	91
5.3	Resin infusion of the liquid resin printed samples	93
5.4	Sample preparation for elemental investigation	95
5.5	Scanning Electron Microscope (SEM) elemental analysis	97
5.5.1	Reference case	101
5.5.2	Comparison reference vs. field (low keV)	102
5.5.3	Co presence – Comparison field vs. reference (high keV).....	104
5.6	Additional investigation for magnetic nanotube migration	112
5.6.1	Fourier Transform Infrared Spectroscopy (FT-IR)	112
5.6.2	Modulated Differential Scanning Calorimetry (mDSC)	113
5.6.3	Dynamic Mechanical Analysis (DMA).....	116
5.6.4	Field application time dependence	117
5.6.5	Scanning Electron Microscopy (SEM) micrograph post-processing for magnetic field exposition time dependence	122
5.7	Conclusions.....	123
6.	Inductive heating modelling	125
6.1	Introduction.....	125
6.2	Induction heating model	125
6.3	Model implementation.....	129
6.3.1	Model geometry and conditions	129
6.3.2	Properties	130
6.3.3	Boundary conditions.....	131
6.3.4	Mesh	131
6.4	Assessment of induction parameters.....	134

6.5	Feasibility of grading - Results	138
6.5.1	Grading of in-plane electrical conductivity	139
6.5.2	Grading of through-thickness electrical conductivity	143
6.6	Conclusions	147
7.	Dielectric measurements	149
7.1	Materials	149
7.2	Sample preparation	151
7.3	Experimental methodology	152
7.4	Results	153
7.5	Case study: cure kinetics characterisation of hybrid dielectric material	159
7.6	Conclusions	165
8.	Conclusions	167
9.	References	171
APPENDIX A - Induction heating experimental analysis		180
A.1	Samples	180
A.2	GFRP sample preparation	180
A.3	CFRP sample preparation	181
A.4	Results and conclusions	185
APPENDIX B – Materials Technical Data Sheets (MTDS)		186
B.1	COOH- functionalised Multi-Walled Carbon Nanotubes (Sigma Aldrich)	186
B.2	Nickel-Coated Multi-Walled Carbon Nanotubes (US Research Nanomaterials)	187
B.3	Epoxy Infusion System PRIME™ 20LV (Gurit)	188
B.4	EPON™ Resin 828 (Hexion)	194
B.5	Benzoxazine 35600 (Araldite®, Huntsman)	203
B.6	Cyanate ester resin PT-30 (Primaset™, Lonza)	208
B.7	Strontium titanate (SrTiO ₃ , Sigma Aldrich)	209
B.8	Barium titanate (BaTiO ₃ , Sigma Aldrich)	210

Table of Tables

Table 2.1. Susceptor parameters influencing the resulting electrical performance [13].	40
Table 2.3. Properties of the composites with various contents of Y5V ceramics [95].	50
Table 4.1. Materials properties for N42 and air.	70
Table 4.2. Parameters used for the MATLAB simulation.	75
Table 4.3. Times required for the single fibre to reach the magnetic pole half width if the initial distance from the centre exceeds 7 mm.	76
Table 4.4. <i>Dynamic viscosities at 25°C and curing times for both systems.</i>	77
Table 4.5. Minimum flux density B_{0min} as a function of the aspect ratio for different alignment probabilities within high viscosity medium (EPON 828, Hexion).	78
Table 4.6. Minimum flux density B_{0min} as a function of the aspect ratio for different alignment probabilities within high viscosity medium (PRIME 20LV, Gurit).	79
Table 5.1. Parameters used for the analysis of $wCNT r$.	111
Table 6.1. Materials properties for the model with externally applied AC magnetic field.	133
Table 6.2. Geometrical properties of the model sections.	133
Table 6.3. LNR and LCR properties used for the temperature estimates [107, 108].	135
Table 6.4. Electrical conductivity values used for the evaluation of the current density needed to achieve heat dissipation according to equation 6.9 and 6.10.	136
Table 6.5. Values of optimum current density J to achieve effective induction heating from Abaqus model.	136
Table 6.6. Values of optimum current density J to achieve effective induction heating from Abaqus model with high conductivity patch.	137
Table 6.7. <i>Electrical conductivities and H_d for LNR with uniform laminate through-thickness properties.</i>	141

Table 6.8. Electrical conductivities and Hd for LCR with uniform laminate through-thickness properties.	141
Table 6.9. Electrical conductivity levels for each laminate ply at the different magnetic patch locations for the case of increasing conductivity from the top ply (Ply 4) to the bottom ply (Ply 1).	144
Table 6.10. Electrical conductivity levels for each laminate ply at the different magnetic patch locations for the case of increasing conductivity from the top ply (Ply 4) to the bottom ply (Ply 1).	144
Table 6.11. Non-uniform through-thickness electrical conductivity conditions and results for the LNR case.	144
Table 6.12. Non-uniform through-thickness electrical conductivity conditions and results for the LCR case.....	146

Table of Figures

Fig. 1.1. Schematic of composite inner structure for fibre alignment by external energy fields [1].	3
Fig. 1.2. Generic schematic of advanced composite patch (left) and scarf (right) repair.	5
Fig. 2.1. Effect of pH on power loss measured at 1.5 T and 50 Hz frequency [58].	17
Fig. 2.2. Schematic illustration of a polarised cylindrical particle in an electric field [29].	19
Fig. 2.3. Network formation of 0.2% CNF dispersed in the amine curing agent in an AC electric field of 400 V cm^{-1} and 1 kHz, before (a), 1 min (b) and 30 min (c) after the application of the field [68].	21
Fig. 2.4. Magnification of the single fibre alignment and fibre agglomeration after 1 minute of exposure to electric field [68].	22
Fig. 2.5. Specific resistance as a function of the CNF weight fraction in the cured composites for the directions parallel and perpendicular to the electric agglomeration field [68].	22
Fig. 2.6. Left: experimental setup of photopolymerisation of SWNT/UH composite under an electric field; Right: top view of the alignment cell [71].	23
Fig. 2.7. Transmission optical micrographs of epoxy composites containing 0.01 wt% MWCNTs during curing at 80°C in a (a) DC field and (b) AC field of 100 V/cm [61].	25
Fig. 2.8. SEM images of MWCNTs/epoxy composites with different nanotubes loading fractions [a] 0.5wt% [b] 1wt% [67].	26
Fig. 2.9. Reinforcement effect on modulus in varied nanotubes loading fractions [67].	26
Fig. 2.11. Temperature dependence of resistivity of magnetically processed CNT-epoxy composites [9].	29
Fig. 2.13. Thermal conductivity of CNT-epoxy composites magnetically processed at 0 and 25 T, compared with neat epoxy sample (processed at 25 T) [9].	30
Fig. 2.14. Schematic diagram of the home-built setup for acoustic nanotubes alignment: (a) the substrate perpendicular to the radiation surface, (b) the substrate bonded on top of the radiation surface and (c) a combination of the “a” and “b” configurations [69].	33

Fig. 2.15. FESEM images of the ultrasonically assembled MWNTs under an AC voltage of 40 V at (a) 5 kHz, (b) 30 kHz, (c) 60 kHz, and (d) 180 kHz to the piezoelectric transducer in accordance with the configuration (a) (arrows: acoustic wave direction) [69].	33
Fig. 2.16. FESEM images of nanotubes on the surface of the Si substrates: two piezoelectric transducers vibrating under an applied voltage of 40 V at (a) 30 kHz, (b) 60 kHz, and (c) 100 kHz (c) (setup c). Inserted arrows: direction of acoustic propagation [69].	34
Fig. 2.17. Schematic of carbon fibre configuration showing induced current due to a transverse magnetic field [15].	35
Fig. 2.18. Joule heating in conductive fibre as a function of the fibre resistance [16].	37
Fig. 2.19. Schematic of the skin effect and control parameters [13].	41
Fig. 2.20. Sample in the centre of the induction heating coil [79].	42
Fig. 2.21. Schematic of the fabric used for induction heating investigation [81].	44
Fig. 2.23. Typical heating pattern of composite strip and the measuring positions for temperature (in °C) [18].	46
Fig. 2.25. Temperature dependence of the dielectric constant of the sintered BST(0.2) and BST(0.4) ceramics [92].	48
Fig. 2.26. Dielectric constant for BST-epoxy composites as function of temperature for different volume fraction at 10 KHz [92].	49
Fig. 2.27. Dielectric constant of BST-epoxy sample with 20 vol% of ceramic content as a function of frequency [92].	49
Fig. 2.28. Dielectric constants of the cured composites as a function of frequency [95].	51
Fig. 2.29. Dielectric heating representation at the non-touching fibre junction [97].	52
Fig. 3.2. TEM micrographs: Ni-coated (a) and Ni-plated (b) and Co-plated (c) MWNTs (different scales). ImageJ software was used for the Ni-coated nanotube diameter value in (a) [1].	59
Fig. 3.4. TEM image of Ni-coated MWNTs (Ni as white regions).	61
Fig. 3.5. Shear viscosity curves as a function of shear rate for 5 vol% and 10 vol% of COOH-MWCNTs and Co30-MWCNTs in PRIME™ 20LV [1].	62
Fig. 3.6. Comparison of PRIMETM 20LV/amine/MWCNT (5 vol%) blend reactivity using MDSC (5 K/min.) [1].	64

Fig. 3.7. Comparison of heats of polymerisation for the different epoxy blends [1].	65
Fig. 3.8. (a) VSM results and (b) plating/stirring comparison for Ni-plated MWCNTs [1]. ..	66
Fig. 3.9. VSM results from sonication plated/magnetically stirred Co-plated MWCNTs [1]..	67
Fig. 4.1. Magnetic model showing magnetic poles and air domain, mesh, element type and materials name.	71
Fig. 4.2. B_x , B_y and resulting $ B $ [T] trends as a function of the normalised x-coordinate [cm] (normalised with respect to the x-coordinate of the left hand side magnetic pole x_0).	72
Fig. 4.4. Fibre (nanotube) migration distance (in mm), as a function of the initial fibre distance from the sample centre (in mm). Magnetic pole width exceeds the dimensions shown on this graph.	76
Fig. 4.5. DC magnetic apparatus, with Electromagnet (Type C, Newport Instruments) [1]. ..	80
Fig. 4.6. SEM micrographs of samples containing as-received multi-walled carbon nanotubes (low aspect ratio) with no DC field application.	83
Fig. 4.7. SEM micrographs of samples containing as-received multi-walled carbon nanotubes (low aspect ratio) after DC field application.	84
Fig. 4.8. SEM micrographs of samples containing as-received multi-walled carbon nanotubes (low aspect ratio) after DC field application.	86
Fig. 4.9. (a) Ni-plated MWCNTs positioning: comparison after DC field and (b) CT scans of PRIMETM 20LV+1 vol.% Ni-plated MWCNTs under 0.25 T and 0.5 T [1].	88
Fig. 5.1. Home-made 3D printing device characterised by 3D moving head and metallic sample support (cable connection to the desktop software).	93
Fig. 5.2. Resin infusion panel after the infusion process.	95
Fig. 5.3. Schematic of the glass NCF sample after CNT-filled resin printing showing the location of the assessed sections for the cobalt distribution (A = injection site).	97
Fig. 5.4. SEM sample for the case of applied magnetic field after sectioning process.	97
Fig. 5.5. Backscattering electron micrographs (a) for the applied field and (b) cases at the sample fracture surface, with Ag associated with silver paint.	99

Fig. 5.6. Secondary electron micrograph showing the fracture surface of the sample subjected to magnetic field. Regions ‘a’, ‘b’ and ‘c’ shown in the micrograph are taken along the sample width to analyse the cobalt content distribution along the sample width.....	99
Fig. 5.7. EDX elemental analysis of the fracture surface of the sample subjected to magnetic field, carried out in three specific location over the surface (a, b, c).	100
Fig. 5.8. Cobalt distribution map on the fracture surface of the sample subjected to magnetic field.....	101
Fig. 5.9. Secondary electron micrograph showing the fracture surface of the sample with absence of applied magnetic field.	101
Fig. 5.10. EDX elemental analysis of the fracture surface of the sample with absence of applied magnetic field, carried out in three specific location over the surface (a, b, c).	102
Fig. 5.11. EDX results for low keV: cobalt peaks (circled in black) for the three regions of interest (a, b and c), as a comparison between field (red curve) and no field (blue curve) cases.	103
Fig. 5.12. EDX results for high keV: cobalt peaks (circled in black) for the three regions of interest (a, b and c), as a comparison between field (red curve) and no field (blue curve) cases.	105
Fig. 5.13. Fracture surface micrograph (left) and the cobalt mapping (right) at the section A (injection point section) for the magnetically treated sample.....	106
Fig. 5.14. Fracture surface micrograph (left) and the cobalt mapping (right) at the section B.	106
Fig. 5.15. Fracture surface micrograph (left) and the cobalt mapping (right) at the section C (where the field is the strongest due to edge effect).	107
Fig. 5.16. Fracture surface micrograph (left) and the cobalt mapping (right) at the section A (injection point section) for the no field case.	108
Fig. 5.17. Fracture surface micrograph (left) and the cobalt mapping (right) at the section B for the no field case.	108
Fig. 5.18. Fracture surface micrograph (left) and the cobalt mapping (right) at the section C (where the field is the strongest due to edge effect) for the no field case.	109
Fig. 5.19. Cobalt distribution results for field and no field case after EDX and ImageJ post-processing.	109

Fig. 5.20. Fourier Transform Infrared Spectroscopy (FT-IR) spectra as a comparison between locations A, B and C in the field case.	113
Fig. 5.21. MDSC results: total heat flow (in mW) as a function of the temperature (in °C) at different sample locations for field and no field case.	114
Fig. 5.22. MDSC results: non-reversing heat flow (in mW) as a function of the temperature (in °C) at different sample locations for field and no field case.	115
Fig. 5.23. MDSC results: glass transition temperature (in °C) as a function of the sample locations for field and no field case.	115
Fig. 5.24. DMA glass transition temperature changes at different locations within the samples for field and no field case.....	116
Fig. 5.25. Hydraulic hot press used for magnetic patch consolidation after application of temperature and pressure cycles.	118
Fig. 5.26. Cobalt distribution at location A after 15 minutes of magnetic field exposition. .	119
Fig. 5.27. Cobalt distribution at location B after 15 minutes of magnetic field exposition...	119
Fig. 5.28. Cobalt distribution at location C after 15 minutes of magnetic field exposition...	119
Fig. 5.29. Cobalt distribution at location A after 30 minutes of magnetic field exposition. .	120
Fig. 5.30. Cobalt distribution at location B after 30 minutes of magnetic field exposition...	120
Fig. 5.31. Cobalt distribution at location C after 30 minutes of magnetic field exposition...	121
Fig. 5.32. Cobalt distribution at location A after no magnetic field exposition.	121
Fig. 5.33. Cobalt distribution at location B after no magnetic field exposition.....	122
Fig. 5.34. Cobalt distribution at location C after no magnetic field exposition.....	122
Fig. 5.35. Cobalt distribution from A to C at different magnetic field application times.	123
Fig. 6.1. (a) Abaqus representation of the composite laminate subjected to AC magnetic field during the electromagnetic simulation; (b) Abaqus model representation of magnetic patch partition; (c) Abaqus representation of the magnetic coil. Dimensions can be found in Table 6.2.....	132
Fig. 6.2. Abaqus model representation of the body current density load applied to the coil within the modelled system (green arrows showing the current flow direction) and the boundary conditions (blue symbols).	134

Fig. 6.3. Abaqus model results of Hd : Test 1 (a), Test 2 (b), Test 6 (c) and Test 8 (d).....	142
Fig. 6.4. Progression of heat dissipation Hd with the location within the patch (zone 0, 1, 2 or 3) for the tests run in the LNR case (no through-thickness grading).	142
Fig. 6.5. Progression of heat dissipation Hd with the location within the patch (zone 0, 1, 2 or 3) for the tests run in the LCR case (no through-thickness grading).....	143
Fig. 6.6. Progression of heat dissipation Hd with the location within the patch (zone 0, 1, 2 or 3) for the tests run in the LNR case (through-thickness grading).	146
Fig. 6.7. Progression of heat dissipation Hd with the location within the patch (zone 0, 1, 2 or 3) for the tests run in the LCR case (through-thickness grading).....	147
Fig. 7.1. Dielectric test sample with geometrical specifications.	152
Fig. 7.2. Initial dielectric measurements on baseline resin systems.....	154
Fig. 7.3. Dielectric test measurements after introduction of SrTiO_3 within PRIME 20LV. .	155
Fig. 7.4. Dielectric test measurements after introduction of BaTiO_3 within PRIME 20LV. .	155
Fig. 7.6. Dielectric test measurements of nanocomposites characterised by an epoxy PRIME 20LV/strontium titanate ratio of 80:20 and cobalt plated carbon nanotube loadings of 0.7 wt.%, 2.5 wt.% and 5 wt.% (around 1 vol.%, 5 vol.% and 10 vol.%, respectively).	157
Fig. 7.9. Modulated DSC results: heat flow (mW) as a function of temperature ($^{\circ}\text{C}$) for neat epoxy PRIME 20LV (blue curve) and the 80/20 epoxy/strontium titanate with 2.5 wt.% of cobalt-plated multi-walled carbon nanotubes.....	161
Fig. 7.10. Modulated DSC results: reversing heat flow (mW) as a function of temperature ($^{\circ}\text{C}$) for neat epoxy PRIME 20LV (blue curve) and the 80/20 epoxy/strontium titanate with 2.5 wt.% of cobalt-plated multi-walled carbon nanotubes.	162
Fig. 7.11. Modulated DSC results: non-reversing heat flow (mW) as a function of temperature ($^{\circ}\text{C}$) for neat epoxy PRIME 20LV (blue curve) and the 80/20 epoxy/strontium titanate with 2.5 wt.% of cobalt-plated multi-walled carbon nanotubes.	163
Fig. 7.12. Modulated DSC results: specific heat capacity ($\text{mJ}/^{\circ}\text{C}$) as a function of temperature ($^{\circ}\text{C}$) for neat epoxy PRIME 20LV (blue curve) and the 80/20 epoxy/strontium titanate with 2.5 wt.% of cobalt-plated multi-walled carbon nanotubes.	163
Fig. 7.13. Modulated DSC results: reversing specific heat capacity ($\text{mJ}/^{\circ}\text{C}$) as a function of temperature ($^{\circ}\text{C}$) for neat epoxy PRIME 20LV (blue curve) and the 80/20 epoxy/strontium titanate with 2.5 wt.% of cobalt-plated multi-walled carbon nanotubes.	164

Fig. 7.14. Modulated DSC results: non-reversing specific heat capacity (mJ/°C) as a function of temperature (°C) for neat epoxy PRIME 20LV (blue curve) and the 80/20 epoxy/strontium titanate with 2.5 wt.% of cobalt-plated multi-walled carbon nanotubes.....	164
Fig. A.1. AC magnetic setup (a) and detail of the ferrite horseshoe core (b).....	180
Fig. A.2. GFRP induction heating samples with 0.75 wt.% CNTs [98].....	181
Fig. A.3. Scarf sample after unsuccessful machining process.....	182
Fig. A.4. Scarf sample after machining process.	183
Fig. A.5. Top view of the two coupon configurations: one-sided magnetic patch and no magnetic patch within the coupons.....	184
Fig. A.6. Side view of the coupons, showing the presence of the scarf angle α	185

List of Abbreviations

(M)DSC	(Modulated) Differential Scanning Calorimetry
AC	Alternated Current
AEM2016	International Conference on Advanced Energy Nanomaterials 2016
APTES	Aminopropyltriethoxysilane
BaCO ₃	Barium Carbonate
BST	Barium Strontium Titanate
CFRP	Carbon Fibre Reinforced Polymer
CNF(s)	Carbon Nanofibre(s)
CNT(s)	Carbon Nanotube(s)
Cr(C)N	Chromium (Carbon) Nitride
CT	Computed Tomography
CVD	Chemical Vapour Deposition
DC	Direct Current
DMA	Dynamic Mechanical Analysis
EDS	Energy-dispersive Sensor (Detector)
EDX	Energy Dispersive X-Ray
EMC3D4	4-node electromagnetic elements
emu	Electro-Magnetic Unit
EPSRC	Engineering and Physical Sciences Research Council
FE	Finite Element
Fe, Ca, Cl, K, Na, Ag, Co, Ni	Iron, Calcium, Chloride, Potassium, Sodium, Silver, Cobalt, Nickel
FEMM	Finite Element Methods Magnetics
FT-IR	Fourier Transform Infrared
GFRP	Glass Fibre Reinforced Polymer
HCl	Hydrochloric Acid
HF	Hydrofluoric Acid
ICANM2016	International Conference & Exhibition on Advanced & Nano Materials 2016
LCM	Liquid Composite Moulding
LCR	Laminate with Conductive Reinforcement
LNR	Laminate with Non-conductive Reinforcement
MW(C)NT(s)	Multi-Walled (Carbon) Nanotube(s)
MWS	Maxwell-Wagner-Sillars
NCF	Non-Crimp Fabric

ODE	Ordinary Differential Equation
Pd/Sn	Palladium/Tin
PdCl ₂ /SnCl ₂	Palladium/Tin Chloride
PDMS	Polydimethylsiloxane
pH	Power of Hydrogen
PhD	Doctor of Philosophy
Prof./Dr/Mr	Professor/Doctor/Mister
PVD	Physical Vapour Deposition
PZT	Lead Zirconate Titanate
rpm	Revolutions per minute
SDS	Sodium Dodecyl Sulfate
SEM/TEM	Scanning Electron Microscopy/Transmission Electron Microscopy
Sr(Ba)TiO ₃	Strontium (Barium) Titanate
SW(C)NT(s)	Single-Walled (Carbon) Nanotube(s)
TDS	Technical Data Sheet
Ti(C)N	Titanium (Carbon) Nitride
UHMR	Ultra High Magnetic Response
UTC	University Technology Centre
Vol. %	Volume Percent
VSM	Vibrating Sample Magnetometer
Wt. %	Weight Percent
Zr(C)N	Zirconium (Carbon) Nitride

1. Introduction

Composite materials are used in various applications, from aerospace to automotive to civil engineering. This type of material offers several advantages in terms of lightweight structure manufacturing and the possibility of co-curing large structures. The latter relates to the ability of manufacturing high volume components in one go, potentially resulting in fewer assembly operations and relatively low process difficulties. These aspects are all beneficial to reducing the overall cost of the process.

However, the limited amount of assembly operations can be detrimental in case of damage of the components, as the components are more difficult to rework or replace. The tendency of composite materials to suffer damage through impact, resulting in barely-visible damage and other failure mechanisms counterbalances the high performance achievable with the composites.

These latter statements highlight the critical importance of repair for composite parts. On the other hand, the repair methodologies currently used in industry are complex and challenging. Particularly, the major difficulty arises in case of restoring the initial performance of the part by ensuring a high-performance bond between the repair patch and the original undamaged component. Therefore, further investigation is required to improve currently used bonding techniques. A crucial parameter to consider in this instance is the heat supply as heat is usually externally supplied to the part, leading to inhomogeneity of the heat distribution as the surface reaches the desired temperature level in a shorter timeframe if compared to the inner sections of the component. This can result in gradients of cure level through the thickness of the part and, consequently, gradients in the overall properties, particularly affecting the final mechanical performance.

The present dissertation presents a feasibility study set up to explore the potential and the limitations of a novel approach to composite repair. Specifically, the manipulation, through externally applied magnetic fields, of embedded additives introduced within the part, is assessed. The generation of tailored conductive pathways through the positioning of the additives can be used to trigger inductive heating by applying an alternated magnetic field to the part. The intrinsic inhomogeneity of the magnetic field could potentially cause the homogeneous inductive heat distribution within the inductively sensitive region. These results could be used in repair to localise the heat generation at the bondline between repair patch and original component, thus leading to a more uniform heat distribution in a mechanically critical

area. The restoration of the original mechanical performance of the part would therefore greatly benefit from this approach.

1.1 Aim of the study

The aim of this work was to assess the feasibility of inductive heating in a composite precursor modified using nano and micro scale additives (such as carbon nanotubes (CNTs) and their agglomerates, respectively) positioned and distributed to optimise the susceptibility of the composite to a magnetic field. The most important and novel angle of the work is how a non-uniformity of CNT distribution can result in a more uniform heat supply and cure. However, the heat uniformity also depends on the coil geometry and the field penetration (skin effect) through the part subjected to the field. The latter depends on the field frequency, and high field frequency could lead to low field penetration and, therefore, less uniformity than what could be potentially achieved. The CNT positioning could be tailored and optimised through the application of an external direct current magnetic field. On the other hand, external application of an alternating magnetic field to a nano-enhanced composite could result in heat generation and subsequent cure of a thermosetting polymer. The degree of cure could therefore be locally optimised through the positioning of the nanotubes. Furthermore, the inclusion of CNTs was expected to improve the through-thickness mechanical and electrical performance of the part in specific locations. This study explores potential for improving the repair process through creating distributed networks of nano-reinforcement. The main application for the present work is the enhanced and controlled cure process for repairing composite components.

The formation of conductive networks could be potentially realised through manipulation of magnetically sensitive nanofibres (represented by the CNTs) through external DC magnetic fields. The tailored architecture of percolative nano-reinforcements could lead to increases in the local electrical and thermal conductance. This is particularly important in the areas where there are connections between the host composite plies at the bondline. A schematic is shown in Fig. 1.1 [1].

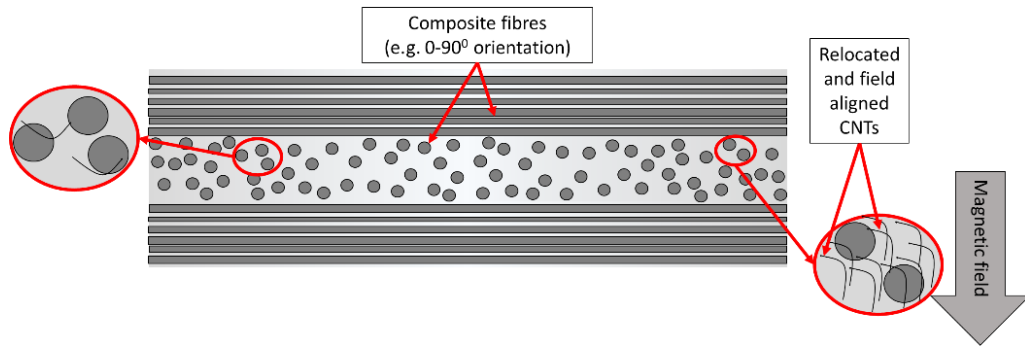


Fig. 1.1. Schematic of composite inner structure for fibre alignment by external energy fields [1].

1.2 Research objectives

The following research objectives were prioritised in this project:

- a) To explore feasibility of magnetic alignment and precise mapping of the nano-reinforcement position within a repair patch;
- b) To study the magnetic susceptibility of commercially available carbon nanotubes (CNTs) through magnetic measurements, microstructural assessment within a host epoxy resin system and modelling analysis;
- c) To explore the potential of using the electroless plating technique to provide the nanotube with magnetic properties;
- d) To investigate a range of metals as candidates for making the CNTs susceptible to magnetic alignment within a medium (initially polymer and then composite);
- e) To study the mechanisms of CNT motion through viscous and reinforced media;
- f) To evaluate the effect of functionalised CNTs on the thermal, magnetic and rheological properties of the host system (resin, composite);
- g) To assess the feasibility of generating sufficient heat by applying an external alternating magnetic field;
- h) To optimise the induction heating process through material modification to achieve the efficient and homogeneous heat supply in repair patches at a minimum supplied energy.

1.3 Repair of aerospace components: problems and solutions

Effective through-service remanufacturing technologies for on-platform repair are of great interest to the aerospace industry. This could reduce the time and costs associated with the rework and repair of composite components.

1.3.1 Repair patches: manufacturing, geometry

Examples of advanced composite repair schemes include patch repair, scarf joint repair, pre-cured doubler, bolted plates, and resin infusion (or injection) repair.

Patch repair is relatively easy to implement in the rework line however, it can also be the cause of significant material wastage and is not able to restore completely the initial performance of the component. Patch repair can be used to improve the strength of undamaged components to support higher loads [2, 3].

Scarf joint repair is often employed when it is important to retain parameters such as strength and the aerodynamic or hydrodynamic profile of a component. A scarf joint repair can restore up to 90% of the original strength of the undamaged component.

The pre-cured doubler is essentially a pre-cured plaster used for emergency temporary repair with the aim of avoiding further damage or permanent solution to minor issues.

Bolted plates are widely used in the aerospace industry and they are characterised by requiring little materials storage and cure equipment, but bolt over-tightening and creation of fixing holes can damage the part. On the other hand, resin infusion (or injection) repair can restore the original compressive and shear strength of the part through under-vacuum injection and cure of low viscosity adhesive within the damaged component. Examples of composite patch and scarf repair schemes are shown in Fig. 1.2 as the most commonly used repair processes in aerospace applications. However, these conventional repair schemes are labour intensive, and therefore costly and time consuming. They are also energy consuming during the repair process, suffer from non-uniform temperature distributions due to the application of external heat sources to cure the part. This results in inconsistent levels of curing where part thicknesses are variable, all of which ultimately lead to compromised performance of the repaired components. Moreover, the low thermal conductivity of the polymeric matrices causes an increase in the time required for the heat to move from the inner sections to the surface of the samples during the cure process. This phenomenon leads to overheating due to the exothermic nature of the cure reactions. The overall process is

therefore highly inefficient in terms of temperature profiles and resulting gradients in mechanical properties.

The main research application relates to the manipulation of nano fillers in host composite structures exposed to external energy fields (specifically electromagnetic fields) for advanced curing purposes. In this regard, the replacement of a damaged composite part, using repair patches, is vital for the restoration of the original performance; this depends crucially on the generation of a conductive network at the bondline between the original structure and the replacement. The nanotube networks are known to have potential to improve the through-thickness thermal conductivity, which is essential for uniformity of temperature. However, percolation is not sufficient to cause a significant increase of thermal conductivity. More importantly, electrical conductivity of the composite laminates; these conductivities are low even in the case of carbon fibre composites, since the through-thickness properties are primarily determined by matrix performance.

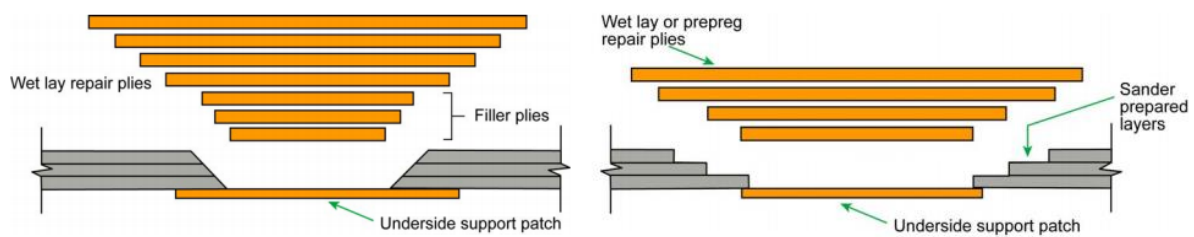


Fig. 1.2. Generic schematic of advanced composite patch (left) and scarf (right) repair.

1.3.2 Functionalising additives

Previous studies [4–6] have demonstrated the importance of the nano filler networks for several applications. Network optimisation would therefore help to accelerate the internal heat supply, decrease temperature gradients along the bondline and evacuate heat upon cooling. However, the improvement in thermal conductivity will be limited, therefore exothermic reactions might still be significant. The main aim of the nano filler network generation is the potential homogenisation of the heat distribution.

Yan *et al.* [4] manufactured nanocomposites of ethylene/1-octene copolymers filled with carbon nanotubes (CNTs) (0.7, 2.0, 3.6, and 6.8 wt%). This work showed that the interactions between the polymer and the CNTs, and the formation of a network structure, could give higher electrical conductivity as a function of CNT content. The nanocomposites filled with 6.8 wt.% of CNTs cured at 100 °C showed the highest conductivity approximately equal to

0.015 S/cm. Moreover, CNTs played as heat transfer medium in the matrix, depending on the CNT content, which improved the thermal conductivity properties of the composite.

The same effect was observed by Wu *et al.* [6] by embedding a dense multi-walled carbon nanotube (MWCNT) network and loosened expanded graphite (EG), within a thermoplastic matrix.

1.3.3 Alignment and positioning of additives

Magnetic field manipulation of short fibres has already been investigated in the literature [6–11]. Kimura *et al.* [7] studied this phenomenon in detail by applying an external direct magnetic field using a super-conducting magnet. Composite samples were made of polyester matrix with embedded MWCNTs. The work showed how electrical and mechanical properties could benefit from the local CNT distribution obtained through magnetic alignment. However, the most important parameter used to quantify the CNT percolation conditions is the percolation threshold, which is the minimum filler volume concentration required to allow a sharp increase in electrical conductivity. This parameter will be discussed in Section 2.1.

Choi *et al.* [9] also confirmed increasing electrical and thermal conductivities of CNT-epoxy composites through magnetic field processing. The magnetic alignment of CNTs in the polymer resin matrix can be considered as the main cause for increase in electric and thermal conductivities. Nanotube clustering, due to the magnetic attraction between metal functionalised nanotubes, could be beneficial to the electrical properties. However, detrimental effects on the thermal properties were discovered and consequently higher degrees of nanotube separation would be desirable for the enhancement of thermal properties.

Le Ferrand *et al.* [11] demonstrated that the spatial distribution and orientation of magnetically functionalised graphene in polymer matrices can be tailored to fabricate cost-effective composite components. Complex shapes can also be manufactured efficiently. Polymer films coated with metal nanowires and nanocarbon materials would be characterised with higher electrical conductivity through higher filler contents but maintaining the film optical transparency. Alternatively, percolation networks of wires or nanotubes would lead to a lower filler content with the required film electrical conductivity.

Literature works also focused on the induction heating phenomena [12–17] to generate heat remotely. This could pave the way for the investigation of alternative methods to cure the composite parts without supplying external heat but relying on the electrical conductivity of the part. This can ensure the most effective repair for structural purposes, with a faster,

energy-efficient technique, as reported in the literature for repair of aluminium components [18] and composite joints [19]. However, the induction heating process is characterised by intrinsic non-uniformity. Therefore, further study can lead to the optimisation of the induction heating as method to efficiently repair composite components.

1.4 Structure of the thesis

This thesis is composed of eight chapters. Chapter 2 collects the most relevant works found in literature and relates these to the objectives of this project. The chapter focuses on the methodologies to promote optimised positioning (depending on the application) for commercially available nanotubes, both with and without functionalisation, within a viscous host medium. Moreover, means for the heat generation through different externally applied stimuli, such as magnetic and electric fields, are also discussed in this chapter. Chapter 3 highlights the initial experimental and modelling investigation in terms of commercially available CNTs. Chapter 4 explains the electroless plating technique to add the required functionalisation to the carbon nanotubes, and the characterisation of the metal plated CNTs with and without introduction within epoxy resin, together with the effect on the rheological and thermal properties of the epoxy matrix. Chapter 5 describes the challenges of positioning and aligning the metal plated CNTs within a more complex host system, and the approaches adopted for this purpose. The influence of the nanotube migration within fabric on the thermal and microstructural properties of the composite samples was also investigated. Chapter 6 studies the induction heating under a numerical point of view, the induction parameters and the effect of grading the electrical conductivity on the heat dissipation within a laminate. Chapter 7 explores the effect of the introduction of dielectric particles and CNTs on the dielectric properties of neat resin and considers the dielectric heating as a way to assist inductive heating. Chapter 8 presents the conclusions to the work and the key findings. Finally, the appendix studies the manufacturing process of the inductive heating samples and the procedure used to investigate inductive heating.

1.5 List of publications and conferences

1.5.1 Publications

G. Ariu, I. Hamerton and D. Ivanov, Positioning and aligning CNTs by external magnetic field to assist localised epoxy cure, *Open Physics*, 14(1), 2016, 508-516.

G. Ariu, I. Hamerton and D. Ivanov, Positioning and Aligning CNT-Reinforcement by External Magnetic Field to Assist Localised Curing in Repair, *ICANM2016 Proceedings*, 2016.

1.5.2 Conference presentation

G. Ariu, I. Hamerton and D. Ivanov, *Positioning and Aligning CNT-Reinforcement by External Magnetic Field to Assist Localised Curing in Repair*. ICANM2016 – International Conference Exhibition on Advanced Nano Materials 2016, August 1-3, Montreal, Canada.

G. Ariu, I. Hamerton and D. Ivanov, *Manipulation of CNT-Reinforcements by External Magnetic Fields to Assist Localised Curing*. AEM2016 - International Conference on Advanced Energy Nanomaterials 2016, September 12-14, University of Surrey, Guildford, United Kingdom.

2. Literature Review

The use of external stimuli with the aim of creating tailored nanotube networks within a host system, have sparked considerable research interest over the past decades. This chapter investigates the alignment of additives and induction heating phenomena from embedded carbon nanotubes (CNTs) along with the challenges related to the remotely activated CNT alignment. Furthermore, the potential for exploiting inductive heating from the embedded nano additives in the context of repair was also considered.

The enhancement of the electrical and thermal properties of composite materials is of interest in various industry sectors such as electronics, automotive and aerospace. This is mainly associated with the need to dissipate heat and reduce the risk connected to static charge phenomena. This effect could be achieved via the manipulation of nano additives, such as nanotubes, appropriately positioned to create conductive pathways. The latter would help dissipate the internally generated heat and increase the electrical properties of the part. Moreover, the introduction of nanomaterials within host composites leads to an increase in physical properties besides conductive and mechanical performance.

Nanocomposites are characterised by at least one filler dimension in the nanometre range [19]. The filler geometry discretises between three main nanocomposite categories: examples of three-dimensional nanomaterials are fumed silica dioxide and nanometallic powder [20, 21], while CNTs are good examples of two-dimensional nanomaterials [22, 23], and clay, mica, and expanded graphite layered fillers can be classified as one-dimensional nanomaterials [19, 24, 25, 26].

The critical factors determining the percolation threshold of CNT–polymer nanocomposites include: i) the aspect ratio of CNTs, ii) disentanglement of CNT agglomerates on the nanoscale, and iii) the uniform distribution of individual CNTs or CNT agglomerates on the microscopic scale. The model formulated in this study can be used to establish the correlations between percolation threshold, dispersion state, and CNT aspect ratio. Percolation phenomena have been widely studied in literature to illustrate how one could optimize the CNT processing conditions to reduce the percolation threshold of CNT–polymer nanocomposites. There is a critical value of the CNT aspect ratio, above which the two dispersion parameters become crucial while allowing the percolation threshold to vary several orders of magnitude. In contrast, below this value the percolation threshold increases rapidly with decreasing aspect ratio. Therefore, the percolation threshold controls the nanotube

content and geometry within a host medium required for the electrical and thermal conductivity increase.

2.1 Electrical percolation threshold theories

The electrical percolation theory describes the correlation between the nanofiller dispersion conditions, filler size, and potential filler agglomeration, together with the electrical properties of the host composite.

Additive content must be increased to improve the electrical properties of the material, due to the electrically resistive nature of the host polymer resin matrix. The increase in electrical conductivity is directly linked to the formation of conductive pathways between the nano additive particles. The conductivity evolves slower with further increase of additive loading above the percolation threshold [20, 21].

It is not possible to discern increases in the overall electrical conductivity of the composite parts in cases of nano additives with low conductivity; this is also true if the content of the nano additive is low. The percolation threshold also depends on the geometry of the nanofillers, so the percolation threshold decreases at increasing aspect ratios of the nanofiller for a given content of additives. High aspect ratios could therefore lead to a reduction of nanofiller content, especially if combined with an efficient dispersion method.

The percolation threshold theory can be modelled as a percolating square lattice composed of different electrical host sites; occupied sites can be considered as conductive, whereas empty sites as insulating. The electrical current can travel across the part thanks to nearest – neighbouring conductor sites [21, 22] and low conductor site concentration can lead to the formation of clusters where two conductor sites are required to belong to the same cluster to generate a conductive path. At low filler concentrations, conductive paths are unlikely to be created, and the composite remains an insulator. Higher filler concentrations can help increase the number of conductive paths which, in turn, improves the electrical conduction and in this case, the composite behaves as a conductor. The percolation threshold lies between these two conditions; specifically, the electrical current begins to percolate across the lattice structure and represents the boundary between insulator and conductor behaviour. This concept of percolation threshold is well referred to a geometrical phase transition, with large clusters in the region distinguishable because of the value. Below this condition, only small clusters can be found in the lattice; at the percolation threshold, a large cluster (the infinite cluster) exists that connects the two edges of the lattice. The percolation threshold increases at decreasing

coordination numbers and increasing lattice size, due to a lower number of connections between conductive filler particles.

Depending on the nature of the nanofiller, relatively large contents are required to exceed the critical percolation value to increase the electrical conductivity. Li *et al.* [24] studied the parameters which affect the percolation threshold of CNT–polymer nanocomposites, such as nanotube aspect ratio, nanoscale disentanglement of CNT agglomerates on the nanoscale, and uniform distribution of individual CNTs or CNT agglomerates. A parametric study showed how to optimize the CNT processing conditions to cause a decrease in percolation threshold.

Li *et al.* [24] found that low CNT aspect ratios cause a decrease in electrical conduction and became the predominant factors that controlled the entire electrical conduction behaviour of the nanocomposite. This suggests that if the CNT aspect ratio is too low, the formation of conduction networks requires a higher CNT weight fraction, regardless of the CNT dispersion state. The percolation threshold of the composite prepared with large, tightly entangled, CNT agglomerates was high, around 0.4 wt%, due to the difficulty to create conducting networks at low filler contents. Loosely entangled and uniformly distributed CNT agglomerates could lower the percolation threshold down to 0.1 wt% [24].

Dispersion parameters become crucial above a specific critical value of CNT aspect ratio. Below this value, the percolation threshold increases dramatically with decreasing aspect ratio. An experimental comparative study was carried out to analyse the differences between the predicted results and the experimental data and good agreement was obtained [24].

The significant improvement in electrical conductivity due to the filler content increase was related to the percolation transition of the conductive network formation [24].

2.2 Conductivity of CNT resins

Carbon nanotubes (CNTs) could be introduced within a polymer based composite material to enhance the electrical and thermal properties. The electrical and thermal conductivities are considerably high in the in-plane direction of the laminate, whereas the influence of the presence of nanotubes within the part would be particularly desirable through the thickness of the component, particularly for carbon fibre composites. In this instance, the presence of polymer resin layers acts as an insulator between the carbon fibre laminate plies. The low electrical conductivity of the epoxy matrix hinders the generation of a conductive network between the plies and inhibits the electric current transfer across the composite component [25]. In the case of glass fibre composites, the presence of nano additives and the generation

of a conductive network lead to a substantial increase of electrical conductivity. This effect can cause the component to show conductive properties whereas insulating properties would be displayed without the presence of nano additives. High aspect ratio and high conductivity fillers are considered as potential replacements for carbon black and copper wire, which would need high contents, therefore decreasing the overall mechanical performance of the component [25]. CNTs are the most appealing candidates as their percolation threshold is relatively low compared to carbon black and copper wire (about 5 wt.% [26]). Specifically, single-walled carbon nanotubes (SWCNTs) are characterised by higher electrical and thermal properties compared to MWCNTs, although the latter are typically selected for their lower cost and higher accessibility.

Optimisation studies were therefore conducted on MWCNTs to reduce the percolation threshold of these nanofillers and achieve higher electrical conductivity values. Previous work has shown that the thermal conductivity of an epoxy resin host matrix could be increased by 125% with the addition of 1 wt.% of SWCNTs [27]. Alternative techniques were explored to improve the dispersion of CNTs within an epoxy matrix and several studies focused on the effective dispersal of CNTs at high concentrations within host polymer resins. CNT chemical functionalization with carboxylates and amines [28], CNT mechanical milling [29], and the use of surfactants [30, 31] was also assessed for the CNT surface coating procedure. Evident downsides of these techniques include CNT breakage and aspect ratio reduction due to the physical and chemical processing. The level of dispersion of the nanofillers within a host matrix highly affects the percolation threshold, as explored by Yuan and Wu [26]. Dispersion of carbon black within polypropylene was achieved by means of single and twin screws extruders. The conductivity of the nanocomposite obtained with these methods was higher in the case of single screw extruder as compared to that made with twin screws extruder, for all values of carbon black content [26]. Li *et al.* [24] also examined the discrete dispersion of high concentration of pre-treated SWCNTs within epoxy resin; the treatment caused the SWCNTs to become highly hydrophobic, but easily dispersible in epoxy resin.

2.3 Manufacturing of electrically conductive composites

Applications for the introduction of CNTs within composite materials range from aerospace to automotive and civil engineering [32, 33, 34, 35], and several manufacturing methods were analysed in previous works with the aim of including carbon nanotubes within a composite component.

Various techniques can be selected for the nanotube introduction within the composite parts, such as the calendering process [36, 37], ultrasonication [38, 39], ball milling [40], stirring, and extrusion [24, 41, 42, 43]. However, the most used processes to introduce nanotubes within a composite component are the deposition of CNTs on fibre surface through grafting and nano-stitching [44], compression moulding of CNT rich films, and liquid moulding.

On the other hand, grafting can lead to fibre damage. Furthermore, the achievable fibre volume fraction is relatively low, and this deposition process is mainly used in lab-scale experiments, due to the difficulty of upscaling the process. In liquid moulding, the CNT suspension is delivered in a suspension of low viscosity reactive resin.

Conventional liquid moulding methods for the introduction of nanotubes within a composite component suffer from several limitations such as cake filtering, long range filtering, elevated viscosity, change in resin cure kinetics. These factors can affect the flow and the homogeneity of the CNT distribution within the part. Examples of vacuum-assisted resin transfer moulding to introduce CNT-based resins within a composite part have been reported in the literature [45, 46, 47]. However, increased viscosity and filtration, due to the presence of the CNTs, limited the process efficiency. Another drawback of the process is that the flow of the resin during impregnation tends to align the CNTs parallel to the fibre orientation, the least desirable orientation for enhancing the matrix-dominated composite performance [48]. Owing to these process limitations, the content of CNTs in LCM manufacture is limited to around 0.5% wt. This is lower than required for the specific application, which is at least 5-10 wt.% [13]. These loadings are sufficient to form conductive network, but the efficiency of inductive heating may be low due to low conductivity.

An alternative method of integrating additives utilises additive manufacturing concepts. In liquid resin printing, low viscosity reactive resin is injected to a dry textile preform through a fine needle (typically 300-500 μm). Every injection creates a thin layer of impregnated reinforcement in the plane of the textile preform. The injected solution spreads through the thickness of the preform due to capillary forces and lower in-plane permeability. A series of injections through thickness creates an impregnated patch within composite laminates, which is then consolidated under elevated temperature and pressure and cured. This concept can be used to deliver CNT in liquid resin [49, 50]. Because of the shorter flow lengths, higher fraction of CNT can be delivered. The sequential through-thickness resin delivery helps to form of percolation network [50]. The process can be easily automated and delivered using conventional resin dispensers or bespoke robotic applicators.

The feasibility study of high precision injections through the thickness of a preform was carried out by Ivanov *et al.* [49]. This was done to validate the liquid resin printing as a viable manufacturing method to introduce nanofillers within a composite laminate for specific localised properties and applications [49]. The proof of concept was conducted and validated for one preform type, although applicable to other textile preforms. This manufacturing method provided the precise delivery of a liquid resin into a bulk preform through local and highly controlled injections [49]. The injection pattern can be modified and tailored to meet the application requirements. Several aspects such as the contrast of longitudinal and transverse yarn permeabilities, the action of intrayarn capillary forces and the non-uniform unsaturated flow needs to be accounted for. Microporosity is caused by unsaturated dual-scale flow. The solution to this would be an optimised consolidation procedure, which was studied at the University of Bristol [49]. However, this issue is not fully resolved and requires further optimisation procedure to model the possible scenarios by considering the internal preform configuration, the injection printer settings and the physical properties of the polymer resin system. The main advantage of the liquid resin printing technique is the precise control over the injection variables, particularly injection speed and therefore the resin pressure gradient around the needle [49].

Growth of carbon nanostructures, particularly CNTs on fibrous substrates, also known as grafting, can be used for introducing MWCNTs on to the surfaces of treated carbon fibres and, therefore, into fibre reinforced composites (FRCs) [51]. This is aimed at increasing mechanical and/or multifunctional properties (such as damage sensing). The process might avoid the contamination of carbon fibres by catalyst needed for the growth of CNTs by chemical vapour deposition (CVD). Qian *et al.* [48] worked on CVD synthesis and grafting of carbon nanotubes on to structural IM7 carbon fibres. The grafting process led to an enhancement of surface area and a moderate decrease of the fibre tensile strength. The latter is mainly due to the dissolution of iron particles on to the carbon fibre surface during the high temperature growth reaction. CNT grafting also showed good wettability by the polymer.

However, several drawbacks could be encountered due to the carbon nanotube grafting through forest growth. Lomov *et al.* [51] investigated the compressibility issues of CNT forest-grafted textiles for use in composite applications. CNT grafting caused an increase in compression resistance of the textile samples manufactured with alumina fibres. Consequently, the fabric thickness increased as well by increasing the aligned CNT grafting load. Moreover, aligned CNTs showed higher thickness increase than random CNT grafting at the same CNT volume fraction and applied pressure. In conclusion, CNT-grafted fibre

composites were characterised by lower compressibility, therefore affecting the laminate thickness.

2.4 Functionalisation of CNTs

As discussed previously, introduction of CNT additives may require a fine-tuning of their position within the structure. Static magnetic field could enable their motion if the CNTs were susceptible to a magnetic field. This can be realised through grafting, which relies on the chemical installation of particles on the outer surfaces of the nanotubes to provide specific functionality [52]. Several methods are used to functionalise additives and used mostly in the context of fuel cells, electrochemical sensors and catalysis [52]. Metal functionalisation by means of implanting nanoparticles onto the CNT walls can enable the nanotube susceptibility to external stimuli. This section explores two types of approaches to CNT grafting: physical functionalisation and chemical functionalisation.

2.4.1 Physical functionalisation

Physical functionalisation is the deposition of additive particles on a substrate through the generation of physical bonds, without the involvement of chemical bond generation between the additive and the substrate. It can be used with the purpose of introducing nanoparticles on to the nanotube walls without the creation of chemical bonds such as covalent bonds.

Thermal evaporation represents a well know technique able to achieve physical functionalisation. This process was used in several research works to graft carbon nanotubes. Chrissanthopoulos *et al.* [53] employed the thermal evaporation method to grow zinc oxide nanostructures on to MWCNTs for semi-conductor applications. Deposition time and substrate temperature were changed and their effect on the final properties of the coating was assessed. The use of chemical routes for the functionalisation of CNT will be treated in the next paragraph to achieve higher and more homogeneous coating extent on the CNT walls and ends.

2.4.2 Chemical functionalisation

2.4.2.1 Electroless plating

The electroless plating technique is discussed in this section. Functionalised nanofillers can be obtained by modifying the nanotube surface by oxidation process. Carbonyl, carboxylic and

phenolic groups are therefore introduced on to the filler surface and then acting as nucleation active sites for the deposition of metals or metal compounds onto the filler [20, 54, 55, 57]; activated nanofillers are required for the specific process.

Ang *et al.* [57] optimised the process to achieve densely functionalised CNTs by means of a single-step activation process. Oxidised nanotubes were introduced in a $\text{PdCl}_2/\text{SnCl}_2$ colloidal solution to activate them with the introduction of tin and palladium on to the nanotube walls. 1 M HCl accelerator was used to remove the nanotube protective layer, therefore providing a greater surface area for the Pd-Sn catalytic sites. This was followed by immersion in the electroless plating bath, which involved the metal deposition on to the Pd-Sn catalytic sites. Metal clusters then acted as further catalytic nuclei for additional metal functionalisation on to the nanotubes.

Goel *et al.* [58] focused on the electroless plating of grain-oriented electrical steel. The aim was the reduction of the specific total power loss and magnetostriction. An electroless deposition of Co-Ni-P was carried out and assessed, showing improved coating performance for electrical steels, both in terms of reduced coating thickness and magnetic properties. The results from this work are summarised in Fig. 2.1, where the effect of the pH on the coating performance is highlighted as the pH affects the redox reactions involved in the electroless plating technique and therefore the coating composition can be changed. The process will be repeated in the current study [58] and pH conditions will be carefully monitored to achieve the best final coating properties for the CNTs.

Caturla *et al.* [59] studied the electroless plating technique to provide graphite with copper and nickel functionalisation. Graphite required surface activation before the electroless copper deposition. However, the distribution of the palladium as activating agent on the graphite surface, was inhomogeneous due to the hydrophobic nature of graphite and the large number of pores of different sizes. This effect can be mitigated at increasing metal coating thicknesses. Moreover, copper and nickel-plated deposits are characterised by different microstructures, fraction of the uncovered pores will cause the graphite to be exposed to the external environment. A solution to this problem was to conduct the electroless nickel-plating on top of a copper layer. This led to an almost complete coverage of the pores by the nickel plating.

The electroless plating procedure involves three main steps: sensitisation of the oxidised nanotubes, activation, and finally the metal deposition step. Li *et al.* [20] worked on attaining nickel coated carbon nanotubes where the nanotube activation was achieved in two steps. The

initial adsorption step of a tin sensitizing layer on to the nanotube walls was followed by the introduction of palladium on to the sensitizing layer.

Kong *et al.* [60] successfully carried out the electroless plating of nickel on to MWCNT walls; the latter were grown through CVD. Continuous and dense plated nickel layer on MWNTs were obtained after the steps of MWCNT purification, sensitisation and activation. TEM analyses showed nickel nanoparticles deposited around catalytic centres on MWNTs and a thin and discontinuous plated layer after 15 minutes of reaction time. Extended reaction times led to elongated plated islands, which grew both laterally and vertically according to the self-catalytic effect, therefore, thicker plated layers could be obtained. The electroless plating of MWCNTs is mainly affected by the high density of uniformly distributed catalytic nuclei on the nanotube surface, which in turn modifies the performance of the final MWNTs reinforced composite component.

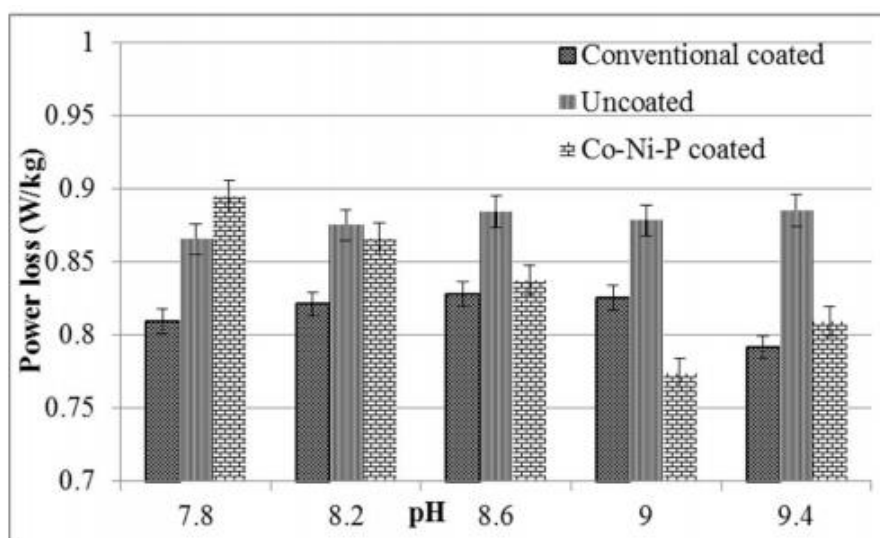


Fig. 2.1. Effect of pH on power loss measured at 1.5 T and 50 Hz frequency [58].

2.4.2.2 Other chemical functionalisation routes

CNTs can be grafted by means of other chemistry-based processes and has Hirsch [61] reviewed the main approaches to the functionalisation of SWCNTs. Increasing curvature of the carbon filler leads to higher extent of addition reactions because of the pyramidalisation of the sp^2 -hybridised C atoms. SWNTs are characterised by graphitic sidewalls with defects. Therefore, their curvature is not sufficient for direct addition reactions. Moreover, SWCNTs are poorly dispersible and tend to cluster, thus SWCNT walls can be functionalised covalently by using high reactive reagent contents. The functionalisation process affects the electronic properties of the SWCNTs by decreasing the electrical conductivity.

SWNT sidewalls are assumed to be inert and so the fluorination process was carried out by using elemental fluorine to create covalent carbon-fluorine bonds, which was confirmed through IR spectroscopy. Wet chemistry could be used after dissolving the fluorinated SWCNTs in alcohol through ultrasonication [62, 63]. The direct SWCNT wall functionalisation with organic groups is possible by reactive species such as nitrenes, carbenes, and radicals [64, 65]. SWCNTs were functionalised by reaction with azomethynylides [66]. High degrees of functionalization of the pyrrolidines caused high solubility in organic solvents.

Chemical routes can therefore be employed successfully for the functionalisation of nano-fillers such as CNTs, which will be explored in the next chapters of the present work. This project focuses on the electroless plating technique as a means of functionalising the walls of the CNTs, as this technique can potentially provide high degree of functionalisation within limited time and accessible experimental conditions.

2.5 Nano-filler alignment

The alignment of nano additives such as CNTs within a composite part might lead to potential benefits for the through-thickness properties of the laminate. The main benefits to the out-of-plane properties relate to the creation of electrically conductive networks, which can create connections between the composite plies. Therefore, this can overcome the electrical insulation layer represented by the resin layers present between the fibre layers in the case of carbon fibre composites. However, the presence of electrically conductive networks could lead to electrical conduction otherwise not possible in the case of glass fibre reinforced polymers. The main purpose of the alignment of nano additives is the enhancement of the local electrical conductance of the non-conductive polymer resins. Another effect of the alignment of nano additives within the host matrix could be the improvement of the overall mechanical and electrical properties of the nanocomposite.

Shear force alignment of nanofillers such as MWCNTs was experimentally verified to increase the overall mechanical properties of the components along the flow direction [67]. This effect was achieved through the generation of an aligned network of nano fillers. However, the main drawback was a decrease in the transverse properties [67]. The mechanical manipulation of nano additives could be potentially employed to locally improve the mechanical properties in the context of repair. On the other hand, the implementation of this process might prove hard to achieve.

The application of external AC/DC electric fields [68] and ultrasonic waves [69] was then performed to overcome the decrease in the nanocomposite transverse properties related to shear force alignment.

2.5.1 Electric field alignment

The general principle of nanofiller orientation towards the external electric field direction relates to the induced dipole moments acting on excess charges of the filler. This triggers the rotation and the orientation of the inclusion [70]. A schematic of the alignment effect for a polarised cylindrical particle in an electric field is shown in Fig. 2.2.

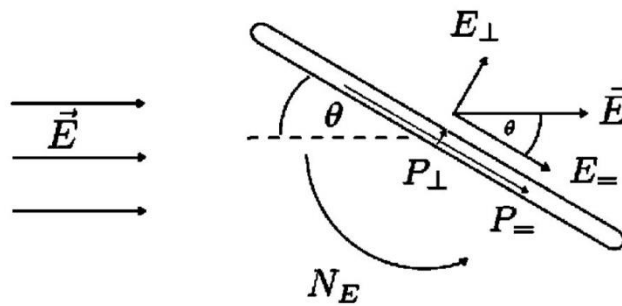


Fig. 2.2. Schematic illustration of a polarised cylindrical particle in an electric field [29].

An example of electrically induced alignment of carbon nanofibres (CNFs) in epoxy resin was studied by *Prasse et al.* [68]. Preliminary analyses were carried out to assess the influence of the electric field frequency on the conductivity of the cured samples. Results showed an almost total independence of the conductivity from the frequency in the range between 50 Hz and 10 kHz. Electric anisotropy properties of the cured samples in the parallel and perpendicular directions to the electric field were also assessed [68].

Fig. 2.3(a) shows the initial distribution of the CNF as 0.2 wt.% in the pure amine hardener at a frequency of 1 kHz. CNFs orient preferably towards the electric field direction. AC conductance measurements were carried out, and increasing conductance is strictly related to the CNF conductive network formation [63]. The formation of a conductive network *via* AC field could be exploited to manipulate magnetically sensitive nanofillers for repair applications. Fig. 2.4(b) shows the alignment of single fibres and fibre agglomeration after 1 minute of exposure to the electric field. A preferential fibre orientation towards the electric field direction can be observed. CNF orientation is then related to the torque M generated

through the interaction force between the dipole moments. The torque M can be calculated as follows:

$$M = m(E) \times E . \quad (2.1)$$

The electric anisotropy of the CNF/bulk material system was investigated by applying an electric field of 100 V cm^{-1} with a frequency of 50 Hz throughout the entire curing process of the samples. Fig. 2.5 shows the results of the investigation. The dotted line shows the 0.2 wt.% of CNF with no evidence of electrical percolation. Electrical percolation can be observed parallel to the external electric field at 0.5 wt.%. CNF network is formed at 0.75 CNF wt.% both in the parallel and in the perpendicular direction to the externally applied electric field. From CNF content of 1 wt.%, a maximal resistance anisotropy of about 10 can be observed. This result can be compared to the behaviour of carbon black/epoxy composites. The high CNF aspect ratio can be the cause of the increasing anisotropy [68]. Park *et al.* [71] analysed the alignment of SWCNTs within a photopolymerisable monomer. This solution was then transferred to the alignment and photopolymerisation setup with electrodes on two narrow sides. A schematic of the experimental setup is shown in Fig. 2.6.

AC field parameters such as electric field strength, application time and frequency were varied to analyse their influence on the SWNT orientation. Blue light was used to start the polymerisation reaction and freeze the alignment together with the application of the electric field.

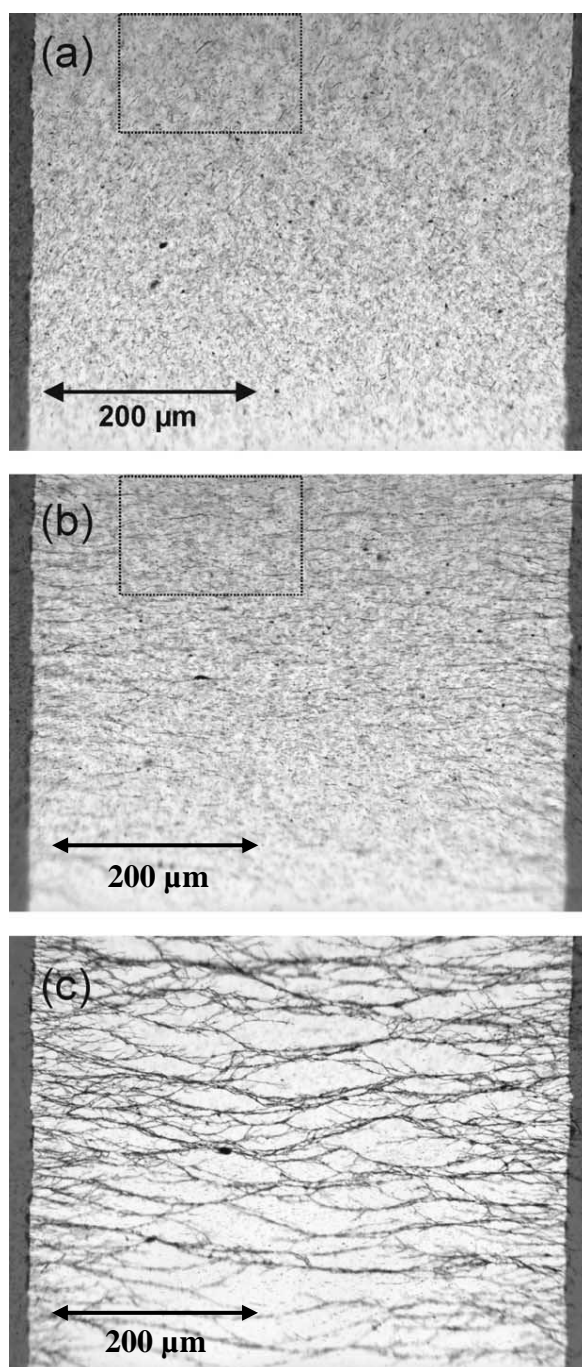


Fig. 2.3. Network formation of 0.2% CNF dispersed in the amine curing agent in an AC electric field of 400 V cm^{-1} and 1 kHz, before (a), 1 min (b) and 30 min (c) after the application of the field [68].

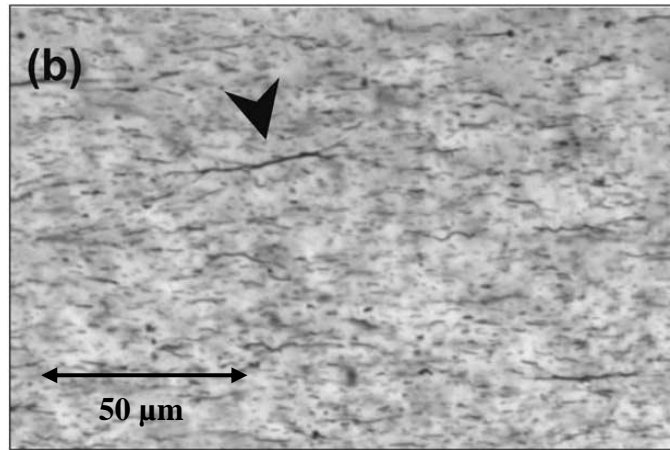
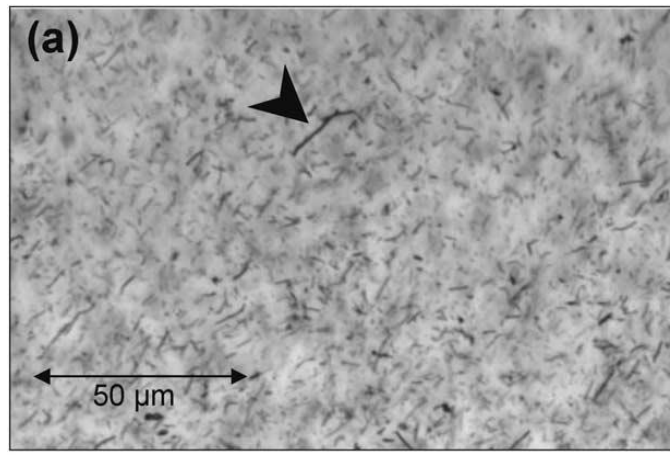


Fig. 2.4. Magnification of the single fibre alignment and fibre agglomeration after 1 minute of exposure to electric field [68].

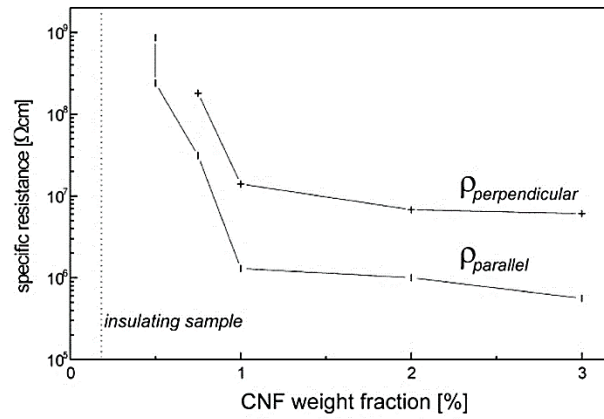


Fig. 2.5. Specific resistance as a function of the CNF weight fraction in the cured composites for the directions parallel and perpendicular to the electric agglomeration field [68].

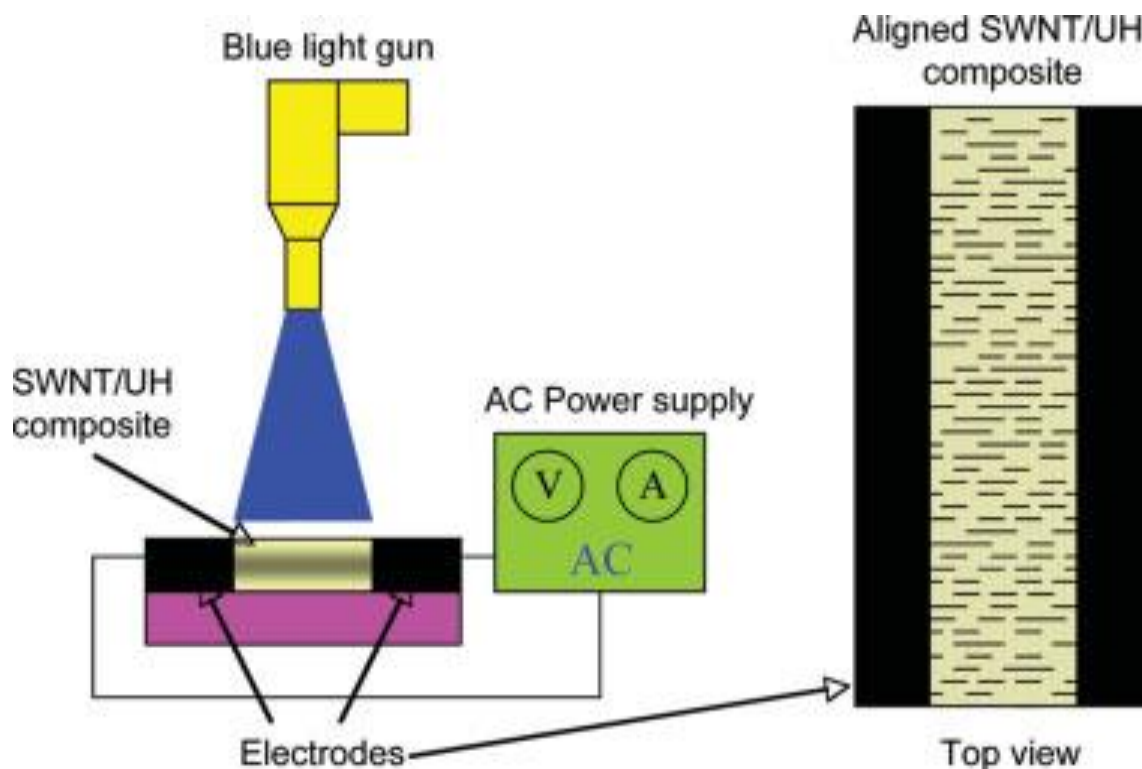


Fig. 2.6. Left: experimental setup of photopolymerisation of SWNT/UH composite under an electric field; Right: top view of the alignment cell [71].

Electric field strength optimisation was carried out by constantly applying the electric field for 10 minutes and by using two AC frequencies, 100 Hz and 10 kHz. The electric field strength was varied as a step function to simulate different processing conditions. The main result from the analyses was that the degree of alignment was strongly dependent on the applied electric field for both AC frequencies used, 100 Hz and 10 kHz. High levels of voltage tended to influence the alignment negatively due to excessive thermal energy. This could lead to disruption or bending of the aligned nanotubes [71], which is undesired for nanotube network formation for the scope of CNT manipulation of this work.

Martin *et al.* [70] used the same electrical approach to assess the influence of the applied electric field on CDV-grown MWCNTs in epoxy resin during the curing process. Epoxy composites were manufactured with 0.01 wt% MWCNTs, which is over the bulk percolation threshold under optimal aggregation conditions [70]. Samples were there exposed to DC and sinusoidal AC fields of 100 V/cm. AC fields were applied at a constant frequency of 1 kHz [70]. Optical micrographs showed a dependency of the nanotube network structure on the field type and the application time. Under DC electric field conditions, some nanotubes appeared to move towards the anode under electrophoresis as shown in Fig. 2.7. This was due

to the presence of negative nanotube surface charges. Successive nanotube discharge occurred with subsequent adsorption onto the anode. The final nanotube network shows relatively strong nanotube agglomeration on the anode possibly due to lower steric three-dimensional hindrance [70].

A more uniform and aligned nanotube network was achieved under AC field conditions, but with a slower initial onset of around 10 minutes. This can be associated with the polarisation of the CNTs which leads to an additional attraction between dispersed individual nanotubes and/or existing network branches through dielectrophoresis [67]. Therefore, the nanotube will move towards the lower field strength region at a terminal velocity if subjected to a force F . The nanotube movement was triggered through the application of the electric field. The curing process of the epoxy resin was then carried out by applying UV light source to freeze the achieved alignment.

By analysing the experimental results, a higher alignment towards the electric field direction next to the electrodes can be observed from the sample fracture surface, as shown in Fig. 2.8. The alignment achieved in the aforementioned SEM image refers to an applied voltage of 250 V peak to peak. Under frequency conditions of 100Hz, positive dielectrophoresis occurred, with the nanotubes moving towards the electrodes. Therefore, the dielectrophoretic force exceeds the polymer matrix drag force. As previously mentioned, polarisation and interaction among the nanotubes are the driving processes for the formation of the nanotube network. This affected the mechanical properties of the MWCNTs/epoxy samples in terms of Young's modulus and hardness [67].

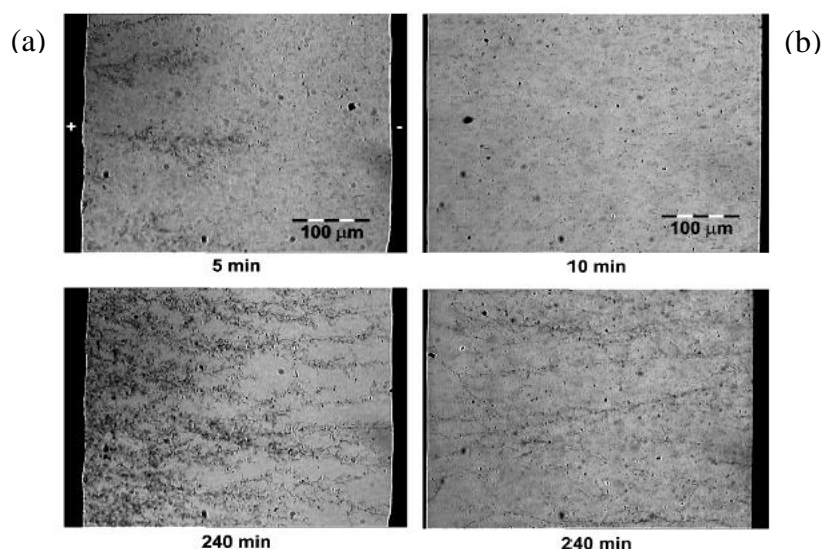


Fig. 2.7. Transmission optical micrographs of epoxy composites containing 0.01 wt% MWCNTs during curing at 80 °C in a (a) DC field and (b) AC field of 100 V/cm [61].

The Young's modulus showed a significant increase with the MWCNTs loading fraction both for random and aligned MWCNTs/epoxy samples, as shown in Fig. 2.9. Mechanical properties of aligned MWCNTs/epoxy composites were higher than randomly distributed composites; this can be enhanced with an increasing MWCNT content in order to optimise the nanotube network [67].

Remillard *et al.* [72] presented a mechanism to align MWCNT on a porous substrate by applying an external electric field and vacuum filtration. The resulting coating is conductive and characterised by lower resistance in the aligned direction compared to the direction perpendicular to the alignment.

A quadratic dependence of alignment on the strength of the electric field, MWCNT concentration, and total number of MWCNT was discovered. The best alignment condition was a MWCNT concentration of 0.01 wt.%. The conductivity of the CNT coating on the PVDF membranes compares favorably with other composite materials. Samples prepared with 0.01 wt% CNT had resistance on the order of 10^{-2} S/m. This alignment procedure also suggested several advantages over existing techniques, such as lower voltages to create polymer-CNT composites compared to methodologies reported in the literature, which allows for the process scale-up. Moreover, a dense network of MWCNT can be obtained with this process, with the deposition density easily monitored and tailored. Also, the solvent used for

the MWCNT suspension is insoluble in the polymer matrix. Aligned MWCNT coatings can be used for several applications such as fuel cells and water filtration devices.

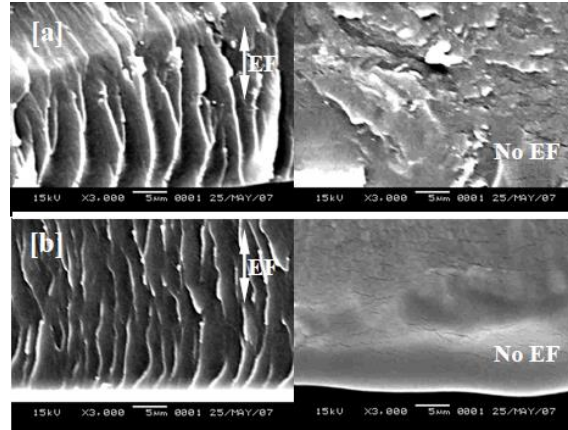


Fig. 2.8. SEM images of MWCNTs/epoxy composites with different nanotubes loading fractions [a] 0.5wt% [b] 1wt% [67].

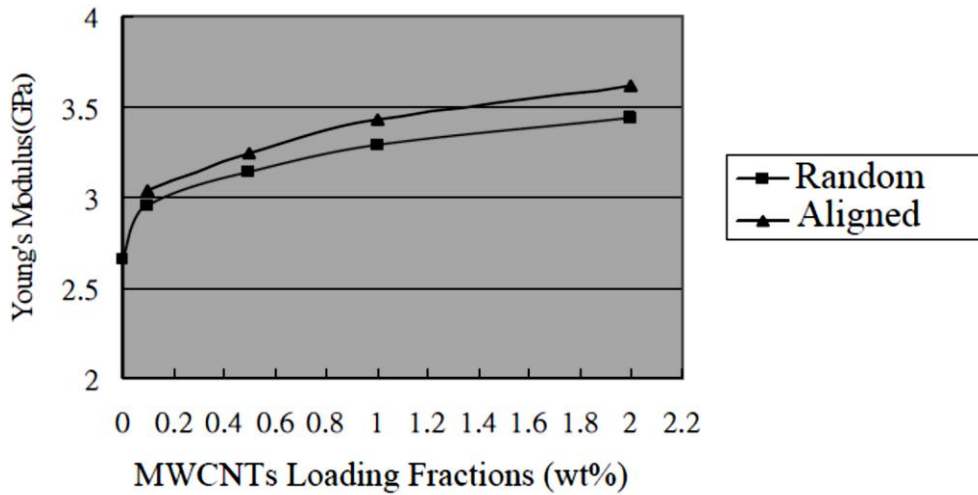


Fig. 2.9. Reinforcement effect on modulus in varied nanotubes loading fractions [67].

2.5.2 Magnetic field alignment

Previous work from Kimura *et al.* [7] assessed the magnetic alignment of MWCNTs by evaluating the diamagnetic susceptibilities parallel ($\chi_{||}$) and perpendicular (χ_{\perp}) to the tube axis. MWNTs align themselves to the magnetic field direction when the rotational energy exceeds the thermal energy. The latter tends to randomise the nanotube distribution. A better MWNT alignment is represented by $|\chi_{\perp}|$ larger than $|\chi_{||}|$ [7]. The analyses were based on the application of a constant 10 T magnetic field to unsaturated polyester mixed with MWNTs. The nanofiller dimensions were diameters of around 5-50 nm and lengths of hundreds of nanometres and micrometres. The main conclusion from the values of parallel

and perpendicular diamagnetic susceptibilities refers to their difference ($\chi_{||} - \chi_{\perp}$). Excessive addition of MWNT reduces this parameter referring to a decrease of magnetic anisotropy with increasing MWNT concentration. This can be related to insufficient MWNT dispersion due to nanofiller agglomeration. This latter phenomenon is associated to tube-tube van der Waals interactions which hinder the MWNT rotation along the externally applied magnetic field. One of the possible solutions to the inefficient MWNT dispersion could be the chemical functionalisation of the fillers [7].

Another interesting study has been carried out by Erb *et al.* [8] as it shows the potential of magnetically driven nano additives within viscous mediums after being subjected to metal functionalisation. This work closely links with the scope of this project, as magnetically sensitive nanotubes will be manipulated *via* external AC field to be positioned locally for repair applications. Composites were manufactured by using suspensions containing magnetite-coated alumina platelets, thermoplastic polyurethane elastomer and polyvinylpyrrolidinone. The coating was obtained by introducing the reinforcing particles to an aqueous suspension containing 12-nm iron oxide nanoparticles. Owing to the opposite surface charge of the oxide nanoparticles at a specific pH, coating absorption could be achieved through electrostatic interactions and short-range van der Waals attraction. Coating was applied to 7.5 μm long, 200 nm thick alumina platelets and 10 μm long, 1 μm thick calcium sulfate hemihydrate rods. They were positively and negatively charged at the surface under pH equal to 7. Ferrofluid suspensions were used for the coating absorption [8].

The experimental results were in good agreement with the modelling analysis in terms of magnetic field required for the filler alignment. Optimum geometry of reinforcement particles could minimise the use of iron oxide particles (0.01 vol% and 30 mT). The so called ultramagnetic response (UHMR) of the coated anisotropic reinforcing particles is particularly interesting for applications involving specific nanofiller orientations at the surface of the final component. This can be achieved by dispersing UHMR anisotropic reinforcing particles in a fluid and aligning them to the magnetic field direction. The next step would be the consolidation of the alignment via solvent evaporation, molten matrix cooling or temperature/light induced polymerisation in case of monomeric solution as matrix [8]. Different orientations were obtained by alternating the direction of the applied magnetic field. Some examples are shown in Fig. 2.10.

Magnetic field orientation can therefore induce specific functionalities within the component and tailor its mechanical, electrical and optical performances in specific directions. The composite sample containing 20 vol.% platelets aligned to the magnetic field direction shows

around 63% and 86% higher yield strength than pure matrix and the platelets aligned perpendicular to the magnetic field, respectively. Moreover, the average elastic modulus of the parallel-aligned platelet sample was almost three times higher than pure polyurethane matrix, whereas a slight improvement in properties compared with perpendicular-aligned platelet composites could be observed [8]. Therefore, the potential improvement in mechanical properties related to the manipulation of magnetic nano additives was highlighted in this work. The positioning of nano additives could therefore be exploited at the bondline between the undamaged composite component and the patch during the repair process. This approach could strengthen the bondline and, consequently, restore the mechanical performance of the part.

Another work, conducted Choi *et al.* [9], investigated the magnetic alignment of SWCNTs in viscous medium. Purified SWNTs (*Carbon Nanotechnologies*) were dispersed in ethanol through room temperature sonication for 30 min. Ethanol was then evaporated *via* ultrasonic hot water bath at 50 °C for another 30 minutes. PH3660 hardener was then added and the mixture was stirred mechanically for 5 min. The resin/hardener mix ratio for each sample was 4:1 in weight [9]. Samples of neat epoxy and compositions of epoxy 13 wt% SWNT were subjected to magnetic fields of 0, 15, and 25 T. The samples were processed for 2 h at room temperature, followed by 2 h at 60°C, with the magnetic field held constant for the entire 4 h period [9].

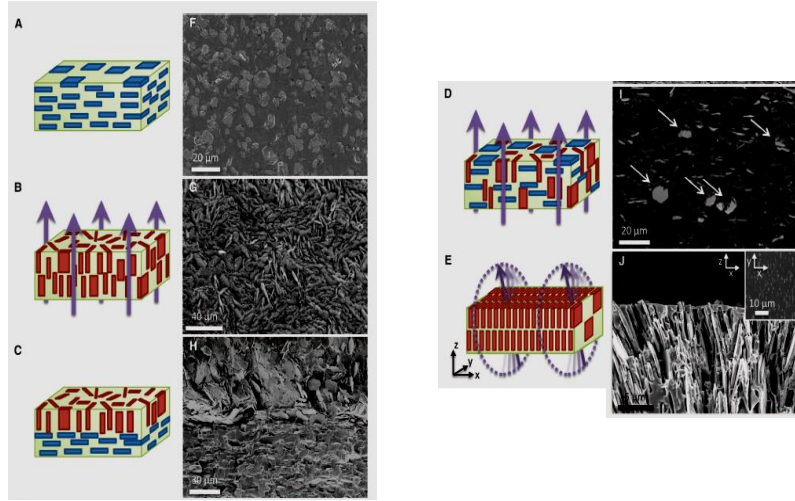


Fig. 2.10. In-plane and out-of plane alignment of UHMR alumina platelets in polyurethane-based composites [8].

Fig. 2.11 and Fig. 2.12 show the mechanisms for the electrical transport. A cooperative effect of magnetic torque and hydrodynamic torque associated with the polymeric chains drag forces can be related to the main results shown in the graphs. In particular, a significant decrease of electrical resistivity can be found with the addition of 3 wt.% of SWCNTs in epoxy resin. Further SWCNT alignment led to a decrease of resistivity as well as the nanotube addition. However, a weak thermal dependence of electrical resistivity anisotropy was obtained [7].

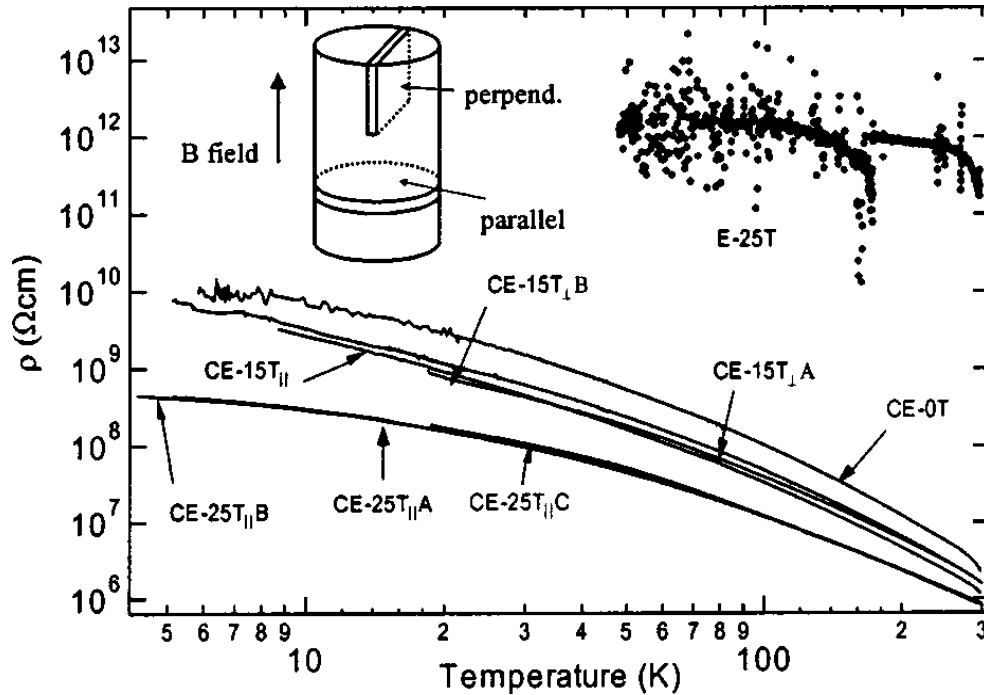


Fig. 2.11. Temperature dependence of resistivity of magnetically processed CNT-epoxy composites [9].

The temperature dependence of thermal conductivity for the composite materials (CE-0T, CE-25T_{II}) and control epoxy (E-25T) is shown in Fig. 2.13. An addition of 3 wt% SWNT could increase the thermal conductivity by up to 300% even without applied magnetic field. The thermal conductivity is also enhanced by the application of a magnetic field. This can be attributed to the effect of bundling due to van der Waals forces between the nanotubes [9].

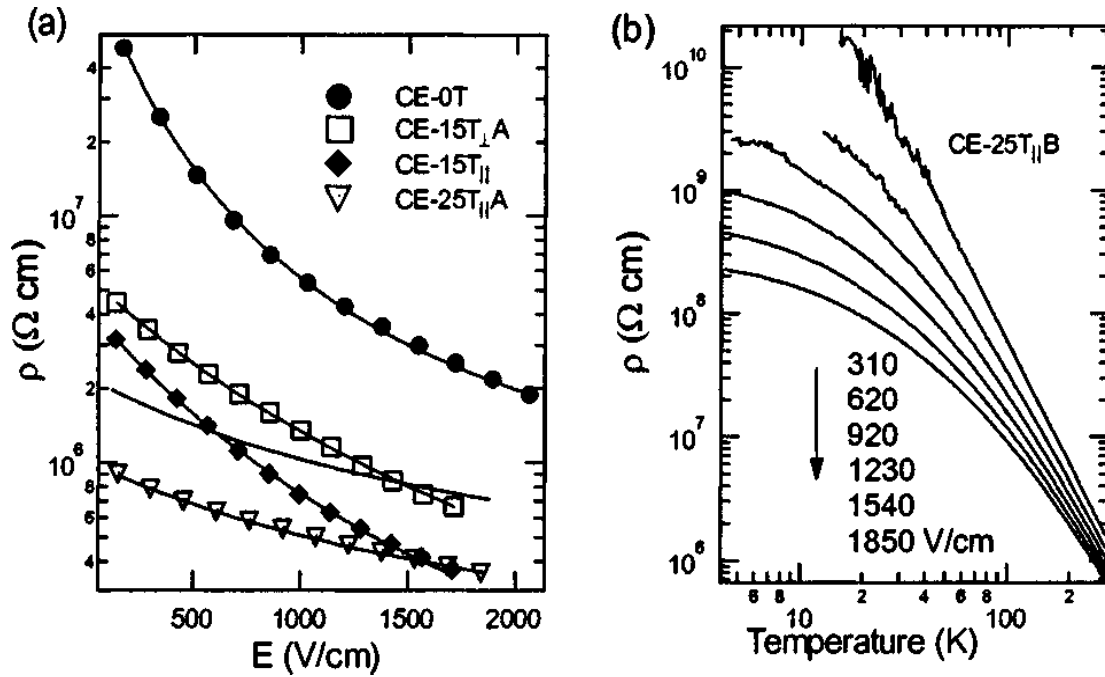


Fig. 2.12. Room temperature resistivity as a function of (a) electric field and (b) electrical resistivity of CE-25T_{II}B as a function of temperature at different electrical fields [9].

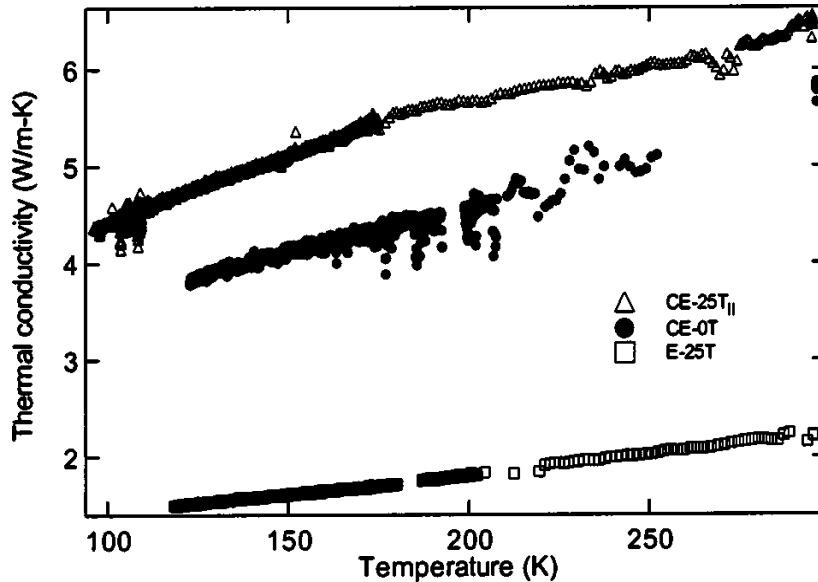


Fig. 2.13. Thermal conductivity of CNT-epoxy composites magnetically processed at 0 and 25 T, compared with neat epoxy sample (processed at 25 T) [9].

2.5.3 Ultrasonic alignment

Another technique worth highlighting for the manipulation of nano additives within a medium is the application of ultrasonic waves. Ultrasonic alignment of fillers within a host medium was considered in the literature as potential means to tailor the filler distribution and locally modify the sample properties.

Lim *et al.* [69] reported the acoustic manipulation study for the parallel alignment of MWNTs on solid substrates such as aminopropyltriethoxysilane (APTES, $\text{H}_2\text{N}(\text{CH}_2)_3\text{Si}(\text{OCH}_2\text{CH}_3)_3$)-functionalised Si substrate. The mentioned nanotube assembly can be applied to other structures such as nanowires and can be achieved *via* a novel solution-based acoustic manipulation method. The contributions to the movement of nanotubes in the suspension under investigation relate to the acoustic radiation and the streaming of the assembly fluid due to the application and transmission of ultrasounds through a fluid. To facilitate the process, the substrate is preferably functionalised [69]. MWCNTs (Chengdu Organic Chemistry Co., Ltd.) were therefore -OH functionalised. Their length and diameter were 2-5 μm and 10 nm, respectively. Sodium dodecyl sulfate (SDS; $\text{CH}_3(\text{CH}_2)_{11}\text{OSO}_3\text{Na}$) was the surfactant used to allow for a more effective dispersion of MWNTs in water. Their concentration in SDS was 0.02 mg/ml [30]. The (100) Si substrate was cleaned in hydrofluoric acid (HF) and piranha solution ($\text{H}_2\text{SO}_4\text{:H}_2\text{O}_2$; volume ratio 7:3). Further silanisation with APTES was carried out under a dry nitrogen (N_2) atmosphere. 4 ml of APTES were heated at 80 $^\circ\text{C}$ to treat the Si substrate surface with APTES vapour flux for 2 minutes. The Si substrate was then cured for 20 minutes at 100 $^\circ\text{C}$ and immersed in 0.5 M aqueous hydrochloric acid (HCl) solution at room temperature for 10 minutes. This allowed for the conversion of NH_2 groups to NH_3^+ groups [69].

A schematic of the homebuilt experimental setup used for the acoustic assembly of MWNTs is shown in Fig. 2.14. A piezoelectric lead zirconate titanate (PZT) ceramic (Shanghai Institute of Ceramics) was used in thickness mode and an alternating electrical voltage was applied. The PZT piezoelectric cell then generated an acoustic wave within the MWNT aqueous dispersion. MWNT alignment was therefore reached by inducing external forces on the nanotubes through the solution [69]. Three setup configurations were used for assessing the assembly of MWNT. These are shown in Fig. 2.14. Fig. 2.14a shows the substrate placed perpendicular to one single radiation surface, whereas Fig. 2.14b shows the substrate bonded on top of a radiation surface. Fig. 2.14c relates to the combination of the two radiation surface configurations of Fig. 2.14a and 2.14b. Process parameters were carefully controlled to obtain the desired MWNT assembly and adsorption density on the substrate surface. Data post

processing involved the use of field emission scanning electron microscopy (FESEM) (JEOL JSM6700) [69]. Fig. 2.15 shows the SEM micrographs of the MWNTs aligned *via* ultrasonic waves at a constant voltage, 40 V for different PZT plate frequencies and following the configuration of Fig. 2.14a. A noticeable improvement of the nanotube adsorption on the substrate can be observed with increasing PZT vibration frequency (from 5 to 180 kHz, Fig. 2.15 a-d). The nanotube alignment slightly improved by increasing the vibration frequency from 5 to 100 kHz, although above 100 kHz such as 180 kHz the alignment decreases drastically as shown in Fig. 2.15d [62]. The large curvature of the nanotubes negatively affects the alignment although this geometrical feature does not relate to the application of the acoustic wave. This can be observed for several types of MWNTs grown and manufactured by different suppliers [7]. Fig. 2.15c shows that, under an applied voltage of 40 V and vibration frequency of 60 kHz, around 60% of MWNTs were within 10° deviation from the acoustic wave direction and more than 80% within 45° deviation [30].

The use of the PZT/substrate configuration (b) leads to a remarkable enhancement of the nanotube adsorption on to the substrate. However, the application of such acoustic waves perpendicular to the substrate surface does not contribute to the nanotube alignment [69]. The combination of configuration of Fig. 2.14a and 2.14b was studied to provide a better nanotube adsorption on to the substrate together with an enhanced nanotube alignment extent. Therefore, acoustic waves were applied both parallel and perpendicular to the substrate surface simultaneously as shown in Fig. 2.14c. Two PZT plates were then placed perpendicular and parallel to the substrate vibrating with the same frequencies (30, 60 and 100 kHz) and same voltage of 40 V [69].

By using the combined PZT configuration, nanotube alignment can be achieved exclusively at low frequencies of 30 kHz and 60 kHz as shown in Fig. 2.16 a-b. However, the achieved alignment does not match the same extent obtained with the configuration (a). This might be attributed to the interference of the two perpendicular acoustic waves with the radiation and drag forces in the desired nanotube alignment direction in the horizontal plane. Randomised nanotube orientation is instead achieved at higher frequencies of 100 kHz as shown in Fig. 2.16c. This might relate to the randomisation of the fluidic forces across the horizontal plane [69]. The study of ultrasonic alignment of nanotubes in viscous mediums can be of interest if combined with the simultaneous application of magnetic field in the same direction. This can substantially improve the nanotube alignment extent.

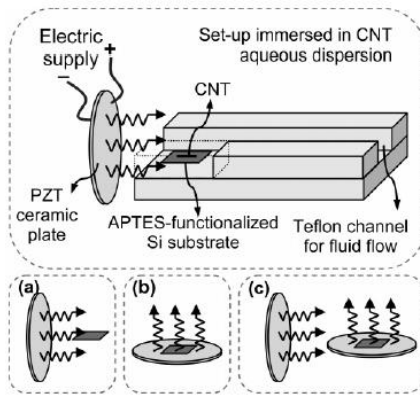


Fig. 2.14. Schematic diagram of the home-built setup for acoustic nanotubes alignment: (a) the substrate perpendicular to the radiation surface, (b) the substrate bonded on top of the radiation surface and (c) a combination of the “a” and “b” configurations [69].

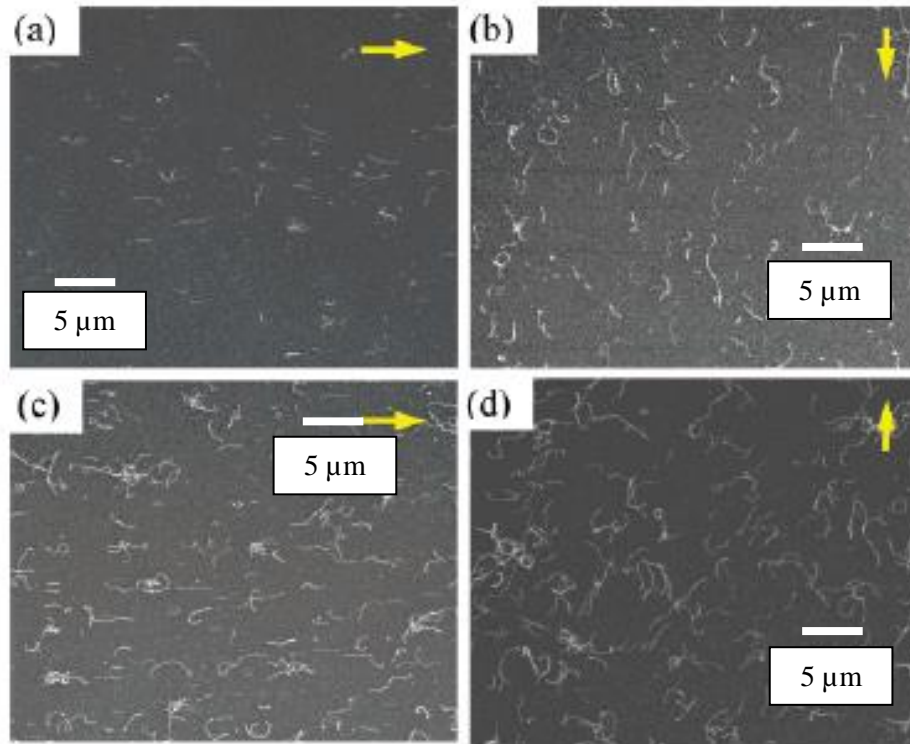


Fig. 2.15. FESEM images of the ultrasonically assembled MWNTs under an AC voltage of 40 V at (a) 5 kHz, (b) 30 kHz, (c) 60 kHz, and (d) 180 kHz to the piezoelectric transducer in accordance with the configuration (a) (arrows: acoustic wave direction) [69].

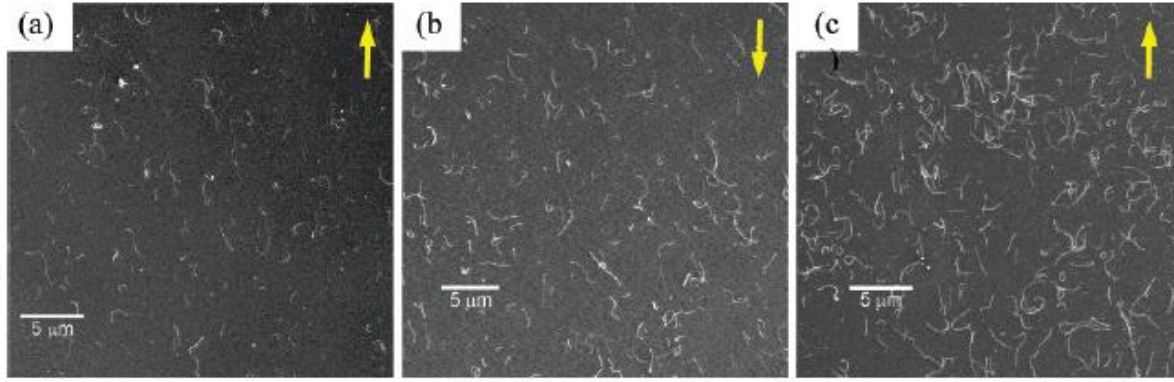


Fig. 2.16. FESEM images of nanotubes on the surface of the Si substrates: two piezoelectric transducers vibrating under an applied voltage of 40 V at (a) 30 kHz, (b) 60 kHz, and (c) 100 kHz (c) (setup c). Inserted arrows: direction of acoustic propagation [69].

2.6 Induction heating

Several heating mechanisms can be considered while discussing the induction heating phenomenon. The most relevant mechanisms are the eddy currents, Joule heating and related sub-mechanisms such as magnetic hysteresis and resistance at fibre crossovers. This section describes them in further detail.

2.6.1 Eddy currents

Another mechanism was previously mentioned as responsible of the induction heating phenomena together with Joule heating: the so-called eddy currents. Eddy currents are current loops formed by the alternating magnetic field externally applied to a magnetically sensitive particle; this mechanism is governed by Faraday's law [15]. This occurs at temperatures below the Curie point, above which the material is no longer ferromagnetic.

Carbon fibre-based composites are considered as low magnetic-permeability materials; therefore, hysteresis phenomena do not occur, and heat cannot be provided in the amount required for the resin cure process [18]. Creative geometries and conductive networks are necessary conditions to enhance the magnetic permeability of the composite structures and attain a synergistic effect of hysteresis and induced currents. These allow for the maximisation of flux field area responsible for the induced current loops [18].

Eddy currents can be described as “global” when they form large loop paths between adjacent plies, whereas micro eddy currents refer to the currents generated within the conductive fibres. The latter are usually negligible compared to the global currents [18].

The creation of conductive paths within cross-ply composites was attempted in the work by Kim *et al.* [18]. Electrical contact between the fibres of the cross-ply component was assumed to occur, although resistance at the junctions can be taken into consideration. This aspect leads to an additional heat dissipation contribution.

A schematic of the charge transfer mechanism is shown in Fig. 2.17. Specifically, a conductive loop made of two sets of two parallel carbon fibres in adjacent planes is reported. The current loop as rotational electromotive force is then induced through the application of an external magnetic field.

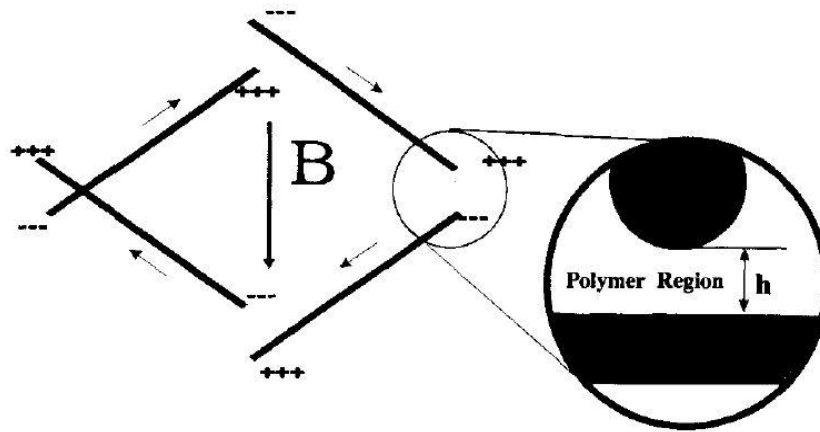


Fig. 2.17. Schematic of carbon fibre configuration showing induced current due to a transverse magnetic field [15].

The heat dissipation is then due to the Joule heating contribution along the fibres and the polymer resistance at the four junctions, with a different extent of contact between the fibres. The temperature of the aluminium substrate used for the experiments increased more rapidly when only the substrate was pre-heated rather than the case of an uncured patch placed on top of it. Specifically, temperatures of 120 °C could be reached within 30 minutes in the first case.

However, the generation of eddy current loops represents a more efficient mechanism for the heat dissipation. Therefore, faster cure rates can be achieved compared to the Joule heating phenomenon occurring along the fibres [15]. This is particularly true in case of maximisation of the electrical contact between the susceptors.

2.6.2 Joule heating

Joule losses from the nanofillers are referred to heat dissipation due to the induced currents running through the fillers. They behave as electrical conductors and their electrical parameter known as electrical resistance R_f can be used to estimate the heat generation extent. The electrical resistance can be calculated as follows (Ohm's law):

$$R_f = \rho_f \cdot \frac{l_f}{A_f}, \quad (2.2)$$

where ρ_f is the fibre electrical resistivity, whereas l_f and A_f are the length and the cross-sectional area of the fibres, respectively. Fig. 2.18 shows a schematic of the Joule heating contributions [16].

Joule heating phenomenon can be studied more in depth by analysing the nanoscale processes. While immersed in a viscous medium and subjected to an external magnetic field, the magnetic moments within the magnetisable nanofillers tend to spin and orient towards the magnetic field direction. This effect is known as Néel relaxation [13]. However, the whole nanoparticle can spin when it is free to rotate due to the low viscosity of the host medium. This effect is also known as Brown relaxation and can occur before the gelation point of the viscous medium (*e.g.* polymer melt) [13].

Network structure can be affected by the processes, which dominate the induction heating phenomenon. This reflects on the distance between conductive particles and, therefore, the crosslinking density. The final induction cured component will be characterised by modified thermal conductivity and volumetric expansion coefficient, together with altered hardness properties [13].

The work of Mas *et al.* [12] focused on nanotube conducting network generation in epoxy resin which would be suitable for repair of composite components *via* Joule heating. This can be an alternative to conventional oven cure processes.

To prove this concept, samples made of CNTs and graphene in epoxy resin were manufactured. *Elicarb* MWCNTs were provided by *Thomas Swan Ltd.* They were characterised by an average diameter of 10 nm and length of a few microns, with a resultant aspect ratio of around 100-1000. Reduced graphene oxide was supplied by *Granph Nanotech.*

This was manufactured through exfoliation process and reduction of vapour grown carbon nanofibres. LY 556 epoxy resin and XB 3473 hardener were purchased [12].

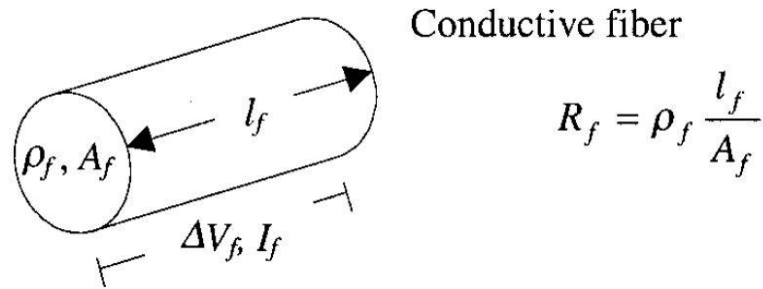


Fig. 2.18. Joule heating in conductive fibre as a function of the fibre resistance [16].

Two identical samples were cured through Joule heating and in the oven for 15 minutes at 180 °C. The glass transition temperature T_g was measured in the centre and the edge of the samples to estimate the gradients in properties. A gradient of 1 °C was observed for the Joule heating cured sample whereas the oven sample showed a gradient of around 11 °C [12].

Oven energy efficiency and Joule heating processes can be therefore compared. A sample of $13 \times 9.5 \times 9 \text{ mm}^3$ and 1.3 g could be cured by using 4.5 kJ (working at 4 W), whereas the oven used 3 MJ at 800 W to cure a sample of the same geometrical specifications. Joule heating can also exploit the exothermic heat generated by the curing process of the epoxy resin (around 350 J/g) [12].

The junction between susceptors can be described as a capacitor. The susceptors can be seen as electrical conductive plates whereas the polymer resin can be associated with the dielectric (insulator). Therefore, this situation can be modelled as an ideal capacitor connected to a sinusoidal voltage applied to the setup through the following equation

$$C = \frac{A}{d} \cdot \epsilon' = C_o \cdot \frac{\epsilon'}{\epsilon_o} = C_o \cdot \aleph, \quad (2.3)$$

where A is the cross-sectional area of the conductive plates, d is the distance between them, whereas ϵ' is the permittivity of the dielectric material, in this case the polymer resin. \aleph represents the relative dielectric constant of the material whereas ϵ_o is the permittivity of vacuum equal to $8.85 \cdot 10^{-12} \text{ F/m}$.

2.6.3 Introduction on induction heating

The inductive heating phenomenon was discussed in detail by Bayerl *et al.* [13] in an extensive review on the topic. The present literature review focuses on specific aspects of the induction heating process. Specifically, the focus is on:

- a) inductive curing in the context of repair and curing of epoxy precursors;
- b) the role of through-thickness electrical conductivity in curing of composites through eddy currents mechanisms;
- c) the role of consolidation pressure (fibre volume fraction) and preform architecture on intrinsic conductivity of carbon composites;
- d) the role of conductive additives in promoting through-thickness conductivity of carbon and glass composites;
- e) the geometry and weight fraction requirements of additives for effective inductive curing;
- f) inductive curing modelling.

The inductive heating phenomenon relies on the generation of a time-varying magnetic field through an inductive coil. The coil is crossed by electric current at a specific intensity after being supplied with high power alternating voltage. The resulting magnetic field will be characterised by an alternating behaviour at the same frequency of the electric current and voltage.

Part of the energy involved in the magnetic field generation and produced by the coil is dissipated as heat through resistive and inductive losses. This is particularly beneficial for induction welding [73, 74, 75, 76, 77] and melting/bonding [78].

The induction heating phenomena were assessed in terms of previously relevant literature work. The main advantages of this process are the heat losses reduction and the increased heating rates achievable with smaller interparticle distances (*e.g.* CNTs acting as internal heat suppliers under Joule effect and magnetic hysteresis) [12]. Other advantages are energy efficiency and cure extent homogenisation. During the Joule heating process, the entire electric energy contribution is converted into thermal contribution. This contribution is therefore available to the resin curing process. In the oven curing, convective and conductive phenomena are dominant for the heat transfer. Therefore, the high extent of heat losses related

to the high thermal mass of the oven compared to the samples reduces the energy efficiency [12].

The small interparticle distance (around 100 nm or 0.4 wt.% of CNTs in epoxy system) and the high nanocarbon surface area allow for incredibly high heating rates up to 740 °C/min [12]. This can be facilitated by a homogeneous dispersion of the nanofillers in the epoxy system. This might lead to the reduction of thermal gradients through the thickness of the component and, therefore, a more uniform cure extent compared to the oven process [12]. Two mechanisms are involved in the induction heating process: Joule heating along the fibres [12, 13, 14, 15] and eddy currents [15, 16, 17]. The induction phenomena can be triggered by the application of an alternating electromagnetic field whose frequency is in the kilohertz/megahertz range. These are related to the induction of eddy currents within the structure and the magnetisation phenomena of the nanofillers within the viscous medium. These effects can be assessed by using Maxwell's electromagnetic equations based on Faraday's previous work [13]. The introduction of susceptors within the viscous medium can be considered, to provide neat polymers with an enhanced electrical conductivity. As previously mentioned, they usually refer to carbon fibre fabrics, dispersed particles and particularly CNTs [13].

2.6.4 Inductive heating parameters

The main induction heating requirement for improved efficiency is the generation of closed electrically conductive loops. Within a composite structure, this condition could be achieved with a cross-ply layup. However, the susceptor volume fraction is required to exceed the electrical percolation. The main susceptor parameters influencing the resulting electrical performance are shown in Table 2.1 [13].

In this case, electrical conductivity plays a relevant role. This is strictly linked to the generation of electrical network which would enable higher levels of dielectric heating and more efficient eddy current loops across it. A factor influencing the efficiency of the induction heating is the energy field penetration depth δ which can be expressed as follows

$$\delta = \sqrt{\frac{\rho}{\mu \cdot \pi \cdot f}} , \quad (2.4)$$

where ρ and μ are the electrical resistivity and the magnetic permeability of the component, respectively. An increase in the field frequency f leads to a decrease of the penetration depth δ . This is detrimental for the homogenisation of the temperature and cure level through the thickness of the component, as the heat energy is limited to the surface and localised overheating can therefore be generated in combination with short coupling distance between susceptors [13].

Another important factor is the magnetic permeability of the component, which can be enhanced by functionalizing the susceptors with metal nanoparticles. This promotes higher hysteretic losses and, therefore, heat generation. Increase in thermal conductivity can be a byproduct of the nanofiller introduction within the host medium.

Induction setup parameters also affect the electromagnetic efficiency of the induction heating effect. These parameters are coil geometry, applied electrical power, coil current, frequency and coupling distance as shown in Table 2.2 [13].

Coil geometry requires specific design depending on the inductively heated sample geometry. However, magnetic field frequency and current are the most influent parameters on the overall efficiency of the inductive curing process. High frequencies (kHz-MHz range) can be used for thin samples, whereas thick samples could be affected by limited penetration (skin depth effect) at high frequencies. Faster heating could be ensured by the application of higher electrical currents through the inductors. However, local overheating could represent a drawback of excessive current levels.

Table 2.1. Susceptor parameters influencing the resulting electrical performance [13].

Property	Effect on heating
Curie temperature	Limiting effect (when hysteresis is dominant heating mechanism)
Density	A lower density is better for faster heating
Electrical conductivity	Minimum conductivity necessary to form conductive loop – a higher electrical conductivity promotes dielectric heating for fibres and fabrics
Heat capacity	The heat capacity should be minimized for faster heating
Magnetic permeability	A higher magnetic permeability results in higher losses and is promoting heat generation (esp. for particles)
Size, amount of domain zones (particles)	No general statement possible since complex aspect and dependent on other material and machine related parameters
Surface morphology	Possible shielding effects by surface contamination can lead to poorer heating
Thermal conductivity	A high thermal conductivity increases heating homogeneity

Table 2.2. Induction heating mechanisms [13].

Parameter	Effect on heating	Remarks
Coil geometry	Dependent on magnetic flux density	Coil geometries should be designed to fit the heating problem
Magnetic flux concentrators	Application usually leads to higher heating rates	Danger of inhomogeneous heating due to locally higher magnetic flux
Coupling distance	The smaller the coupling distance the higher is the heating effect	Homogeneous heating sometimes requires less efficient coupling distance (danger of local overheating)
Frequency	A high frequency is generally better for the fast heating of composites	Very high values limit penetration, also dependent on size for particulate susceptors, high-frequency generators less efficient
Inductor current	A high current leads to more power in the system and thus a faster heating	Risk of local overheating (micro-level)

As reported on Table 3, a reduced coupling distance can cause local overheating which decreases the temperature homogeneity and the cure extent in the final component. The same detrimental effect at the interface between host medium and susceptors can be encountered with an increasing inductor current [11].

Skin effect and local overheating need to be particularly accounted for to ensure a homogeneous heat distribution throughout the entire curing component. Skin effect relates to the limited penetration of the magnetic field through the thickness of the sample. A schematic of the skin effect is shown in Fig. 2.19. The skin effect can be attributed to the application of high frequency magnetic fields although high frequencies provide more power for the induction effect [13]. High field frequencies can lead to the generation of induced fields opposing the externally applied energy field and therefore reducing the extent of magnetic field influence over the component [13].

On the other hand, proximity effect refers to the presence of magnetically sensitive materials in the experiment region, which can interact with the energy field source. Magnetic field lines can therefore be deflected, and this can disturb the electromagnetic field causing the reduction of the efficiency and reproducibility of the test. For this reason, diamagnetic materials must be selected for the experimental setup such as polymers, austenitic stainless steel, aluminium or brass [13].

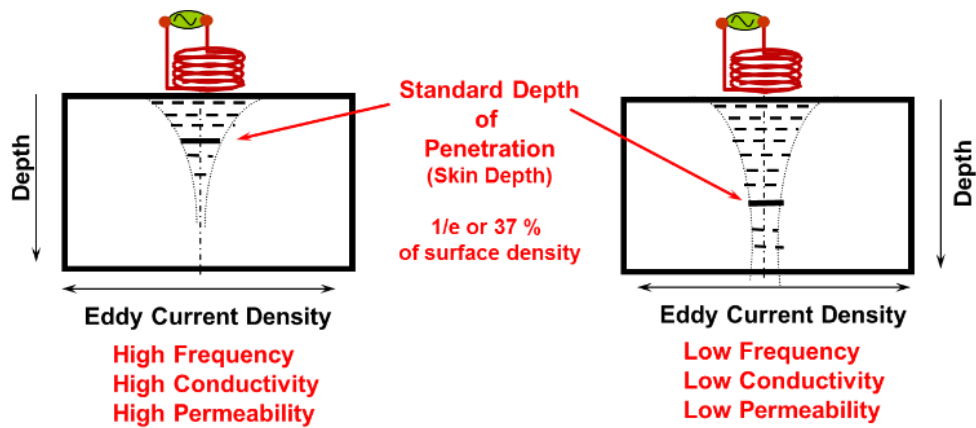


Fig. 2.19. Schematic of the skin effect and control parameters [13].

2.6.5 Induction heating literature

Several studies have been conducted to investigate the heat remotely generated by magnetic nanoparticles [78, 79]. Among them, the work from Tsamasphyros and Christopoulos [79] investigated the benefits of induction heating for polymer self-healing purposes, particularly

the outward heat generation from the inner surfaces. Another peculiar advantage of such technique is the local heat generation which selectively allows for localised curing of the matrix.

The experimental setup used in this work was a bespoke induction heating apparatus, EasyHeat 8310 (Ambrell). This featured a power output capacity of 10 kW, and a frequency range of 150-400 kHz (Fig. 2.20). The coils were specifically designed for the application, and the sample temperature profile was monitored through IR camera.

Their investigation focused on assessing the most efficient heat generation rate among different nanoparticles such as iron nanoparticles with a carbon layer, iron oxide nanoparticles and cobalt iron oxide nanoparticles. This was carried out together with the assessment of the minimum nanoparticle concentration required to trigger the self-healing mechanism.

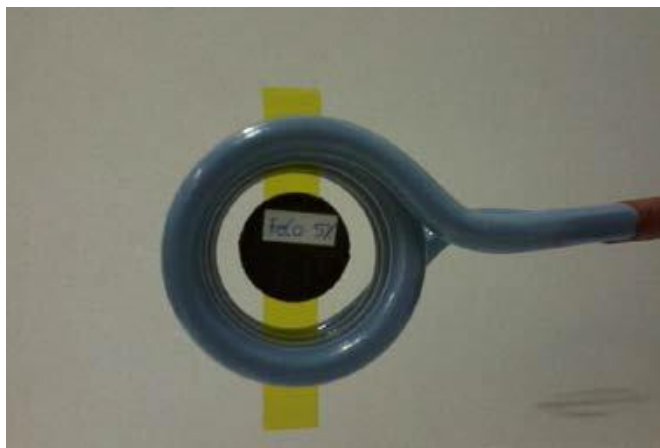


Fig. 2.20. Sample in the centre of the induction heating coil [79].

Two set of samples were manufactured. The first samples were obtained as composite disks of 2 cm diameter and 2 mm thickness by embedding nanoparticles with weight concentrations of 3%, 4% and 5% in commercial epoxy resin. Initial degassing and room temperature polymerisation for 24 hours were carried out. The second samples were manufactured by introducing 3 wt.% of iron oxide nanoparticles within self-healing polymer made of furan and maleimide reagents. Samples were incised on the surface to study the induction heating effect on the self-healing process. Experiments were carried out both with commercial resin and self-healing resin to estimate the magnetic field necessary to reach 100 °C through induction heating. The maximum magnetic field estimated during the tests was around 25 kA/m. The inductively heated samples showed the potential of magnetic nanoparticles to activate the

self-healing mechanism; in particular, iron oxide nanoparticles were the most effective in terms of energy consumption to reach a specific temperature requirement.

Studies carried out by Fink *et al.* [15] indicated very slight heating at the frequency of 3 MHz from samples made of PEEK-based unidirectional prepreg, after preliminary tests attempting to heat UD fabric at various frequencies unsuccessfully due to skin depth limitations.

Induction heating of composite materials has been explored in the work from Rudolf *et al.* [80]. Specifically, continuous carbon fibre reinforced thermoplastics were tested to analyse the contribution of the electromagnetic process parameters, such as field frequency, generator power, inductive coil geometry, air gap between inductive coil and samples and the sample layup. These would affect the heat generation in terms of temperature profile and heating rate.

This work carefully assessed the importance of fibre junctions within a laminate to tailor closed current loops. These allow the current to flow and, therefore, the heat to be generated.

Non-magnetic but electrically conductive materials can generate heat when exposed to an alternating magnetic field due to resistive losses induced by eddy current loops.

Magnetic materials exhibit hysteretic losses which provide an additional heat generation mechanism. Therefore, carbon fibre reinforced thermoplastics can be inductively heated without additional magnetic material due to the electrically conductive nature of the carbon fibres [80].

Miller *et al.* [81] and Fink *et al.* [15] worked on explaining the induction heating mechanisms in depth, although Miller related the eddy currents to the fibres and associated the electrical current conduction with the fibre junctions. Fink focused his attention on the dielectric losses due to the polymeric resin between the fibres, which hinders the effective fibre-to-fibre junctions. Uncertainty rises for the mechanisms related to the heat generation. Work from Rudolf mainly delved into the fundamentals of the aforementioned mechanisms.

An induction generator with a power output of 5.2 kW and frequency range of 650-1000 kHz was used to create the alternating magnetic field. The apparatus could adapt itself to the frequency changes, although the voltage was held constant at 220 V.

The investigation was carried out on samples made of carbon fibre reinforced poly(phenylene sulphide) (5-harness satin; fibre volume fraction of 46% and thickness of 2 mm) for the process parameter influences, and carbon fibre reinforced polyamide 6,6 (fibre volume fraction of 50%) for the influence of the laminate layup.

Frequency changes can drastically affect the heat generation phenomena. Samples could not be heated beyond 50°C at 20 kHz, although they could reach temperatures of 300°C at 1 MHz in roughly 5 s and in 1 s at 26 MHz. However, the contribution of the frequency on the heating rate is remarkably relevant even for a frequency range 750-1100 kHz. These results refer to tests carried out with a triangular coil at 5 mm from the top surface of the laminate (generator power of 20%). Heating time was measured when the sample top surface reached the temperature set point.

Generator power and coil distance from the samples also contributed to the heating rate. The heating time tended to increase quadratically with the distance between the coil and the sample as shown in Fig. 2.20. On the other hand, the heating time showed a quadratic decrease with the power (Fig. 2.20).

Other aspects to be accounted for which could cause a through-thickness temperature gradient are the skin effect due to a skin depth smaller than the sample thickness, and a strong through-thickness field intensity decrease.

The sample structure and layup also have a relevant influence on the heating rate. Plain weave, 5-harness satin weave, fleece and unidirectional tape were analysed. For this purpose, the distance between coil and sample and the power were held constant at 5 mm and 20%, respectively. The fleece and unidirectional tape could not reach the desired temperature due to the absence of effective conductive paths between the laminate plies. On the other hand, the plain weave could be heated faster than the satin weave, which is an indication of higher content of electrical conductive loops in the plain weave laminate, due to the higher curvature at the fibre junctions (Fig. 2.21).

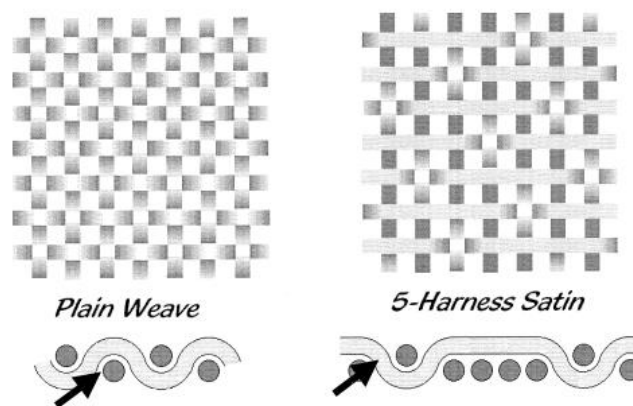


Fig. 2.21. Schematic of the fabric used for induction heating investigation [81].

This causes a current flow increase at the junctions which leads to a higher heating rate [82]. Another experiment compared a polyamide 12 composite containing a plain weave layer with a pure plain weave without polymer matrix in terms of inductive heating. The temperature which could be achieved was the same in both cases. This confirmed that the polymer matrix did not affect the induction heating process, therefore dielectric losses proposed by Fink [15] could be neglected for the specific process parameters used.

Induction heating from magnetic nanoparticles embedded in a polymer matrix was also investigated for other applications such as shape memory polymers. They can recover the original shape after exposure to an external stimulus [83].

Keblinski *et al.* [82] studied the limits to localised electromagnetic heating from excited nanoparticles. The most relevant part of their study relates to the multiple nanoparticle heating, which can potentially lead to an overall temperature increase of the system under investigation. However, local temperature effect can often be considered negligible.

Two specific timescales are of relevance in the process: the time scale needed for the additive effect of neighbouring thermal fields to occur, and the time scale for the overall heat diffusion in the sample.

The main outcomes of this study were that continuous heating by nanoscale heaters could not generate a significant temperature rise in proximity to the surface of a nanoparticle unless the heating power reached extremely high values. As previously stated, the experimental evidence proved that the overall temperature rise due to continuous heat source is homogeneous and orders and much larger than the local scale temperature increase. The localisation of the nanoscale temperature increase requires short duration heating processes by using high-power optical pulses to be effective.

Menana *et al.* [84] studied the induction heating phenomenon by applying an AC field at frequencies in the MHz range to a carbon fibre reinforced polymer multi-ply quasi-isotropic laminate under a purely numerical viewpoint. Another cases of frequency application in the MHz range was studied by Hergt *et al.* [85], who estimated an upper limit of heat generation by hysteresis losses on the order of 104 W/cm^3 at 2 MHz for samples made of fine magnetite Fe_3O_4 particles. A superficial temperature increase of 0.1 mK was observed from a 100 nm diameter particle [85].

Kim *et al.* [18] used the experimental setup shown in Fig. 2.22 to measure the contact resistance and the influence of specific parameters such as prepreg surface finish and material properties, pressure and temperature applied on the composite system.

Four strips of AS-4/PEI carbon thermoplastic prepreg (*Cytec Fiberite*) characterised by a fibre volume fraction of 60% were used.

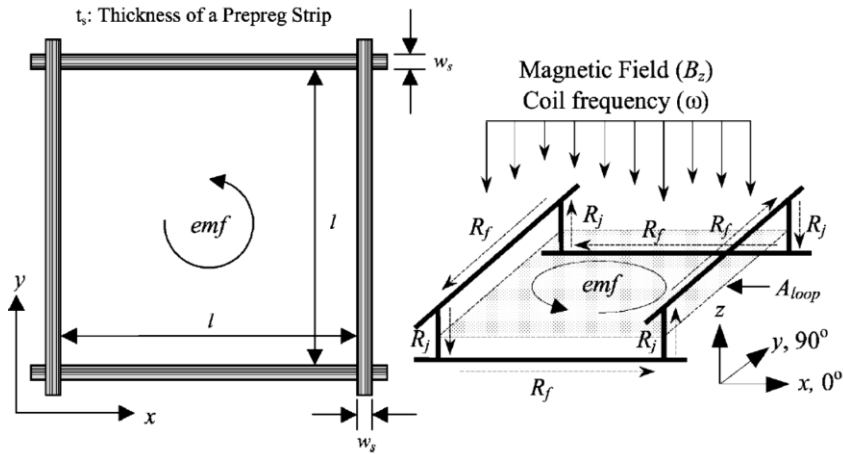


Fig. 2.22. Schematic for the heating test with prepreg strips [18].

The alternating magnetic field was generated through a 2.5 kW *Lepel* induction unit. The prepreg strips were heated with different constant powers through a pancake magnetic coil. The strip setup formed a $[0/90\pm]$ loop as shown in Fig. 2.23. An AGEMA Thermovision 900 Infrared camera was used to monitor the temperature at the four strip junctions. Results are shown in Fig. 2.23 as heating patterns; J1-J4 and S1-S4 are referred to temperature measurement locations.

The major contribution of the junction heating to the global heating mechanism compared to the heat developed along the prepreg strips is shown in Fig. 2.24. The parameter P represents the heat generated. Short time scales were used to discard conductive/convective and radiative heat losses.

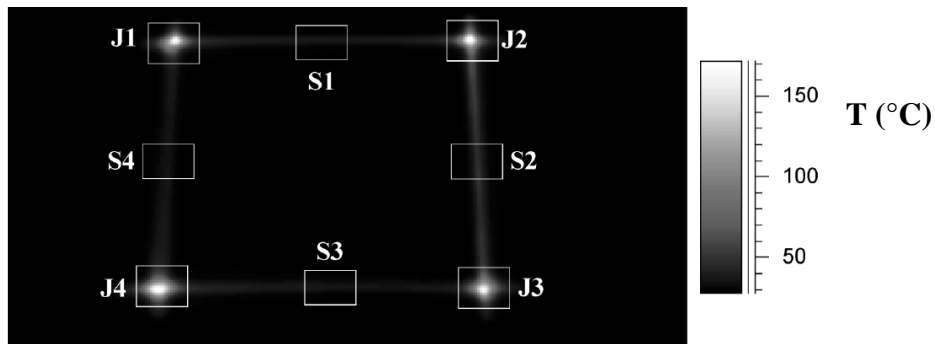


Fig. 2.23. Typical heating pattern of composite strip and the measuring positions for temperature (in $^{\circ}\text{C}$) [18].

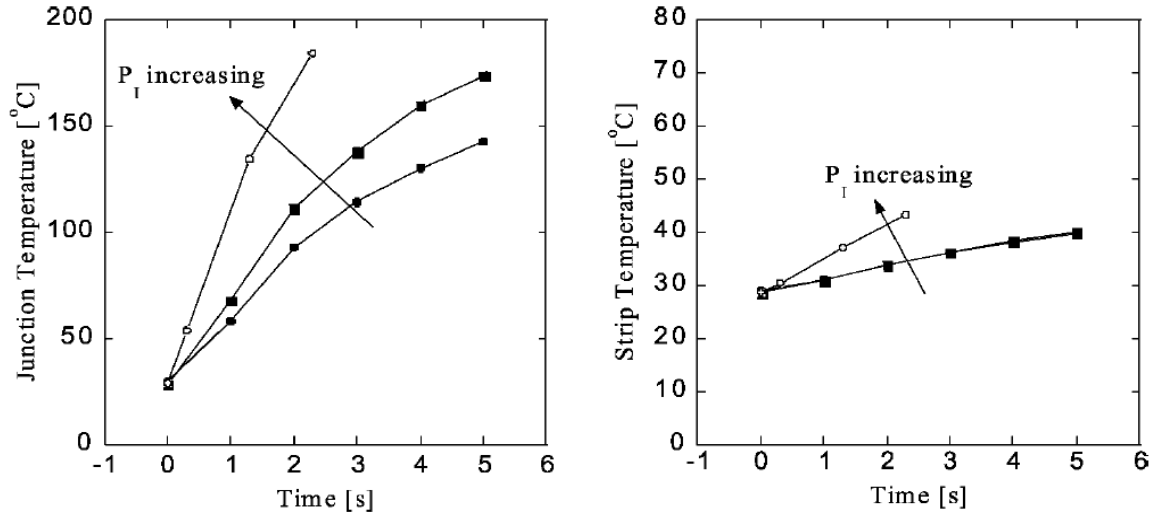


Fig. 2.24. Temperature change at the junction and centre of the strip with time [18].

2.7 Dielectric heating

Recent studies showed an increasing interest in a new generation of composite materials characterised by high dielectric properties. These would combine with lower size, weight and therefore higher cost effectiveness. A potential application for increasing dielectric properties of composite materials would be to aid the resin cure process through dielectric heating, which could be used to provide the necessary thermal energy to trigger and facilitate the resin cure mechanisms.

The parameter which indicates the dielectric properties of a system is the dielectric constant. This is also called relative permittivity and is expressed as the ratio between the absolute permittivity and the vacuum permittivity.

More specifically, permittivity relates to the capacity of a material to store an electric charge after application of an electric field, compared to the electric storage capacity of the vacuum.

The procedure to increase the dielectric constant of a polymer matrix is the dispersion of high dielectric constant ceramics in the powder form [86, 87, 88, 89, 90, 91]. Processability of the resulting nanocomposite can be reduced by the introduction of high ceramic powder content. Many aspects need to be accounted for to manufacture nanocomposites with high dielectric properties, such as grain size of the ceramic powders [88], their homogeneous distribution, the thickness of the sample, interfacial effects and the porosity level [92].

Hadik *et al.* [92] focused their study on ceramic-epoxy composites consisting of $\text{Ba}_{1-x}\text{Sr}_x\text{TiO}_3$ ($x = 0.2$ and 0.4) and bisphenol A epoxy. The ceramic powders were manufactured from high purity barium carbonate (BaCO_3 , Fluka 98.5%), strontium carbonate (SrTiO_3 , Riedel-de Haen). Filler contents used in the study were 5, 10, 15 and 20 vol%, analysed as a function of temperature. The dielectric measurements were performed to estimate the dielectric constant of the ceramic-filled epoxy systems. Samples were covered with an aluminium electrode through vacuum thermal evaporation. Dielectric tests were carried out from 100 to 360 K in the frequency range of 40 Hz to 100 kHz. Fig. 2.25 shows the dielectric properties of sintered ceramics (1400°C for 75 minutes). The temperature peaks, corresponding to the Curie temperature (ferroelectric-paraelectric transition), are 353 K and 280 K for BST(0.2) and BST(0.4), respectively.

The maximum values of dielectric constant at 10 kHz are 1665 and 1880 for BST(0.2) and BST(0.4), respectively. Fig. 2.26 reports the dependence of the dielectric constant on the ceramic powder loading at different temperatures.

The dielectric constant of pure epoxy remained practically constant, with a slight increase from 5.5 to 6.3 above 350 K. Both for BST(0.2) and BST(0.4), the dielectric constant increases with increasing ceramic loadings, and the temperature dependent behaviour is the same at all ceramic contents. The dielectric constants at 300 K and at 10 kHz for 5, 10, 15, and 20 vol% of ceramic particles were 8.3, 11.3, 13.3, 17.7, and 8.8, 12.1, 15, 19.3, respectively for composites with BST(0.2) and BST(0.4). The introduction of epoxy resin causes a decrease in dielectric constant if compared with the case of pure ceramics.

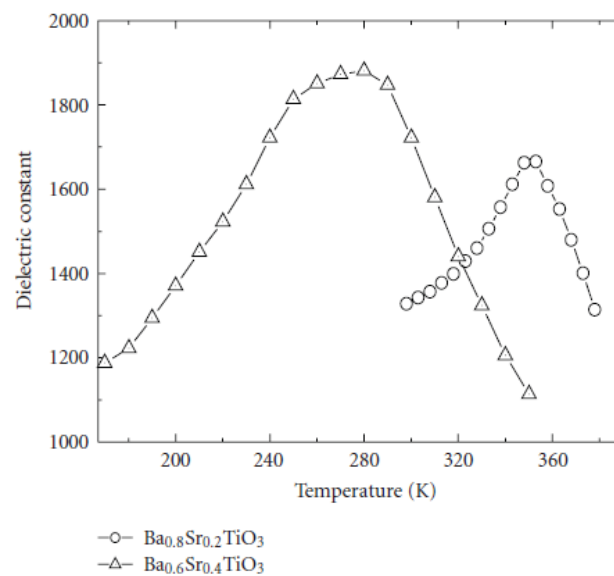


Fig. 2.25. Temperature dependence of the dielectric constant of the sintered BST(0.2) and BST(0.4) ceramics [92].

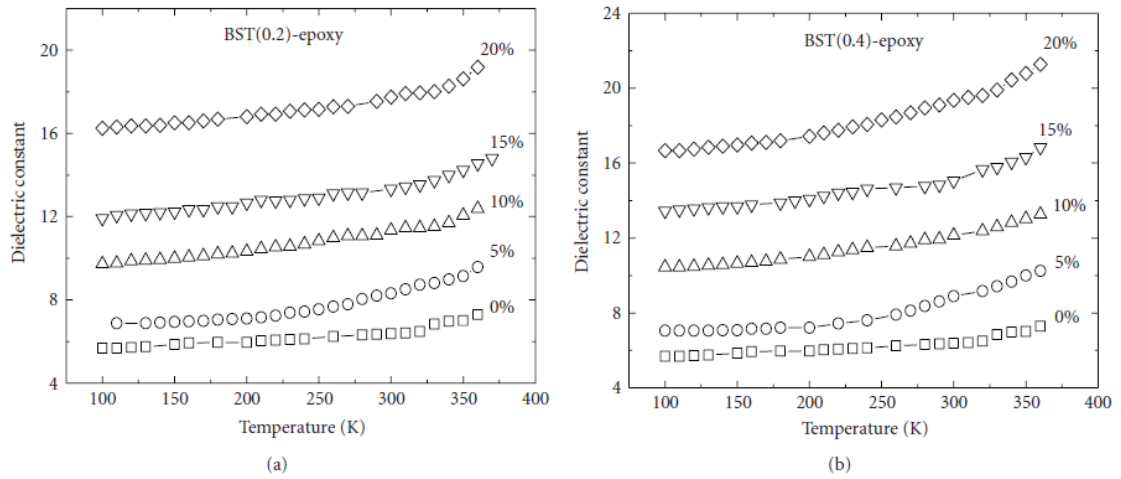


Fig. 2.26. Dielectric constant for BST-epoxy composites as function of temperature for different volume fraction at 10 KHz [92].

The dependence of the dielectric constant on the frequency was also investigated, as shown in Fig. 2.27.

The dielectric constant of the composites decreases with increasing frequency, mainly due to a decrease in the matrix dipolar polarisation. This behaviour gives a more important contribution at high temperatures and low frequency for epoxy-barium titanate composites [93]. The interfacial or Maxwell-Wagner-Sillars (MWS) polarisation could be a cause of this behaviour, due to the heterogeneity of the composite [94].

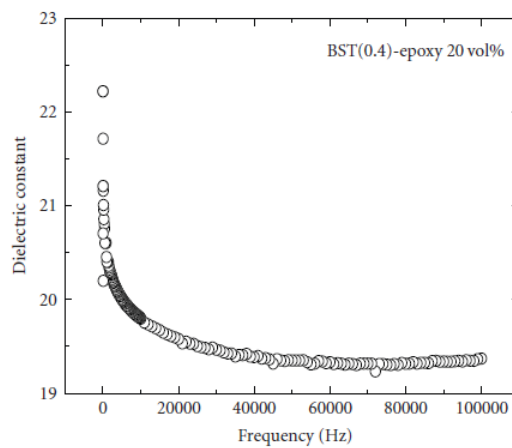


Fig. 2.27. Dielectric constant of BST-epoxy sample with 20 vol% of ceramic content as a function of frequency [92].

Cheng *et al.* [95] studied the dielectric properties of barium titanate filled-epoxy composites, particularly at high frequencies. This was carried out to assess the dielectric constant changes with the frequency and, therefore, with the loss properties of the composites under investigation. The diglycidyl ether of bisphenol A epoxy resin was used as the host matrix for the sample in this work (Dow Chem.). The curing agent was diaminodiphenyl methane (DDM, Jensen). Y5V ceramic fillers (Prosperity Dielectrics Co., Ltd., PDC, Taiwan) were used to increase the dielectric constant of the systems [95]. The epoxy resin and ceramic particles were initially mixed at 70°C, followed by the stoichiometric addition of the curing agent. After mechanical stirring and degassing in a vacuum oven, the mixture was cured in a mould for 3 h at 150°C, and subsequently for 10 h at 220°C. An impedance analyser (Hewlett Packard, model 4291B) was used to measure the dielectric constant and loss tangent at room temperature (25°C) and between 1 MHz and 1 GHz. Thermal measurements through differential scanning calorimetry (DSC) were conducted to estimate the glass transition temperature transitions of the cured samples.

Table 2.3 reports the main results from the thermal and dielectric investigations. The dielectric constant ϵ showed an increase by enhancing the ceramic content in the composite, from 3.2 for the neat resin to 13.1 at 45 vol.% of ceramic filler within the epoxy matrix. On the other hand, the glass transition temperature slightly decreased at increasing ceramic contents [95]. The dielectric constant also tended to decrease at low frequency, before stabilising at higher frequencies, as shown in Fig. 2.28.

Table 2.3. Properties of the composites with various contents of Y5V ceramics [95].

Y5V filler	T_g (°C)	ϵ (1 GHz)	$\tan\delta$ (1 GHz)
0%	167	3.2	0.022
25 wt.% (6 vol.%)	166	3.9	0.023
40 wt.% (12 vol.%)	166	4.6	0.026
60 wt.% (24 vol.%)	166	6.5	0.027
70 wt.% (33 vol.%)	157	10.3	0.028
80 wt.% (45 vol.%)	162	13.1	0.025

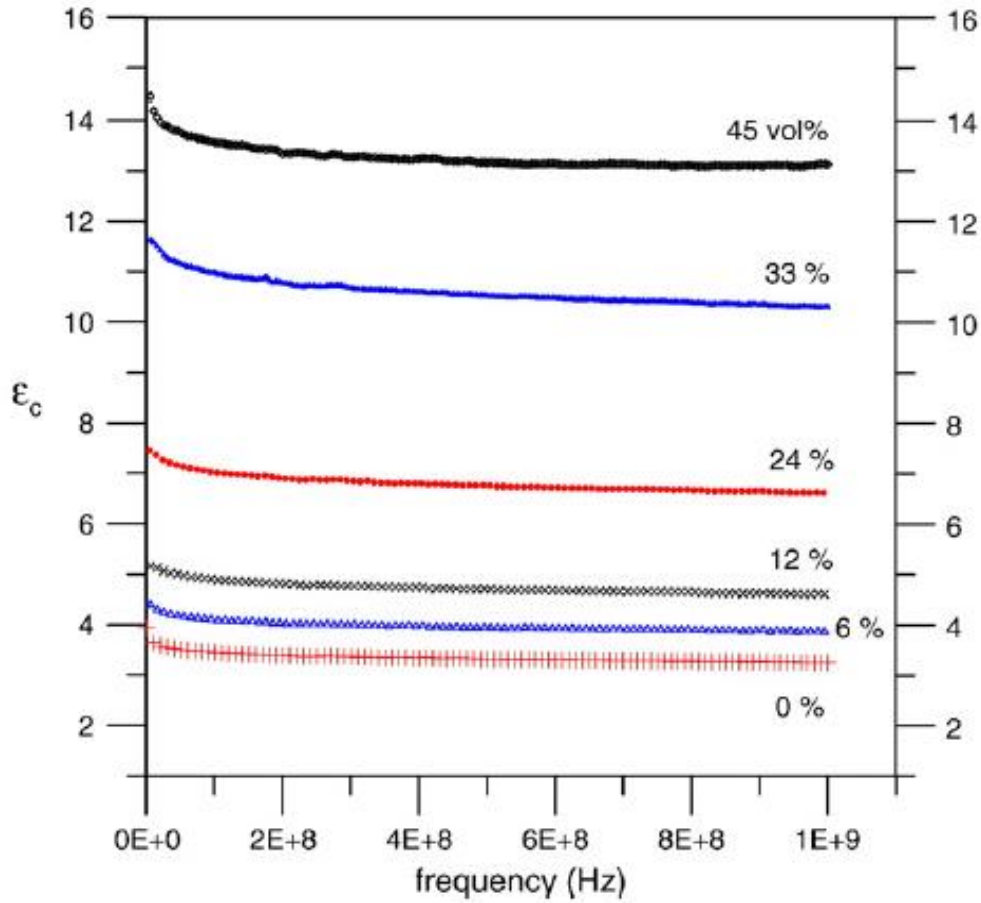


Fig. 2.28. Dielectric constants of the cured composites as a function of frequency [95].

Barium titanate was studied in several works as most suitable candidate to increase the dielectric properties of a host polymer matrix. Dang *et al.* [96] analysed the effect of the barium titanate particle size on the dielectric properties of the composites manufactured with epoxy resin as host matrix.

An increase in the dielectric constant for a host resin matrix by introducing dielectric additives could be beneficial to the inductive heating properties of a composite part, as detailed by Yarlagadda *et al.* [97]. They studied how higher dissipation related to the electrical conductivity of the resin blend could be achieved. In the case of a composite characterised by a dielectric matrix, the dielectric matrix between non-touching fibres behaves as a capacitor and resistor connected in parallel. Therefore, an induced current loop can be generated as shown in Fig. 2.29 [97].

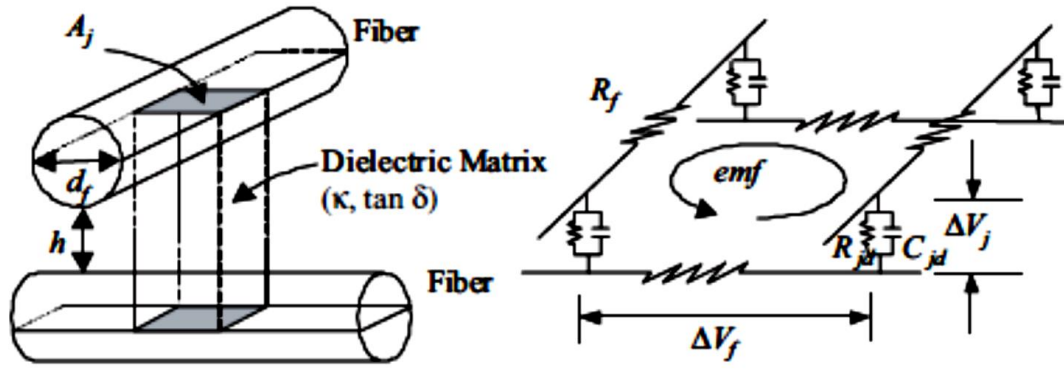


Fig. 2.29. Dielectric heating representation at the non-touching fibre junction [97].

The equation below shows the relationship between the resistance at a dielectric junction between the dielectric matrix junction resistance R_{jd} and the dielectric constant κ :

$$R_{jd} = \frac{h}{\omega \cdot \epsilon_0 \cdot \kappa \cdot (\tan \delta) \cdot d_f^2}, \quad (2.5)$$

where h is the inter-fibre distance, ω is the frequency of the applied magnetic field, ϵ_0 is the vacuum permeability ($= 8.85 \cdot 10^{-12}$ F/m), $\tan \delta$ is the dissipation factor and d_f is the fibre diameter [97].

Nanocomposites characterised by the presence of ceramic particles could therefore be used as host systems for the inductively cured patches in the repair applications, which are the focus of the present work.

2.8 Summary and outlook

Relevant work has been carried out in the study of the alignment of nanofillers within viscous media through different external stimuli such as magnetic and electric fields, and ultrasonics. Significant improvement of the mechanical, electrical and thermal properties of the nanocomposites was observed through the creation of effective nanotube networks within the host mediums. Further investigation needs to be carried out to evaluate the feasibility of the induction heating through the generation of eddy currents from the mentioned networks. Dielectric heating from the host matrix was also investigated. The introduction of ceramic fillers within a polymer matrix caused an increase in dielectric properties (*i.e.* dielectric

constant), which is desirable for this project. Temperature, frequency and ceramic filler content effect on the dielectric properties was analysed to understand the feasibility of the dielectric heating mechanism as potential candidate for an additional processing method to assist thermoset resin cure. However, further investigation of the effect of metal-plated carbon nanotube introduction within a composite component on the repair process needs to be accounted for. Specifically, the electrical conductivity enhancement through the thickness of the composite part by means of metal-plated nanotubes was not explored. This project mainly focuses on tackling this aspect by investigating different methods to introduce and position nanotubes such as magnetic positioning and liquid resin printing. This approach has not previously been tried in context of repair and will be tested in this project. The potential of spatially positioning the CNTs in an accurate fashion is particularly appealing to this project. The method is also compatible with other methods of aligning the positioning of the CNTs such as application of static magnetic field. The main reasons for the selection of liquid resin printing to manufacture repair patches are the local CNT positioning, and therefore has a potential of tailoring the heat distribution map through material high precision distribution of conductive networks.

3. Manufacturing of functionalised additives and functionalised resins

As literature review showed, to enable inductive heating the material of repair patches needs to exhibit certain properties. The heat can either be generated by means of eddy currents, which sets requirements on electrical conductivity, or through magnetic hysteresis, which requires it be magnetically susceptible. The review also shows that inductive heating, though having potential of making the cure more homogenous, still suffers from a non-uniformity of the heat supply due to the skin effect, exponential decay of magnetic field, and finite geometries of inductive coil and patch itself. As shown in Chapter 5, these issues can be addressed by doping resin with additives and distributing them within the patch in a controlled fashion.

The summary of these requirements determined the choice of the additive system. This research work focuses on metal-functionalised carbon nanotubes (CNT). CNT are known for the low-percolation threshold for electrical conductivity and hence, only small fraction of CNT is needed to change the behaviour of non-conductive resin carrier and ensure heat supply at low frequencies of inductive current. The metal-functionalisation of the CNT can be used two-fold: (a) the presence of metal enables magnetic hysteresis at high frequencies of inductive AC current, (b) the presence of metal on fibre surface makes particles susceptible to DC magnetic field and hence provides means to move the CNTs within the patch.

The current chapter explores the process of functionalizing CNT and matrices. It examines the impact of functionalization on cheomorphorheological and magnetic properties of a commercially available resin commonly used for liquid moulding of composites. The material systems selected in this chapter are then employed to explore the potential of CNT positioning described in Chapters 4 and 5.

3.1 Functionalisation of CNT additives

This section focuses on the methodologies to provide CNTs with a specific functionalisation depending on the required properties for the CNT application. In this project, metal functionalisation is critical to alter the sensitivity of the CNT to an externally applied magnetic field and, consequently, manipulate their position and alignment within a viscous medium, as discussed in Chapters 4 and 5.

3.1.1 *Materials*

The feasibility of utilising several different types of CNTs, with and without metal functionalisation, was explored in this study [1]:

- 1) MWCNTs (manufactured by Sigma Aldrich). These CNTs are characterised by high aspect ratio (around 1500; cross section diameter of 6-13 nm) and further details are provided in Appendix B Section B.1.

Electroless plating was used to deposit metal on their surface.

- 2) Commercial nickel coated CNTs (manufactured by US Research Nanomaterials, Inc.). These CNTs show purity higher than 98%, outer diameter of 5-15 nm and aspect ratio higher than 1000. Further details are provided in Appendix B Section B.2.

3.1.2 *Methods*

There are two most common methods for CNT functionalisation:

- a) Chemical approach: for the deposition of homogeneous and chemically strong metal functionalisation coatings on the sides and ends of the multi-walled nanotubes. However, this approach can lead to substrate damage due to the disruption of a chemical bond. This then leads to the creation of a new bond to functionalise the substrate. The chemical functionalisation was used to locate metal nanoparticles onto the nanotubes and enhance the nanotube electrical properties together with the sensitivity to an externally applied magnetic field.
- b) Physical approach: this approach is used to create physical bonds between the functionalising particles and the substrate. However, the advantage of this approach is the absence of chemical bond disruption; therefore, substrates are not damaged during this process.

Both the approaches were considered in the current study. The theoretical comparison between the two approaches was carried out to better evaluate the most suitable methodology to functionalise nanotubes. Ultimately, chemical deposition was preferred. The advantage of chemical deposition is that stronger adhesion can be obtained for the metal coating onto the nanotube sides and walls, whereas physical functionalisation relies on physical interactions between nanotubes.

3.1.2.1 Chemical approach

An electroless plating technique was employed to deposit homogeneous, chemically-stable, metal functionalised coatings (*e.g.* nickel, cobalt, and nickel-iron) on both sides and ends of the MWCNTs [20, 54, 55, 57]. The nanotubes will be characterised by low aspect ratio of around 10. The procedure for Ni/Co deposition entailed a nanotube sensitization step with tin(II) chloride, an activation step by palladium(II) chloride and plating bath through sonication or magnetic stirring forces [1]. The plating bath required a reducing agent (hypophosphite), a complexing agent (citrate) and the salt of the metal to be reduced on to the nanotubes under specific pH and temperature conditions [20]. Nanotube aspect ratio decreased significantly during the sensitization and activation steps involving sonication [1]. This event could therefore ease the final plating step for the nanotube metal functionalization, whilst reducing nanotube bending and fracture during incorporation within a host medium *via* sonication [1]. A schematic of the electroless plating procedure can be observed in Fig. 3.1 [55].

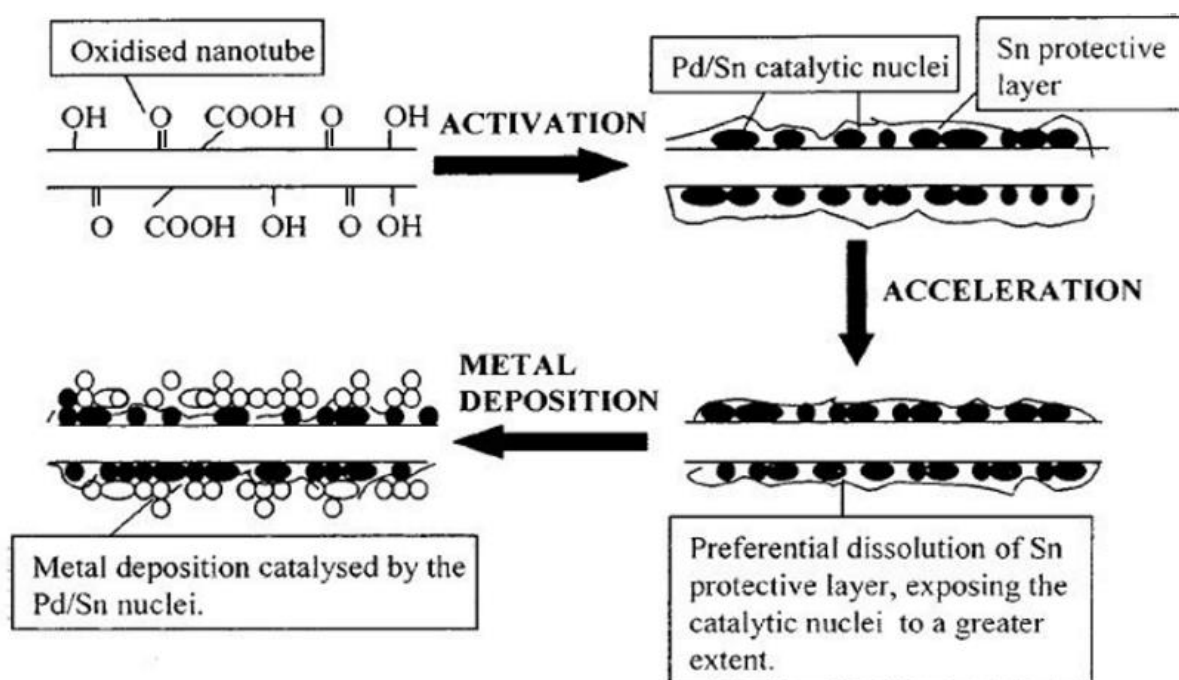


Fig. 3.1. Schematic of electroless plating technique [55].

Specifically, the plating step was carried out at specific pH and temperature conditions optimized after laboratory trials at the University of Bristol. The plating step for cobalt functionalisation onto multi-walled carbon nanotubes consists of the following steps:

1. Disperse following reagents in 150 ml of deionised (DI) water using a hot plate/magnetic stirrer for 15 minutes [55]:
 - cobalt chloride [4.5 g/150 ml DI water];
 - sodium hypophosphite Hydrate [3 g/150 ml DI water];
 - sodium citrate [5.25 g/150 ml DI water];
 - ammonium chloride [7.5 g/150 ml DI water];
2. Introduce MWNTs (0.05 g in suspension with deionized water prepared in ACCIS nanomaterials lab) into the reagent suspension, with the nanotubes, which had previously been activated with tin chloride and palladium chloride in ACCIS nanomaterials lab;
3. Adjust pH of the suspension and keep it constant above 9 by using ammonium hydroxide;
4. Sonication at 60 °C for 15 minutes, with a pH = 9 or above;
5. Introduce deionized water suspension with cobalt-functionalised multi-walled carbon nanotubes into Falcon tubes, with suspensions been made in ACCIS nanomaterials lab;
6. Centrifugation of deionised water suspension with cobalt-functionalised multi-walled carbon nanotubes at 4200 rpm for 6 minutes;
7. Rinse suspensions with deionised water and repeat centrifugation.

The functionalisation procedure with cobalt nanoparticles turned out to be more time consuming but potentially more efficient in terms of bond strength. TEM analyses were carried out to estimate the efficiency of the functionalisation process both in terms of metal nanoparticle presence and distribution along the nanotube length. The functionalisation of the CNTs was carried out at the Wolfson Centre for Magnetism in the School of Engineering of Cardiff University and at the University of Bristol, together with magnetic characterisation of the functionalised nanotubes *via* the use of Vibrating Sample Magnetometer (VSM).

3.1.2.2 *Physical approach*

Physical deposition method will be also used to provide the chemical approach with a baseline for the deposition efficiency. Thermal evaporator deposition was selected for the purpose.

Thermal evaporation belongs to the Physical Vapour Deposition (PVD) techniques. PVD is a vacuum coating technique which relates to the vaporisation of a metal to a plasma of atoms or molecules and their deposition on a wide range of substrates. Several types of PVD coatings can be used such as Zirconium Nitride (ZrN), Zirconium Carbon Nitride (ZrCN), Titanium Nitride (TiN), Titanium Carbon Nitride (TiCN), Chromium Nitride (CrN) and Chromium Carbon Nitride (CrCN). The carbides, nitrides, silicides and borides used as PVD coating materials are tailored to specific applications.

The substrate to be coated is secured in a fixture and placed in the vacuum deposition equipment chamber. The equipment is set to the optimum pressure which is different depending on the coating materials, substrate and process used. The substrate to be coated is often preheated and sputter cleaned. Vacuum levels within the PVD chamber are around 10^{-2} to 10^{-4} millibar, and the PVD process temperatures are between 150 and 500 °C.

The metallic material needed for the nanotube coating is heated in a vacuum chamber until its surface atoms have enough kinetic energy to leave the surface. They will therefore travel through the vacuum chamber at thermal energy less than 1 eV and coat the substrate (*e.g.* nanotubes) and positioned above the evaporating material. Average travel distances are 200 mm to 1 metre.

The chamber pressure needs to be monitored not to exceed the point where the mean free path (as average distance an atom or molecule can travel in a vacuum chamber before it collides with another particle thereby disturbing its direction) is longer than the distance between metal source and the nanotube substrate. The pressure is selected at the higher limit of the range for the ion beam source to be used both for film densification and process parameter modification.

3.2 Characterisation of functionalised CNT

Functionalised CNT were characterized using Transmission Electron Microscopy (TEM) JEOL JEM-1400. The aim of the TEM investigation was to study the CNT coating distribution after functionalization with metal nanoparticles. Droplets of tested solutions were prepared from powdered nanotubes, subjected to ultrasonic bath dispersion in ethanol and ultimately analysed.

3.2.1 Microstructural analysis of metal particles on MWCNTs

Plating methodologies such as nickel, cobalt and nickel-iron plating were investigated. The functionalized MWCNTs were characterized using TEM to investigate the position and density of metal particles. Commercial nickel coated nanotubes were compared to nickel plated nanotubes prepared experimentally in house, to visually assess the distribution of the nickel coating along the length of the nanotubes. Nanotube micrographs for the commercial nickel coated- and nickel-plated nanotubes are shown in Fig. 3.2 [1]; dark regions and spots in the micrographs refer to the metal nanoparticles on the CNT walls. Fig. 3.2(a) [1], that the heterogeneous nickel coating distribution reflects the low efficiency of the coating process regardless of it being chemically based (CVD). In contrast, Fig. 3.2(b) [1] shows more uniform wall coating distribution for single MWCNTs. Fig. 3.2(c) [1] shows the micrograph for the cobalt plated MWCNTs. The latter were obtained through a magnetically stirred plating bath. Agglomeration greatly influences the nanotube distribution. However, both nickel and cobalt seem to adhere efficiently and uniformly to the nanotubes, although to a lower extent for the cobalt plated nanotubes potentially due to the magnetic stirring process [1].

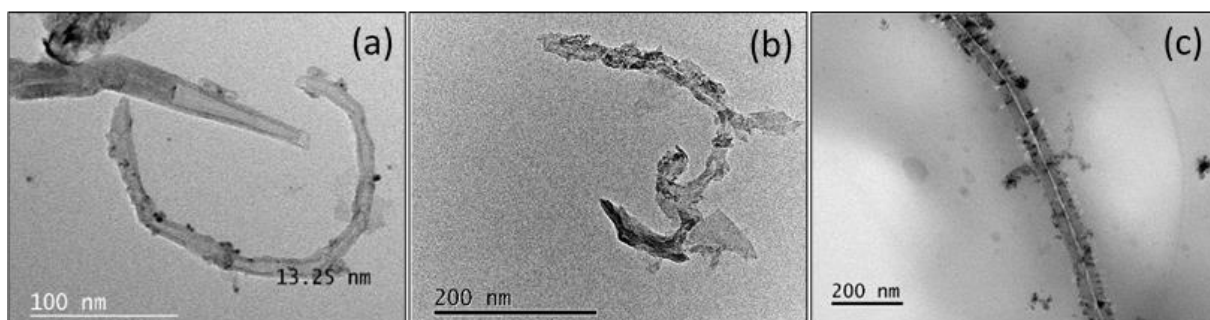


Fig. 3.2. TEM micrographs: Ni-coated (a) and Ni-plated (b) and Co-plated (c) MWCNTs (different scales). ImageJ software was used for the Ni-coated nanotube diameter value in (a) [1].

Transmission electron microscope (TEM) images were obtained from commercially available Ni-coated multi-walled carbon nanotubes (US Nano; expected Ni coating of 60 wt.%). This was carried out to assess the integrity and the distribution of the nickel coating along and at the ends of the nanotubes. The nanotubes were characterised by purity higher than 98% and cross section outer diameter of 5-15 nm (aspect ratio higher than 1000), as shown in Fig. 3.2(a) [1]. The nanotubes were dispersed in ethanol before the TEM analysis to prepare the micrography samples. Fig. 3.2(a) [1] shows the presence of black dots along the length of the nanotubes. These refer to the nickel nanoparticles, which provide the metal functionalisation

of the nanotubes. However, the noticeable inhomogeneous nature of the coating is clear from the weak distribution of the black dots. This might be related to an ineffective deposition process of the nickel nanoparticles, supposedly carried out with the creation of physical bonds *via* Physical Vapour Deposition (PVD) techniques. To prove the effective presence of nickel along the nanotube length, energy-dispersive detector (EDS) measurements were carried out. The EDS analysis is shown in Fig. 3.3.

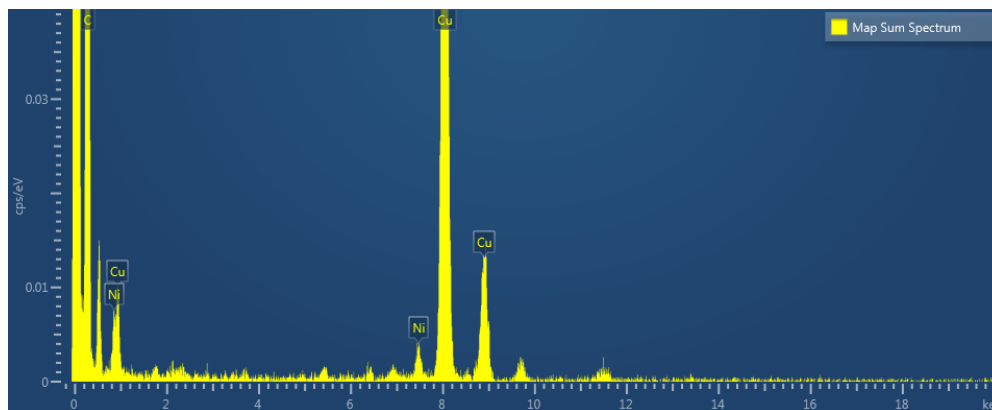


Fig. 3.3. Energy-dispersive detector EDS analysis.

The presence of Ni atoms can be clearly observed according to the graph peaks at 1 and 7.5 keV. An elemental mapping was also performed to localise the Ni nanoparticles as further confirmation of their distribution. As shown in Fig. 3.4, the Ni nanoparticles tend to distribute in specific regions along the nanotube length. This can be related to an ineffective deposition method and the potential detachment of the coating due to the sonication forces applied during the TEM sample preparation.

In conclusion, Ni coating of commercially bought multi-walled carbon nanotubes seems not to withstand the sonication forces applied during the TEM sample preparation. This typically leads to the nanotube disruption and bending as also studied by Li *et al.* [24], which can be related to the high nanotube aspect ratio (higher than 1000).

The Ni coating was distributed along the length of the nanotubes with no evidence of functionalisation at the nanotube ends, which therefore involves that the conductive nanotube networks relied on interactions between nanotubes along the length and not due to end-to-end phenomena.

Therefore, the use of low aspect ratio nanotubes might help overcome the mentioned issues related to weak nanotube functionalisation and nanotube disruption under sonication force application also investigated by Li *et al.* [24]

The potential use of chemistry-based techniques for the deposition of chemically strongly bonded and homogeneous metal coatings is therefore recommended.

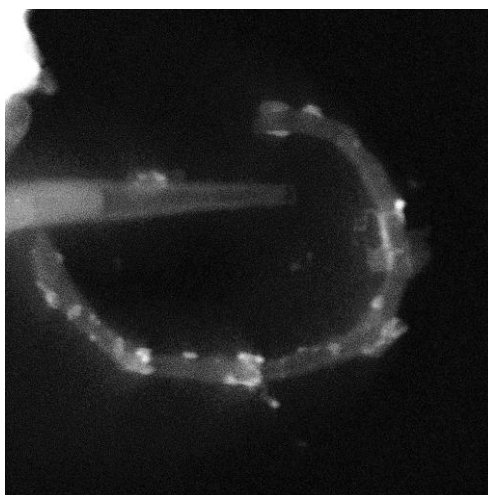


Fig. 3.4. TEM image of Ni-coated MWNTs (Ni as white regions).

3.3 Manufacturing of functionalised matrices

Functionalised matrices were studied to understand the effect of the metal-functionalised nanotube introduction within host epoxy resin on the rheological and thermal properties of the resin itself. The metal functionalised MWCNTs were introduced into the epoxy at different volume fractions (5 wt.% and 10 wt.%) by using a hand-held shear mixer. Rotational speed of 5000 rpm and 10 minutes of mixing times were used as overheating was observed at higher rotational speed and times. This was carried out to facilitate the CNT dispersion within the epoxy matrix. The slow amine hardener was added to the suspension facilitate the chemical crosslinking of the polymeric chains.

The low viscosity host epoxy resin system was PRIME™ 20LV (manufactured by Gurit) designed for liquid moulding processes. The epoxy comprises a slow amine hardener, has a viscosity of 1010-1070 cP at 20°C, and a cure schedule of 7 hours at 65°C as per supplier's instructions [1].

3.3.1 Rheological properties of the epoxy-MWCNT blends

Rheological measurements were carried out to investigate the flow properties of the metal-plated CNT-filled resin systems [1]. The aim of the rheological investigation was to assess the

processability of CNT-filled epoxy nanocomposites by using liquid resin printing. The suitability of the process was analysed for use in repair patches for aerospace applications.

Rheological measurements were performed using a cone/plate viscometer (Kinexus, Malvern). Samples with 5 vol.% and 10 vol.% of metal functionalised carbon nanotubes (magnetically stirred plating step) in PRIME™ 20LV and hardener were prepared as mixed solutions immediately before the tests and subjected to shear rates ranging from 0.1 s^{-1} to 100 s^{-1} (calculated automatically by the rheometer at the furthest gap location between cone and plate, equal to 0.15 mm) [1]. Shear viscosity curves (in Pa·s) as a function of the shear rate (in s^{-1}) are shown in Fig. 3.5 for Co30 and carboxyl functionalised nanotubes embedded in PRIME™ 20LV. The scale for the y-axis values of shear viscosity was chosen logarithmic for a clearer representation of the curves.

The introduction of MWCNTs in the epoxy resin causes a pronounced increase in viscosity. The variation in viscosity in the range of 5-10% weight fraction of CNT and different types of CNT appears much less relevant than the drop in viscosity due to shear thinning at the rates of 0.1-50 1/s. Therefore, the shear rate plays a significant role in the shear viscosity changes and increasing shear rates could facilitate the processability of the nanotube-filled resin systems due to shear thinning effect. Dispersion efficiency of the blends was not considered in this work and a parallel project at the University of Bristol [98] focused on the means to optimise the CNT dispersion in epoxy mediums.

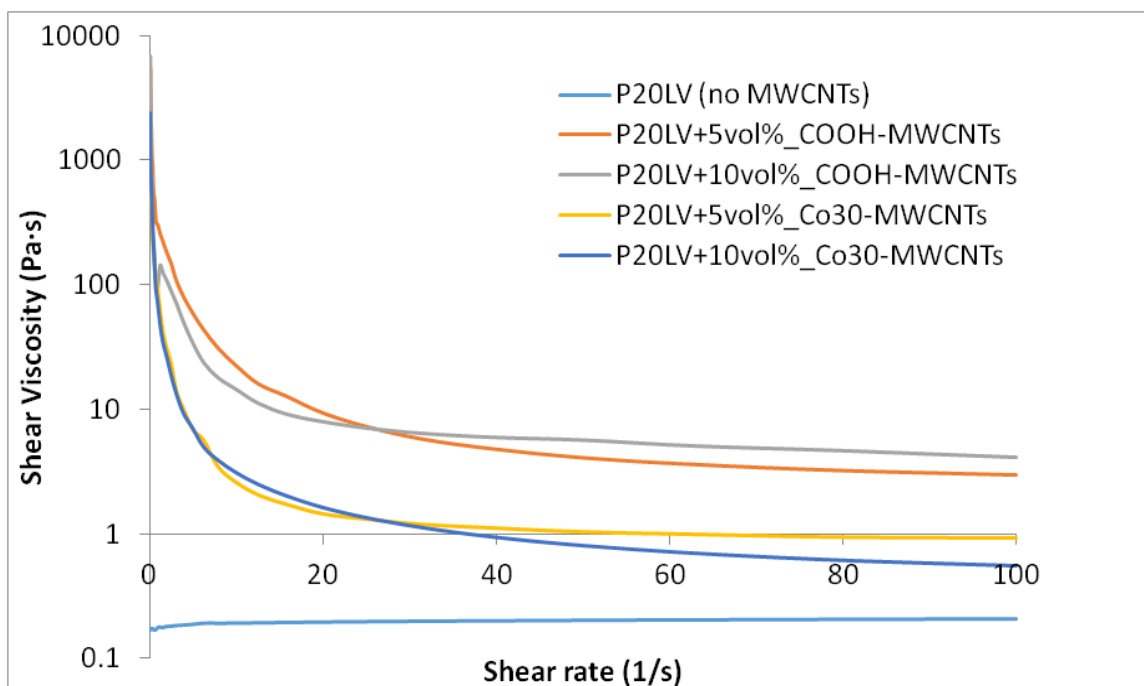


Fig. 3.5. Shear viscosity curves as a function of shear rate for 5 vol% and 10 vol% of COOH-MWCNTs and Co30-MWCNTs in PRIME™ 20LV [1].

3.3.2 Cure kinetics characterization of the epoxy-MWCNT blends

Preliminary MDSC analyses [99] were needed to estimate the effect of the metal functionalised nanotube introduction on the cure cycle of neat epoxy resin. The changes in heat flow could give a clear indication on the different time required to crosslink the polymeric chains in the presence of functionalised CNTs. The final aim is to assess whether the metal plated nanotubes can aid the cure process by reducing the heat application time to achieve full cure and by controlling the exothermic reactions. Tests were performed on nanocomposite systems with low viscosity epoxy resin PRIMETM 20LV (plus amine hardener) containing 5 vol.% of metal functionalised MWCNTs [1]. The total and reversing heat flow obtained could help to assess the influence of the presence of nanotubes and added metal functionality on the thermal behaviour of the system. Fig. 3.6 [1] shows the preliminary total heat flow results from the analysis performed at a ramp rate of 5 K/min [1].

Neat resin results were considered as a baseline for the assessment of thermal changes due to the presence of the carbon nanotubes. An endothermic peak at 23°C could be observed: this was related to the nanotube dispersion (bond breakage and macroscopic reorganisation) within the resin system, which requires an additional external heat supply [1]. However, the onset of the exothermic peak due the resin cure process clearly showed a shift towards lower temperatures for the metal functionalised nanotubes [1]. Moreover, the peak intensity increased for the metal plated nanotubes. Therefore, the beneficial effect of the nanotubes to the cross-linking process can be stated, especially for Ni-plated nanotubes [1]. In this case, the appropriate balance of carboxyl functional groups and nickel nanoparticles leads to the highest compatibility and stability with the host matrix, which is represented by the higher exothermic heat value. However, the greater exothermic heat generated during cure might lead to a more complicated cure process of the magnetic patches, with a careful monitoring of the cure cycle required [1].

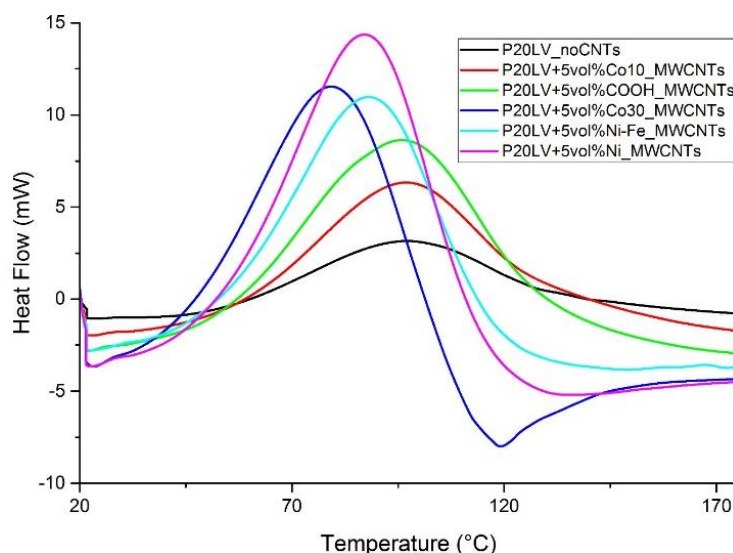


Fig. 3.6. Comparison of PRIMETM 20LV/amine/MWCNT (5 vol%) blend reactivity using MDSC (5 K/min.) [1].

The metal functionalised CNTs clearly affect the resin gelation and cross-linking processes and the exothermic energy from the MDSC curves is shown in Fig. 3.7 [1]. These values were obtained by accounting for both the epoxy equivalent weight and the amine equivalent weight in the MDSC samples. The introduction of MWCNTs in PRIME™ 20LV causes an increase in the exothermic heat generated during polymerisation compared to the neat resin. The carboxyl functionalised nanotubes present the highest value of exothermic energy (around 55 kJ/mol). However, the exothermic peak onset appears at higher temperatures than the metal-plated nanotubes (except the Co10-plated CNTs) [1] owing to the metal nanoparticles on nanotubes which accelerate the creation of reactive regions with the polymeric chains. On the other hand, their chemical compatibility with the epoxy resin is lower than the compatibility between carboxyl groups and epoxy. Nonetheless, metal-plated MWCNTs could be exploited within viscous media to localise the heat generation where functionalised nanotubes are placed and therefore selectively curing specific regions [1].

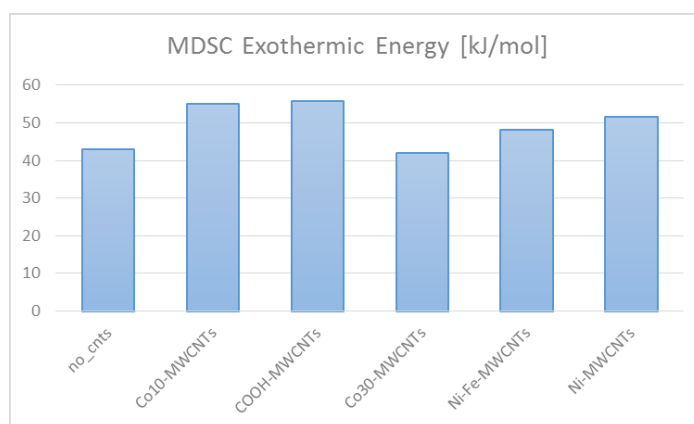


Fig. 3.7. Comparison of heats of polymerisation for the different epoxy blends [1].

3.3.3 Determining the magnetic susceptibility of the blends

Magnetic characterisation was performed to evaluate the magnetic sensitivity of different metal coatings onto nanotubes, which would affect the nanotube ability to be magnetically positioned within an epoxy medium [1]. The characterisation was carried out using a vibrating sample magnetometer (VSM) wherein samples (solid or fluid), located between parallel pickup coils, were mechanically excited at a known frequency and simultaneously subjected to a uniform DC field, ranging from -0.1 T to 0.1 T. The detection of the magnetic field level occurs using a Gauss meter placed on the magnetic poles of the apparatus [100]. Thermal characterisation was carried out on samples (10-15 mg) in hermetically sealed using modulated differential scanning calorimetry (MDSC, TA Instruments Q200). Samples were equilibrated at the initial temperature of 20°C with the modulation of $\pm 1.00^\circ\text{C}$ for 60 seconds, followed by a ramp rate of 5 K/min to reach the final temperature of 180°C [1].

Metal-plated, carboxyl functionalised MWCNTs as dry powder were characterised using VSM to determine several key magnetic properties, such as magnetisation and magnetic moment, as a function of the externally applied magnetic field (the applied DC field ranging from -0.1 T to 0.1 T.) [1]. Magnetic analysis is reported as graphs of magnetic moment (in $\mu\text{A}\cdot\text{m}^2$) as a function of the applied magnetic flux density (in T) through the VSM apparatus. Typical profiles of magnetic moment vs. magnetic flux density show three distinct regions: increasing magnetic moment (magnetisation phenomena) at increasing flux densities, magnetic saturation (plateau of magnetic moment at increasing flux densities as all magnetic domains are fully aligned towards the externally applied magnetic field direction) and magnetic remanence when the field is no longer applied. The homogeneity of the sample batch can be understood by checking the saturation behaviour. If the magnetic moment tends to show an increase followed by a decrease at increasing magnetic flux density, this is an

indication of anisotropy in magnetic performance of the tested sample. The graph in Fig. 3.8(a) [1] shows the results from the magnetic analysis. Specifically, Co10 and Co30 represent the cobalt-plated nanotubes obtained after 10 and 30 minutes of plating, respectively. The Co10- and nickel-plated nanotubes showed the highest magnetic moments at low magnetic flux densities, but the magnetic moment decreased significantly at higher flux densities in both cases. Indeed, the heterogeneity of the coating on the nanotube walls and among several nanotubes and their agglomerates reflects the presence of poorly functionalised nanotube regions, which can be magnetically sensitive at higher field levels [1]. The decrease in magnetic moment, particularly for Co10, proves that the magnetically-stirred plating bath provides higher gradients of magnetic properties for the metal functionalised CNTs if compared to other methods, *e.g.* sonicated bath, therefore leading to less homogeneous magnetic performance of the CNTs in the same blend. CNTs tend to cluster in proximity to the magnetic stirrer as expected, therefore a film resistance to the functionalisation is encountered by the surrounding nanotubes. As a result, gradients in metal functionalisation, and therefore magnetic properties, between single nanotubes or agglomerates become relevant in the investigated samples [1].

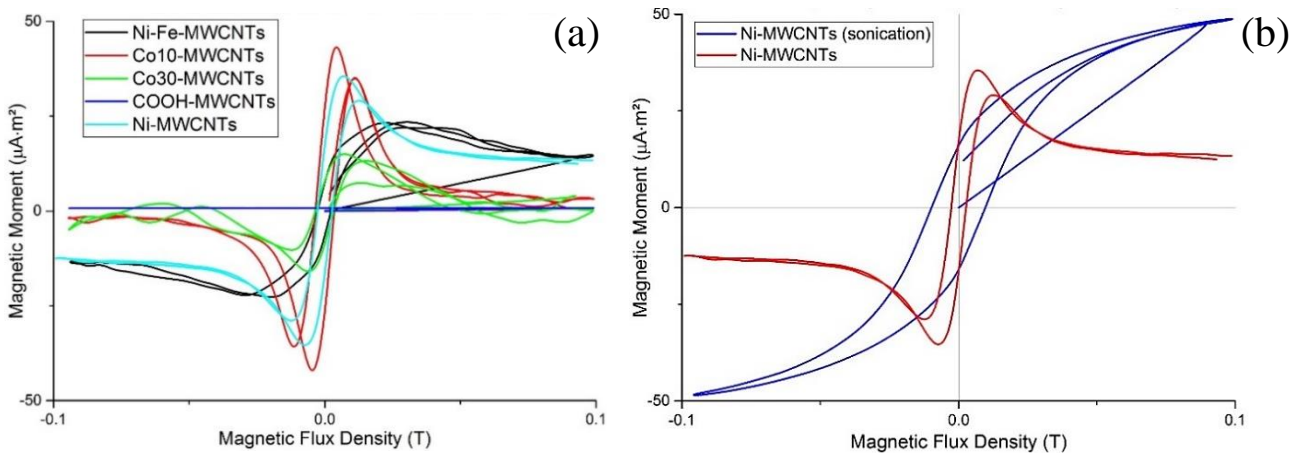


Fig. 3.8. (a) VSM results and (b) plating/stirring comparison for Ni-plated MWCNTs [1].

Fig. 3.8(b) [1] presents the magnetic moment for nickel-functionalised carbon nanotubes after sonication and magnetical stirring. The dependence of the magnetic moment on the applied flux density, for the sonicated nickel-plated nanotubes (blue line in Fig. 3.8(b) [1]), shows three distinct regions: magnetisation at increasing flux densities, magnetic saturation for flux densities approaching 0.1 T, and magnetic remanence when the field is no longer applied. The magnetic remanence is not influenced by the plating method although the magnetic moment and saturation clearly benefit from the plating bath homogenisation achieved through

sonication. The magnetic moment for Ni-plated nanotubes after sonication is around $50 \mu\text{A}\cdot\text{m}^2$ whereas, after a magnetically stirred plating bath, the magnetic moment does not exceed $30 \mu\text{A}\cdot\text{m}^2$. Different results can be observed for Co-plated and Ni-Fe-plated MWCNTs (Fig. 3.9 [1]): in the first case, the plating procedure alters the magnetic remanence and the coercivity [1].

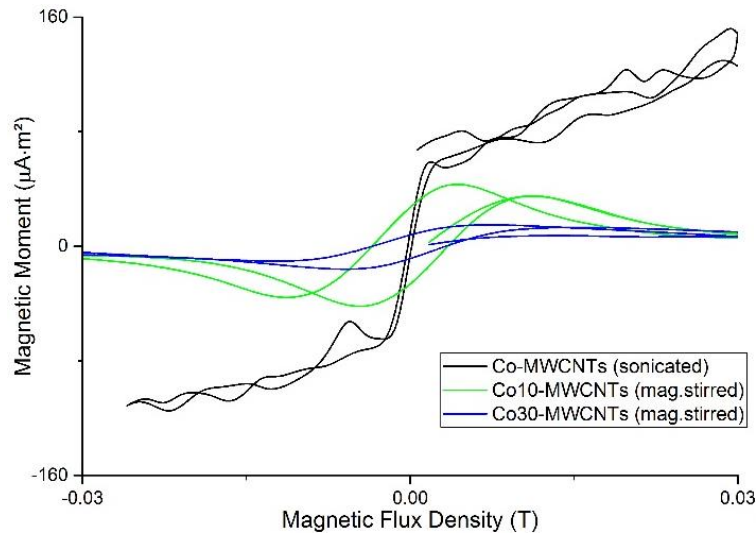


Fig. 3.9. VSM results from sonication plated/magnetically stirred Co-plated MWCNTs [1].

Furthermore, Co-plated nanotubes plated through a sonicated bath show a higher magnetic moment, around $160 \mu\text{A}\cdot\text{m}^2$, which represents the highest figure achieved among the investigated nanotube coatings. Additionally, the extremely low coercivity of sonicated Co-plated nanotubes favours the magnetisation changes and, therefore, the hysteresis loss generation, although the hysteresis loop shown in Fig. 3.9 is relatively limited. Further investigation is required for the electroless plating of carbon nanotubes with metal compounds.

3.4. Conclusions

The current chapter explored the functionalisation of CNTs and matrices. It also assessed the influence of functionalization on chemorheological and magnetic properties of a commercially available resin commonly used for composite liquid moulding. Chemical deposition was preferred over physical deposition due to the stronger adhesion obtainable for the metal coating onto the nanotube sides and walls, whereas physical functionalisation relies on physical interactions between nanotubes.

An electroless plating technique was used to create homogeneous, chemically-stable, metal functionalised coatings (*e.g.* nickel, cobalt, and nickel-iron) on the MWCNT sides and ends. The functionalisation procedure with cobalt nanoparticles turned out to be more time consuming but potentially more efficient in terms of bond strength. TEM analyses showed that Ni coating of commercially bought multi-walled carbon nanotubes seems weaker and less efficient than the Ni coating obtained experimentally at the University of Bristol.

The metal-functionalised MWCNTs were introduced into the epoxy at different volume fractions (, 5 wt.% and 10 wt.%) within host epoxy resin PRIMETM 20LV to understand the effect of the metal-functionalised nanotube introduction on the rheological and thermal properties of the resin.

Rheological measurements were conducted to study the changes in flow properties of the metal-plated CNT-filled resin systems. MWCNTs in the epoxy resin cause a significant increase in viscosity compared to neat resin. The variation in viscosity in the range of 5-10% weight fraction of CNT and different types of CNT appears much less important than the drop in viscosity due to shear thinning at the rates of 0.1-50 1/s.

MDSC analyses were conducted to assess the influence of the metal functionalised nanotubes on the neat resin cure cycle. An endothermic peak at 23°C was obtained and related to the nanotube dispersion (bond breakage and macroscopic reorganisation) within the resin system, requiring an additional external heat supply. The exothermic peak onset related to the resin cure process clearly showed a shift towards lower temperatures for the metal functionalised nanotubes. The peak intensity also increased for the metal plated nanotubes. To conclude, Ni-plated nanotubes can assist and facilitate the cross-linking process.

Magnetic characterisation through VSM was carried out to discover the magnetic sensitivity of different metal coatings onto nanotubes, which would affect the nanotube ability to be magnetically positioned within an epoxy medium. The Co10- and nickel-plated nanotubes showed the highest magnetic moments at low magnetic flux densities, although the magnetic moment decreased significantly at higher flux densities, particularly for Co10. This indicates that the magnetically-stirred plating bath shows to be less efficient than other procedures (*i.e.* sonicated bath). Co-plated nanotubes obtained using a sonicated bath present a higher magnetic moment (around 160 $\mu\text{A}\cdot\text{m}^2$), which is the highest value among the investigated nanotube coatings. This result will be used in Chapter 5 for the investigation of nanotube magnetic manipulation within fabric preforms, potentially beneficial for application in induction heating processing of composites.

4. Magnetic alignment and placement of functionalised additives within epoxy resin

Successful experimental trials with resin doped with functionalised CNT additives enable the next step of this study: exploring possibility of controlled positioning of the additives. Manipulating particles by means of DC field presents a particular interest as it allows not only to tune the position of additives with high degree of control, but also to align the CNT with external field thus having potential to improve through-thickness properties critical both for performance and processing. Magnetic positioning is envisaged to complement more robust CNT deposition technique, such as liquid resin print [49, 50], which is explored in the Chapter 4. The current chapter will focus on (a) establishing process parameters for magnetic alignment, such as field strength, spatial field gradient, exposure time, and (b) relating these parameters to the material systems selected in the previous chapter. The discussion departs with analytical model estimating time required to align arbitrarily distributed CNT in uniform magnetic field for resin with the various rheological profiles. It then assesses time required to propagate a particle in a non-uniform field at a distance characteristic for a patch. A numerical FE model is then used to assess the non-uniformity of the magnetic field for an experimental set-up. Eventually, the experiments on magnetic alignment/positioning are conducted and the results are assessed using CT and optical observations.

4.1. Assessment of non-uniform DC magnetic field

Positioning and aligning of the functionalised additives set different requirements for magnetic field. Alignment requires uniform field in the direction of nano-tube orientation axis whereas the positioning requires a gradient in magnetic field in the direction of motion. A simple set-up described below allows achieving both the features. It represents two magnetic poles, 32-mm in width and separated by the distance of 28 mm. Each pole is a square iron core with 4900 windings. The experiments with this set-up will be described further. The current study explores the distribution and the components of a non-uniform DC magnetic field, and how the magnetic flux density gradients develop on the plane of the magnetic pole under a numerical viewpoint. This eventually influences the positioning of magnetically sensitive nano-fillers embedded within a viscous medium and subjected to the externally applied magnetic field.

4.1.1 Non-uniform DC field assessment: numerical model specification

A model of a magnetic field distribution for a representative set-up used for experimental trials, is considered below. It is needed to assess the uniformity and strength of the field that can be generated. The numerical analysis was based on the solutions from the constitutive equations to retrieve the magnetic flux density values, the Maxwell equations. Finite element analysis was carried out using the software FEMM (which stands for Finite Element Methods Magnetics) 4.2 to replicate the magnetic field applied through the thickness of the samples as shown in Fig. 4.1.

The air gap between the poles, g , is equal to 28 mm, whereas the magnetic pole in-plane width, p , equals 25.4 mm [1]. The poles are made of neodymium iron boron N42, whereas the surrounding environment presents air. Continuity conditions were set between the two domains. Materials properties are shown in Table 4.1.

Table 4.1. Materials properties for N42 and air.

Material	Relative magnetic permeability μ_x	Relative magnetic permeability μ_y	Magnetic coercivity H_c [A/m]
N42	1.05	1	1006582.16
Air	1	1	0

2D analysis was considered sufficiently representative of the phenomenon as the simple and symmetrical square geometry of the magnetic poles did not require a 3D investigation. Moreover, the purpose of the study was the assessment of the magnetic flux density gradients on the magnetic pole horizontal coordinate (x-coordinate). Therefore, the magnetic problem was defined planar with the depth equal to 1. The first step was to define the rectangular domains of the magnetic poles and set their dimension. The air domain was then outlined to enclose the magnetic poles. The air domain was chosen sufficiently large ensuring that the magnetic B-field at the boundaries of the domain surrounding the magnetic poles is negligibly small. Hence, the error of setting zero B-field at the boundaries does not affect the solution. Material properties shown in Table 4.1 were then specified within the software and assigned to the specific domains. The next step was to set the continuity boundary condition between domains. Meshing was then carried out and optimised by using triangular elements. The model encountered 7528 elements and 3891 nodes. Mesh is shown in Fig. 4.1. Direct current conditions were used, entailing a non-alternating current.

The highest value of magnetic field can be observed at the edge of the magnetic poles, where the magnetic moments of adjacent magnetic domains do not counterbalance each other as in the magnetic bulk, leading to a resulting magnetic moment greater than zero. The magnetic flux density colour scale shows a gradient between the centre and the edges of the poles. The x and y contributions of the magnetic flux density B_x and B_y , and the resulting $|B|$ are shown in Fig. 4.2 as a function of the normalised x-coordinate with respect to the x-coordinate of the left hand side magnetic pole x_0 as per representation in Fig. 4.1.. The highest contribution to the resulting $|B|$ can be attributed to B_x , leading to a magnetic flux density increase at the pole edges by around 40% compared to the pole centre. This heterogeneity of the magnetic field is responsible for the motion of the particles. A more defined alignment pattern can be achieved through a stronger field as expected and shown in Fig. 4.3 [1]. The model presents an input to proving the potential manipulation of metal functionalised nanotubes in a viscous medium *via* external magnetic fields [1]. Further investigation is required for the nanotube manipulation in higher viscosity systems *e.g.* with the presence of structural fibres in fibre reinforced polymer composites.

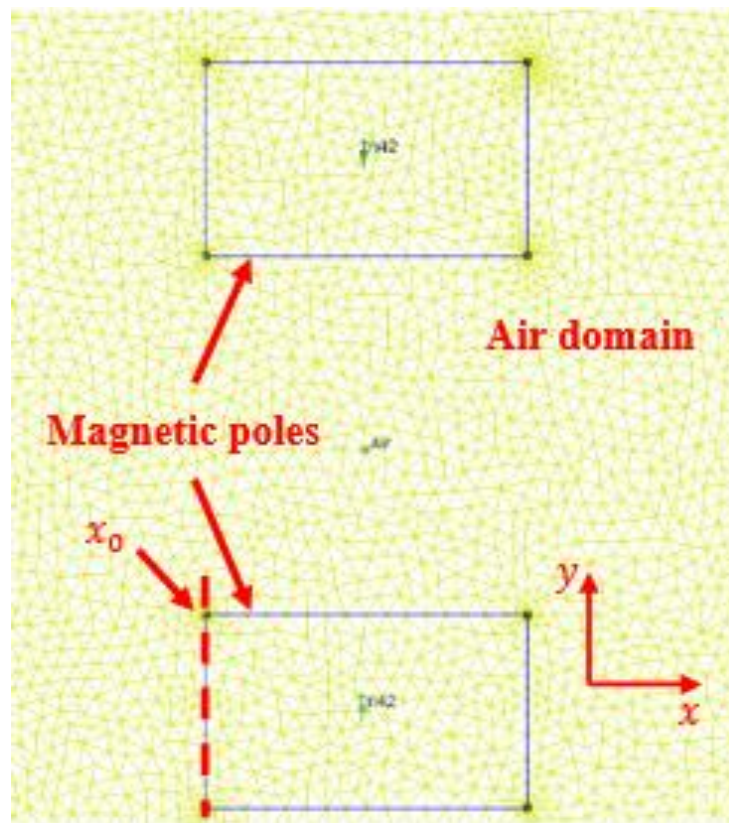


Fig. 4.1. Magnetic model showing magnetic poles and air domain, mesh, element type and materials name.

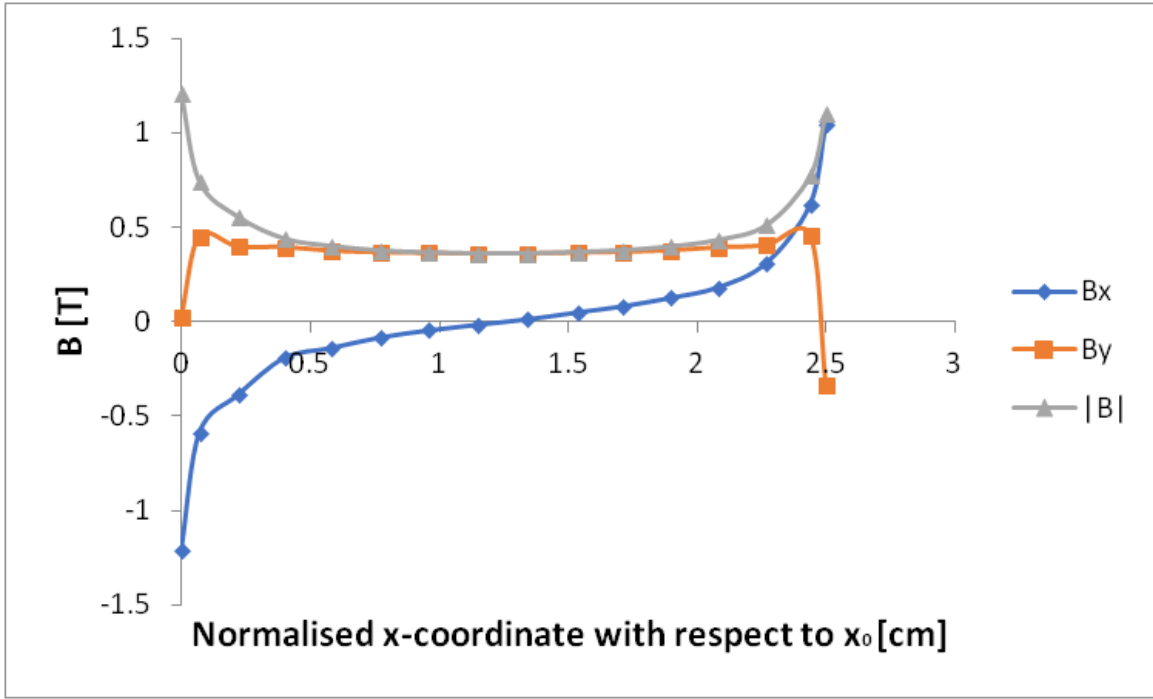


Fig. 4.2. B_x , B_y and resulting $|B|$ [T] trends as a function of the normalised x-coordinate [cm] (normalised with respect to the x-coordinate of the left hand side magnetic pole x_0).

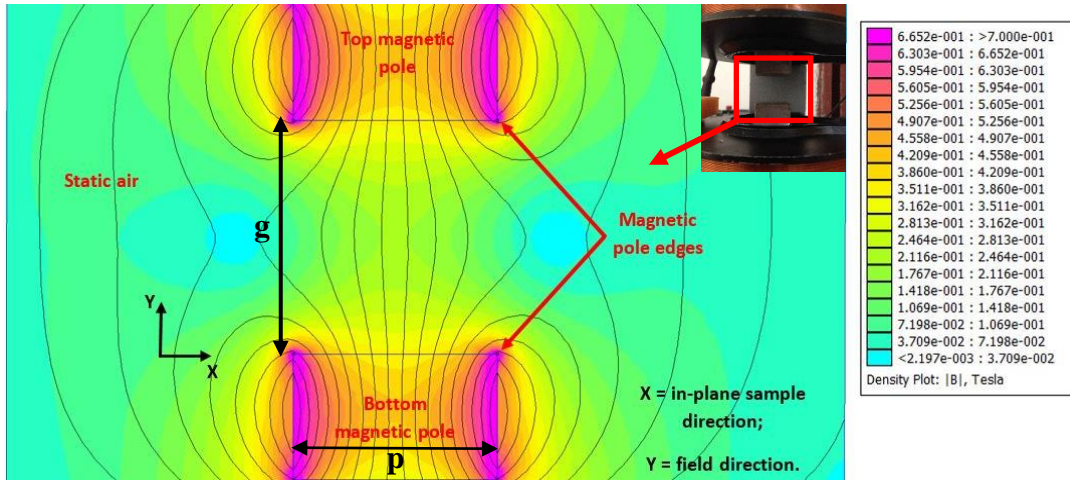


Fig. 4.3. Finite Element Methods Magnetics (FEMM) model: magnetic flux density gradients between centre and edges of the DC magnetic poles [1].

4.2 Magnetic alignment and placement of functionalised particles in DC field

To estimate characteristic time of exposing the CNT/epoxy solution to magnetic field and required magnetic field strength, an analytical model was developed by Kimura *et al.* [101] and Erb *et al.* [8]. This model considered the motion of an idealised paramagnetic fibre in viscous medium under action of external magnetic field. Ciambella *et al.* [102] extended this

model by considering viscosity evolution of reactive resin and successfully validated it in a study on the alignment of nickel coated carbon nanofibres in a polydimethylsiloxane (PDMS) matrix. In the current study these estimates will be adopted not to analyse the process in great details but to assess the feasibility of the magnetic processing of the CNT solution. For instance, one important practical question is whether the time required to position the fibre is sufficient, *i.e.* lower than the pot life of the resin when it undergoes gelation and the fibre motion becomes impeded.

The model is built on considering the balance of hydrodynamic drag forces imposed on fibre by resin and forces generated by magnetic field driving fibre reorientation and motion. For a fibre with orientation defined by the vector \bar{n} and its centre by the vector \bar{r} the equations of motion are given by the following expressions:

$$\frac{d\bar{r}}{dt} = - \left(\frac{1}{d_{II}^0} (\bar{n} \otimes \bar{n}) + \frac{1}{d_{\perp}^0} (I - \bar{n} \otimes \bar{n}) \right) \bar{F}(\bar{r}) , \quad (4.1)$$

$$\frac{d\bar{n}}{dt} = - \frac{1}{d_{\theta}^0} (\bar{T} \times \bar{n}) , \quad (4.2)$$

where $\bar{F} = -V\nabla\Psi$ is the magnetic force, Ψ is the magnetic energy, $\bar{T} = v(\mathcal{M} \times \mathcal{B})$ is the magnetic torque, with v being the fibre volume, \mathcal{M} being the fibre magnetisation and \mathcal{B} the flux density direction vector, and

$$d_{II}^0 = \frac{4\pi\eta_0 l}{\ln(2a_r) - \frac{1}{2}}, d_{\perp}^0 = \frac{8\pi\eta_0 l}{\ln(2a_r) + \frac{1}{2}}, d_{\theta}^0 = \frac{8\pi\eta_0 l^3}{3[\ln(2a_r) - 1/2]} , \quad (4.3)$$

are the scalar translational and rotational drag coefficients calculated in the case of a spheroid particle with aspect ratio $a_r \gg 1$ and half-length l embedded within a fluid with viscosity η_0 [102].

To simplify the coupled problem (4.1-4.2), it can be divided on two independent sub-problems. First one is set to estimate time and flux density required for move the fibre of fixed orientation (\bar{n} is constant) at a specific distance in a non-uniform magnetic field. The second problems aim at estimating time and flux density required to reorient fibre in uniform magnetic field (\bar{r} is constant). The uniformity of the field is understood in the sense that characteristic variation of the magnetic field is much larger than the size of the CNT.

Although orientation and displacement of CNT occur simultaneously in reality, the problem was decomposed to ease the investigation and reorientation and propagation motions were considered as sequential processes happening at different length and timing scales.

The next paragraph uses the FE simulation of magnetic set-up to derive the field $\bar{F}(\bar{r})$ in experimental set-up followed by the solution of ODE (4.1).

4.2.1. Analytical assessment of CNT motion

The first independent sub-problem of Section 3.2 was studied to estimate the motion of a single fibre at a specific distance from the centre of the sample in a non-uniform magnetic field. The single fibres were approximated as nanotubes with aspect ratio $ar = l/r$, where l is the nanotube half-length and r is the outer radius of the nanotube. The volume of the nanotube V was calculated as $4\pi/3r^2l$ as the nanotube was approximated as an oblate spheroid. The migration distance as a difference between the final and initial position of the fibre at a specific time t when the gelation starts occurring, *i.e.* the pot life, was assessed. The resin considered for the study was PRIME 20LV (Gurit) which is characterised by a pot life of one hour if a slow hardener is used. Moreover, processing parameters required for the particle positioning were estimated. The model discussed in Section 4.1 described the magnetic field in a characteristic set-up. It was shown that the field generated by the DC current can be assumed to be constant in through thickness direction and varies on the plane of the magnetic pole, in the x direction. Specifically, the magnetic intensity increases towards the edges of the magnetic poles, causing the magnetic migration of the particles.

Motion of the fibre aligned with the magnetic field and moving perpendicular to its direction ($\bar{n} = \{0 \ 1 \ 0\}$, $\bar{B} = \{0 \ b(x) \ 0\}$) was considered. CNT was aligned with the field at the centre of the patch and propagating towards the edge due the gradient in $b(x)$. The equation 4.1 is then transformed to:

$$\frac{dr_x}{dt} = -\frac{1}{d_{\perp}^0} F_x(r_x) = -\frac{V}{d_{\perp}^0} \nabla \Psi = \frac{V}{d_{\perp}^0} (1 + \chi_{mII}) b(r_x) \frac{db(r_x)}{dx} . \quad (4.4)$$

where $F_x(r_x)$ is the x -component of the magnetic force dependent on the x -component of the radius, V is the applied voltage, Ψ is the magnetic energy, χ_{mII} is the component of the magnetic susceptibility parallel to the fibre axis, $b(r_x)$ is the magnetic flux density

component dependent on the x-component of the radius and d_{\perp}^0 is scalar translational drag coefficient perpendicular to the fibre axis. This ODE is solved in MatLab to derive the time of particle propagation towards the edge for a field derived from the FE simulations. Parameters used for the simulation are shown in Table 4.2.

Table 4.2. Parameters used for the MATLAB simulation.

Nanotube length L [mm]	Nanotube radius r [mm]	Resin viscosity [N mm ⁻² s]	χ_{mII} [102]	Resin pot life [s]
0.0015	9.5e-6	0.47564e-6	0.03	3600

Fibre (nanotube) initial positions r were considered as 0.1 mm, 1 mm and then up to 12 mm with intervals of 1 mm. The magnetic pole half width was 12.5 mm and considered as the limit for the fibre migration. MATLAB results showed the time dependence of the fibre position for different fibre initial positions. Values at $t = 3600$ s as per resin pot life from manufacturer's technical data sheet were considered and the fibre migration distance was retrieved. Fig. 4.4 shows the fibre migration distance, in mm, as a function of the initial fibre distance from the sample centre, in mm. Results were considered up to an initial fibre distance from centre of 7 mm. This is because a single fibre tends to reach the magnetic pole half width before 3600 s for initial fibre distances from centre of 8 to 12 mm. Table 4.3 shows the times required for the single fibre to reach the magnetic pole half width if the initial distance from the centre exceeds 7 mm.

Fig. 4.3 shows that the migration distance increases considerably at distances from the centre over 4 mm. This is because the flux density gradient $b(r_x)$ is approximately zero around the centre of the sample as shown in Fig. 4.2, whereas it tends to increase towards the edge of the magnetic pole, as shown in Section 4.1. Therefore, the magnetic migration driving force acts on the fibre in a higher extent towards the pole edge, causing the fibre to migrate by 0.2 mm from the initial distance from centre of 4 mm, and by 1.8 mm for an initial distance of 7 mm. Moreover, Table 4.3 shows how the fibre reaches the pole edge in progressively shorter times when the initial distance from the centre increases, from 54.2 minutes at 8 mm, to 1.6 minutes at 12 mm. These results validate the FEMM model studied in Section 3.1. The next section will focus on the fibre magnetic orientation by considering the solutions of equation 4.2.

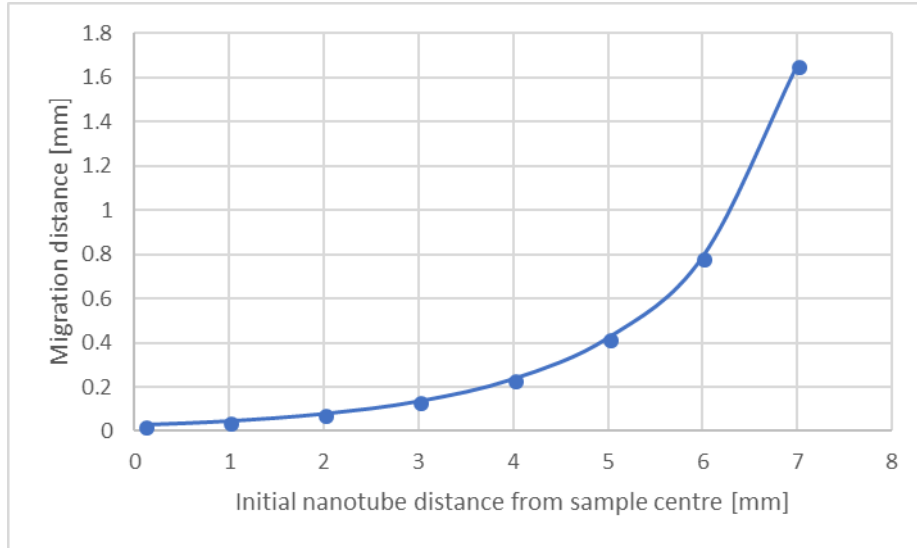


Fig. 4.4. Fibre (nanotube) migration distance (in mm), as a function of the initial fibre distance from the sample centre (in mm). Magnetic pole width exceeds the dimensions shown on this graph.

Table 4.3. Times required for the single fibre to reach the magnetic pole half width if the initial distance from the centre exceeds 7 mm.

	8 mm	9 mm	10 mm	11 mm	12 mm
Time [s]	3254	1768	904	393	97
Time [min]	54.2	29.5	15	6.5	1.6

The model findings were considered for the experimental assessment of the alignment and positioning of nanotubes within epoxy resin outlined in Section 4.3.3.1.

4.2.2. Analytical assessment of CNT orientation

The aim was the assessment of the minimum flux density B_{0min} required for the alignment of commercially available and nickel coated carbon nanotubes within commercially used low and high viscosity resin systems. For the purpose, only rotational and translational movements of the nanotubes were accounted for without considering the contribution of gravity effects. These are particularly relevant in case of nanotubes as sedimentation phenomena can occur at different time scales. Therefore, the application time might affect the importance of the gravity effects on the nanotube positioning. Another approximation of the model refers to the curing process and exothermic heat generation not included in the analysis. Assumptions of

Stokes flow (dominant viscous forces over inertial forces) and uniform magnetic field applied to the control volume system were also made. PRIME 20LV (Gurit) and EPON 828 (Hexion) were considered as low and high viscosity resins, respectively. However, EPON 828 was not used for experimental validation, but only as a reference for higher viscosity mediums as available for use and extensively characterised at the University of Bristol. An analytical model was used to estimate the time interval required to position an additive within a viscous medium by means of an externally applied direct current (DC) magnetic field. The time interval was referred to as characteristic curing time τ_c , as the additives have no longer the ability to migrate under the magnetic field effect after the cure of the viscous medium (*e.g.* epoxy resin). Dynamic viscosities at 25°C and curing times for both systems are shown in Table 4.4.

Other relevant constant parameters for the analytical model are: the vacuum magnetic permeability μ_0 , which is equal to $1.257 \cdot 10^{-6} \text{ N A}^{-2}$; the fibre angle spread with respect to the applied magnetic field φ_i (which is relative to a specific probability of aligning nanofillers within a viscous medium p_i); and the magnetic susceptibility of the nanofiller constituent material χ .

The nanotube alignment is strongly influenced by the geometrical specifications of the nanotubes (Section 3.2.1). The model is most accurate for $ar < 100$ [102].

Table 4.4. Dynamic viscosities at 25°C and curing times for both systems.

	Dynamic viscosity η [P]	Curing time τ_c [s]
PRIME 20LV (slow hardener)	0.15-0.17	86400
EPON 828	110-150	604800

The main output variable of interest for the assessed analytical model was the minimum flux density B_{0min} calculated as follows:

$$B_{0min} = \left[\frac{\eta}{\tau_c} \frac{\mu_0}{\chi_a} \frac{2a_r^2}{\ln(2a_r) - 0.5} \ln \left(\frac{\pi}{2} \frac{p_i}{\tan(\varphi_i)} \right) \right]^{0.5}, \quad (4.5)$$

where χ_a represents the anisotropic magnetic susceptibility, which can be calculated as

$$\chi_a = \chi_{m\parallel} - \chi_{m\perp} , \quad (4.6)$$

as a difference between the parallel contribution to the fibre axis $\chi_{m\parallel}$ and the perpendicular component to the fibre axis $\chi_{m\perp}$:

$$\chi_{m\parallel} = \frac{\chi}{(1+N_{\parallel}\chi)^2} , \quad (4.7)$$

$$\chi_{m\perp} = \frac{\chi}{(1+N_{\perp}\chi)^2} . \quad (4.8)$$

The minimum flux density B_{0min} was then estimated for as-received multi walled carbon nanotubes without metal functionalization as a baseline analysis. The selection of non-functionalised nanotubes was to verify the potential of influencing the position of nanotubes in the worst-case scenario of limited susceptibility to an external magnetic field without altering the magnetic properties by metal functionalisation. The magnetic susceptibility of the CNTs without functionalisation χ was assumed equal to $-9 \cdot 10^{-6} \text{ emu g}^{-1}$ as per investigation carried out by Grzelczak *et al.* [54]. The angle spread ϕ_i was assumed equal to 20° as the additives might show variability in orientation towards the magnetic field direction due to mutual interaction between additive particles and flow properties of the viscous medium. The aspect ratio was considered equal to 10, 50 and 100 as per values retrieved by the study from Ciambella *et al.* [102], although the particle shape was different (carbon rods instead of nanotubes). The latter value represents the validity limit of the model. The parameter B_{0min} was studied for alignment probabilities p_i of 50%, 80% and 90%. Results are shown in Table 4.5 and 4.6.

Table 4.5. Minimum flux density B_{0min} as a function of the aspect ratio for different alignment probabilities within high viscosity medium (EPON 828, Hexion).

Probability p_i [%]	Aspect ratio	Min B_{0min} [T]
50	10	0.819
	50	0.948
	100	1.181
80	10	1.040
	50	1.203
	100	1.499
90	10	1.088
	50	1.258
	100	1.569

Table 4.6. Minimum flux density B_{0min} as a function of the aspect ratio for different alignment probabilities within high viscosity medium (PRIME 20LV, Gurit).

Probability p_i [%]	Aspect ratio	Min B_{0min} [T]
50	10	0.380
	50	0.439
	100	0.548
80	10	0.482
	50	0.558
	100	0.695
90	10	0.505
	50	0.584
	100	0.728

These results show that higher alignment probabilities require stronger magnetic fields externally applied to the control volume. For example, a magnetic flux density of 0.728 T would be required to align nanotubes with an aspect ratio of 100 with a probability of 90% compared to 0.548 T for the same aspect ratio and a probability of 50%. Under the same alignment probability assumption, higher aspect ratios need a stronger magnetic field (over 1 T for EPON 828, around 0.7 T for PRIME 20LV). Indeed, the translational contribution of the nanotube movement becomes relevant at high aspect ratios, leading to higher required magnetic driving force. This contribution can interfere with the rotational force component experienced by the nanotube under application of the external energy fields.

As previously mentioned, the analytical model is valid for aspect ratios below 100. For higher aspect ratios, the model allows for unreliable results as unable to predict the major contribution of the translational displacement component. In the case of PRIME 20LV, the lower viscosity of the resin system and, therefore, the lower extent of viscous forces acting on the nanotubes reduce the magnetic field requirement for the nanotube alignment. However, the condition of DC field limits the homogeneity of the rotational alignment compared to AC field application, as previously observed from literature works [70]. Therefore, a better control over the nanotube alignment can be ensured by the application of AC fields as the oscillating magnetic driving force can help overcome the viscous forces of the host medium. The next section will focus on experimental validation of the particle placement by an external magnetic driving force.

4.3 Experimental demonstration of particle placement

The present paragraph describes experiments to position particles within a viscous medium through magnetic field application. The aim of the investigation is to study the feasibility of tailoring the position of additives to locally alter the mechanical and electrical properties of the component. The results of the previous paragraph showed a theoretical possibility of aligning and displacing the particles.

Measurements of the magnetically induced alignment of MWNTs were carried out with an experimental setup including an electromagnet supported by a wooden support. The sample dimensions were selected to replicate characteristic dimensions of a real-life application repair patch [3]. The experimental setup was available at the University of Bristol as a two-sided magnetic source, although a one-sided magnetic source would be more representative of the real repair procedure. The distance between the magnetic poles could be altered to increase or decrease the magnetic flux density available to the sample. A voltage amplifier and a power controller were connected to the electromagnet to modify the magnetic field frequency applied to the sample.

4.3.1 Magnetic DC set-up

A magnetic setup, shown in Fig. 4.5 [1], was used to induce and apply a magnetic field on a system composed of metal functionalized nano additives within epoxy resin and fabric. The magnetic field was used to manipulate the alignment and positioning of the metal plated CNTs. DC field was generated to induce the particle alignment. Magnetic coils count 9800 turns and a total electric current through the coils reaches 1.5 A. The magnetic DC field (flux density of 0.5 T) was applied through two magnetic poles (pole edge size equal to 25.4 mm) [1].



Fig. 4.5. DC magnetic apparatus, with Electromagnet (Type C, Newport Instruments) [1].

The electromagnet (Type C, Newport Instruments) available for the experimental analysis is composed of two coils with a number of turns equal to 4900 for each opposite pole (wire

thickness of 0.559 mm). The total cold resistance is 90 Ω whereas the hot resistance at the maximum rating corresponds to 126 Ω . The maximum electric current allowed to run through the coils before electrical breakdown depends on the cooling condition which can be supplied via water through metal pipes attached to the main body of the coil: 1.1 A (per coil) with water cooling and 0.75 A (per coil) without cooling (this condition might be preferred for electrical safety issues). The pole distance can be also adjusted so that the air gap between the poles and the sample can be modified. The magnetic field strength H can be calculated as follows:

$$H = \frac{\pi \cdot I \cdot N}{d}, \quad (4.9)$$

where I is the electric current intensity, N is the number of coil turns and d is the air gap between magnets. The coil turns N is important because the increasing number of turns can lead to relevant coil resistance which enhances the voltage requirements for the magnetic setup. Evaluation with voltage amplifiers and capacitors connected to the electromagnet provides the available magnetic flux density B (in Tesla) for the experimental analysis. This can be obtained as follows

$$B = \mu_0 \cdot H, \quad (4.10)$$

where μ_0 is the vacuum magnetic permeability equal to $1.257 \cdot 10^{-6}$ N A⁻².

The electromagnet poles were placed vertically to induce through-the-thickness magnetic field in a horizontal sample mould. A bespoke wooden, therefore diamagnetic, carved mould was used. The electromagnet was placed vertically, and it could move horizontally if not fixed into place with blockers.

4.3.2 Implementation of experiments

The sample mould was chosen circular and characterised by a diameter of 92 mm and a thickness of 25 mm. This was done to approximately replicate the repair patch dimension to be placed in the damage location of on-platform composite components. Owing to the sample

mould thickness, the minimum distance between the poles was chosen equal to 28 mm to have enough space for the sample positioning between the magnetic poles. This condition will ensure the minimum contribution of fringing effect and therefore the most homogeneous magnetic field applied locally to the sample.

4.3.3 *Experimental analysis*

Samples of nanocomposite systems containing 1 wt.% of as-received multi-walled carbon nanotubes embedded in low viscosity epoxy resin system PRIME 20LV (Gurit, slow hardener) were manufactured with a 100 : 26 ratio by weight (100 : 31.4 ratio by volume). The as-received multi-walled carbon nanotubes were introduced within the host matrix and well dispersed by using shear mixing (5000 rpm for 1 hour). The slow hardener was therefore added to the suspension to facilitate the chemical crosslinking of the polymeric chains. The CNTs were characterised by low aspect ratio (equal to 10, with cross section diameter of 80-100 nm; GSI Creos) and high aspect ratio (around 1500, with cross section diameter of 6-13 nm; Sigma Aldrich). Three samples with low aspect ratio CNTs were exposed to magnetic DC field with flux density of 0.5 T until gel time was reached after around 200 minutes. These samples were compared with three samples containing low aspect ratio CNTs but not subjected to DC field. The samples were assessed to understand the effect of an externally applied DC magnetic field to the initial orientation of the CNTs. The electromagnet mentioned in section 4.3.1 was used for the application of the DC field through the sample thickness. Furthermore, three samples containing high aspect ratio CNTs and subjected to DC field were studied to assess the influence of the CNT aspect ratio on their alignment towards the DC field direction. Scanning electron microscope (SEM) images were obtained from said nanocomposite systems after curing process at room temperature. SEM micrograph were taken from the sample through-thickness cross sections. .

. Fig. 4.6(a), (b) and (c) refer to the three nanocomposites obtained by including low aspect ratio nanotubes within epoxy resin and without applying DC field. Fig. 4.7(a), (b) and (c) show the samples containing low aspect ratio nanotubes within epoxy after application of DC field. The magnetic field direction is shown as a red arrow in the figures.

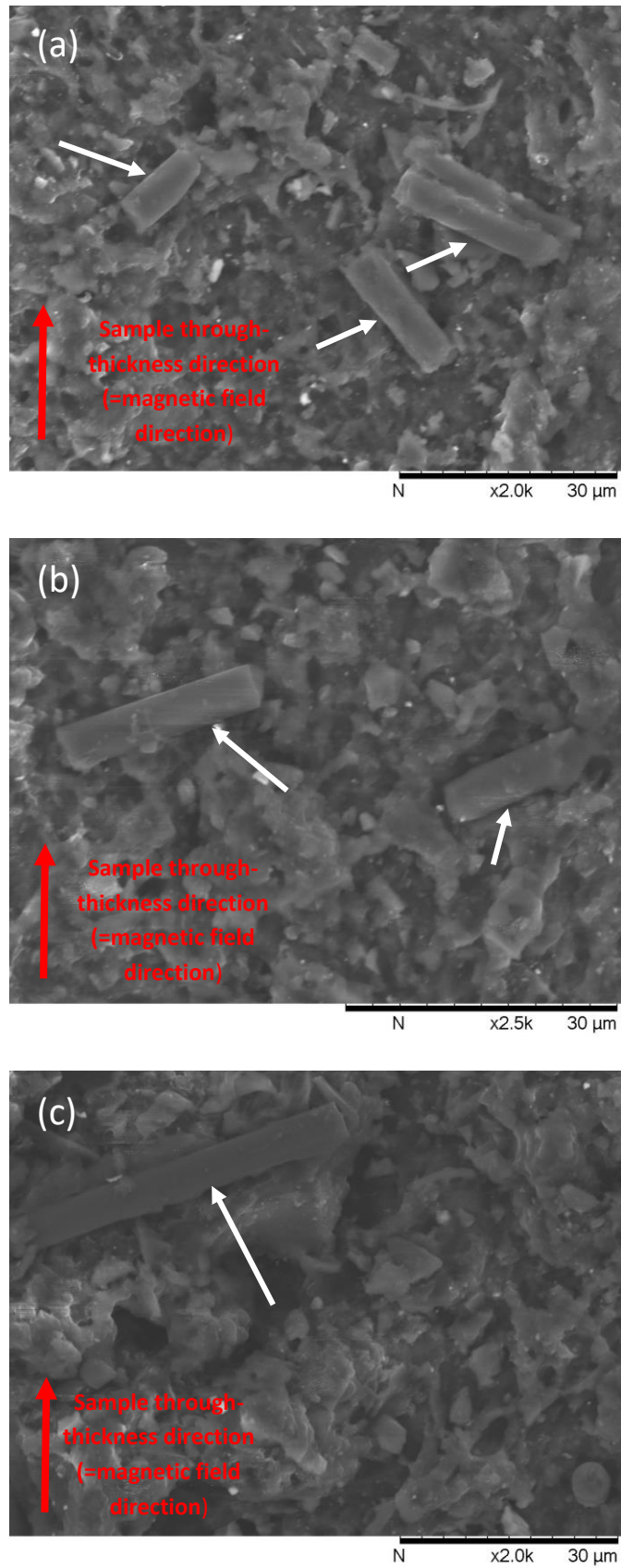


Fig. 4.6. SEM micrographs of samples containing as-received multi-walled carbon nanotubes (low aspect ratio) with no DC field application.

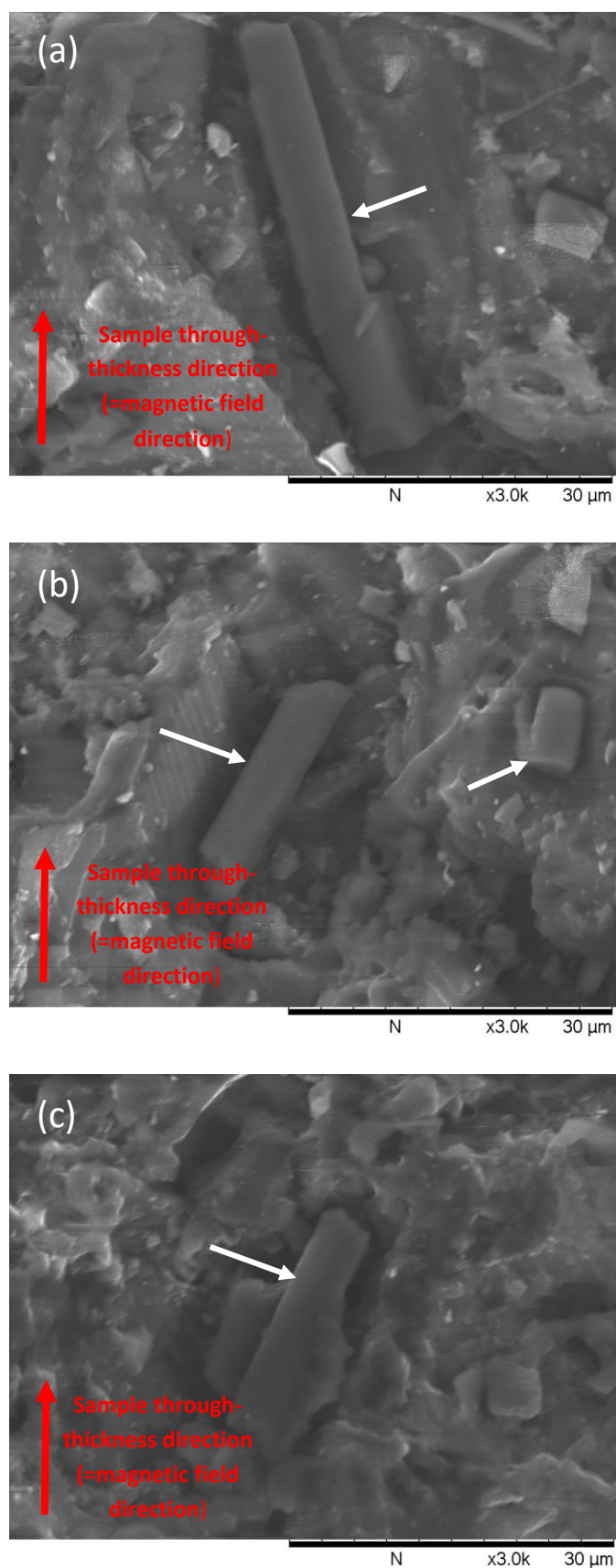


Fig. 4.7. SEM micrographs of samples containing as-received multi-walled carbon nanotubes (low aspect ratio) after DC field application.

Fig. 4.6 shows that the CNTs seem to display disordered orientation within the medium with no clear alignment towards the magnetic field direction, which is shown with the red arrow in the images. On the other hand, Fig. 4.7 shows a more ordered alignment of the CNTs towards the direction of the magnetic field. This could be an indication that the CNT alignment changed from the initial orientation due to the DC field application until resin gelation.

Fig. 4.8(a), (b) and (c) refer to the three nanocomposite samples obtained by including high aspect ratio nanotubes within epoxy resin after the application of DC field. A reduction in aspect ratio due to the sonication forces is expected in the case of high aspect ratio CNTs. In this case, the initial aspect ratio of the CNTs is 1000, and the micrographs in Fig. 4.8 reveal a much lower aspect ratio. Nanotube breakage can be observed at the ends of the nanotubes, as shown by the red circle in Fig. 4.8(a), (b) and (c). In addition, the nanotube does not align completely in the direction of the magnetic field.

On the other hand, low aspect ratio CNTs in Fig. 4.6 and 4.7 show a limited reduction in aspect ratio due to sonication forces. The nanotube ends show a neater fracture surface compared to the case of high aspect ratio nanotubes. Slightly clearer alignment towards the direction of the direction of the magnetic field (sample thickness) can be observed if compared to high aspect ratio nanotubes under the same DC field application time and strength conditions; this can be associated with the rotational forces which overcome translational forces thanks to the low aspect ratio, also responsible for the almost total absence of breakage phenomena. These results were predicted by the analytical model of CNT alignment previously mentioned.

In conclusion, low aspect ratio MWNTs showed slightly clearer alignment extent due to the rotational forces which overcome translational forces. However, the SEM investigation could not provide a definitive answer to the CNT alignment dependence on the aspect ratio. Reduced sonication-induced breakage was visually observed on low aspect ratio MWNTs from Fig. 4.6 and Fig. 4.7, and neater nanotube ends compared to high aspect ratio MWNTs.

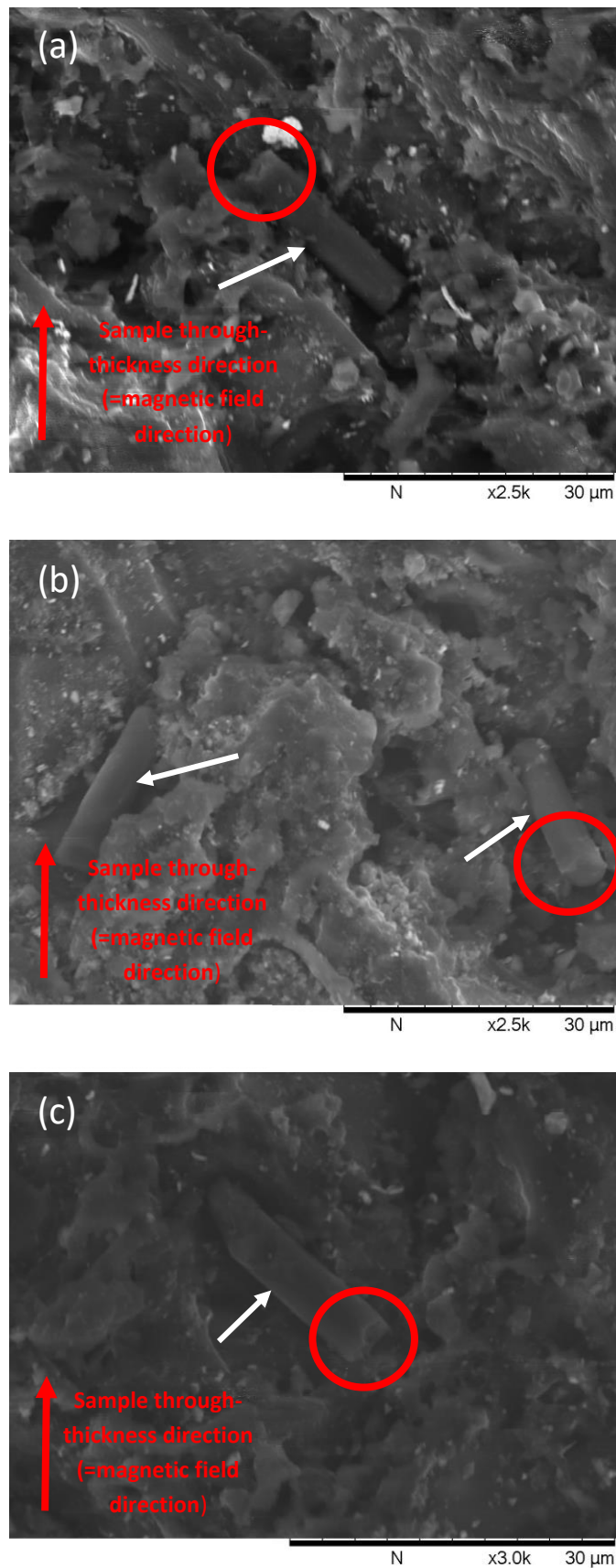


Fig. 4.8. SEM micrographs of samples containing as-received multi-walled carbon nanotubes (low aspect ratio) after DC field application.

4.3.3.1 Results of experiments on CNT alignment and positioning

Initial work consisted of modelling analysis and experimental validation for the magnetic field manipulation of non-functionalised multi-walled carbon nanotubes in low viscosity epoxy resin for alignment and network generation purposes. Magnetic equipment (Fig. 4.5) was used for the through-thickness nanotube alignment in the epoxy resin. Approximated values of magnetic flux density for the alignment of uncoated nanotubes in PRIME™ 20LV were in the range of 0.5-0.7 T. This finding provided a guideline for the design of a magnetic DC setup used for further experimental analysis. The epoxy/MWCNT blends were exposed to magnetic DC field with flux density of 0.5 T until gel time was reached after around 200 minutes.

Nickel plated and carboxyl functionalised MWCNTs obtained through a sonicated plating bath, were introduced in low viscosity epoxy resin (PRIME™ 20LV with amine hardener) with a volume fraction equal to 2.5 wt.%. The sample holder had an outer diameter of 35 mm and thickness of 10 mm. Both nanotube types were subjected to an external magnetic field with flux density of 0.5 T. Consequently, further analysis involved the application of lower fields of 0.25 T and 0.1 T to two samples with 2.5 wt.% of nickel-plated nanotubes in PRIME™ 20LV to investigate the nanotube magnetic alignment at different field levels. The magnetic flux density values were selected lower than 0.5 T to assess if lower energy processes could be suitable and lead to the same results. Nickel plating process was used as well established at Cardiff University, where the first functionalization attempts for this project were made. The field was held until gelation occurred. Samples then allowed cooling naturally to room temperature to complete the resin cure. No external heat sources were applied during the field application, although the magnetic setup may have heated up due to internal coil resistance and accelerated the gelation process.

Computed tomography (CT) scans were carried out using a Nikon XTH225ST CT Scanner [1]. This technique relies on the application of x-rays for the 2D characterisation throughout the sample and, ultimately, the combination of the 2D scans to obtain the 3D sample mapping. Samples presented circular epoxy resin/MWCNT tabs with diameter of 35 mm and thickness of 10 mm. Computed tomography (CT) scans were carried out for the nickel plated reinforced epoxy systems subjected to flux densities of 0.25 T and 0.5 T for the qualitative assessment of the preferential distribution and through-the-thickness alignment of the nickel plated and carboxyl functionalised MWCNTs. Fig. 4.9(a) [1] shows the epoxy/nickel-plated nanotube samples subjected to different magnetic field levels; the square alignment pattern can be observed. The square pattern can be linked to the square shape of the magnetic core poles as

described in Section 4.1.1 [1]. The edge effects lead to a higher magnetic flux density at the edges of the rectangular magnetic poles, driving the CNTs towards creating the rectangular positioning pattern.

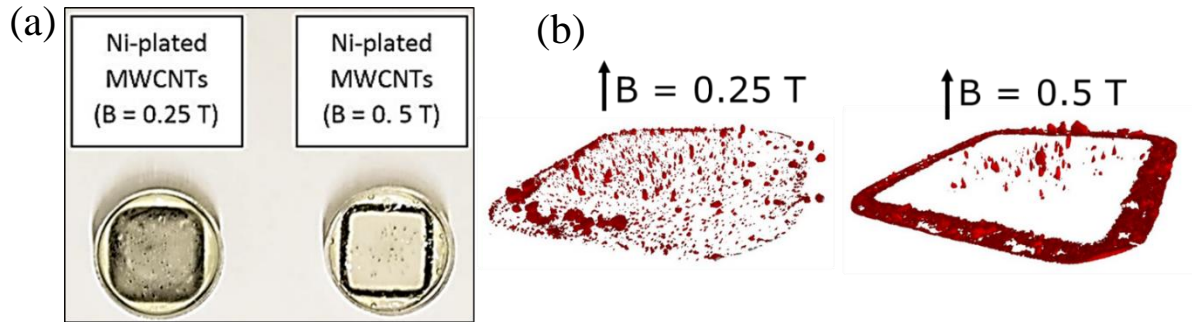


Fig. 4.9. (a) Ni-plated MWCNTs positioning: comparison after DC field and (b) CT scans of PRIMETM 20LV+1 vol.% Ni-plated MWCNTs under 0.25 T and 0.5 T [1].

SEM images were subsequently obtained from the nanocomposite systems after curing process at room temperature. However, computed tomography could provide clearer results for the identification of the CNT positioning within the sample if compared to SEM [1].

4.4 Conclusions

The feasibility of the magnetic alignment of commercially available and metal functionalised nanotubes was assessed both analytically and experimentally. An analytical model was created from previous investigations to evaluate the magnetic positioning of commercially available nanotubes within viscous mediums. Specifically, the minimum magnetic field required to position the nanotube at an angle spread of 20° before the cure of the viscous medium, was assessed and found equal to 0.5 T. This value was used for future experimental validation of the nanotube positioning within epoxy resin and fabric. A DC experimental setup available at the University of Bristol was used as magnetic source. Magnetic manipulation of metal functionalised nanotubes within epoxy resin was successful as a clear square nanotube pattern was induced magnetically and observed *via* Computerised Tomography. The pattern geometry was due to the magnetic pole geometry, as the magnetic flux density is the highest at the pole edges. The latter phenomenon was proved both experimentally and numerically through FEMM. Therefore, the magnetic positioning of metal plated nanotube is a promising technique which might serve to locally place and affect the thermal and mechanical properties of a composite component. This is particularly important

in repair application, as the efficient resin cure at bondline between a repair preform and the original part is critical for the adhesion of the patch and the restoration of the original mechanical properties of the component. Further investigation of the nanotube magnetic manipulation within fabric systems is required and will be treated in Chapter 5.

5. Functionalised repair patches with graded properties

The controlled distribution of CNT within the patch means that material properties can be tailored to the geometry of the patch and coil to achieve optimum heating arrangements. Previous chapter established the feasibility of positing and aligning patterns of CNT-reach area in pure epoxy. This chapter attempts to translate and extend this concept to manipulation of CNT within textile preform. Propagation of the particles in reinforced media presents further challenges. Fibre reinforcement impedes particle propagation and it can be expected that their motion would be constrained by filtration, particularly when the motion happens within narrow inter-fibre spaces (characteristics sizes are comparable to fibre diameter dimensions). This is why it is important to conduct experiments aiming at testing the conceptual possibility of grading patch properties through the application of external magnetic field.

The success of positioning the additives is strongly determined by (a) initial distribution of particles within the domain, (b) constraints imposed on the fabric at the stage of field application. This study departs from considering deposition of the CNT using sequential layer-by-layer injections of CNT suspension into uncompacted preform as suggested in [49, 50]. The magnetic field is then applied to drive the CNT away from the injection location towards a desired position. This can be area where higher conductivity is needed to compensate for the lower magnetic field or where better control of the heating is needed, e.g. at patch boundaries. The chapter discusses the manufacturing procedure and the inspection methods used to validate the positioning of the particles upon full consolidation and cure. This includes the use of liquid resin printing for the sample manufacture, EDX/SEM together with FT-IR, DSC and DMA for sample characterisation. The tests were performed to understand the influence of the externally applied magnetic field on the position of the nanotubes and the local thermal and chemical properties.

5.1 Materials

According to the procedure described in Chapter 3, the CNT used in these experiments were functionalised through electroless plating technique. The screening of various CNT systems showed that this technique ensures the optimum magnetic properties and uniformity of metal particles along the CNT length. Carboxyl-functionalised MWCNTs (Sigma Aldrich), which is the same system as used for demonstrating particle alignment in pure resin, were used as

precursors for the electroless functionalisation of the nanotubes, subjected to sensitisation, activation and plating steps.

Specifically, the plating step was carried out as *per* Chapter 3. The resulting metal-plated nanotubes were therefore embedded within low viscosity epoxy resin PRIME 20LV (Gurit) with a volume fraction of 5 vol.%, as previously explained in Chapter 3.

An E-glass $\pm 45^\circ$ biaxial non-crimp fabric (NCF; Saertex SA) with an areal density of 440 gsm and CPT of 0.35 mm was used for this study. The optimised fabric structure minimise the yarn crimp and improve in-plane performance. The high areal density of the fabric reflects on the limited inter-tow space for movement of the solution. Therefore, a complicated scenario for epoxy/CNT blend movement is presented in this study. Non-structural polyester stitching was used to hold the tows in place. Glass fabric was selected as non-susceptible to the magnetic field; therefore, this represented the most challenging scenario to assess the generation of inductive heating from the embedded nanotubes. The architecture of the NCF implies that the fibre free zones are smaller compared to other textile forms and hence, the success of CNT motion in fabric means that it is likely to be applicable for other preforms as well. In addition, the NCF is characterised by optimal in-plane properties compared to woven or braided preforms and hence, often preferred in the context of patch repair. Finally, the architecture of non-crimp fabric is relatively simple; therefore, the results from the magnetic positioning study were easier to interpret. A cross-ply layup was used for the sample manufacture and magnetic patch injection. The laminate was characterised by four plies with layup $[0, 90]_s$ with a laminate overall thickness of around 2 mm.

5.2 Liquid resin printing: sample preparation and procedure

IKA T-18 Ultra Turrax digital shear mixer (Cole-Palmer UK) was used for the epoxy resin/CNT suspension homogenisation. A degassing procedure was then carried out to remove the excess moisture and volatiles introduced within the suspension during the mixing step. PRIME hardener was then introduced within the CNT-resin suspension with a 100 : 26 ratio by weight (100 : 31.4 ratio by volume) after homogenisation but before degassing to facilitate the crosslinking process. The aim of the homogenisation was to distribute the nanotubes across the entire suspension to avoid a preferential concentration of nanotubes during the first injections, therefore leading to a gradient of nanotube concentration through the thickness.

CNT-filled resin must be delivered from the printing syringe nozzle before resin gels and, therefore, the crosslinking phenomenon between the polymeric chains of the resin hinders the

delivery of the resin through the thickness of the preform. CNT suspension might also not flow within the nozzle if the resin dwells inside the syringe until gel time. Moreover, magnetic manipulation of the CNTs embedded in the resin can only be carried out before gel time. Therefore, the printing process time must account for the subsequent magnetic field application and CNT positioning.

The liquid resin print technique was selected particularly for the possibility of localised and efficient high-precision delivery of the resin suspension within unconstrained fabric preforms, the efficient resin delivery to unconstrained preform. Therefore, less filtration would occur at the injection stage. Moreover, multiple injections can be carried out through the thickness of the preform, *i.e.* at least one per each ply of the laminate. A potentially more uniform through-thickness distribution of CNTs within the preform could therefore be achieved. The through-thickness conductivity could highly benefit from this approach, as shown in the studies from Ivanov *et al.* [49, 50]. A study from University of Bristol [98] shows conductivity levels in GFRP of up to 1 S/m.

An in-house 3D printing device was used for the injection of the CNT-filled resin within the NCF preforms. The 3D printer was connected to a desktop software to control and monitor the 3D printing head movements in x, y and z direction. A specific code was therefore used for the generation of the magnetic patch after the zero-position calibration step of the 3D printing nozzle. The 3D printing equipment is shown in Fig. 5.1.

A tapered needle was inserted through the ply thickness. Hence, to infuse the bottom ply, the glass fabric was taped onto a silicone support to ease the injection process and avoid damage of the 3D printer metallic board.

Pronterface software was used to control the printer head movements in the three dimensions. The positioning and injection commands can be programmed using g-code. This allows the user to create bespoke print patterns across the samples. In the current experimental programme, a patch was manufactured using a single injection site in the plane of the preform, therefore the code was set to prescribe a series of injection through the laminate thickness. The injections were spaced at 0.25 mm through the preform thickness and a total of 9 injections were applied for 4-ply preform. CNT-resin suspension volumes of 5 ml were used for each single print process and distributed equally through the preform thickness in the z-direction. Each injection was 40 μ l and estimated to create a patch of 60 mm diameter in plane. Injections were carried out on a single location represented by the centre of the glass fabric layup. Syringe nozzle initial position was set in the three dimensions x, y, z prior to injection.

Post-compression was therefore performed with a hot-press apparatus at the University of Bristol. This step was carried out to obtain samples with consistent properties and less variability of intra-yarn volume fraction. The applied pressure was 0.35 MPa.

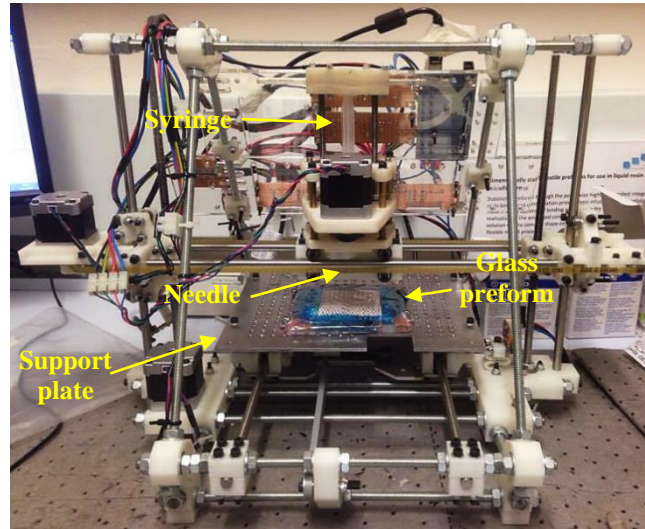


Fig. 5.1. Home-made 3D printing device characterised by 3D moving head and metallic sample support (cable connection to the desktop software).

This step was carried out to force the resin to flow through the fabric yarns along the fibre direction and distribute to generate the desired resin patch size. Sample curing procedure was similar to the process used for pure epoxy. The application of a cure cycle other than the cycle used would hinder the nanotube ability to migrate by following the externally applied magnetic field. Homogeneous pressure was applied to the entire sample surface.

Two sample batches were generated: reference samples and magnetically treated samples. Specifically, samples were then either placed between the poles of the magnetic setup shown previously in Fig. 4.5 and then cured at room temperature, or directly left to cure at room temperature without applied magnetic field. The samples under the magnetic field were subjected to a flux density of 0.5 T. The field was held until gelation occurred, around 3:20 hours at 25°C in the case of slow hardener.

5.3 Resin infusion of the liquid resin printed samples

After the injection and magnetic exposure, the samples were infused with resin PRIME 20LV epoxy resin blended with slow amine hardener. This was carried out to ease the sample

cutting, machining and polishing. Tacky tape was applied along the sides of the aluminium tool plate used for the infusion process to secure the vacuum bag on top of the samples. The samples were placed on the centre of the plate onto the release film, and subsequently surrounded by a frame of tacky tape. This was done purposely to ensure the resin inlet and vacuum outlet pipes onto the plate and avoid resin leakage across the plate.

Peel ply (also called release fabric) was laid onto the sample area. This is a synthetic cloth draped over the samples and, once the epoxy resin is cured, the peel ply can be removed off the sample. The release film is used to separate the resin distribution mesh, which ensures the flow of resin at the surface of fabric, from the material. The resulting surface is rather rough in these infusion processes.

An infusion spring was placed above the top section of the sample and connected with the resin inlet. The purpose was to homogenise the resin distribution across the sample and reduce the resin rich areas and potential voids generated from resin gradients throughout the fabric. An additional layer of infusion mesh was laid onto the peel ply to help the resin distribution across the sample fabric.

Ultimately, the resin inlet and vacuum outlet pumps were positioned on opposite ends of the sample. The inner vacuum bag was then placed on the inner tacky tape frame. The vacuum was then tested to verify the presence of air leakage from the vacuum bag. The breather cloth was then positioned over the inner vacuum area. The aim was the homogenisation of the vacuum level across the tool plate and a higher vacuum level for the outer vacuum bag.

Vacuum valves were positioned on opposite corners of the aluminium tool plate to apply the vacuum to the outer vacuum bag and monitor the vacuum level through a pressure gauge. The vacuum level acceptable to obtain a performing final product was set from -28 to -30 inHg (from -0.95 to -1 bar).

The vacuum level was monitored, and the vacuum bag adjusted along the tacky tape frame to remove potential air leakage from the vacuum bag, which could lead to inefficient vacuum levels and therefore unsatisfactory resin infusion process. The resin infusion was carried out at room temperature and the samples were left to cure at room temperature. [Fig. 5.2](#) shows the resin infusion panel after the infusion process.

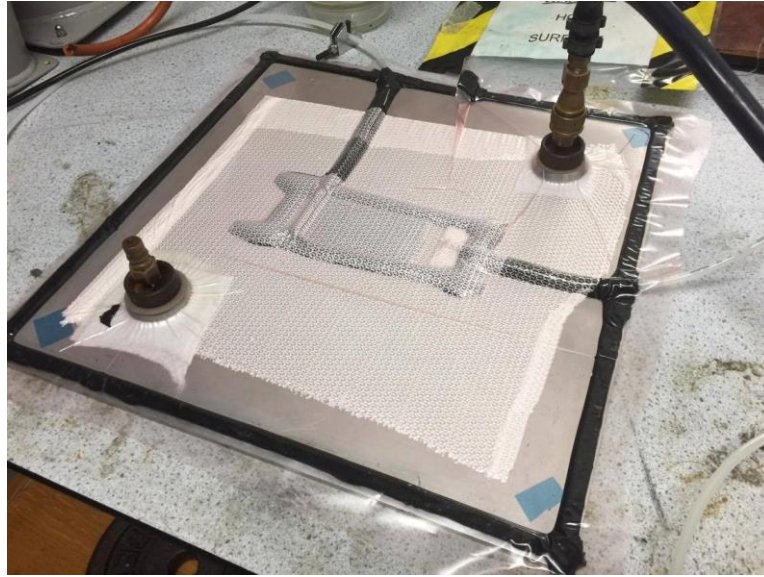


Fig. 5.2. Resin infusion panel after the infusion process.

5.4 Sample preparation for elemental investigation

There are challenges associated with the characterisation of non-uniform CNT distributions within a composite patch. CNT embedded in fabric are difficult to detect due to the interference of the fabric, *e.g.* with computerised tomography scans. Moreover, in a manufacturing procedure as opposed to testing environment, the patch would then be compacted to achieve an appropriate fibre volume fraction. The aim of this study was to manipulate and locally position the CNTs and, subsequently, to fix their position to examine the magnetic migration extent. Electrical conductivity measurements were also conducted to evaluate the conductivity gradients induced by the CNT magnetic migration. These measurements were carried out by applied conductive silver paint on discrete locations on the bottom and top ply of the laminate and evaluate the electrical conductivity by measuring the change in resistance through a multimeter. However, the fabric preform (patch) was not consolidated, therefore no measurements were possible due to the inefficient conductive network created between the perform plies. In addition, the electrical resistance of the resin surface layer represented an additional obstacle to the detection of the through-thickness electrical conductivity, although the electrical conductivity could potentially exist through the laminate thickness. Therefore, the approach presented in this chapter represents a novel alternative to conventional characterisation procedures for CNT distribution within fabric.

After the room temperature resin cure, the samples were removed from the vacuum bag and machined. The samples showed higher thickness across the CNT-filled resin patch compared

to the subsequently infused fabric. This is because the CNT-filled resin was left to gel before resin infusion. Therefore, the effect of the compaction forces during vacuum assisted resin infusion on the sample thickness in the resin patch region was minor. Moreover, fibre volume fraction was higher in the thinner regions away from the printed resin patch as expected, due to the pressure gradients generated by the presence of the patch.

Samples were sectioned by diamond saw near the middle section (see [Fig. 5.3](#)), where the injection point was located. The section was sliced to obtain thin injected and infused samples, with the width of around 2 mm. The width was chosen to fit the sample holder used for the investigation through scanning electron microscopy (SEM). The approach of characterising the nanotube distribution across the fracture surface by means of SEM was not assessed before. This methodology gave useful information in terms of particle distribution and preferential migration due to filtration and magnetic field.

The detection of the presence of cobalt was aimed to show the cobalt-plated CNT magnetic migration. Samples were characterised through SEM at the injection section and at 16 mm from the injection point, as this represents the distance between the centre of the magnetic pole and the pole edge. The edge of the magnetic pole is characterised by the highest magnetic flux density as per FEMM model shown in Chapter 4. Hence, the assessment of the cobalt presence at the patch edge in correspondence with the pole edge is necessary to fully comprehend the nanotube magnetic migration mechanisms.

Sample for the case of applied magnetic field is shown in [Fig. 5.4](#). The samples were coated with silver paint at the fracture surface to maximise the electrical conductivity, therefore the sample sensitivity to the electrons used for the SEM investigation.

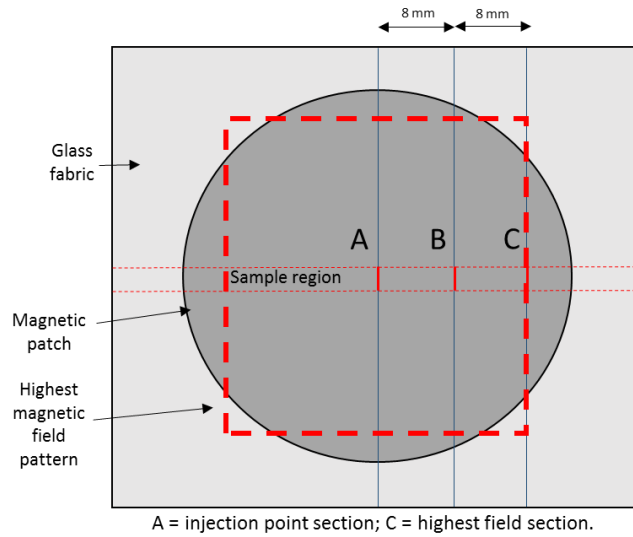


Fig. 5.3. Schematic of the glass NCF sample after CNT-filled resin printing showing the location of the assessed sections for the cobalt distribution (**A = injection site**).

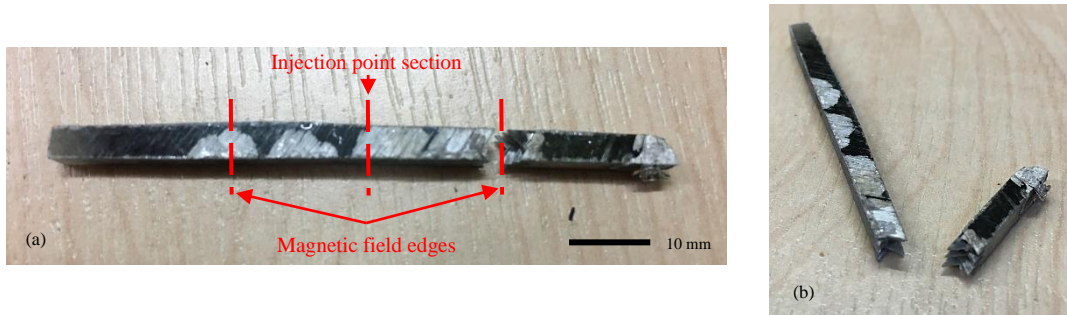


Fig. 5.4. SEM sample for the case of applied magnetic field after sectioning process.

5.5 Scanning Electron Microscope (SEM) elemental analysis

The presence of cobalt could help indicate the location of the nanotubes within the samples and, potentially, the nanotube migration due to the application of an external magnetic field. This approach was used due to the difficulty in extracting information on the nanotube presence and position within a laminate with other methods, such as computer tomography used in Chapter 4, due to fibre interference. Backscattering electron micrographs were obtained from both sample types at the fracture surface. These micrographs are shown in Fig. 5.5(a) and Fig. 5.5(b) for the applied field and reference cases, respectively.

These images clearly show the glass fibre tows and how the fracture surface was highly uneven along the width and thickness. Cobalt particle agglomerates can be observed as white dots and clusters in the figures. The cobalt clusters are present sparingly through the thickness of the samples. This could be linked to the optimised mixing of the epoxy/CNT blend which

caused the CNTs to be distributed homogeneously in the solution and therefore with a limited clustering effect.

Elemental analysis through energy-dispersive x-ray (EDX) analysis was carried out to detect the cobalt presence in the present samples as nanotubes were functionalised with cobalt through electroless plating technique. The elemental analysis was performed in three regions (a, b and c) along the width of the sample across the same fracture surface, therefore at the same distance from the injection location. Fig. 5.6 shows the fracture surface of the samples, chosen to analyse the entire sample width.

The analyses show the presence of cobalt in all the assessed regions, with higher density of the cobalt, associated with higher peak intensity values on the y-axis, in the middle section (region “b”) for the location at 16 mm from the injection point. The cobalt peaks can be identified at 0.8 keV and around 6.9-7.7 keV.

Presence of Fe, Ca, Cl, K and Na can be related to the electroless functionalisation process of the carbon nanotubes. On the other hand, the silver (Ag) peaks are associated to the silver paint applied on top and bottom sample surfaces. However, Fig. 5.5(b) shows silver paint between the plies. The silver paint was applied on the top and bottom plies prior to resin infusion for electrical conductivity investigation, which did not lead to any significant results. Therefore, the silver paint might have filtered through the top ply and reached the underneath plies.

The relevant presence of carbon is related to the presence of carbon nanotubes and epoxy resin within the area of interest, which is an indication of the successful deposition process of the glass fabric laminate as the nanotubes appear to be uniformly distributed in all the plies through thickness. However, the epoxy resin was homogeneously present within the infused laminate, therefore the highlighted bright regions can be associated to the cobalt plated nanotubes.

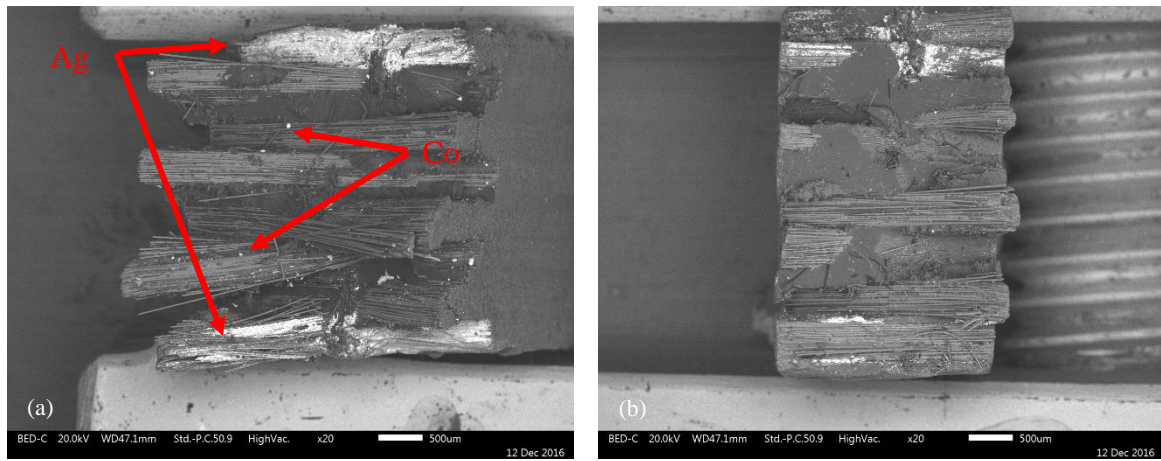


Fig. 5.5. Backscattering electron micrographs (a) for the applied field and (b) cases at the sample fracture surface, with Ag associated with silver paint.

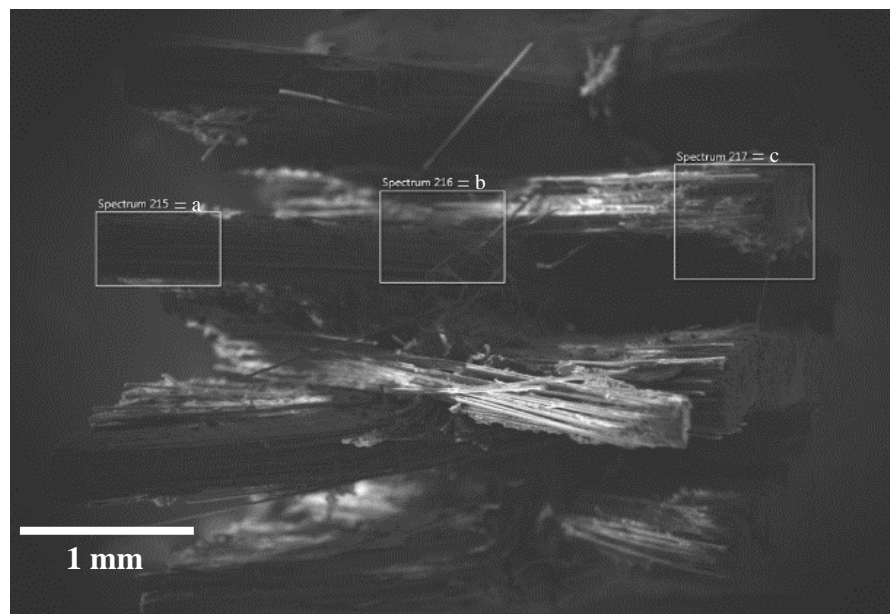


Fig. 5.6. Secondary electron micrograph showing the fracture surface of the sample subjected to magnetic field. Regions ‘a’, ‘b’ and ‘c’ shown in the micrograph are taken along the sample width to analyse the cobalt content distribution along the sample width.

Elemental analyses in the locations “a”, “b” and “c” along the width of the fracture surface of the sample subjected to the magnetic field are shown in Fig. 5.7. The intensity of the single element peak, measured in eV, represents the energy retrieved from the excitation of the specific element, therefore directly proportional to the element presence within the assessed EDX sample. For this reason, comparative analysis between peaks can give an indication of the tendency of a specific element to appear at certain regions of interest.

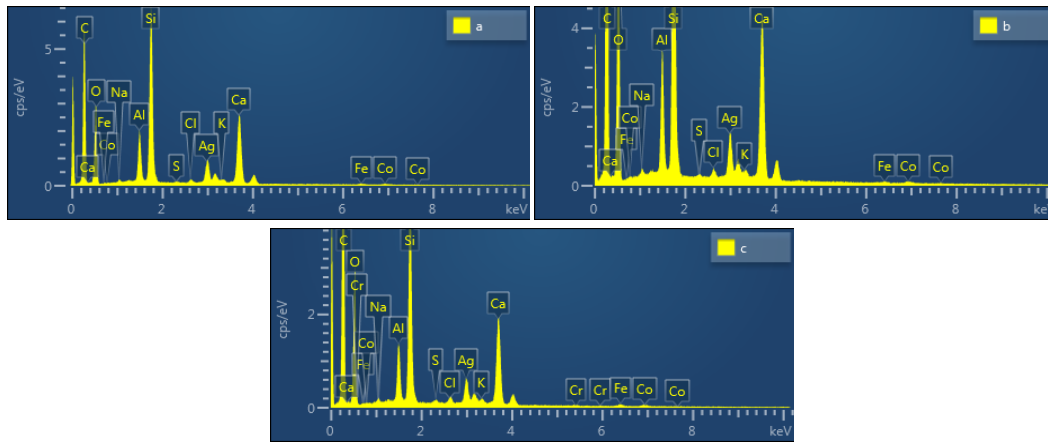


Fig. 5.7. EDX elemental analysis of the fracture surface of the sample subjected to magnetic field, carried out in three specific location over the surface (a, b, c).

Fig. 5.8 shows the distribution of cobalt at the fracture surface of the sample subjected to the magnetic field at the location away from the injection section. Cobalt particles are reported in yellow. The cobalt particle distribution suggests that cobalt migrated from the injection section towards the edge of the sample under the magnetic field effect. The nanotube presence can only be detected in the fibre bundles normal to the plane of the image as the map resolution could not detect the presence of cobalt in the distant fibre bundles.

On the other hand, a cobalt map was not detected for the sample not subjected to magnetic field at the location away from the injection section. This was evidenced by the weak cobalt presence on the sample fracture surface which suggests the absence of the cobalt-plated nanotube magnetic migration.

Cobalt particles are present through the thickness of the sample, particularly in the upper half where the injection site is located. This may be associated to the printing process, which delivered a higher CNT-filled resin content during the final injections in the upper part of the laminate due to the unconstrained upper surface. For this reason, the printer nozzle delivered an excess of resin on the top surface of the samples, which was free to redistribute before cleaning the samples and collect them from the printing area.

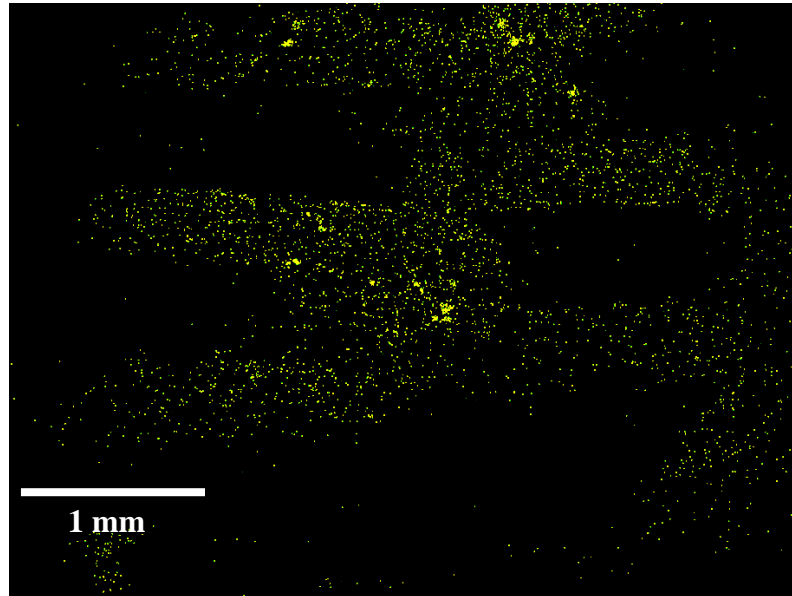


Fig. 5.8. Cobalt distribution map on the fracture surface of the sample subjected to magnetic field.

5.5.1 Reference case

The reference sample was characterised via EDX in three regions (a, b and c) along the width of the fracture surface, accordingly with the sample subjected to magnetic field. Fig. 5.9 shows the location of the three regions of interest for the analysis.

The EDX graphs are shown in Fig. 5.10 and labelled accordingly with the respective region of interest (a, b or c).

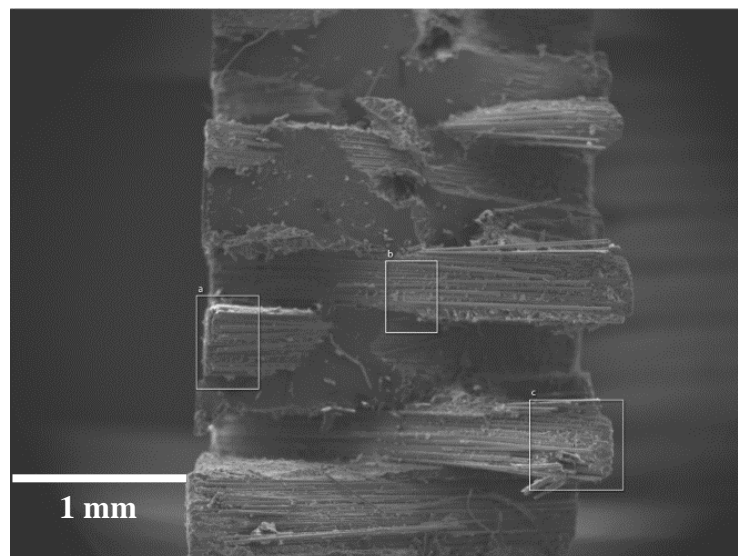


Fig. 5.9. Secondary electron micrograph showing the fracture surface of the sample with absence of applied magnetic field.

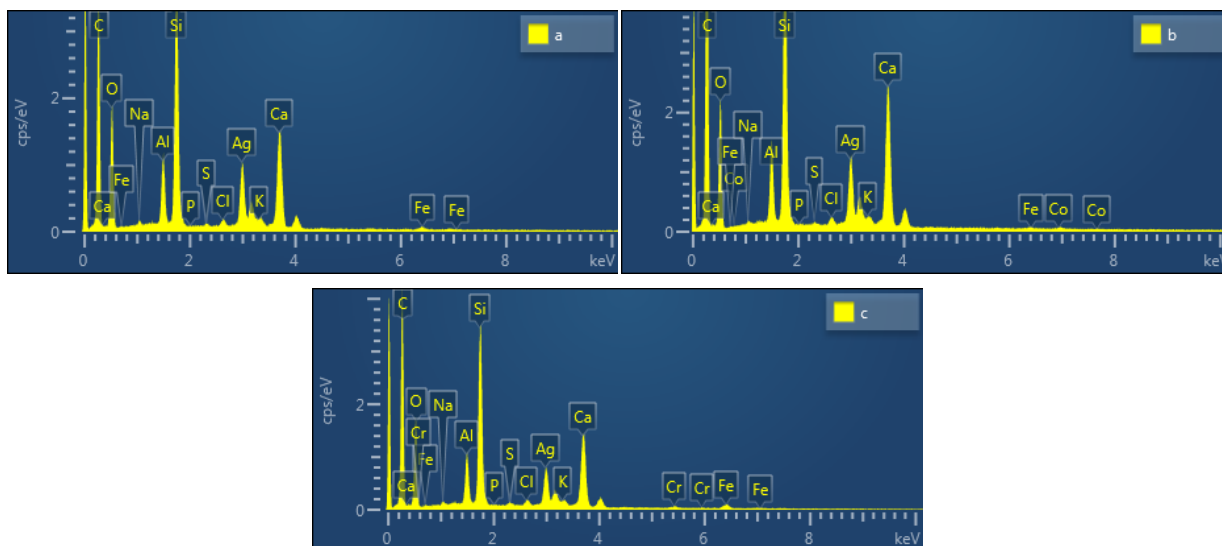


Fig. 5.10. EDX elemental analysis of the fracture surface of the sample with absence of applied magnetic field, carried out in three specific location over the surface (a, b, c).

The presence of cobalt can be detected only in the region labelled as “b”, whereas the other two assessed regions are characterised by almost complete absence of cobalt. This indicates that the cobalt plated nanotube migration towards the region of interest can be potentially associated to inter- and intra-nanotube filtration effects. This reinforces the statement related to the magnetically induced migration of the cobalt-plated nanotubes towards regions of high applied magnetic flux density.

5.5.2 Comparison reference vs. field (low keV)

Spectra were obtained with both low energy (keV) or high energy applied to the samples to record the elemental excitation in eV, directly associable with the element presence. Both low energy and high energy peaks from Fig. 5.7 and Fig. 5.10, for reference and field samples. This was done to assess the cobalt presence within the samples, as cobalt peaks appear at both low and high energy. Fig. 5.11 shows the EDX results from the postprocessing of the cobalt peaks for the low energy part of the elemental analysis spectrum. The cobalt peaks are highlighted by black circles.

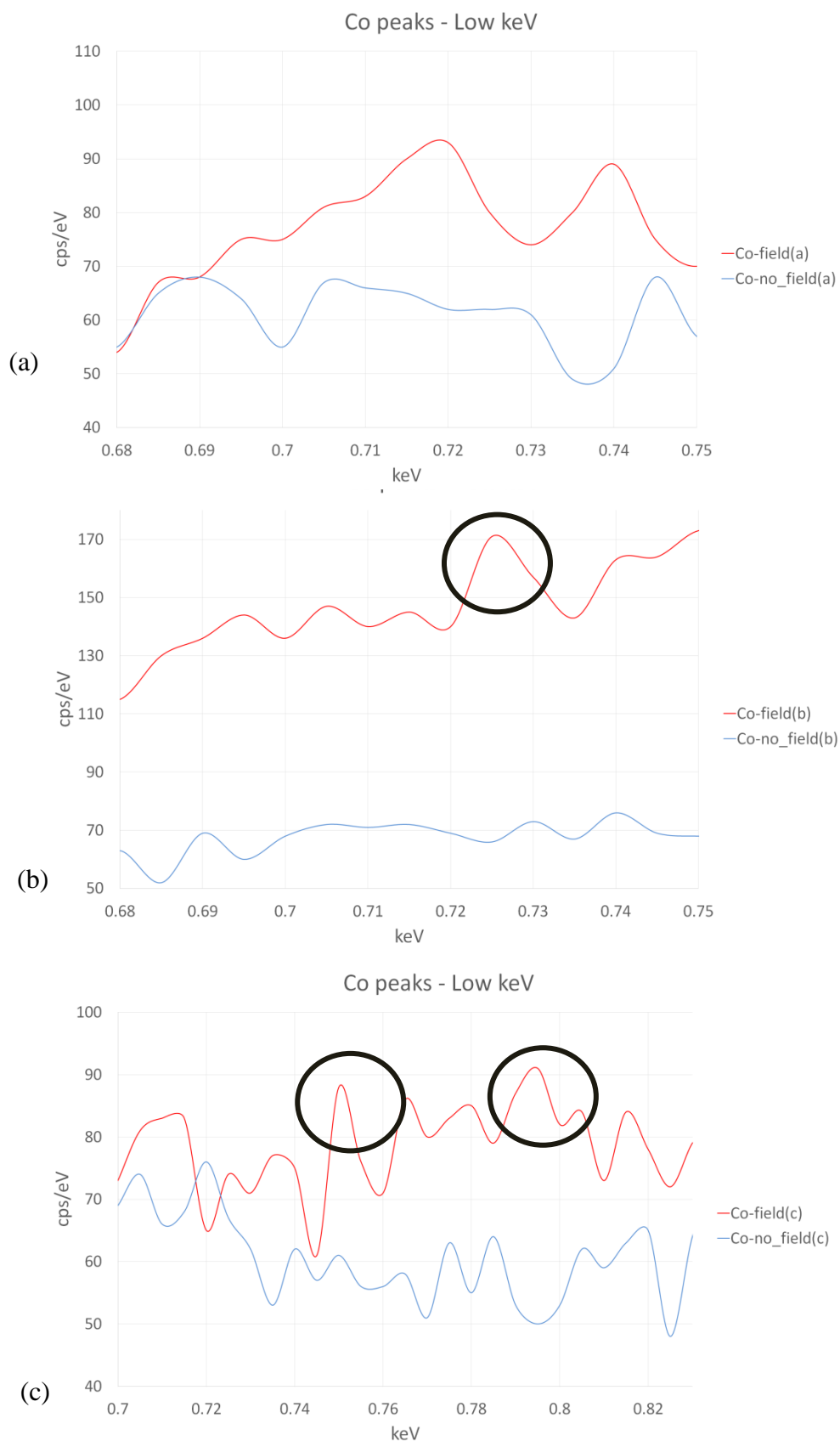


Fig. 5.11. EDX results for low keV: cobalt peaks (circled in black) for the three regions of interest (a, b and c), as a comparison between field (red curve) and no field (blue curve) cases.

The graphs reported above show a clear mismatch between the reference sample and the magnetically treated sample. Specifically, the peak intensity in the field case exceeds the intensity of the no field case. This is particularly valid for the location b along the sample width, with a difference of up to 100 eV between the two curves at 0.725 keV applied to the sample. Moreover, this is particularly evident in the centre of the sample, which is parallel to the injection point. This might be related to the layup and the fabric architecture.

5.5.3 Co presence – Comparison field vs. reference (high keV)

The investigation of the cobalt peaks for the field and no field case was also carried out for the region characterised by high energy (keV). [Fig. 5.12](#) shows the results from this study.

Likewise, the cobalt peaks related to the case of externally applied field reach higher values compared to the case of field absence. However, the signal is slightly more scattered than in the low keV region, and the mismatch between the curves for reference and magnetically treated samples is less obvious.

These results confirm the cobalt tendency to enrich the location at 16 mm away from the injection point in the case of magnetically treated samples. This phenomenon indicates the potential migration of the cobalt-plated nanotubes towards the investigated areas under the effect of the driving force provided by the externally applied magnetic field.

Reference and magnetically treated samples were investigated further. Specifically, samples were cut along their length. Cobalt presence on the fracture surface via EDX analysis was therefore assessed at other locations away from the injection section. The elemental analysis through EDX at the injection section and away from the injection section gave an indication of the cobalt migration towards the edge of the samples due to the applied magnetic field. Cobalt mapping was therefore retrieved to validate the above statement, with successful results. Therefore, a more complete further study to characterise the cobalt distribution and progression from the injection point is required. The fracture surface locations are represented as A, B and C and schematised in [Fig. 5.3](#).

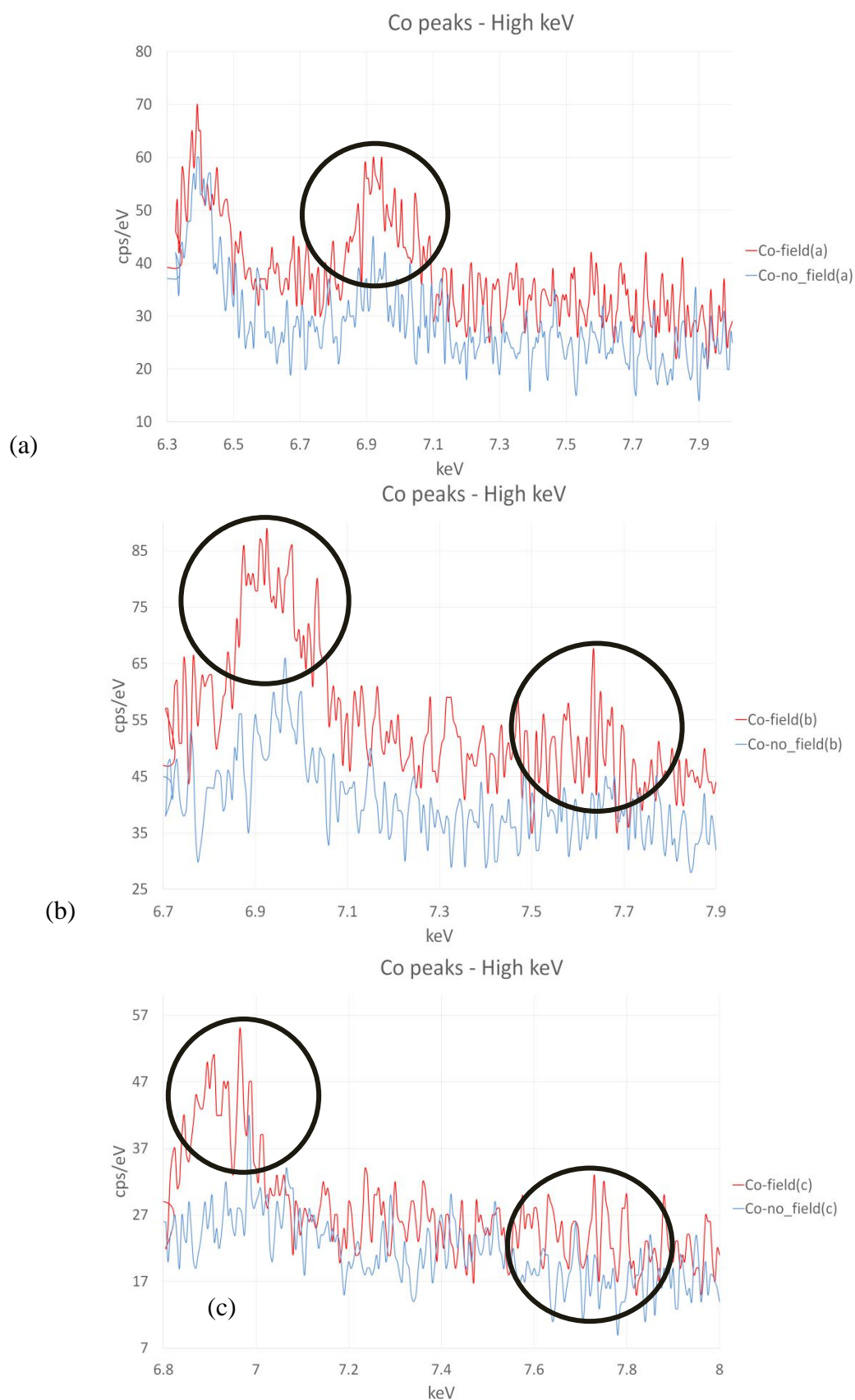


Fig. 5.12. EDX results for high keV: cobalt peaks (circled in black) for the three regions of interest (a, b and c), as a comparison between field (red curve) and no field (blue curve) cases.

The fracture surface micrographs were postprocessed using ImageJ software. Fig. 5.13, Fig. 5.14 and Fig. 5.15 show the fracture surface micrograph (left) and the cobalt mapping (right) at section A (injection section), section B, and section C. The latter location is subjected to the strongest magnetic flux density due to field edge effects, already explored numerically in Chapter 3. The micrographs in Fig. 5.13 (a), Fig. 5.14 (a) and Fig. 5.15 (a) represent the secondary electron images of the sample fracture surfaces, whereas Fig. 5.13 (b), Fig. 5.14 (b) and Fig. 5.15 (b) relate to the cobalt mapping on the sample fracture surface.

The cobalt maps clearly show the cobalt distribution at the fracture surface, which matches the respective micrograph. The relative cobalt spot percentage was retrieved for each map at different sample locations. Cobalt mapping images were post-processed through ImageJ. This was carried out to evaluate the cobalt distribution and magnetically driven migration towards the outer high magnetic flux density pattern related to the externally applied DC field.

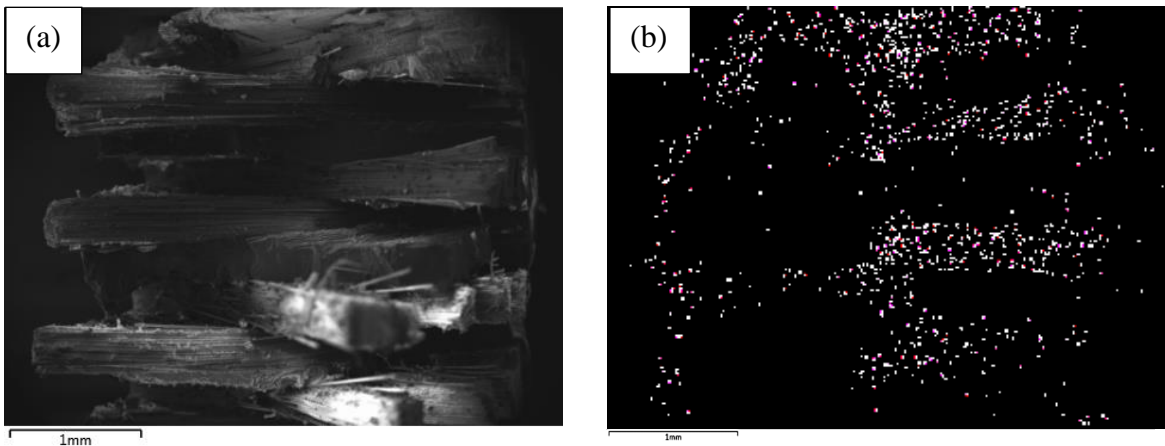


Fig. 5.13. Fracture surface micrograph (left) and the cobalt mapping (right) at the section A (injection point section) for the magnetically treated sample.

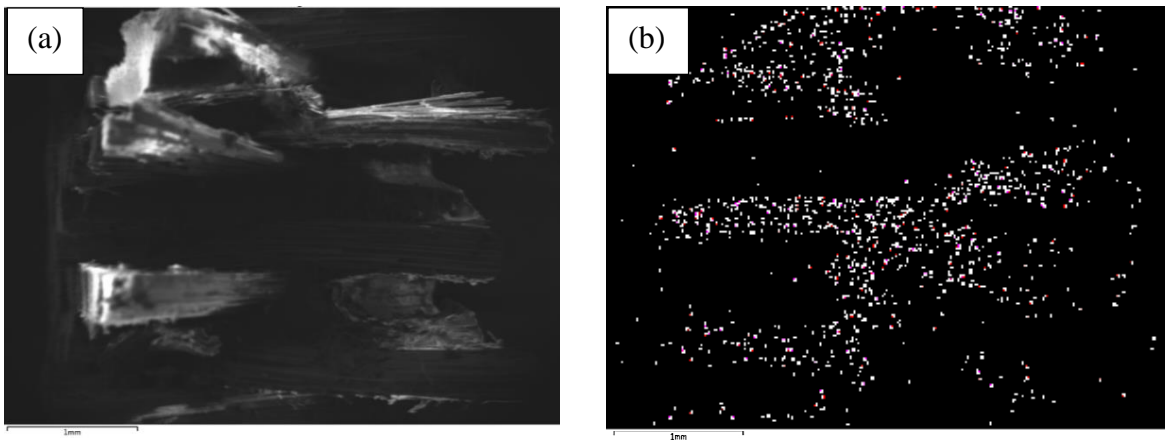


Fig. 5.14. Fracture surface micrograph (left) and the cobalt mapping (right) at the section B.

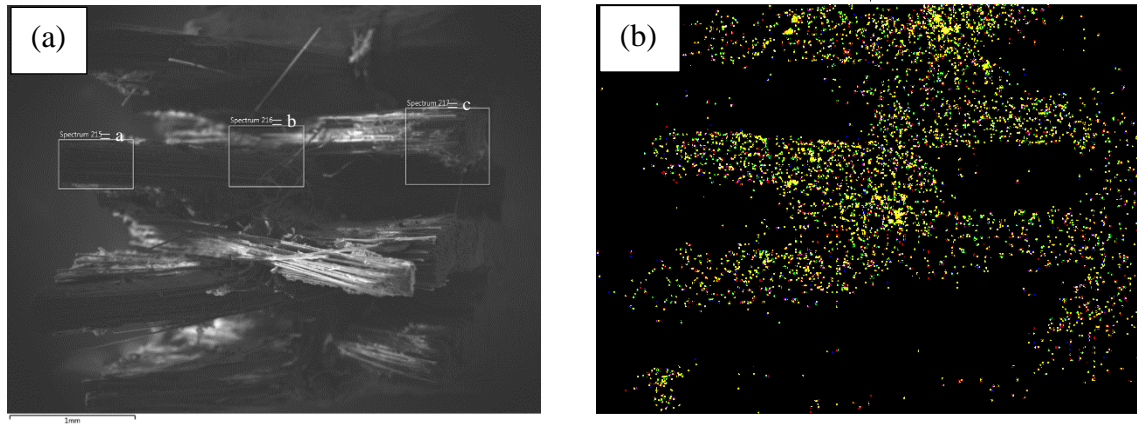


Fig. 5.15. Fracture surface micrograph (left) and the cobalt mapping (right) at the section C (where the field is the strongest due to edge effect).

The cobalt percentage at the injection (section A) calculated through ImageJ post-processing of the cobalt area fraction equals 0.557%. The percentage value was referred to the visual post-processing of the micrograph for comparative purpose, therefore not directly related to weight of volume fraction of CNTs. The magnetic migration causes the cobalt content to increase at the section B up to 1.798%. However, the cobalt percentage decreases at the location C in correspondence with the highest magnetic flux density contour, reaching values of around 1.32%. The cobalt concentration gradient might be affected by two main concurring phenomena: magnetic migration and flow filtration. The former is associated to the magnetic driving force provided by the externally applied magnetic field. On the other hand, the latter can be related to the flow gradient imposed by the mechanical compaction carried out through hot press after the printing process. This might cause nanotube migration as the resin is forced to flow away from the injection point as per filtration effect. The filtration is combined with the magnetic field contribution.

The cobalt presence in the map related to section C appears visually denser than the section B case, although the cobalt percentage measured *via* Image-J post-processing of the micrographs, suggests the reverse consideration. Coarse cobalt plated nanotube agglomerates might be considerably limited in their mobility by their density, therefore not able to migrate farther. However, the finer agglomerates would be able to translate towards the outer locations where the magnetic flux density reaches the highest values. This explains the higher cobalt density in the section C map compared with section A and section B.

On the other hand, [Fig. 5.16](#), [Fig. 5.17](#) and [Fig. 5.18](#) report the fracture surface micrograph (left) and the cobalt mapping (right) at the section A, the section B and section C, respectively.

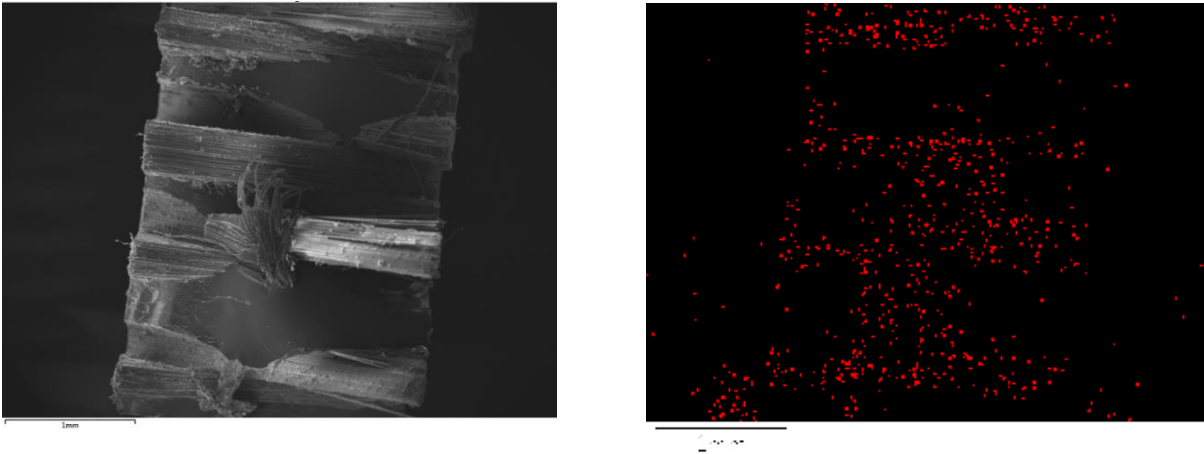


Fig. 5.16. Fracture surface micrograph (left) and the cobalt mapping (right) at the section A (injection point section) for the no field case.

In this case, the cobalt percentage at the injection point reaches values of around 1.53%, with a slight increase up to 2.03% at the section B. However, the cobalt presence drops to values approaching zero at the location C, as shown by the elemental distribution analysis of Fig. 5.18 (right). The filtration effect only cannot allow the nanotubes to migrate farther than region B. The EDX peaks at low energy were considered more reliable in terms of signal stability compared with the high energy scans. Therefore, the low energy cobalt peaks were post-processed to evaluate the area under the peaks. The area under the peaks gave a qualitative and quantitative indication of the cobalt presence at different locations along the sample width.

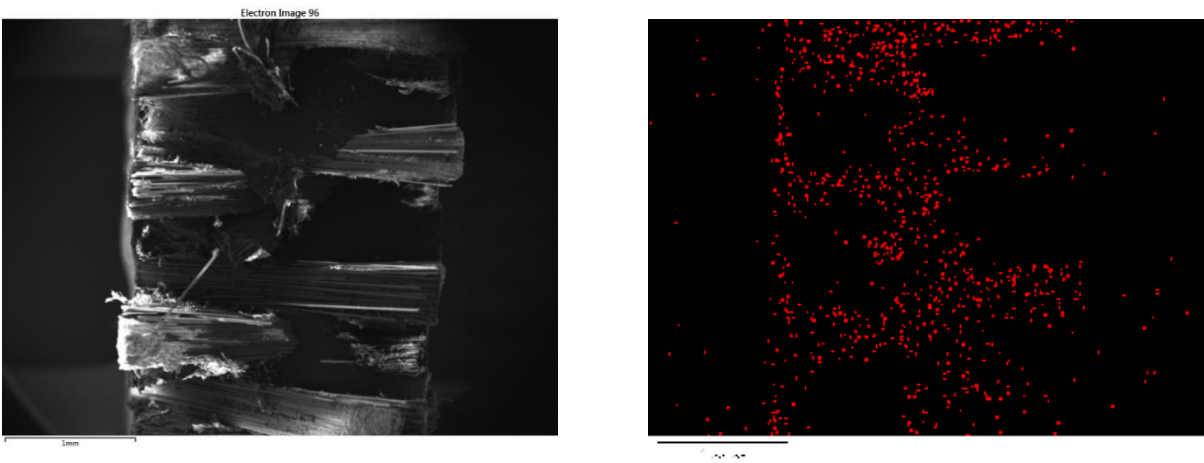


Fig. 5.17. Fracture surface micrograph (left) and the cobalt mapping (right) at the section B for the no field case.

Graphs showing the cobalt mapping post-processing were used for this purpose, as shown below in Fig. 5.19. The left y-axis shows the area under the EDX curves, whereas the right y-

axis shows the value of cobalt area fraction (in %) after post-processing the SEM micrographs.

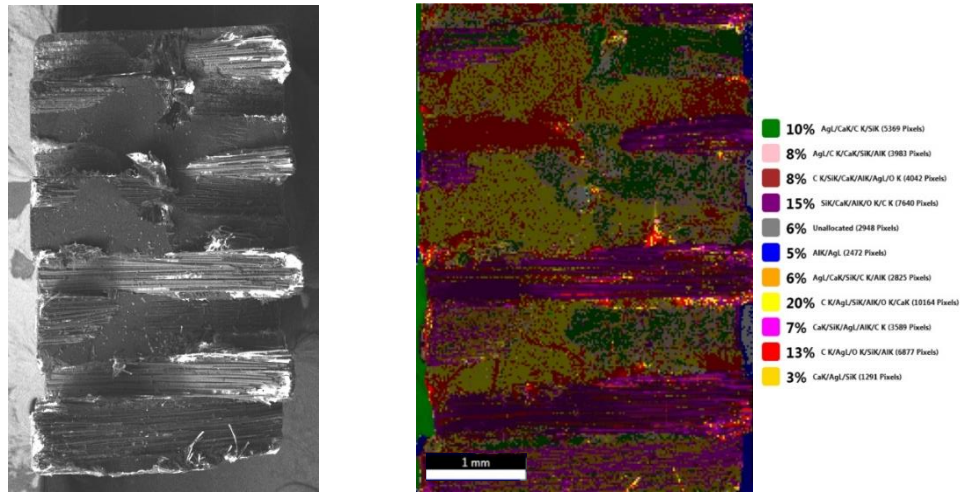


Fig. 5.18. Fracture surface micrograph (left) and the cobalt mapping (right) at the section C (where the field is the strongest due to edge effect) for the no field case.

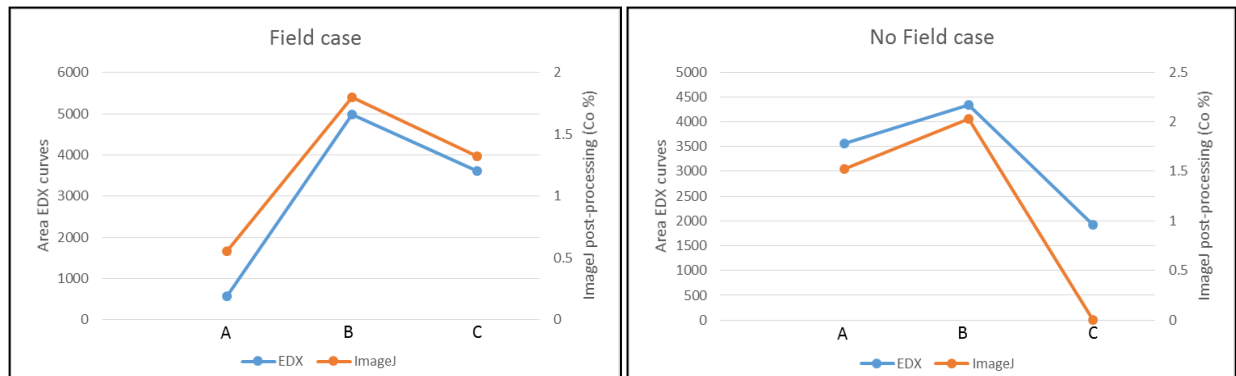


Fig. 5.19. Cobalt distribution results for field and no field case after EDX and ImageJ post-processing.

EDX curve post-processing shows the same trend as the ImageJ results for both field and no field case. In the field case, the cobalt presence increases from the injection point to region B due to both magnetic migration and filtering effect after the sample compaction. A slight decrease in cobalt can be observed towards region C, mainly associated with the magnetic migration of fine cobalt-plated CNT agglomerates. On the other hand, the sample without field exposition shows a high cobalt concentration in the injection region, comparable with the cobalt presence in region B. The no field scenario was taken as a reference initial case with nanotube filtration only, due to the geometry of the weave and the flow effects of the

viscous medium. In this case, the cobalt concentration at the location C was considerably lower than the location A and B. On the other hand, the case of magnetic field applied caused the further migration of the particles due to the magnetic driving force. This led to a higher cobalt concentration at location C in this instance.

The weight fraction of cobalt in the specific locations A, B and C after the magnetic positioning can be calculated from the values of cobalt areal fraction $\%_{Co}(r)$ from Fig. 5.20. From the experimental analyses, a total weight fraction of CNTs w_{CNT} in the suspension equal to 2.5 wt.% can be assumed. Assuming that the nature of the problem is 2D, and so are CNTs, a proportionality between w_{CNT} and the local weight fraction of cobalt w_{Co} can be estimated as shown below, and also between $\%_{Co}(r)$ taken from the images, and w_{CNT}

$$w_{Co}(r) = \lambda \cdot w_{CNT|_{tot}} , \quad (5.1)$$

$$\%_{Co}(r) = \lambda \cdot w_{CNT|_{tot}} , \quad (5.2)$$

where λ is a proportionality factor which needs to be calculated.

In first instance, the assumption of uniform cobalt content across the patch can be considered. In this case:

$$\%_{Co}(r) = \%_{Co|_{tot}} , \quad (5.3)$$

where $\%_{Co|_{tot}}$ is the total weight fraction of cobalt in the solution. Therefore, λ could be calculated from the following equation as per 5.2

$$\%_{Co|_{tot}} = \lambda \cdot w_{CNT} , \quad (5.4)$$

However, a more realistic representation of the phenomenon assumes that the cobalt is not uniformly distributed across the magnetic patch. In this case, the total cobalt weight fraction in the patch could be retrieved from the integral of all the infinitesimal contributions of cobalt content at each radius r from 0 (injection site) to R (outer patch radius, assumed 20 mm as scaled from Fig. 5.3), as follows

$$\int_0^R \%_{Co}(r) \frac{2\pi r}{\pi R^2} dr = \%_{Co}|_{tot} . \quad (5.5)$$

Substituting the equation 5.3 into 5.4 and simplifying π , λ can be calculated as shown below

$$\lambda = \int_0^R \%_{Co}(r) \frac{2rdr}{R^2} \frac{1}{w_{CNT}} = \%_{Co}(r) \frac{2}{R^2} \frac{1}{w_{CNT}} \left[\frac{r^2}{2} \right]_0^R = \frac{\%_{Co}(r)}{w_{CNT}} . \quad (5.6)$$

Substituting λ into 5.1, the local weight fraction of cobalt can therefore be estimated.

Assuming that 50% of the nanotubes are covered in cobalt, then the local weight fraction of CNTs $w_{CNT}|_r$ in location A, B and C can be calculated as follows

$$w_{CNT}|_r = 2 w_{Co}|_r . \quad (5.7)$$

The values of $w_{CNT}|_r$ at location A, B and C for field and reference cases can be observed in Table 5.1.

The values of $w_{CNT}|_r$ can therefore give an estimate of the conductivity gradients present in the patch after magnetic migration, which can also give an approximate estimate of the local electrical conductivity after magnetic migration occurred.

Table 5.1. Parameters used for the analysis of $w_{CNT}|_r$.

	$\%_{Co} _r$ [%]	λ	$w_{Co} _r$ [%]	$w_{CNT} _r$ [%]
A (field)	0.6	0.2	0.6	1.1
B (field)	1.8	0.7	1.8	3.6
C (field)	1.3	0.5	1.3	2.6
A (reference)	1.5	0.6	1.5	3.1
B (reference)	2.0	0.8	2.0	4.1
C (reference)	0	0	0	0

5.6 Additional investigation for magnetic nanotube migration

Fourier Transform Infrared Spectroscopy (FT-IR), Modulated Differential Scanning Calorimetry (mDSC) and Dynamic Mechanical Analysis (DMA) were carried out. The aim was to understand how the optical and thermal properties were influenced by the magnetic migration of the cobalt-plated CNTs.

5.6.1 *Fourier Transform Infrared Spectroscopy (FT-IR)*

Fourier Transform Infrared Spectroscopy (FT-IR) investigation was conducted by assessing the infrared peaks at specific wavelength ranges and the generation of chemical bonds due to a higher cure extent, aided by the present of cobalt-plated nanotubes.

Fig. 5.20 shows the Fourier FT-IR spectra of normalised absorbance as a function of the incident wavelength, related to the three different locations, A, B and C, in the presence of an externally applied magnetic field. As previously mentioned, test samples were cure at room temperature for 24 hours. Therefore, a full cure could not be reached with this cure cycle. The cure cycle at room temperature was selected appropriately to assess the contribution of the magnetic positioning of the nanotubes to achieving the full cure after an incomplete cure process. The spectra related to the location C in the field case showed that the primary amine and carbonyl peaks lessened their intensity compared to the location A and B cases. This is an indication of the further level of cure in the location C. This effect can be attributed to the presence of cobalt-plated nanotubes at the outer sample locations, where the magnetic field reaches the highest values.

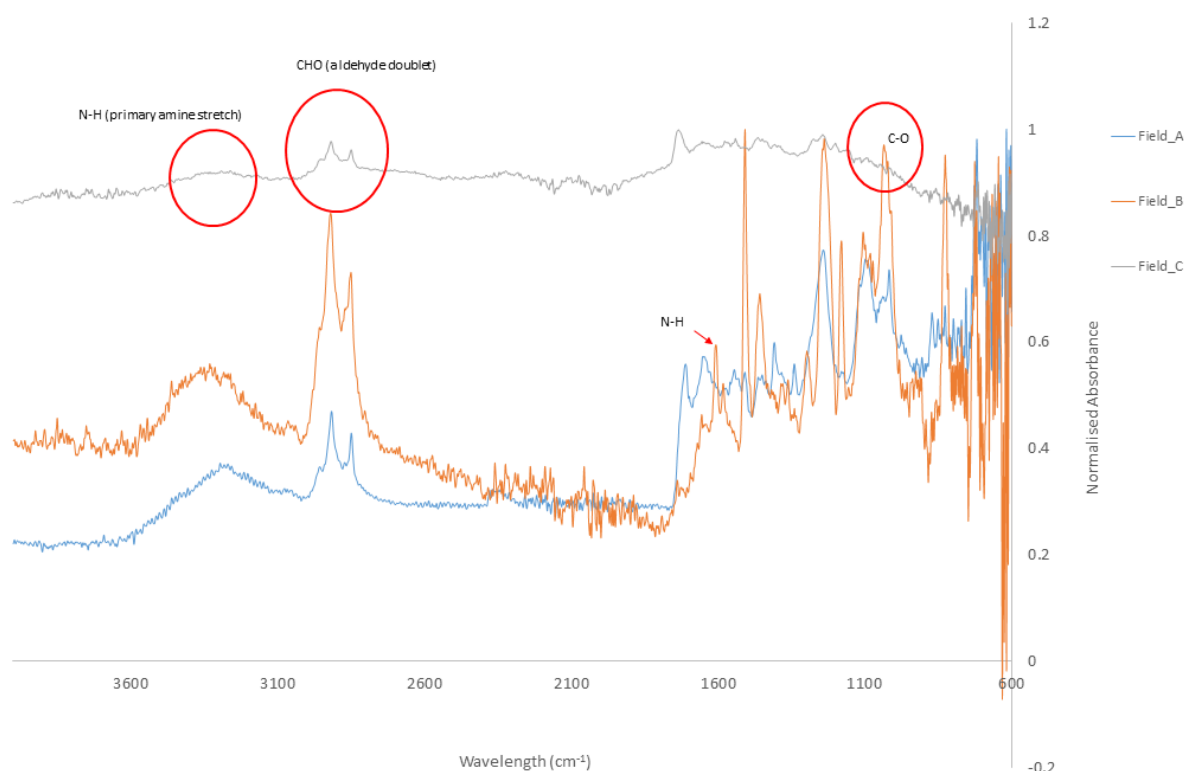


Fig. 5.20. Fourier Transform Infrared Spectroscopy (FT-IR) spectra as a comparison between locations A, B and C in the field case.

5.6.2 Modulated Differential Scanning Calorimetry (mDSC)

Modulated Differential Scanning Calorimetry (mDSC) tests were carried out to estimate the effect of the magnetic migration and localised positioning of cobalt plated nanotubes on the cure cycle of the epoxy resin embedded within a fabric system through liquid resin printing. The changes in heat flow could give a clear indication on the different time required to crosslink the polymeric chains in the presence of functionalised CNTs. The final aim is to assess whether the magnetic positioning of the nanotube can influence the glass transition phenomena, therefore locally modifying the cure process and the exothermic contribution. Tests were carried out as a further validation of FT-IR and EDX visual assessment of the cobalt plated nanotube migration. Test temperature was set to increase from 20°C to 150°C at 2°C/min. After cooling down to room temperature, the same temperature cycle was applied to the same samples to investigate the glass transition changes throughout the sample width. Samples were obtained destructively from the fracture surfaces of the regions A, B and C previously characterised through SEM/EDX.

The total and reversing heat flow could help to assess the influence of the presence of cobalt-plated nanotubes on the thermal behaviour of the system at different sample locations. Fig. 5.21 shows the total heat flow results.

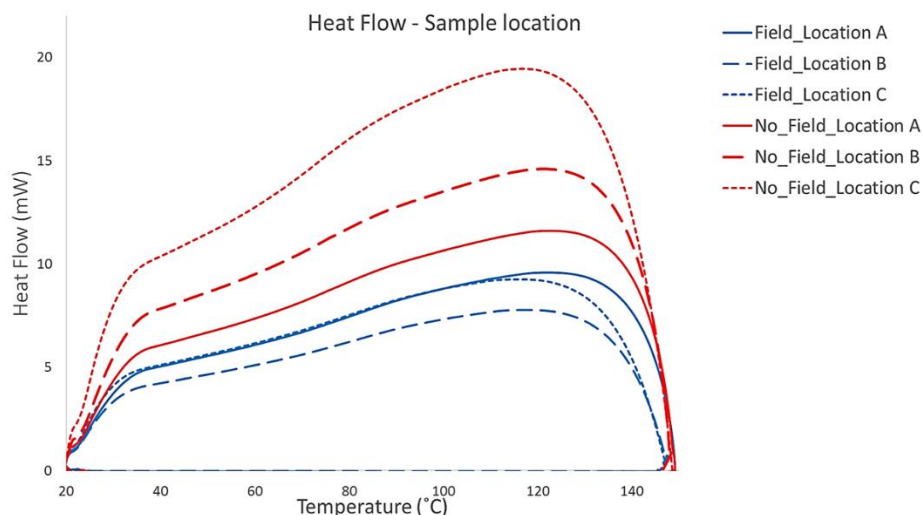


Fig. 5.21. MDSC results: total heat flow (in mW) as a function of the temperature (in °C) at different sample locations for field and no field case.

The curves in Fig. 5.21 show the same exothermic trend for all the sample locations. However, an increasing area underneath the curves can be observed from field to no field case. This directly reflects the higher cure degree in the field case. The mentioned phenomenon can be related to the additional heat supplied by the DC magnetic setup during the field exposition until resin gelation, due to the resistive losses of the magnetic coils. This led to a higher cure extent for the sample exposed to magnetic field.

The field curves match the results obtained through SEM/EDX analysis. Specifically, the region B shows the lowest curve, indication of a higher cure level. The curve for location A shows the highest heat flow values at around 130°C. This relates to a more incomplete cure process compared with location B and C.

However, the sample not exposed to magnetic field shows a highly uncured sample for the region C. This validates the effect of the presence of cobalt-plated nanotubes on the resin cure kinetics. Nanotubes seem to help the cure by accelerating the cross-linking process of the polymer chains.

Fig. 5.22 shows the non-reversing heat flow results which helped to determine the glass transition temperature values in all the cases investigated through mDSC.

Five samples for the field and no field cases were tested to assess the glass transition temperature changes between location A and location C. Results are shown in Fig. 5.23.

The field case results show an overall tendency of the glass transition temperature to increase from location A to location C. Glass transition temperature increases can be observed up to 7 °C. This effect proves that the migration of cobalt-plated nanotubes affects the cure kinetics as the glass transition temperature tends to increase away from the injection point.

On the other hand, the no field case shows a decrease of glass transition temperature from location A to location C. This could be related to the lack of cobalt plated nanotube migration from the injection point as the magnetic field was not applied to the samples. Therefore, the presence of cobalt-plated nanotube at specific locations within the fabric can affect the cure of the epoxy resin and, therefore, the heat distribution within the samples.

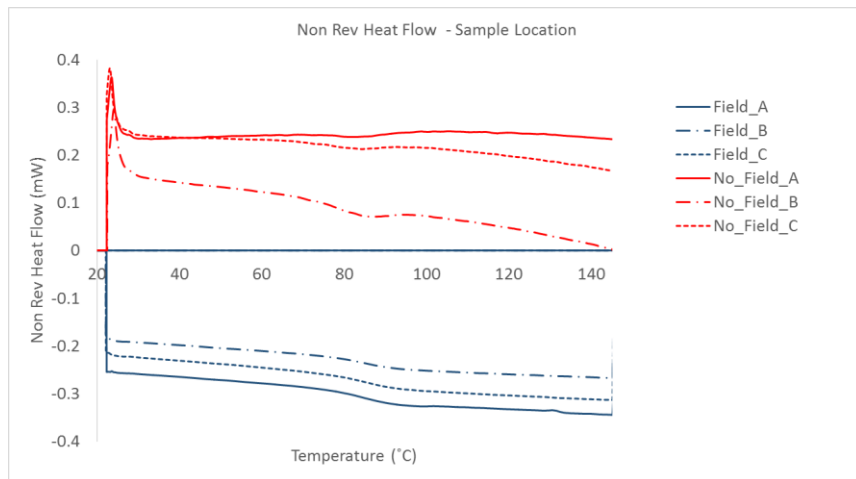


Fig. 5.22. MDSC results: non-reversing heat flow (in mW) as a function of the temperature (in °C) at different sample locations for field and no field case.

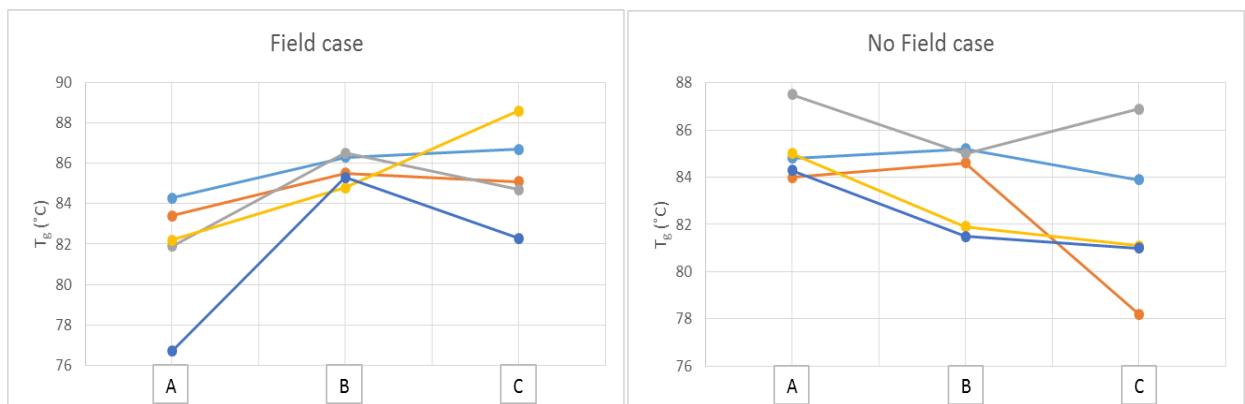


Fig. 5.23. MDSC results: glass transition temperature (in °C) as a function of the sample locations for field and no field case.

5.6.3 Dynamic Mechanical Analysis (DMA)

Dynamic Mechanical Analysis (DMA) tests were carried out to estimate the effect of the magnetic positioning of the cobalt functionalised nanotubes on the glass transition temperature in a repair patch. The present study was conducted to further validate the results obtained with the DSC investigation. The final aim would be the tailoring of the glass transition temperature across the repair patch to locally influence the cure cycle and, therefore, the heating mechanisms. The latter effect would be particularly beneficial for the selective cure at the bondline between the preform patch and the original undamaged component in composite repair. Tests were carried out on samples both after field application and without applied field. Tests were carried out at the National Composites Centre in Bristol, UK. The instrument used for the analysis was a DMA Q800 from TA Instruments. Five samples were tested for each location on the injection area, 8 mm from the injection point and 16 mm from the injection point. DMA results were retrieved from the tan delta peaks during the results post-processing as more reliable than the storage and loss moduli. Results are shown in Fig. 5.24.

In this case, the field case results do not show a clear tendency to magnetic migration towards regions away from the injection point. Moreover, glass transition temperature trends tend to be incongruent from sample to sample. It is fair to conclude that DMA could not provide a further validation for the results obtained through DSC analysis. This could be due to the fact that DMA is not suited to fully capture the phenomena of magnetic migration and nanotube filtration occurring within the sample with and without magnetic processing.

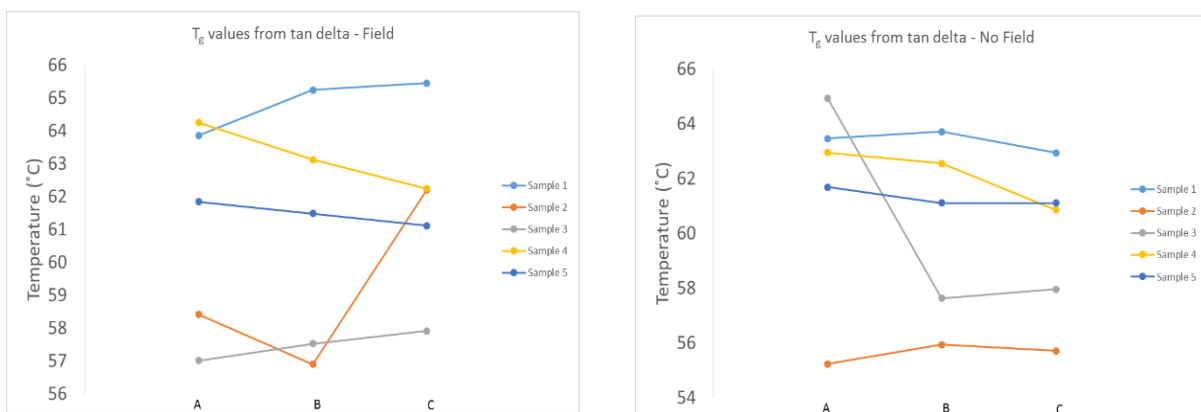


Fig. 5.24. DMA glass transition temperature changes at different locations within the samples for field and no field case.

5.6.4 Field application time dependence

The dependence of the cobalt-plated nanotube magnetic positioning and manipulation on the field application time was also analysed. The aim of the present investigation was to understand the extent of the magnetic manipulation of the nanotubes within a known viscous system before gelation and cure. The study could therefore provide with a procedure by which the working time of the metal functionalised CNT-filled resin could be assessed, and the repair times could be optimised in respect to the overall repair process timescales.

Three square samples were manufactured by creating cobalt-plated CNT-filled resin patches through the thickness of a 4-ply NCF glass fabric laminate. The injection volume was 130 μl , with nine injections performed throughout the sample thickness. The sample edge was 80 mm long. Three different magnetic time exposure conditions were applied to each of the samples. One of the samples was not subjected to external magnetic field, whereas the other two samples were exposed to magnetic field (0.5 T) for 15 minutes and 30 minutes, respectively. The samples were subjected to mechanical compaction through hydraulic press shown in [Fig. 5.25](#). The compaction load applied to the samples was 1 kN, which equals to 0.16 MPa as per sample area. The samples were introduced in a dry ice box in order to freeze the patch conditions and potential magnetically driven alignment after field exposition. The first sample obtained through liquid resin printing was not subjected to field application. It was introduced in a dry ice box in order to freeze the position of the nanotubes after injection. The second sample to be printed was placed between the magnetic poles of the electromagnet shown in [Fig. 4.5](#) and subjected to magnetic field for 15 minutes. Subsequently, the sample was introduced within the same dry ice box mentioned previously to freeze the magnetic CNT alignment obtained after 15 minutes. The same procedure was carried out for the sample subjected to magnetic field for 30 minutes.



Fig. 5.25. Hydraulic hot press used for magnetic patch consolidation after application of temperature and pressure cycles.

Samples were then subjected to a temperature and pressure cycle through hydraulic press. Samples were heated up to 45°C and maintained under pressure (0.16 MPa) for 7 hours in order to ensure the resin gelation.

Samples were then machined at the injection point A, location B and location C, as previously carried out. This was performed in order to obtain samples for elemental investigation through Energy Dispersive X-Ray (EDX) analysis.

5.6.4.1 15 minutes field case

Cobalt migration from the injection location A to location B could be detected after applying the magnetic field for 15 minutes. The bright dots outside the sample contour refer to the sample holder made of a cobalt alloy. The main result from this investigation is that the cobalt-plated CNT distribution changes over time. After 15 minutes, the concentration of cobalt observed at the location B was equal to 1.6% (areal concentration in the micrographs after post-processing with ImageJ software) and lower than the cobalt concentration at the locations A and C, equal to 4.3% and 3.2%, respectively. Fine CNT agglomerates might have travelled towards the location C through filtration and influence of the externally applied magnetic field. The results of cobalt concentration after 15 minutes of field exposition also

indicate that the cobalt migration required a longer time to occur for the coarse agglomerates. The cobalt distribution at locations A, B, and C after 15 minutes of magnetic field exposition can be observed in Fig. 5.26, 5.27 and 5.28, respectively.

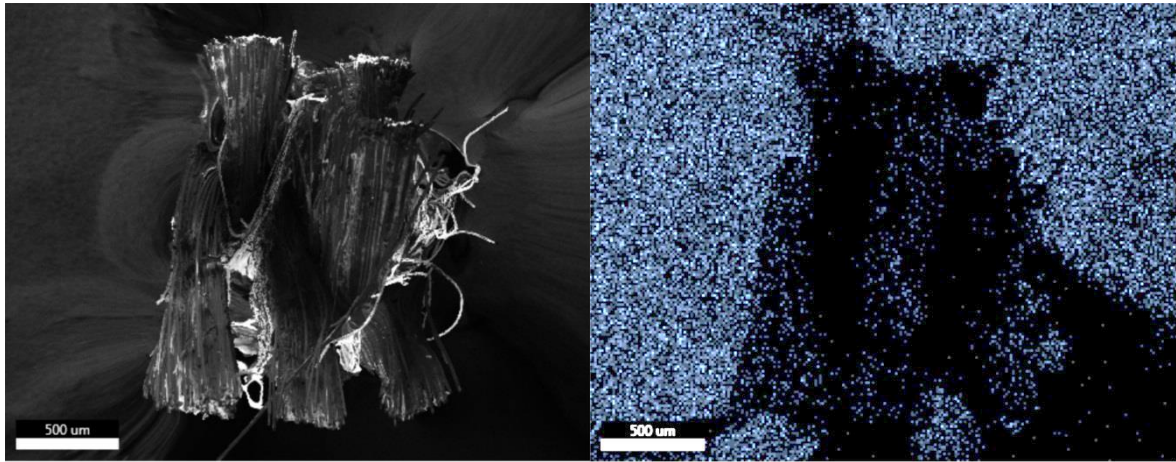


Fig. 5.26. Cobalt distribution at location A after 15 minutes of magnetic field exposition.

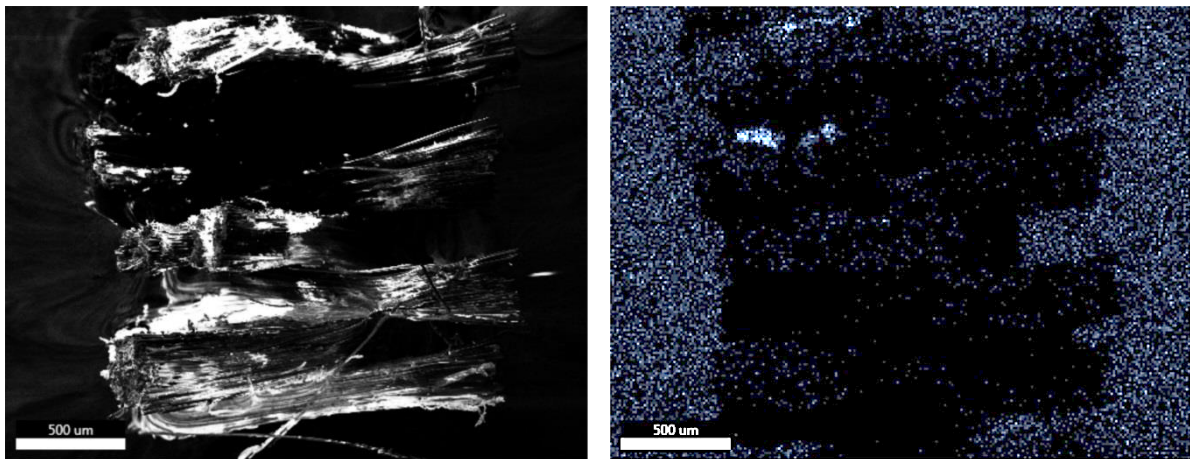


Fig. 5.27. Cobalt distribution at location B after 15 minutes of magnetic field exposition.

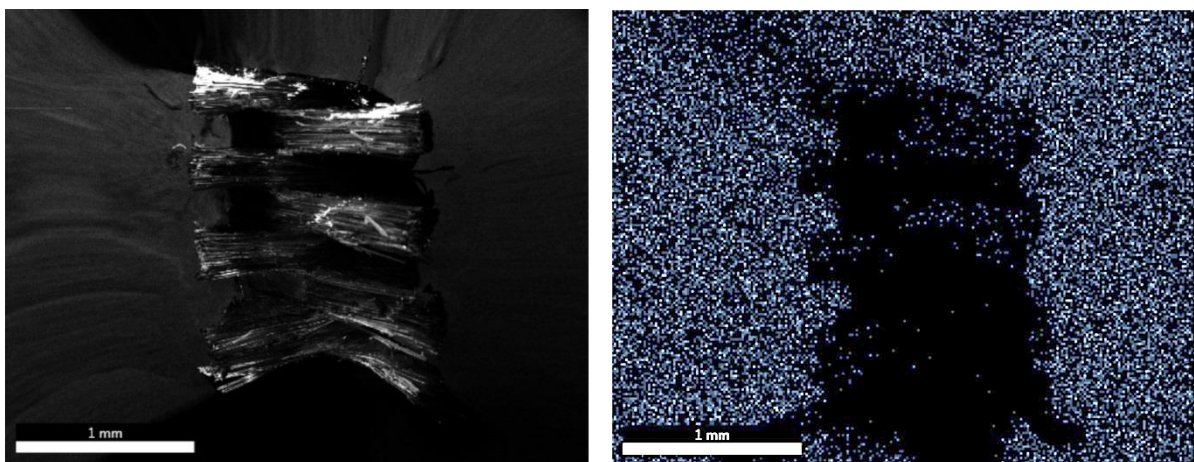


Fig. 5.28. Cobalt distribution at location C after 15 minutes of magnetic field exposition.

5.6.4.2 30 minutes field case

Magnetic field application for 30 minutes led to an enrichment in cobalt concentration of coarse agglomerates at the location B and C compared to the case of 15 minute field application. In this case, the cobalt concentration appeared to be increasing from location A to B, from 3.1% to 3.2% and, ultimately, slightly decrease at location C, with cobalt concentration of 2.9%. This pointed out the magnetically driven cobalt migration after 30 minutes, which could not be fully attained for the coarse agglomerates after 15 minutes of field application. The cobalt distribution at locations A, B and C after 30 minutes of magnetic field exposition is shown in Fig. 5.29, 5.30 and 5.31, respectively.

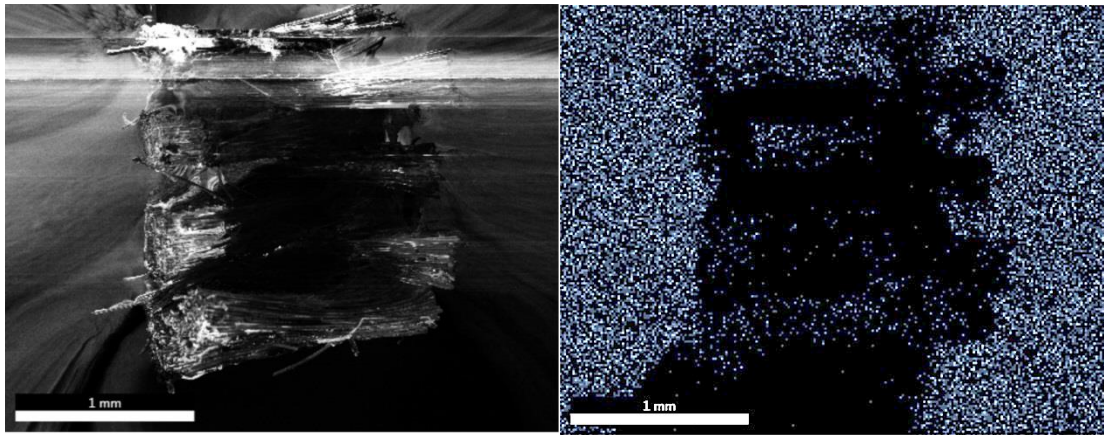


Fig. 5.29. Cobalt distribution at location A after 30 minutes of magnetic field exposition.

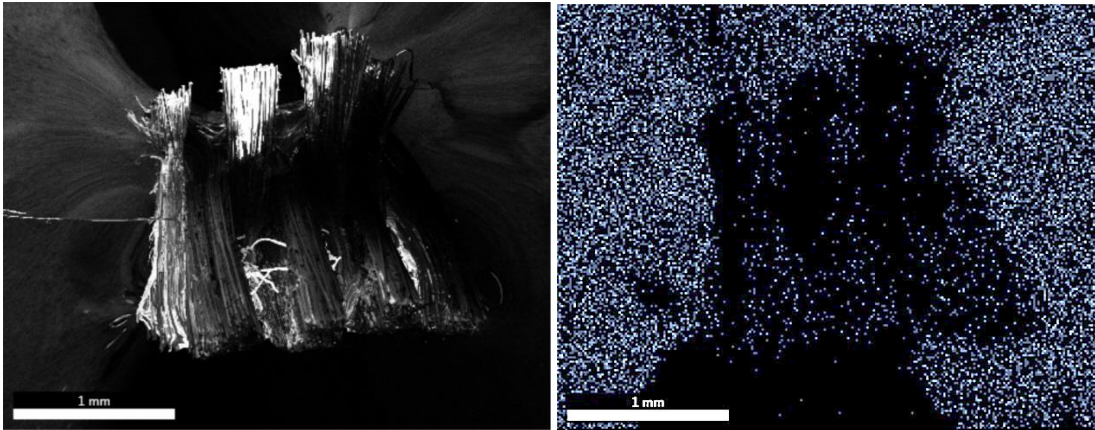


Fig. 5.30. Cobalt distribution at location B after 30 minutes of magnetic field exposition.

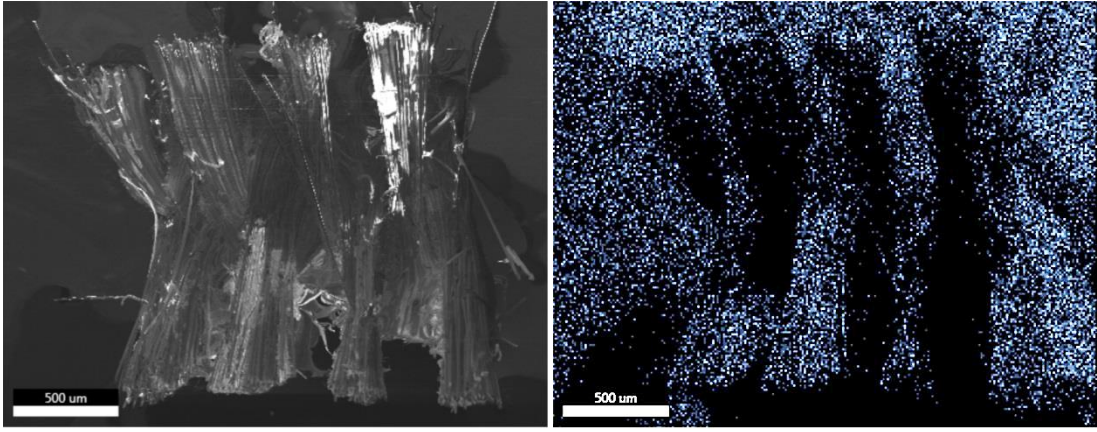


Fig. 5.31. Cobalt distribution at location C after 30 minutes of magnetic field exposition.

5.6.4.3 No field case

The case of no field application showed a weaker cobalt concentration at the location C, equal to 1.19%, if compared to the cases of 15 minutes and 30 minutes of field application (equal to 3.2% and 2.9%, respectively). These results indicate a lower extent of cobalt migration from the injection section A to the location C after micrograph post-processing with software ImageJ. Moreover, the cobalt concentration appeared higher in the injection location A, around 4.5%, if compared with location B, equal to 2.4%, with a decreasing distribution towards the location C. This suggests that the weak cobalt migration towards the location C was mainly attributed to the filtration and viscous mechanisms. The cobalt distribution at locations A, B and C in the case of absence of magnetic field exposition is shown in Fig. 5.32, 5.33 and 5.34, respectively.

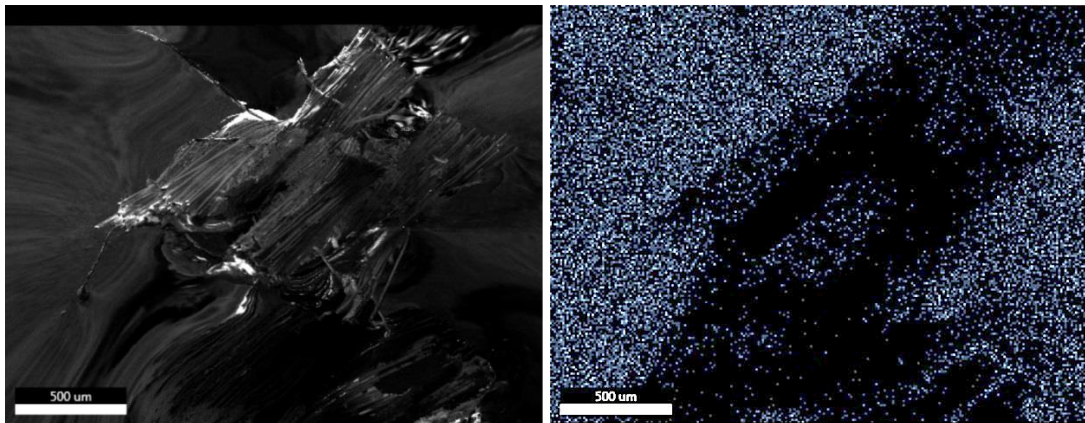


Fig. 5.32. Cobalt distribution at location A after no magnetic field exposition.

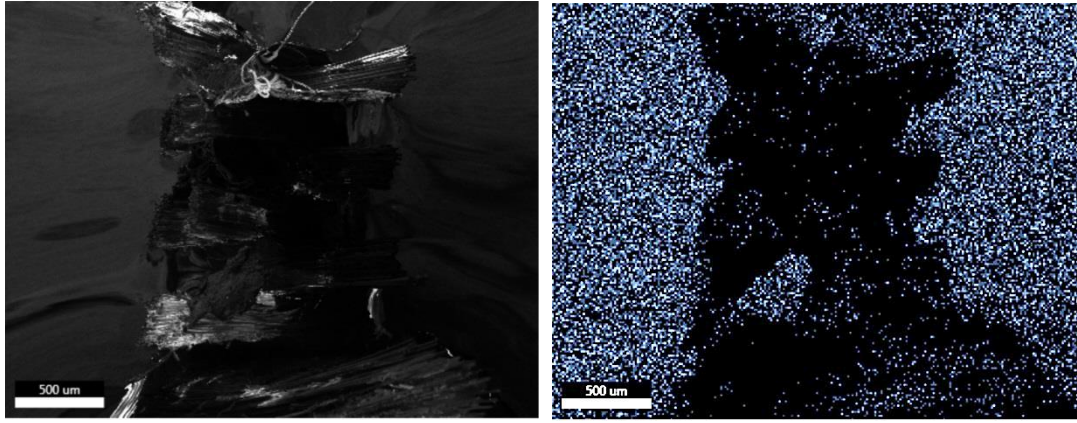


Fig. 5.33. Cobalt distribution at location B after no magnetic field exposition.

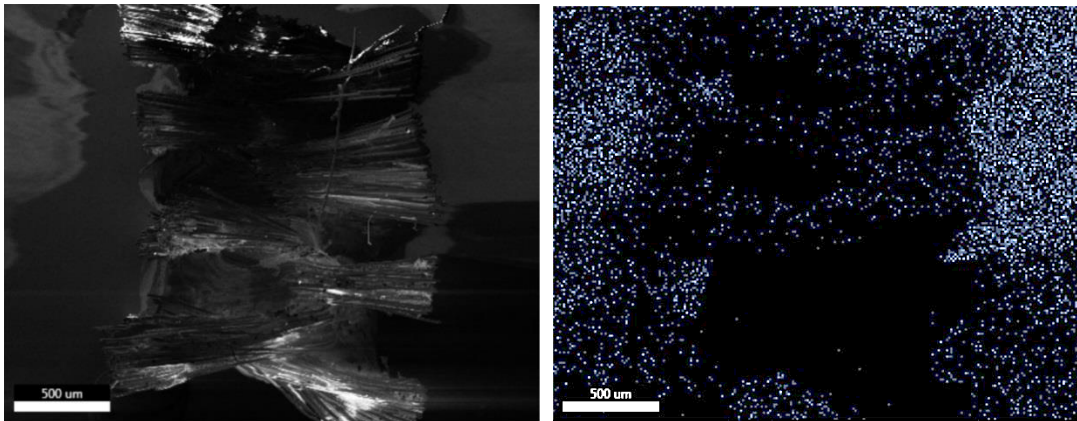


Fig. 5.34. Cobalt distribution at location C after no magnetic field exposition.

5.6.5 Scanning Electron Microscopy (SEM) micrograph post-processing for magnetic field exposition time dependence

Samples were obtained destructively from the fracture surfaces of the regions A, B and C previously characterised through SEM/EDX, as mentioned in the previous paragraph.

SEM images were postprocessed with the software ImageJ to analyse the cobalt percentage present on each surface under investigation. The results are reported in Fig. 5.35, which shows the cobalt percentage evolution from location A to location C as a function of the field application time.

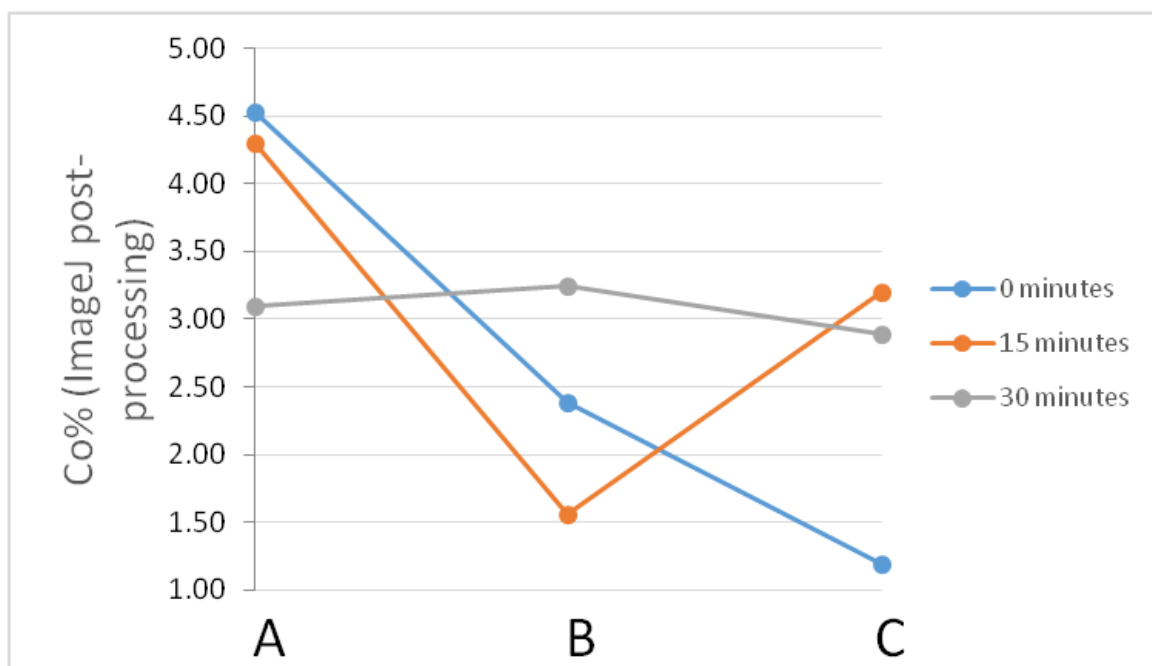


Fig. 5.35. Cobalt distribution from A to C at different magnetic field application times.

The blue curve related to the no field case (0 minutes of field application time) shows a decreasing cobalt content from location A to location C. This indicates that the cobalt-functionalised nanotubes could not migrate towards location C in absence of applied magnetic field. On the other hand, the orange curve related to 15 minutes of field application shows a significant decrease of cobalt content from location A to location B, whereas an increasing cobalt fraction is observed towards location C. This refers to the magnetically driven migration of cobalt-plated nanotubes towards the region of highest magnetic flux density.

The grey curve representing the condition of field application time of 30 minutes shows a slight enhancement in cobalt content from A to B, followed by a decreasing cobalt percentage towards location C. However, the cobalt concentration does not vary excessively throughout the sample width. This indicates an increasing difficulty in magnetically positioning the nanotubes due to higher levels of viscosity as temperature and time progress.

5.7 Conclusions

The feasibility of the manipulation and positioning of nanotubes within fabric was investigated. The combination of liquid resin printing and magnetic positioning of nanotubes within fabric was not explored in the previous literature works. Moreover, the novelty of the presented approach lies in the characterisation of the magnetically treated samples through

SEM as means to detect the discrete nanotube distribution at various locations away from the injection site. Liquid resin printing was used to introduce the cobalt-plated nanotubes within the fabric system. Magnetic field exposition was proven to affect the nanotube distribution at locations away from the injection point. Specifically, nanotubes showed a higher content with concentration increments of over 1% from the injection point to the edge of the magnetic patch. The cobalt-plated nanotubes were therefore driven towards the edges of the sample by magnetic field applied externally. Higher CNT fractions are needed to achieve higher CNT concentration, and magnetic positioning gives an additional instrument to obtain this result. The electrical conductivity could benefit in terms of homogeneity from the nanotube magnetic positioning. The higher cobalt presence observed with the SEM study was also verified by FT-IR spectroscopy. In this case, spectra related to the location C in the field case showed a further level of cure in the location C. This effect can be attributed to the presence of cobalt-plated nanotubes at the outer sample locations, where the magnetic field reaches the highest values. Moreover, cure kinetics mechanisms were influenced by the presence of the cobalt-plated nanotubes, as the glass transition temperature showed increasing values at increasing CNT contents. An extended time exposition to the magnetic field also affected the glass transition temperature. Specifically, a glass transition temperature increase could be observed at locations away from the injection point, which can be related to the higher content of nanotubes. Magnetic migration and filtration were the responsible mechanisms for this effect. The outcome of this investigation is that magnetic manipulation does work in the fabric preforms. Therefore, the positioning of nanotubes within fabric could help tailor the mechanical properties and thermal properties of the composite preform.

The approach used in the present chapter could help suggest what CNT fraction could be achieved according to various measurements. Electrical conductivity measurements could have also been used to identify the gradients in nanotube distribution across the magnetic patch. However, the preliminary results did not show any readings, and this led to exploring the alternative route of SEM/EDX investigation.

Effective nanotube network generation at the bondline could result from the localised nanotube positioning. Ultimately, induction heating mechanisms could benefit from the magnetic positioning of the nanotubes, as detailed in Chapter 6. The effect of nanotube distribution and conductivity gradients on the induction heat dissipation will be extensively discussed.

6. Inductive heating modelling

6.1 Introduction

The previous chapters examined possibility of material modification to make it susceptible to both responsive to heating by means of magnetic hysteresis and heating by means of Joule losses associated with eddy currents. Both mechanisms require a significant fraction of additives to maximise the heat sources in one case and electrical conductivity in another case. Local deposition of additives and magnetic positioning of the functionalised CNTs were considered as the most promising ways of maximising CNT content. The experiments shown in the previous chapter allow suggesting that maximum CNT fraction achievable using local deposition and magnetic alignment methods can be in the range of 3.5-4 wt.% in the areas of interest. This content of CNT is estimated to provide through-thickness electrical conductivity of an order of 1 S/m for glass preforms [98]. The purpose of this chapter is to assess the required induction parameters to provide sufficiently rapid rates of heating.

The assessment is performed through numerical modelling. The main question posed by this study is whether the level of conductivity created by CNT alone is sufficient to make the inductive heating efficient and comparable to other forms of heating externally applied.

In addition, the modelling shows how a tailored CNT distribution can be used to improve further uniformity of heating associated with finite shape of the coil, reduction of magnetic field through thickness, and skin effect.

The chapter is structured as a collection of several case studies. The first part focuses on assessing the induction heating parameters required to obtain sufficient heat dissipation from a magnetic patch within a composite laminate for resin cure. The second part explores the effect of grading the electrical conductivity within the magnetic patch, both in- and out-of-plane, on the heat dissipation levels and distribution.

6.2 Induction heating model

The numerical model, which simulates an induction heating of a patch in a composite laminate, implements classical Maxwell equations describing current induced in susceptors in response to time variation of electric field in the inductor [103, 104]. The four constitutive equations brought together by Maxwell to model electromagnetic wave propagation can be written as follows:

- Magnetic flux equation (the magnetic flux \mathbf{B} through any closed surface is equal to zero):

$$\nabla \cdot \mathbf{B} = 0 . \quad (6.1)$$

- Maxwell-Gauss equation (the electric flux density \mathbf{D} gradient through any closed surface is equal to zero):

$$\nabla \cdot \mathbf{D} = 0 . \quad (6.2)$$

- Maxwell-Faraday equation (the line integral of the electric field \mathbf{E} around any closed loop is equal to minus the time rate of change of the magnetic flux \mathbf{B} through the loop):

$$\nabla \times \mathbf{E} = -\frac{\partial \mathbf{B}}{\partial t} . \quad (6.3)$$

- Maxwell-Ampere equation (the line integral of the magnetic field \mathbf{H} around any closed loop is equal to the electric current density associated with free charges \mathbf{j} plus the time change rate of the electric flux density \mathbf{D}):

$$\nabla \times \mathbf{H} = \mathbf{j} + \frac{\partial \mathbf{D}}{\partial t} . \quad (6.4)$$

Ultimately, the system of equation presented above require constitutive relations to consider material properties such as electrical conductivity σ , dielectric constant ε and magnetic permeability μ . Magnetic flux density \mathbf{B} and magnetic field \mathbf{H} are connected through $\mathbf{B} = \mu \cdot \mathbf{H}$, whereas Ohm's law connects current density \mathbf{J} and electric field \mathbf{E} as per $\mathbf{J} = \sigma^E \cdot \mathbf{E}$.

The equations 6.1-6.4 could be brought and solved together. It is convenient to introduce a magnetic vector potential, \mathbf{A} and write resolving equations in terms of this variable. The magnetic potential is defined in terms of the magnetic flux density: $\mathbf{B} = \nabla \times \mathbf{A}$.

The present study considers a time-harmonic electromagnetic oscillation of current, which can be described as $\mathbf{A}_0 \exp^{i\omega t}$, where \mathbf{A}_0 represents the amplitude of the magnetic vector

potential, ω is the current frequency. The magnetic field is caused by excitation of volume current density defined as $\mathbf{J}_0 \exp^{i\omega t}$, where \mathbf{J}_0 is the amplitude of the volume current density vector. Therefore, Maxwell's equations 6.1-6.4, in absence of conductor motion, can be defined in terms of magnetic potential as follows:

$$\nabla \times (\boldsymbol{\mu}^{-1} \cdot \nabla \times \mathbf{A}_0) + i\omega \boldsymbol{\sigma}^E \cdot \mathbf{A}_0 = \mathbf{J}_0 , \quad (6.5)$$

where $\boldsymbol{\mu}$ is the magnetic permeability tensor and $\boldsymbol{\sigma}^E$ is the electrical conductivity tensor. The model is complemented with boundary conditions defining magnetic potential on the periphery of the considered domain. The domain includes laminate, inductive coil, surrounding magnetically permeable media. The domain is chosen sufficiently large to consider zero potential on all surrounding surfaces.

The model can assess the intensity of eddy currents in the functionalised laminate and calculate the correspondent Joule loss under assumption that all electrical energy generated within conductive composite was converted to heat. Abaqus 6.14 was used to model the induction heating from a laminate subjected to an externally applied magnetic field by running electric current through a coil. The magnetic field is modelled by setting harmonic AC current with frequencies ranging from 10 kHz to 1 MHz. The range of these frequencies is characteristic for induction set-ups reported in literature. MHz frequencies are mostly used for inductive heating through hysteresis losses but they make the skin effect more pronounced and requires significantly higher power input for induction heating set-up. However, examples of application of MHz range in the context of eddy current heating also exist. For instance, MHz frequency was used by Menana *et al.* [84] for the case of a carbon fibre reinforced polymer multi-ply quasi-isotropic laminate. Likewise, the MHz range was used in the studies of Fink *et al.* [15].

kHz frequency was implemented by Kim *et al.* [18] for experimental trials on induction heating in double-lap shear samples. The induction heating unit could deliver a peak-to-peak current of 0–70 A with frequencies in the range of 135–400 kHz.

Rudolf *et al.* [80] explored induction heating of continuous carbon-fibre reinforced thermoplastics. Experiments were carried out between 650 and 1000 kHz.

The motivation for using higher or lower frequencies is driven by several factors. First, skin depth (length at which magnetic field can propagate) is inversely proportional to the

frequency and inversely proportional to conductivity. Hence, low conductive materials heated at lower frequency have a better possibility for being heated uniformly. In addition, low conductivity set-up is more energy efficient and simply more accessible. On the other hand, the efficiency of heat supply when the frequency and amplitude of the applied field increase, which, as will be shown below, is critical for the low conductivity materials. This relation, on the other hand, is not straightforward when magnetic coil is explicitly considered. Secondary eddy currents in the coil itself lead to lower amplitude of current and hence lower amplitude of the magnetic field. This may lead to lower heat dissipation at higher frequencies. Due to inductive nature of the copper coil and its reactance under AC circuit, the current I (in Ampere, A) can be calculated as shown below:

$$I = \frac{V}{X_L} , \quad (6.6)$$

where V is the voltage (in volts, V) and X_L is the inductive reactance (in ohms, Ω). The inductive reactance X_L is dependent on the AC frequency f (in Hertz, Hz) as follows:

$$X_L = 2 \cdot \pi \cdot f \cdot L , \quad (6.7)$$

where L is the inductance in Henries (H).

The inductive losses within the copper coil tend to decrease the current running through the coil itself, hence decreasing the overall magnetic flux density and causing a reduction in induced heating generating in the affected laminate.

Overall, due to these factors and the nature of solution itself, the relations between the frequency, current density and heat supply is highly non-linear. Therefore, the model considers a relatively wide range of parameters to identify what is suitable for the considered material. The model of laminate is set to consider a variation of electrical conductivity both in plane and through thickness of the laminate. As discussed in the previous chapters, the variation of the conductivity can be achieved through a variety of methods and the model is set to explore benefits of having non-uniform distribution of conductive elements. The next section will detail the model implementation in terms of model geometry, properties, mesh, loads and boundary conditions prior to considering. It is followed then by two sets of case

studies: one to assess induction parameters and another one to characterise the effect of grading on heat distribution within the repair patch.

6.3 Model implementation

6.3.1 Model geometry and conditions

To explore benefits of material grading, the laminate is separated onto distinct zones both in-plane and out-of-plane of the laminate. The size of each zone is selected with respect to the resolution of printing and magnetic motion that can be achieved relatively easy. These zones are characterised by constant conductivity within the zone and varying conductivity from area to area. The distribution of conductivity through thickness of the laminate is approximated by four blocks of plies with 5 mm thickness each. The laminate is sufficiently thick to ensure that the magnetic field is reduced to zero within the laminate for a field generated by one-sided coil on the surface. This ensures that the depth of heating (dependent on frequency and conductivity of the material) is addressed along with the other parameters. The in-plane segmentation of zones was realised as three concentric regions in-plane of the laminate as shown in Fig. 6.1(a). This is a minimum number of partitions to describe a variation in the conductivity observed experimentally. The circular shape of the regions with constant conductivity was chosen as it is the simplest form of presenting the magnetic alignment in repair patches. The conductive patch was located away from the edges and the zones in the conductive patch are labelled as Zone 1, Zone 2 and Zone 3 and correspond to the inner region of the magnetic patch characterised by a radius of 15 mm, middle and outer magnetic patch region were 30 mm and 40 mm, respectively. Zone 0 stands for the non-conductive area beyond the perimeter of the patch. A template model was created to carry out various simulations with both constant and varying properties in-plane and through the thickness of the laminate to explore the grading conductivities within the part.

A one-sided copper coil with magnetic core was modelled as cylindrical volume with an external diameter of 100 mm, an internal diameter of 50 mm to cover the entire magnetic patch area, and a depth (h) of 50 mm to reproduce realistic dimensions of the coil. These dimensions were selected to match experimental samples treated in Chapter 4. The coil was placed over the magnetic patch of the laminate top ply and surrounded by an air domain. The coil was placed at a distance equal to the thickness of a ply block as the direct contact between the coil and the plies could, in a real-life application, cause fibre distortion and interference with the resin flow within the top ply block. The coil shape was chosen to

resemble the experimental setup shown in Fig. 4.5. Fig. 6.1(b) shows the magnetic coil, whereas Fig. 6.1(c) shows the composite laminate sample and the air domain.

A uniform mesh was used in the model for all parts. The coil was separated from the sample by means of a 5-mm layer of air to avoid direct interaction of electrical current of the coil and eddy current.

Two main cases were studied: LNR (laminate with non-conductive reinforcement) and LCR (laminate with conductive reinforcement), both with the presence of a magnetic patch to compare the heat dissipation in both cases. In-plane electrical conductivity distribution was distributed in two cases, with decreasing conductivity towards the outer edge of the patch, and by having uniform electrical conductivity across the magnetic patch. Both cases were studied for LNR and LCR by applying an AC field with two frequency cases, 10 kHz and 1 MHz [84]. Following a previous work from the University of Bristol [105], the current density in the coil was applied along the ϕ coordinate of a cylindrical coordinate system (r, ϕ, z), as shown in Fig. 6.2. The application of the current density along the ϕ coordinate allowed the model to assign a magnetic flux density through the thickness of the laminate in the z -direction, according to Fleming's right-hand rule. The main plane of the sample was observed on the x - y plane of the model.

6.3.2 Properties

The range of electrical properties of the materials used in the model was based on the values found in literature and the content of nano-tubes obtained in the experimental studies reported in Chapter 5. The characteristic values for conductivity associated with printing of nano-tubes suspension to non-conductive glass fibre preform can be found in the work from Ivanov *et al.* [49] and Radharkrishan [98] – it is in the range of 10^{-2} -10 S/m. Characteristic values of well-dispersed CNT suspension as function of the weight fraction can be found in [49]: for 4 wt. % of CNTs in pure resin, an electrical conductivity of 0.0027-0.0001 S/m could be estimated. Characteristic values of in-plane conductivity of carbon fabric are in the order of magnitude of 3000-14000 S/m for in-plane [106] and 0.7-10 S/m for out-of plane conductivity [106]. The fibre volume fraction and the manufacturing process affect the conductivity levels. Indeed, autoclave processing allows for a more controlled pressure cycle, therefore higher laminate compaction leading to higher volume fractions (around 60 vol.%) [106]. The resulting improved connection between the plies causes an increase in electrical conductivity [106].

Although a clear distinction between in-plane and out-of-plane conductivities was discussed, one of the limitations of the current analysis in Abaqus is that only isotropic conductivities can be assigned to the material. Hence, the values taken for the analysis are taken to represent generic non-conductive (LNR) and conductive (LCR) fabrics. The materials properties are shown in [Table 6.1](#).

The section geometrical properties are shown below in [Table 6.2](#).

6.3.3 *Boundary conditions*

Boundary conditions were selected to study the effect of an enclosed through-thickness magnetic flux density on the heat dissipation within the laminate due to the electrical property gradients. A magnetic vector potential equal to zero was set to the external boundaries of the model, as shown in blue in [Fig. 6.2](#). This step was carried out to enclose the magnetic flux density within the model domain.

6.3.4 *Mesh*

A tetragonal mesh type (*tet*) was used for the analysis. EMC3D4 elements consisting of 4-node linear tetrahedron, were selected for the model. The approximate element size was 5 mm for all the parts. Curvature of the elements was controlled by setting a maximum deviation factor of 0.1 for the element distortion.

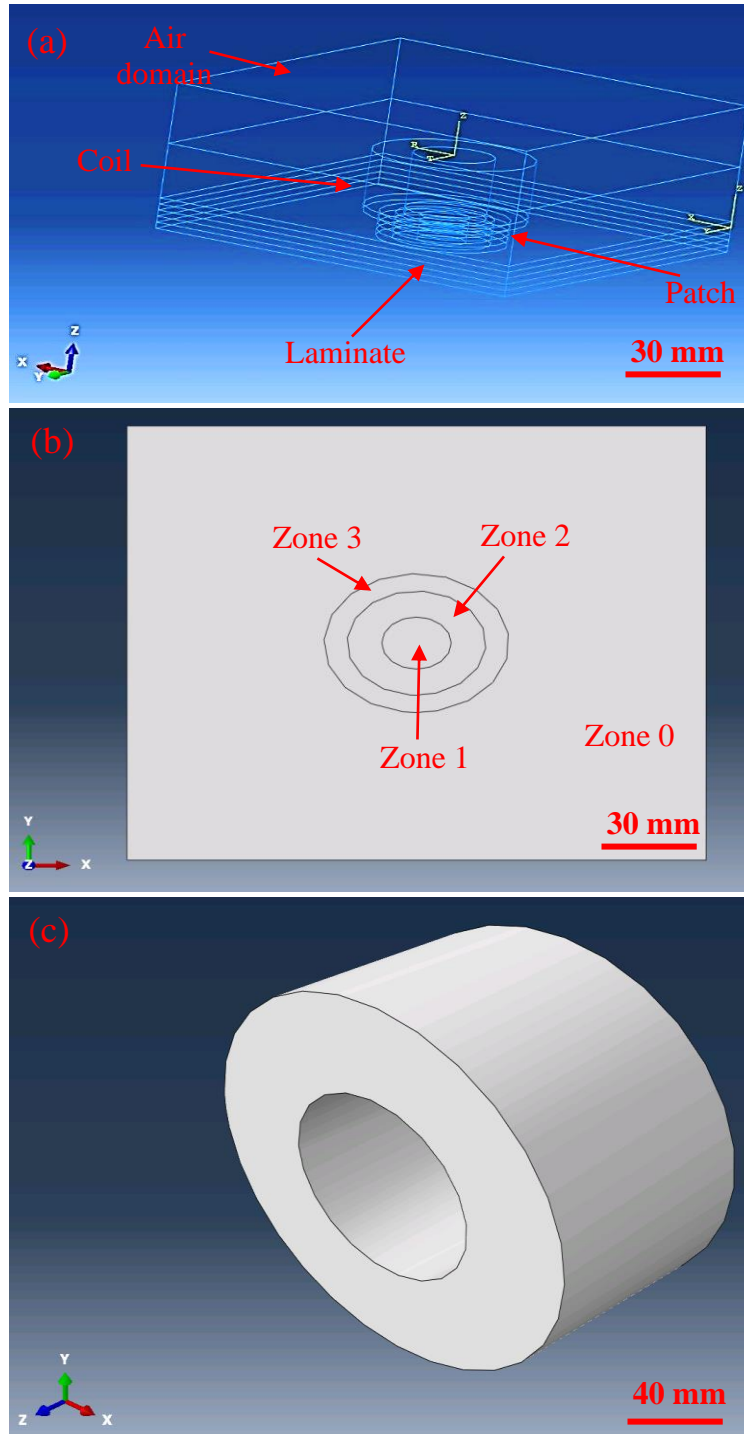


Fig. 6.1. (a) Abaqus representation of the composite laminate subjected to AC magnetic field during the electromagnetic simulation; (b) Abaqus model representation of magnetic patch partition; (c) Abaqus representation of the magnetic coil. Dimensions can be found in [Table 6.2](#).

Table 6.1. Materials properties for the model with externally applied AC magnetic field.

Materials	Electrical Conductivity [S/m]
Air	$3e^{-13}$
Coil (Copper)	$5.96e^7$
Zone 0 (LNR)	negligible
Zone 0 (LCR)	100*

* Same order of magnitude as T300B Carbon from [49].

Table 6.2. Geometrical properties of the model sections.

Section	Radius [mm]	Length [mm]	Width [mm]	Thickness [mm]
Air	-	250	250	100
Coil (Copper)	50/25 (outer/inner)	-	-	50
Zone 0 (LNR) – laminate	-	250	250	20
Zone 0 (LCR) - laminate	-	250	250	20
Zone 1 – Ply 1	15	-	-	5
Zone 1 -Ply 2	15	-	-	5
Zone 1 – Ply 3	15	-	-	5
Zone 1 – Ply 4	15	-	-	5
Zone 2 – Ply 1	30	-	-	5
Zone 2—Ply 2	30	-	-	5
Zone 2 – Ply 3	30	-	-	5
Zone 2 – Ply 4	30	-	-	5
Zone 3 – Ply 1	40	-	-	5
Zone 3 – Ply 2	40	-	-	5
Zone 3 – Ply 3	40	-	-	5
Zone 3 – Ply 4	40	-	-	5

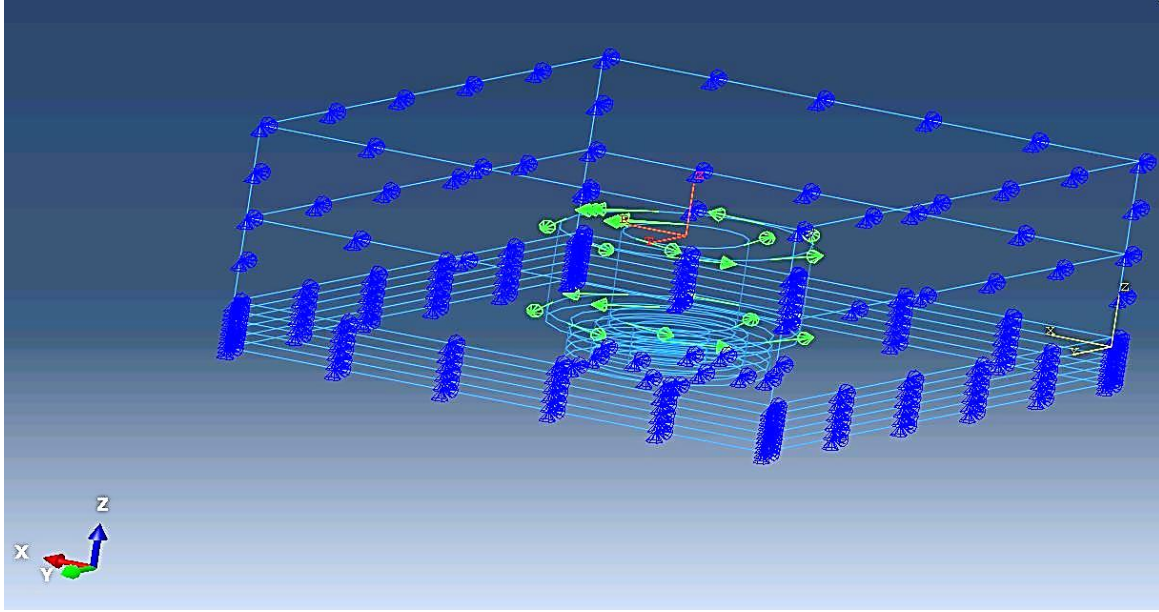


Fig. 6.2. Abaqus model representation of the body current density load applied to the coil within the modelled system (green arrows showing the current flow direction) and the boundary conditions (blue symbols).

6.4 Assessment of induction parameters

This paragraph assesses inductive heating parameters, such as current density, that are needed to provide reasonable rate of heating for given level of patch conductivity. Temperature values reached through induction heating are of interest to understand whether this methodology could replace the currently used cure processes through external heat application. Therefore, the rate of Joule heat dissipation H_d (amount of heat dissipated per unit volume per unit time) in conductor regions, needs to be calculated. The model results can help predict the change of temperature within a medium in response to heat dissipation, generated by induction phenomena, considering the mass density ρ of the medium (LNR or LCR) and the medium heat capacity C_p . The values of heat dissipation H_d needed to cause a temperature increase ΔT ($= T - T_0$) and obtain the resin cure temperature, were calculated by multiplying the ΔT by medium density and heat capacity and dividing by the gel time t_g of the epoxy resin embedded within the composite laminate, as shown below

$$H_d = \frac{\Delta T}{t_g} \cdot \rho \cdot C_p \quad . \quad (6.8)$$

Gel time t_G equal to 3600 s (as per manufacturer's data sheet of PRIME 20LV) was used, and LNR and LCR cases were considered and the properties on [Table 6.3](#) were used for the calculation.

Therefore, for LNR case:

$$H_{d_{\text{LNR}}} = \frac{\Delta T}{t_G} \cdot \rho_{\text{LNR}} \cdot C_{p_{\text{LNR}}} = \frac{(343.15-298.15)\text{K}}{3600\text{ s}} \cdot 2.63 \frac{\text{g}}{\text{cm}^3} \cdot 0.84 \frac{\text{J}}{\text{g}\cdot\text{K}} = 0.0276 \frac{\text{J}}{\text{cm}^3\cdot\text{s}}, \quad (6.9)$$

whereas, for LCR case:

$$H_{d_{\text{LCR}}} = \frac{\Delta T}{t_G} \cdot \rho_{\text{LCR}} \cdot C_{p_{\text{LCR}}} = \frac{(343.15-298.15)\text{K}}{3600\text{ s}} \cdot 1.77 \frac{\text{g}}{\text{cm}^3} \cdot 0.71 \frac{\text{J}}{\text{g}\cdot\text{K}} = 0.0157 \frac{\text{J}}{\text{cm}^3\cdot\text{s}}. \quad (6.10)$$

The values of H_d from equation 6.9 and 6.10 were used as target values for the Abaqus iterations to evaluate the body current density applied to the coil to achieve the values of heat dissipation necessary to achieve 70°C (cure temperature of epoxy resin PRIME 20LV as per manufacturer's data sheet). The applied frequency was 10 kHz as higher heat dissipation is expected due to the inductive reactance of the coil, as detailed in Section 6.2.

Table 6.3. LNR and LCR properties used for the temperature estimates [107, 108].

	Mass density ρ [g/cm ³] [107]	Specific heat capacity C_p [$\frac{\text{J}}{\text{g}\cdot\text{K}}$] [108]
LNR	2.63	0.84
LCR	1.77	0.71

In-plane conductivities of the conductive patch for both LNR and LCR cases are shown in [Table 6.4](#). Variations in conductivities were selected arbitrarily in the conductive (LCR) case to reflect homogeneous conductivity case across the conductive patch. The following formula could give the electric current to be applied through the coil

$$J = \frac{I}{A} , \quad (6.11)$$

where I is the current flowing through the coil and A is the cross-sectional area faced by the current flow as per Fig. 6.2, calculated as shown below

$$A = h \cdot (R_o - R_i) = 5 \text{ cm} \cdot (5 \text{ cm} - 2.5 \text{ cm}) = 12.5 \text{ cm}^2 . \quad (6.12)$$

with R_o and R_i respectively outer and inner radiuses of the circular coil, and h the coil depth.

Table 6.4. Electrical conductivity values used for the evaluation of the current density needed to achieve heat dissipation according to equation 6.9 and 6.10.

	Electrical conductivity [S/m]			
	Zone 0	Zone 1	Zone 2	Zone 3
LNR (non-conductive)	0.01	10	1	0.1
LCR (conductive)	100	105	105	105

The values of optimum current density σ are shown in Table 6.5, calculated through several model runs.

Table 6.5. Values of optimum current density J to achieve effective induction heating from Abaqus model.

	Current density J [A/cm ²]	H_d [$\frac{J}{\text{cm}^3 \cdot \text{s}}$]
LNR (non-conductive)	$8.4 \cdot 10^5$	0.0283 (> 0.0276)
LCR (conductive)	$4.3 \cdot 10^5$	0.0170 (> 0.0157)

The value of electric current flowing through the coil can therefore be retrieved from equation 6.11 as follows

$$I_{\text{LNR}} = J_{\text{LNR}} \cdot A = 1.05 \cdot 10^7 \text{ A} , \quad (6.13)$$

$$I_{\text{LCR}} = J_{\text{LCR}} \cdot A = 0.54 \cdot 10^7 \text{ A} . \quad (6.14)$$

Both values obtained above are unrealistic in terms of the order of magnitude. Therefore, the patch requires material modification to increase the electrical conductivity of the laminate. The conductivity across the entire patch was set to 10^4 S/m as realistically achievable. This level of conductivity cannot be achieved with additives, but comparable with the level of conductivity that can be realised using through-thickness reinforcement in 3D woven, braided, tufted, textile or pinned with carbon rods. Initially, the trials with more conductive material were carried out by using electric current values up to 10 A, although results were not showing any significant improvement to the heat dissipation levels. Therefore, the current was then set to 220 A, which agrees with the current values reported by Wasselynck *et al.* in [109]. Therefore, the current density used in the model resulted equal to $17.6 \frac{\text{A}}{\text{cm}^2}$. However, this model run showed negligible heat dissipation values and at higher patch conductivity levels. This effect shows that the heat dissipation is mainly dependent on the current density used to induce the heating from the laminate. An additional investigation was carried out for both LNR and LCR cases. The electrical conductivity was still set to 10^4 S/m. The model was run several times to calculate the values of current density. The results are shown in Table 6.6.

Table 6.6. Values of optimum current density J to achieve effective induction heating from Abaqus model with high conductivity patch.

	Patch electrical conductivity [S/m]	Required current density J [A/cm ²]	Heat dissipation H_d [$\frac{\text{J}}{\text{cm}^3 \cdot \text{s}}$]
LNR (high cond. patch)	10^4	$4.85 \cdot 10^5$	0.02956 (> 0.0276)
LCR (high cond. patch)	10^4	$3.8 \cdot 10^5$	0.01815 (> 0.0157)

Comparing the results from Table 6.5 and 6.6, a significant decrease of required current density from $8.4 \cdot 10^5$ A/cm² to $4.85 \cdot 10^5$ A/cm² (which relate to $1.05 \cdot 10^7$ A and $0.6 \cdot 10^7$ A, respectively, compared to achievable 220 A [109]) could be achieved by increasing the overall patch electrical conductivity from 105 S/m to 10^4 S/m. However, the model suggested that the conductivity across the patch has a lower contribution to the heat generation than the current density through the coil calculated from equations 6.9 and 6.10. Work from Rudolf *et*

al. [80] showed that the heating time increases quadratically with the induction coil/laminate distance and decreases quadratically with the generator power. The maximum induced temperature within the laminate was also strongly dependent on power and induction coil/laminate distance. Hence, reducing the gap between the laminate from 5 mm to 1mm (characteristic value for bagging materials) could further increase heat dissipation to the values shown in Tables 6.5 and 6.6.

Moreover, thinner coil means that no parasitic currents occur and higher frequency could be achieved. Therefore, further investigation is needed to assess the level of conductivity across the patch required for sensible values of current density and field frequency. The use of transistors or super conductive materials for the coil could help achieve the required current density, and therefore facilitate the heat dissipation process. Alternatively, a coil characterised by a smaller cross-sectional area can be used. The reduction in coil cross-sectional area is realistically applicable and could help maximise the electric current density while amplifying the electric current. For instance, by considering the current running through a single copper wire, the cross-sectional area A considered would be equal to $\pi \cdot r^2$, with r representing the radius of the wire. In this case, the radius required to achieve the current density levels reported in Table 6.6 for a patch electrical conductivity of 10^4 S/m could be calculated as follows

$$r = \sqrt{\frac{I}{\pi \cdot J}}, \quad (6.15)$$

obtaining values of 0.12 mm and 0.13 mm for LNR and LCR cases, respectively. Such values of copper wire diameter can be found in the market [110], therefore validating the assumption of smaller cross-sectional areas for the real-life application of the model.

The next section focuses on the effect of grading on the heat distribution across the laminate in an ideal scenario where such high levels of current density could be achieved to induce heat dissipation phenomena.

6.5 Feasibility of grading - Results

The investigation was carried out to assess the feasibility of grading the in-plane and out-of-plane electrical conductivity of the magnetic patch and understand whether the grading approach could help homogenise the heat dissipated through induction mechanisms. The results were assessed in terms of the heat dissipation H_d , which represents the rate of Joule heat dissipation (amount of heat dissipated per unit volume per unit time) in conductor

regions. The investigation was carried out by fixing the current density applied to the coil equal to $1e^7$ A/cm² [111]. This value chosen as a reference from previous work found in the Abaqus library and applied to the coil along the ϕ coordinate. However, Section 6.4 showed that higher current density values could be used by reducing the cross-sectional area of the coil, not considered in the current section as purely qualitative and focused on the effect of grading on the heat dissipation distribution across the patch.

6.5.1 Grading of in-plane electrical conductivity

The non-conductive laminate (LNR) and the conductive laminate (LCR) were characterised by different electrical conductivities across the patch in the three partitioned regions, from Zone 1 (inner region corresponding to the injection location) to Zone 3 (outer magnetic patch region). Table 6.7 and Table 6.8 show the electrical conductivity levels and the H_d values for the different numerical analyses carried out on Abaqus in the case of uniform electrical conductivity through the laminate thickness, for LNR and LCR, respectively. Highly-graded conductivity model runs were called Test 1, 3, 5 and 7, whereas non-graded conductivity cases were named Test 2, 4, 6 and 8, for simplicity. Table 6.7 shows the results for Tests 1 to 4, whereas Table 6.8 shows the results for Tests 5 to 8.

H_d is dependent on the eddy current distribution and the conductivity in-plane gradients. Eddy currents are generated through the laminate creating a conductive loop, which will result in heat generation to aid the panel cure. In this case, results show that a lower frequency (10 kHz) allows for a higher value of H_d , therefore more heat dissipation because of the applied magnetic field. This phenomenon could be observed in both LNR and LCR cases and related to the inductive reactance of the coil.

The values of heat dissipation which could be reached in the conductive case C were considerably higher, 69.9 and 67.84 J / (cm³ s) at 10 KHz compared with 4.0 and 3.0 J / (cm³ s) at 10 kHz for the non-conductive LNR case. This effect can be associated with the higher electrical conductivity values of the LCR laminate, which allow for higher heat dissipation contribution at the same level of frequency due to a more efficient network within a carbon fibre laminate. Moreover, the heat dissipation at 10 kHz is higher than the dissipation at 1 MHz for both LNR and LCR cases. Therefore, higher heat dissipation could be found at a lower magnetic field frequency. The electrical conductivity was chosen uniform across the magnetic patch regions with values of 0.05 S/cm and 1.05 S/cm for LNR and LCR, respectively. This caused an increase of dissipated heat for both 10 kHz and 1 MHz in the

case of LNR, whereas a slight decrease of dissipated heat was observed for the LCR case. Fig. 6.3 shows the heat dissipation H_d results from the Abaqus model for Test 1 and Test 2 (LNR, Fig. 6.3(a) and Fig. 6.3(b) respectively), Test 6 and Test 8 (LCR, Fig. 6.3(c) and Fig. 6.3(d) respectively). Different heat dissipation patterns can be observed from Test 1 and Test 2 for LNR by considering an average electrical conductivity across the patch for Test 2. The higher heat dissipation can be noticed as the map shows a larger area manifesting heat dissipation if compared to Test 1.

Furthermore, results for the LCR case can be observed from Fig. 6.3(c) and Figure Fig. 6.3(d). The H_d map shows a contrasting distribution between Test 6 (10 kHz) and Test 8 (1 MHz), with higher heat dissipation from Test 6, as shown in the table above. This reinforces the results obtained in the LNR case and shown in Table 6.3 and Table 6.4.

Another interesting conclusion can be drawn from Fig. 6.4 and 6.5, where the graphs show the progression of heat dissipation H_d with the location within the patch (zone 0, 1, 2 or 3) for all the tests run in the LNR and LCR case, respectively. The tests carried out at the frequency of 1 MHz (Test 3, 4, 7 and 8) show lower heat dissipation but a more uniform heat distribution across the patch. Moreover, the use of constant in-plane conductivity across the patch leads to a less homogeneously distributed heat dissipation between Zone 0 and Zone 3 as shown in Fig. 6.4 and 6.5.. Specifically, Zone 2 shows higher level of heat dissipation in both LNR and LCR cases. Therefore, an intermediate frequency between 10 kHz and 1 MHz could help achieve higher levels of conductivity while still reducing the heat distribution gradients.

Table 6.7. Electrical conductivities and H_d for LNR with uniform laminate through-thickness properties.

	Test 1			Test 2			Test 3			Test 4		
	Electrical conductivity [S/m]	Frequency [kHz]	Max H_d [J/(cm ³ ·s)]	Electrical conductivity [S/m]	Frequency [kHz]	Max H_d [J/(cm ³ ·s)]	Electrical conductivity [S/m]	Frequency [kHz]	Max H_d [J/(cm ³ ·s)]	Electrical conductivity [S/m]	Frequency [kHz]	Max H_d [J/(cm ³ ·s)]
Zone 0	0.01	10	4.605e-4	0.01	10	4.651e-4	0.01	1000	3.17e-6	0.01	1000	2.94e-6
Zone 1	10		2.976	5		1.372	10		0.370	5		8.191e-2
Zone 2	1		0.774	5		4.007	1		0.576	5		0.898
Zone 3	0.1		1.706e-3	5		2.227e-2	0.1		1.112e-3	5		3.979e-3

Table 6.8. Electrical conductivities and H_d for LCR with uniform laminate through-thickness properties.

	Test 5			Test 6			Test 7			Test 8		
	Electrical conductivity [S/m]	Frequency [kHz]	Max H_d [J/(cm ³ ·s)]	Electrical conductivity [S/m]	Frequency [kHz]	Max H_d [J/(cm ³ ·s)]	Electrical conductivity [S/m]	Frequency [kHz]	Max H_d [J/(cm ³ ·s)]	Electrical conductivity [S/m]	Frequency [kHz]	Max H_d [J/(cm ³ ·s)]
Zone 0	100	10	3.214e-4	100	10	3.238e-4	100	1000	1.671e-5	100	1000	1.671e-5
Zone 1	110		20.09	105		19.04	110		5.332e-3	105		5.574e-3
Zone 2	101		67.84	105		69.9	101		0.1226	105		0.1181
Zone 3	100.1		0.1596	105		0.1633	100.1		2.648e-4	105		2.548e-4

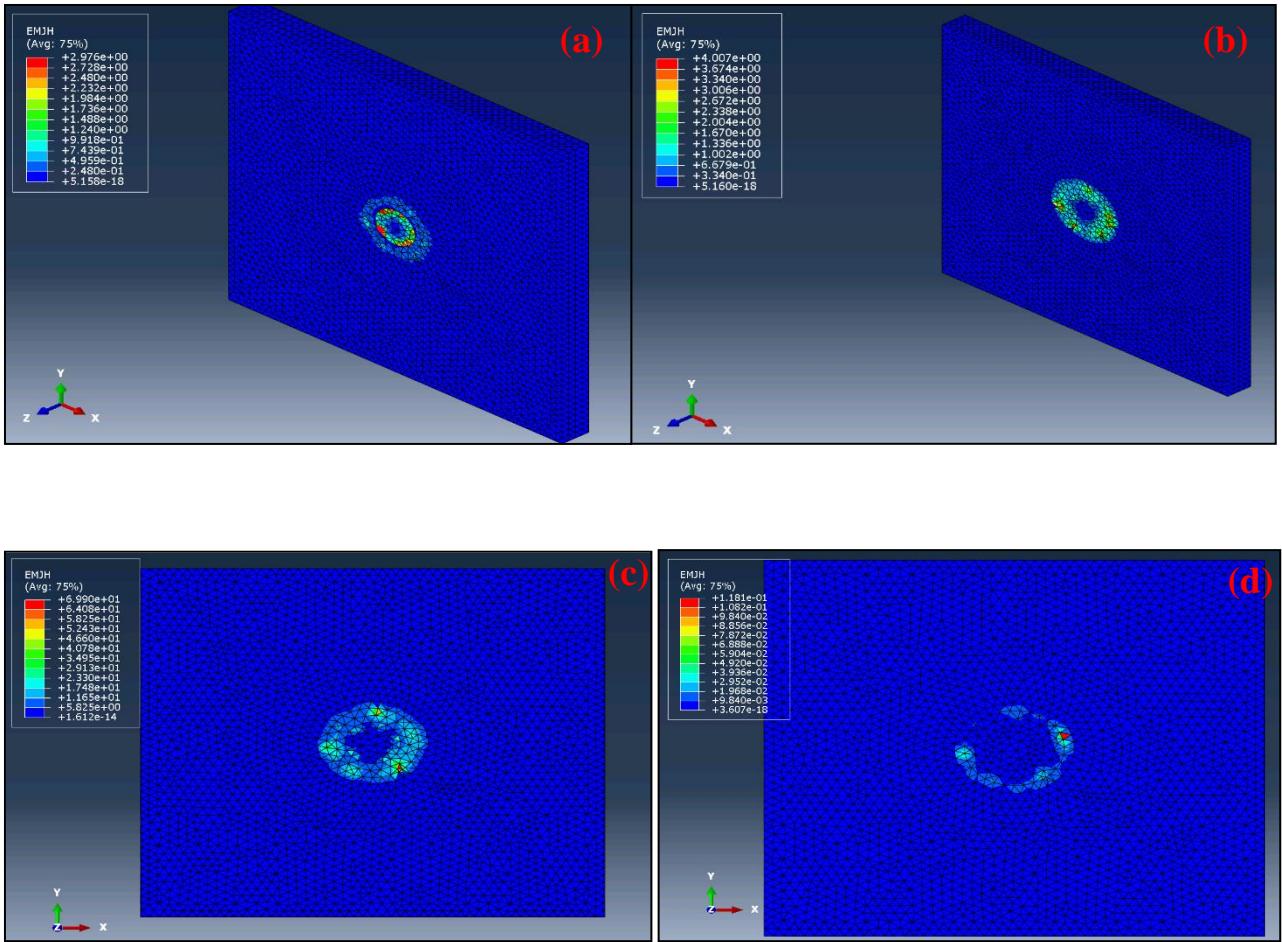


Fig. 6.3. Abaqus model results of H_d : Test 1 (a), Test 2 (b), Test 6 (c) and Test 8 (d).

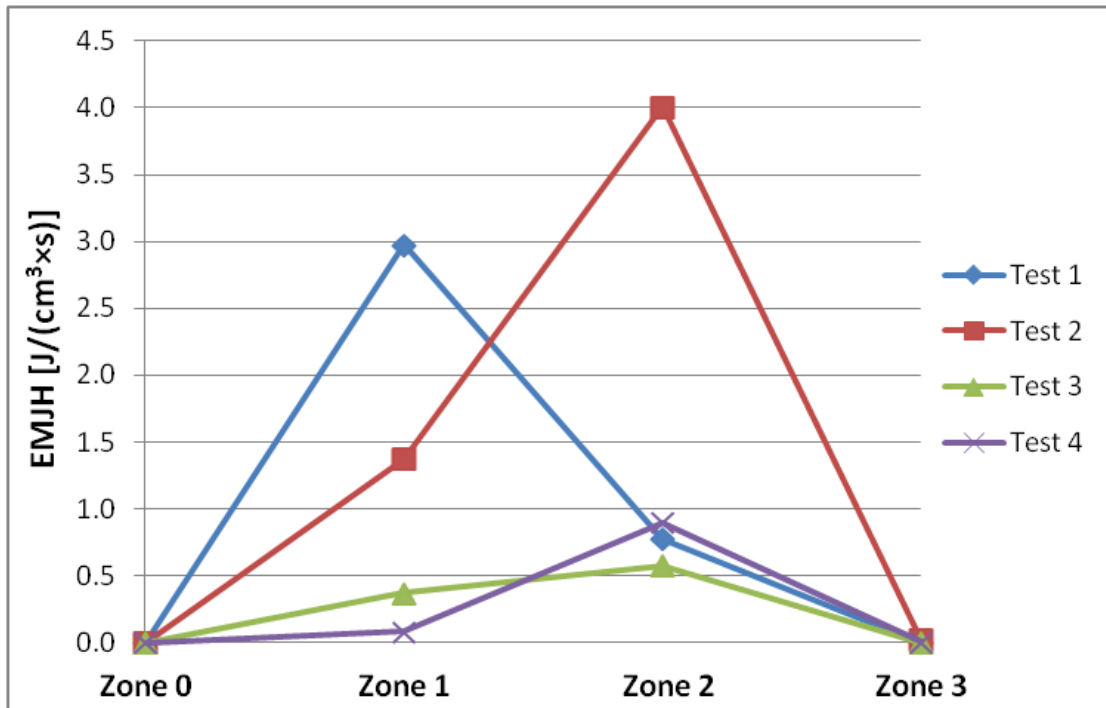


Fig. 6.4. Progression of heat dissipation H_d with the location within the patch (zone 0, 1, 2 or 3) for the tests run in the LNR case (no through-thickness grading).

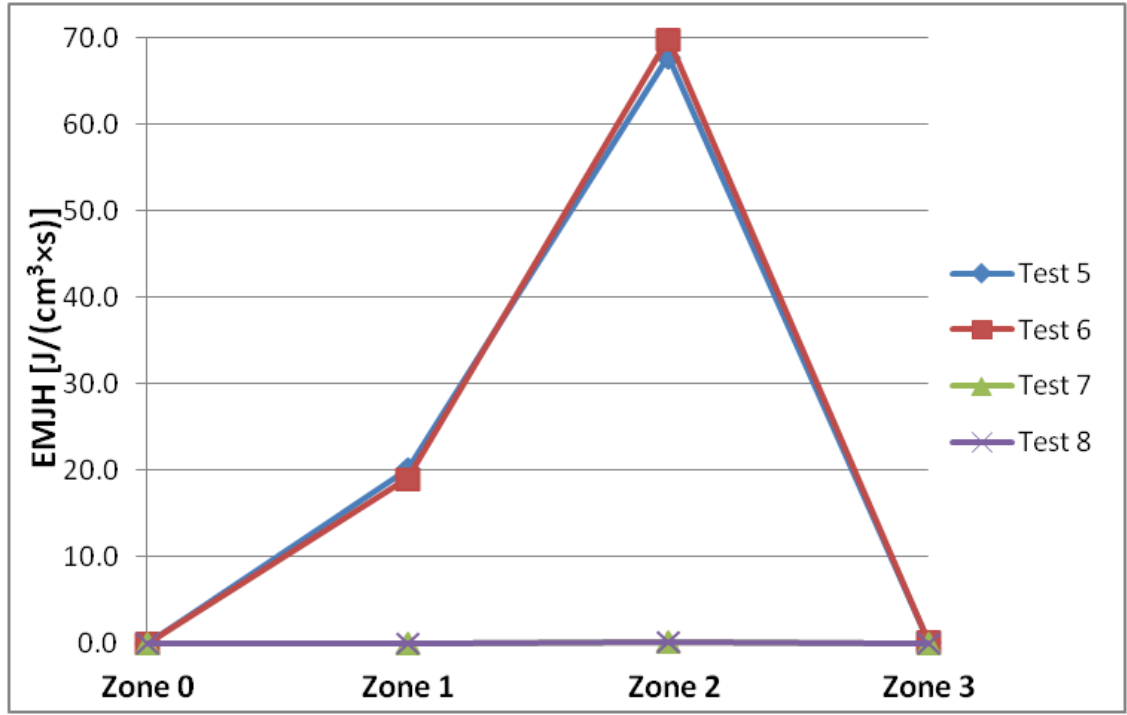


Fig. 6.5. Progression of heat dissipation H_d with the location within the patch (zone 0, 1, 2 or 3) for the tests run in the LCR case (no through-thickness grading).

6.5.2 Grading of through-thickness electrical conductivity

It was interesting to consider a specific grading of material properties through thickness (as well as in-plane) which could potentially achieve a more uniform heat supply in the sample. Table 6.9 and Table 6.10 show the electrical conductivity levels for each laminate ply at the different magnetic patch locations, from Zone 0 to Zone 3, for the case of increasing conductivity from the top ply (Ply 4) to the bottom ply (Ply 1), and for the reversed case of increasing conductivity from Ply 1 to Ply 4, respectively. LNR case was studied by running Tests 9, 10, 11 and 12. Test 9 and 10 were conducted with the condition of increasing conductivity from Ply 4 to Ply 1 at different frequencies, 10 kHz and 1 MHz. On the other hand, Test 11 and 12 were carried out with the reversed condition of increasing conductivity from Ply 1 to Ply 4. The values of electrical conductivity shown in Table 6.9 and Table 6.10 were used as material properties for the numerical analyses carried out on Abaqus. The results of maximum heat dissipation H_d obtained through said numerical analyses from each conductivity region (Zone 0, Zone 1, Zone 2 and Zone 3) are reported in Table 6.11.

Table 6.9. Electrical conductivity levels for each laminate ply at the different magnetic patch locations for the case of increasing conductivity from the top ply (Ply 4) to the bottom ply (Ply 1).

	Zone 0	Zone 1	Zone 2	Zone 3
Ply 1	0.0001	1	0.5	0.2
Ply 2	0.0001	0.5	0.2	0.1
Ply 3	0.0001	0.1	0.05	0.01
Ply 4	0.0001	0.01	0.001	0.0001

Table 6.10. Electrical conductivity levels for each laminate ply at the different magnetic patch locations for the case of increasing conductivity from the top ply (Ply 4) to the bottom ply (Ply 1).

	Zone 0	Zone 1	Zone 2	Zone 3
Ply 1	0.0001	0.01	0.001	0.0001
Ply 2	0.0001	0.1	0.05	0.01
Ply 3	0.0001	0.5	0.2	0.1
Ply 4	0.0001	1	0.5	0.2

Table 6.11. Non-uniform through-thickness electrical conductivity conditions and results for the LNR case.

	Test 9	Test 10	Test 11	Test 12
Conductivity condition	Ply 1 > Ply 4	Ply 1 > Ply 4	Ply 1 < Ply 4	Ply 1 < Ply 4
Frequency [kHz]	10	1000	10	1000
Max H_d Zone 0 [J/(cm³·s)]	4.654e-4	2.979e-6	4.654e-4	2.979e-6
Max H_d Zone 1 [J/(cm³·s)]	22.49	5.777e-3	22.49	5.777e-3
Max H_d Zone 2 [J/(cm³·s)]	38.11	0.2346	38.11	0.2346
Max H_d Zone 3 [J/(cm³·s)]	0.1202	8.316e-4	0.1202	8.316e-4

As shown in Table 6.11, the conductivity condition did not change the results in terms of heat dissipation because the ply blocks used in the model are too large and all the variations in magnetic field occur in the top block. The heat dissipation showed the same value in the case of Ply 1 > Ply 4 and Ply 1 < Ply 4. Moreover, the tests carried out at the frequency of 1 MHz (Test 10 and 12) show lower heat dissipation but a more uniform heat distribution across the patch, as shown in Fig 6.6. In all the tests associated with the LNR case, Zone 2 shows higher level of heat dissipation. An intermediate frequency between 10 kHz and 1 MHz could help achieve higher levels of conductivity while still reducing the heat distribution gradients.

LCR case was assessed by running Tests 13, 14, 15 and 16. Test 13 and 14 were carried out with the condition of increasing conductivity from Ply 4 to Ply 1 at different frequencies, 10 kHz and 1 MHz. On the other hand, Test 15 and 16 were carried out with the reversed condition of increasing conductivity from Ply 1 to Ply 4, as shown in Table 6.12. Table 6.12 also shows the values of maximum heat dissipation H_d from the Abaqus analyses for the mentioned four cases. The LCR case shows the same results as the LNR case, with no change occurring between the two conductivity conditions. This could be related to the levelled electrical properties between the in-plane and the out-of-plane gradients, leading to similar properties between the LNR and LCR cases studied. The same results shown in the LNR case can be observed in the LCR case from Fig. 6.7. Therefore, grading of properties through the thickness of the laminate could help homogenise heat dissipation distribution particularly at high frequencies (MHz).

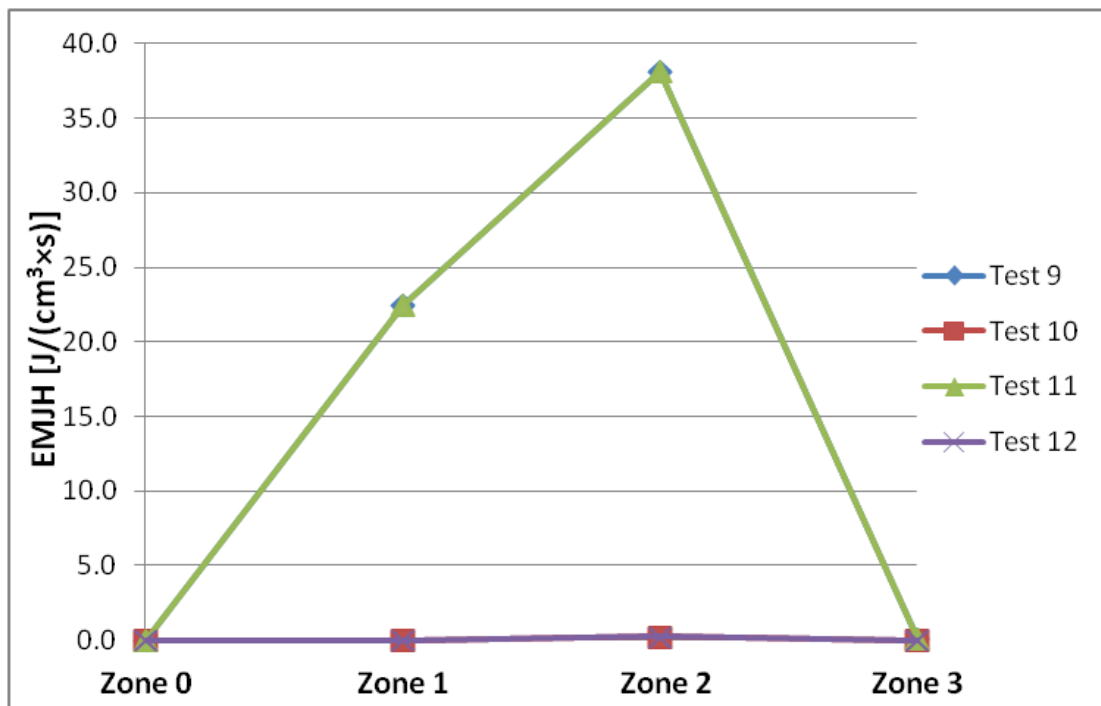


Fig. 6.6. Progression of heat dissipation H_d with the location within the patch (zone 0, 1, 2 or 3) for the tests run in the LNR case (through-thickness grading).

Table 6.12. Non-uniform through-thickness electrical conductivity conditions and results for the LCR case.

	Test 13	Test 14	Test 15	Test 16
Conductivity condition	Ply 1 > Ply 4	Ply 1 > Ply 4	Ply 1 < Ply 4	Ply 1 < Ply 4
Frequency [kHz]	10	1000	10	10000
Max H_d Zone 0 [J/(cm³·s)]	1.944e-4	1.676e-5	1.944e-4	1.676e-5
Max H_d Zone 1 [J/(cm³·s)]	22.51	5.777e-3	22.51	5.777e-3
Max H_d Zone 2 [J/(cm³·s)]	38.06	0.2346	38.06	0.2346
Max H_d Zone 3 [J/(cm³·s)]	0.1169	8.236e-4	0.1169	8.236e-4

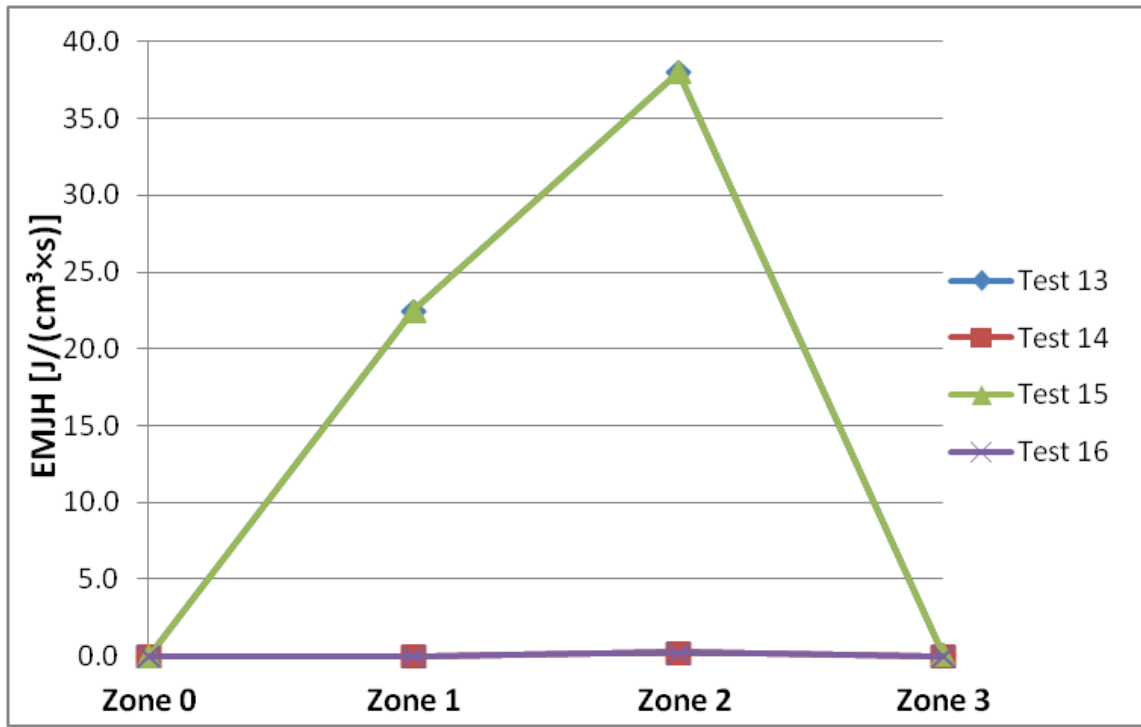


Fig. 6.7. Progression of heat dissipation H_d with the location within the patch (zone 0, 1, 2 or 3) for the tests run in the LCR case (through-thickness grading).

6.6 Conclusions

The modelling study of the induction heating phenomena within a LNR and LCR composite laminate was considered. Specifically, the integration of the conductive patches graded in plane and through the thickness of the laminate, was studied. Functionalizing patches by nano-reinforcement is particularly relevant for preforms with electrically non-conductive fibres, such as glass, Kevlar, or natural fibres. However, the numerical study shown in this Chapter suggests that for maximum electrical conductivity that can be achieved even with the advanced manufacturing approaches may not be sufficient to produce reasonably high rates of heating. The limitations of the model do not permit conclusive rejective statements on the overall feasibility of the concept but suggest that more work needs to be done on concurrent optimisation of both the induction set-ups parameters and materials to make this happen. On the other hand, studies on conductive mediums (*i.e.* carbon fabric) showed that induction heating can be achieved without magnetic modification due to its high in-plane conductivity [84, 109]. Yarlagadda *et al.* [97] suggested that moderate improvement of through thickness conductivity of carbon fabric could lead to significant change in conductive loop formation within the material and have a strong impact on heat dissipation.

The study showed that the parameters of inductive heating have a more pronounced effect than the change in electrical conductivity. Higher values of heat dissipation were recorded for the LCR case, and higher frequencies led to a more uniform distribution of heat dissipation, for both LNR and LCR cases, although the skin effect could influence this result if considered in the model. Higher heat dissipation was recorded in the case of uniform in-plane conductivity, although secondary to the scope of the grading investigation. These results could be beneficial to investigate the effect of nanotube positioning within composite laminate on the inductive heat generation for composite repair application.

The heat dissipation rate was translated into time required to heat material through equation 6.8 under assumption that conductive mechanisms of heating are not dominant. Further work is required to modify either the magnetic patch within the laminate or the coil geometrical properties to maximise the current density while amplifying the electric current. Moreover, the heat dissipation due to eddy current generation within the laminate could be combined with the dielectric heating from the resin matrix if the matrix is modified by the introduction of dielectric additives [86-92, 97]. Dielectric heating mechanisms and the benefits on the overall heating performance through external magnetic field application will be explored in Chapter 7.

7. Dielectric measurements

In Chapter 4 and 5, the investigation was focused on the nano-additive metal functionalisation to affect the nano-additive sensitivity to an externally applied magnetic field and manipulate the additive position. This approach was chosen to locally modify the electrical and magnetic properties of the resin system, and therefore provide a specific functionality where required. The aim was to locally enhance the electrical performance of the resin to overcome the through-thickness resin electrical resistance and generate an efficient electrical network within the host matrix by means of induced eddy currents. Other mechanisms could be exploited to induce internal heat from the system as part of the same framework. Yarlagadda *et al.* [97] discuss improvement in the induction heating due to the dielectric properties of matrix between different layers of fabric. The dielectric matrix between non-touching fibres behaves as a capacitor and resistor connected in parallel. Therefore, an induced current loop can be generated as shown in Fig. 2.29 [97]. Enhanced dielectric properties of the host matrix could lead to efficient dielectric heating mechanisms [86-92]. Improving dielectric properties of resins by means of powder additives is assessed in this chapter. A case study was carried out to evaluate the effect of the ceramic particle introduction on the resin cure mechanisms and understand whether the dielectric heating enhanced by the dielectric additives could assist the cure process.

Equation 2.5 shows the relationship between the resistance at a dielectric junction between the dielectric matrix junction resistance R_{jd} and the dielectric constant κ , confirming that an increase in resin dielectric constant could cause a decrease in the junction resistivity, leading to higher electrical conductivity between the host composite fibres and, potentially, more efficient electric network within the part. Synergetic effect between the magnetic properties of functionalised nano-additives and the enhanced resin dielectric constant could be used to optimise the heat dissipation through the combination of dielectric heating and eddy currents and hysteretic losses from the nano-additives.

Therefore, dielectric characterisation of polymeric resin systems was carried out with the aim of assessing the most suitable candidate to generate remotely triggered inductive heating.

7.1 Materials

Benzoxazine 35600 (Araldite®, Huntsman; Appendix B.5), cyanate ester resin PT-30 (Primaset™, Lonza; Appendix B.6), and epoxy resin PRIME 20LV (Gurit, Appendix B.3) were initially characterised to assist the dielectric characterisation as baseline tests.

Strontium titanate (SrTiO_3 , Sigma Aldrich) was selected as potential candidate for the introduction within epoxy resin to increase its dielectric performances. Strontium titanate is a strontium and titanium oxide. It is a white to off-white, centrosymmetric paraelectric material in powder form with a perovskite structure at room temperature. On the other hand, low temperatures lead the oxide to a ferroelectric phase transition characterised by a very large dielectric constant of around 104. Quantum fluctuations occurring at the lowest temperatures measured make it a quantum paraelectric.

Synthetic strontium titanate possesses a very large dielectric constant at room temperature and low electric field, equal to around 300. Its specific resistivity exceeds $10^9 \Omega\cdot\text{cm}$ for very pure crystals. This property is widely exploited in high-voltage capacitors. Strontium titanate becomes superconducting through doping process below 0.35 K, although it has an indirect band gap of 3.25 eV and a direct gap of 3.75 eV.

Strontium titanate features a specific gravity of 4.88 in its natural form, whereas it reaches values of 5.13 in the synthetic form. Barium titanate (BaTiO_3 , Sigma Aldrich) was also used as filler within the epoxy resin PRIME 20LV (Gurit) and characterised as a candidate to increase the dielectric performance of the host resin. It is a white to grey powder with a perovskite structure at room temperature. It is soluble in many acids (including sulfuric, hydrochloric and hydrofluoric acids), but insoluble in alkalis and water. It shows electrically insulating properties in its pure form, but it becomes semiconducting after doping process with metal particles such as scandium, yttrium, neodymium and samarium. At the Curie temperature, barium titanate shows a positive temperature coefficient of resistivity in the polycrystalline form, therefore exhibiting an increase in resistivity. Moreover, barium titanate changes phase from tetrahedral to cubic at the Curie temperature. Barium titanate also behaves as a good ferroelectric and photorefractive material.

Introduction of CNTs within the host epoxy resin together with ceramic particles was investigated to understand the synergetic effect between CNTs and ceramic fillers on the dielectric performance of the blend. MWCNTs from Sigma Aldrich (Appendix B.1) were used and are characterised by an average diameter of 9.5 nm and a length of 1.5 μm . Electroless plating was used to deposit metal on their surface as outlined in Section 3.1.2.1.

Table 7.1 shows the properties of said fillers used for the dielectric investigation and treated in this chapter.

Table 7. 1 Properties of fillers used for the dielectric investigation.

Filler	Type	Size	Supplier	TDS** location
SrTiO₃	Nano-powder	≤ 100 nm	Sigma Aldrich	Appendix B.7
BaTiO₃	Nano-powder	50 nm	Sigma Aldrich	Appendix B.8
COOH-functionalised CNTs*	Nano-powder	9.5 nm x 1.5 μ m (D x L)	Sigma Aldrich	Appendix B.1

*used as precursors to obtain Co-plated CNTs through electroless plating technique.

** Technical Data Sheet

7.2 Sample preparation

The dielectric investigation was carried out on samples prepared to assess the dielectric properties of neat resins and the effect of the introduction of high dielectric constant additives on the dielectric properties of the blend. Samples were prepared from neat resins to obtain reference values of dielectric constant. Additional samples made of resins and dielectric additives were prepared and characterised, and the dielectric constant values resulting from the tests were compared with the reference figures.

Rectangular samples characterised by a length of 30 mm, width of 10 mm and thickness of 3 mm were manufactured by placing the blend in an addition-cure silicone rubber mould and further cured in a conventional oven as per manufacturer's data sheet.

Benzoxazine 35600 resin was heated up to 180 °C with a ramp rate of 2 K/min, followed by a 2-hour dwell and subsequently heated to 200 °C with a ramp rate of 2 K/min. An additional 2-hour dwell was then performed, immediately followed by a gradual cool to room temperature.

Cyanate ester resin PT-30 was subjected to a ramp rate of 2K/min up to 90 °C, followed by a temperature increase to 150 °C (1-hour dwell), to 200 °C (3-hour dwell) and a post-cure at 260 °C (1-hour dwell). Gradual cool down to room temperature was therefore allowed to the samples.

Low viscosity PRIME 20LV epoxy resin, homogeneously mixed with PRIME slow hardener, was heated up to 65 °C with a ramp rate of 2 K/min, followed by a 7-hour dwell and gradual cool to room temperature.

Samples were therefore sanded and polished to obtain smooth surfaces for the creation of the electrical contacts. These were manufactured by using copper wire, carefully wound and

attached at the ends of the samples through silver conductive paint (RS Components Ltd.), as shown in Fig. 7.1.

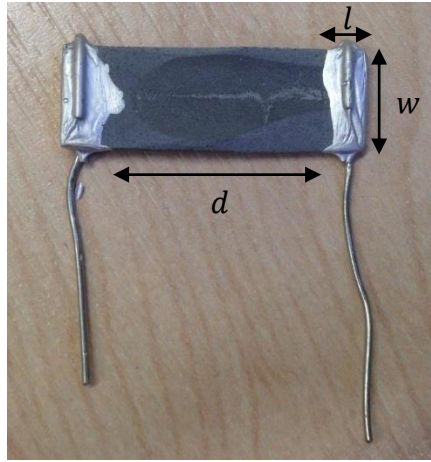


Fig. 7.1. Dielectric test sample with geometrical specifications.

The viscosity of the particles increased visually by introducing the dielectric additives and CNTs within the resin, making the blend processability more complicated. The weight fractions used for the dielectric investigation were up to 5 wt.%. However, the blends with the highest concentration of dielectric additives could still be mixed manually. Therefore, the introduction of said blends within fabric by means of resin infusion could be achieved and the blends could be used as a replacement for the neat resins currently used in composite manufacturing.

7.3 Experimental methodology

An impedance analyser (Wayne Kerr Electronics) was used to investigate the dependence of the capacitance on the frequency of the applied AC field.

Frequencies ranged from 50 Hz to 1 GHz. Tests were carried out for 15 minutes to allow for the signal stabilisation and data collection. The dielectric constant D was therefore calculated as follows:

$$D = (C \cdot d) / (\epsilon_0 \cdot A) , \quad (7.1)$$

where C is the sample capacitance (in F), d is the distance between the contacts (in m), ϵ_0 is the vacuum permittivity (in F/m) and $A (= l \cdot w$, where l is the electrical contact length and

w is the electrical contact width) is the electrical contact cross sectional area (in m^2), as visually explained in [Fig. 7.1](#).

7.4 Results

Initial tests were carried out on the neat epoxy resin PRIME 20LV compared to other resin systems previously enlisted, such as Benzoxazine 35600 and cyanate ester resin PT-30. Results are shown in [Fig. 7.2](#).

The cyanate ester resin PT-30 shows a slightly higher dielectric constant at all frequencies, around 6, whereas the dielectric constant for the epoxy resin PRIME 20LV reaches values around 5. However, epoxy resin PRIME 20LV is more commonly used for this project; therefore, the modification of this resin system will be investigated in detail.

The introduction of high dielectric constant ceramics was studied in the present work. Volume fractions of 5 vol.% and 10 vol.% of strontium titanate were chosen for the dielectric analysis. The sample cure cycle replicated the cycle used for the neat epoxy resin. Careful homogenisation between the epoxy resin and the ceramic material is required for the reliability of the results. The mixing process was carried out through the handheld shear mixer for 10 minutes prior to the oven cure. However, further investigation is required for the effect of the high dielectric constant ceramic on the epoxy resin curing process. Results from the dielectric tests are shown in [Fig. 7.3](#).

The introduction of strontium titanate within PRIME 20LV causes a dielectric constant increase up to 7.5 and 9 for 5 vol.% of SrTiO_3 and 10 vol.% of SrTiO_3 , respectively. This indicates the sterical and chemical suitability of strontium titanate with the epoxy resin polymeric chains. Inductive heating could be optimised through the combination of resin dielectric properties and the generation of electric pathways represented by the metal-plated MWCNTs.

Another high dielectric constant ceramic, barium titanate BaTiO_3 , was analysed as potential additive to the epoxy resin PRIME 20LV with the aim of increasing the dielectric performance. Results are shown in [Fig. 7.4](#).

The introduction of BaTiO_3 inhibits the dielectric constant both with 5 vol.% and 10 vol.%. This may be associated with the inability of the resulting material to be polarised by the externally applied field. Replacement of hydrogen with fluorine result in lowering of dielectric constant since fluorine occupies higher volume. Thus, besides being characterised

by low polarisability, introduction of fluorine induces a significant decrease of dielectric constant through an increase in free volume. This could be explained by the dielectric relaxation of the material due to the introduction of the dielectric ceramic. This leads to the inefficient energy storage of the epoxy resin, which instead dissipates the electric charge provided by the applied field.

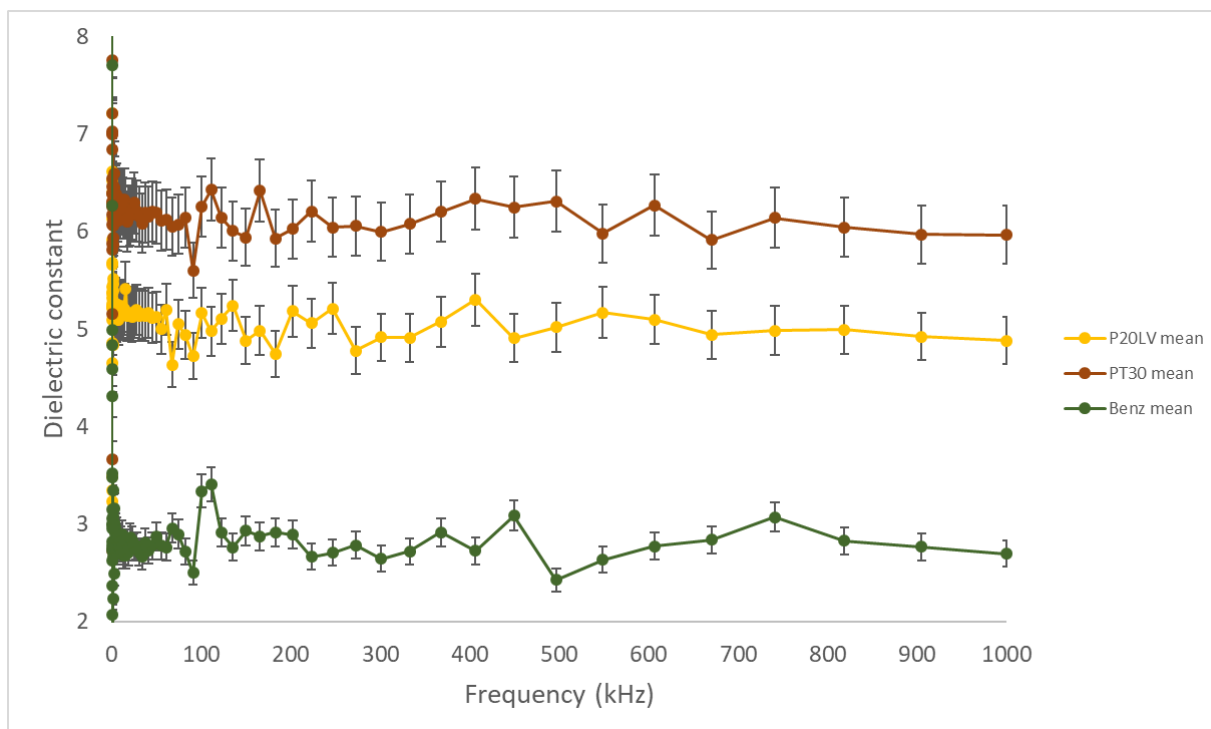


Fig. 7.2. Initial dielectric measurements on baseline resin systems.

Strontium titanate was introduced as an additive within the epoxy resin system in 80:20 and 70:30 epoxy:strontium titanate proportions but equal loadings of cobalt-plated carbon nanotubes, equal to 5wt.%. The aim of this analysis was to evaluate the optimum proportion epoxy resin/ ceramic filler to maximise the dielectric properties of the nanocomposite system. Results of the investigation are shown in [Fig. 7.5](#).

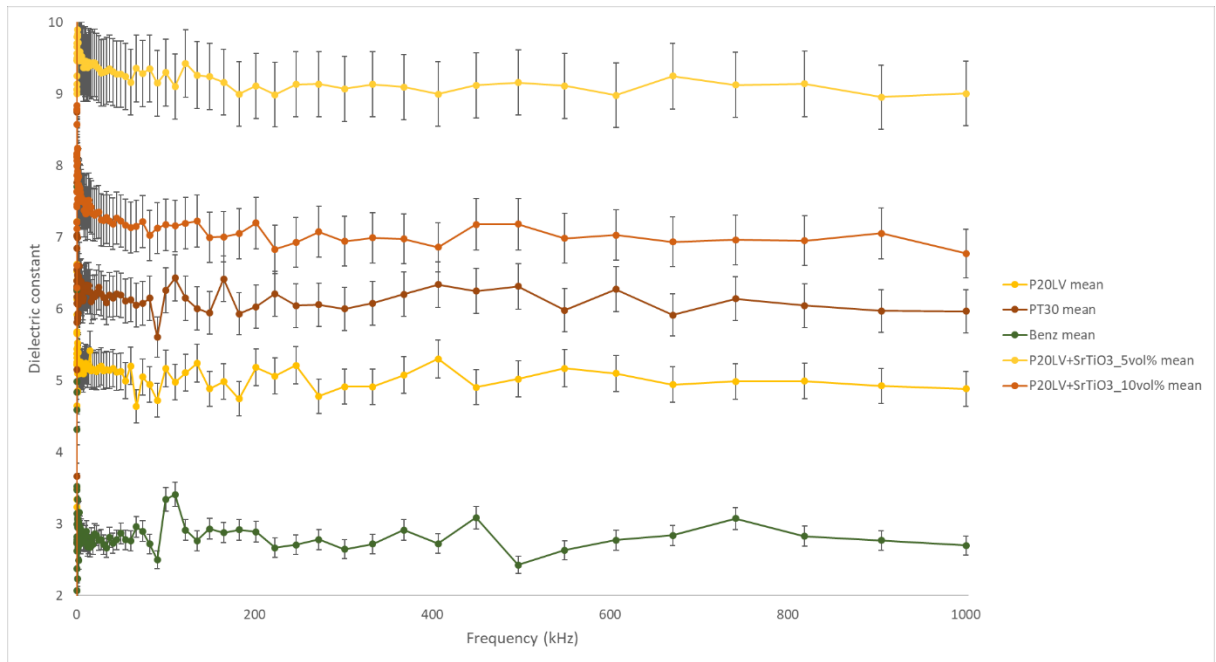


Fig. 7.3. Dielectric test measurements after introduction of SrTiO_3 within PRIME 20LV.

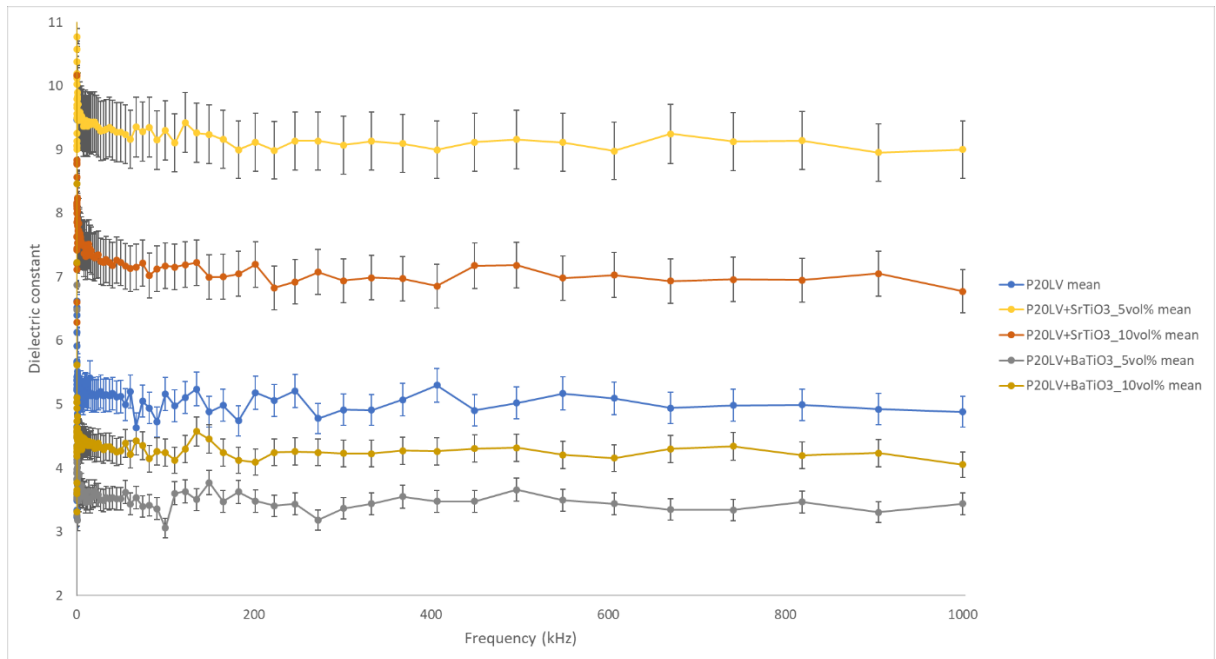


Fig. 7.4. Dielectric test measurements after introduction of BaTiO_3 within PRIME 20LV.

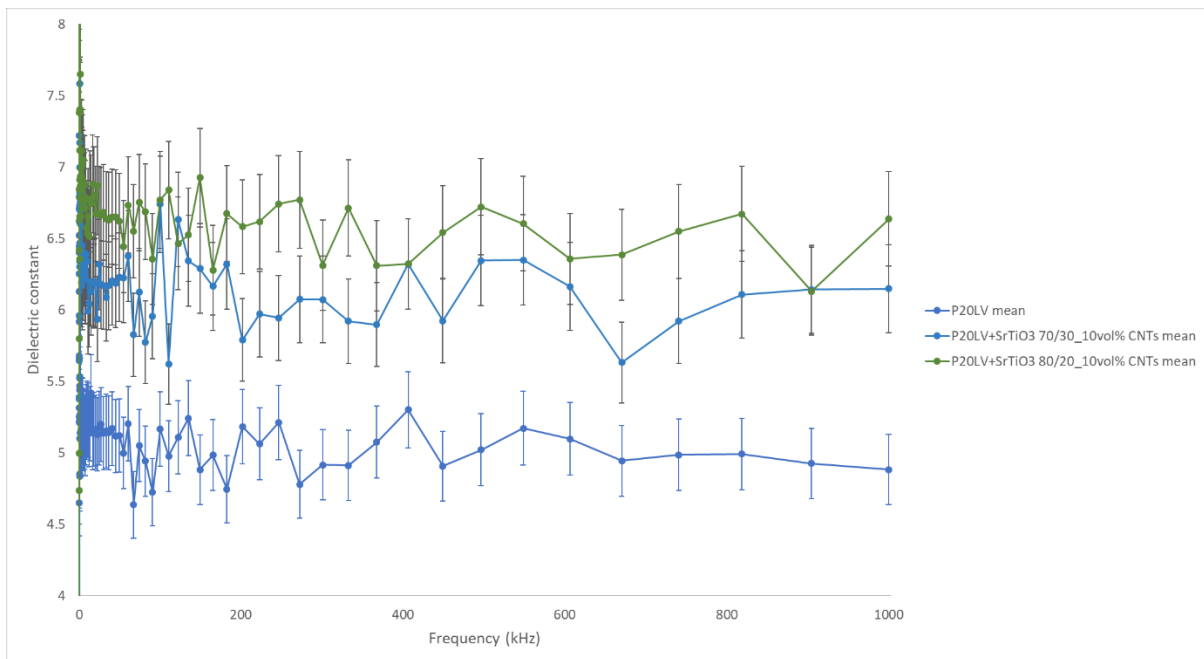


Fig. 7.5. Dielectric test measurements of nanocomposites characterised by an epoxy PRIME 20LV/strontium titanate ratio of 70:30 and 80:20 and cobalt plated carbon nanotube loadings of 5 wt.% (approximately 10 vol.%).

The introduction of the ceramic filler leads to a substantial increase of dielectric constant as expected. However, the resin:ceramic filler proportion also plays an important role in the dielectric properties. Indeed, an epoxy:strontium titanate ratio equal to 70:30 causes the dielectric constant to approach values of 6. On the other hand, the reduction of strontium titanate content from a ratio of 70:30 to 80:20 leads to an increase of dielectric constant up to 7. This could be associated to the increasing role played by the generation of nanotube conductive networks at lower strontium titanate contents, which exceeds the contribution of the ceramic filler. A more detailed investigation was therefore carried out on the nanocomposite characterised by an epoxy:strontium titanate ratio equal to 80:20.

The introduction of slow amine hardener and different weight fractions of cobalt functionalised carbon nanotubes was carried out. The weight fractions used for the dielectric investigation were 0.7 wt.%, 2.5 wt.% and 5 wt.% (equal to around 1 vol.%, 5 vol.%, and 10 vol.%, respectively). Fig. 7.6 shows the results from the investigation.

Samples were manufactured as previously mentioned and clamped at both ends to provide a better electrical contact with the energy supply. The geometry of the samples was unchanged compared to the previous tests, and the electrical contacts were manufactured to provide the samples with the same contact area.

Neat epoxy resin blended with slow amine hardener shows a dielectric constant of around 5 throughout the entire frequency range of application. However, the introduction of strontium titanate clearly affects the dielectric properties of the epoxy resin. Strontium titanate was therefore introduced within the epoxy resin with different weight loadings, as previously mentioned.

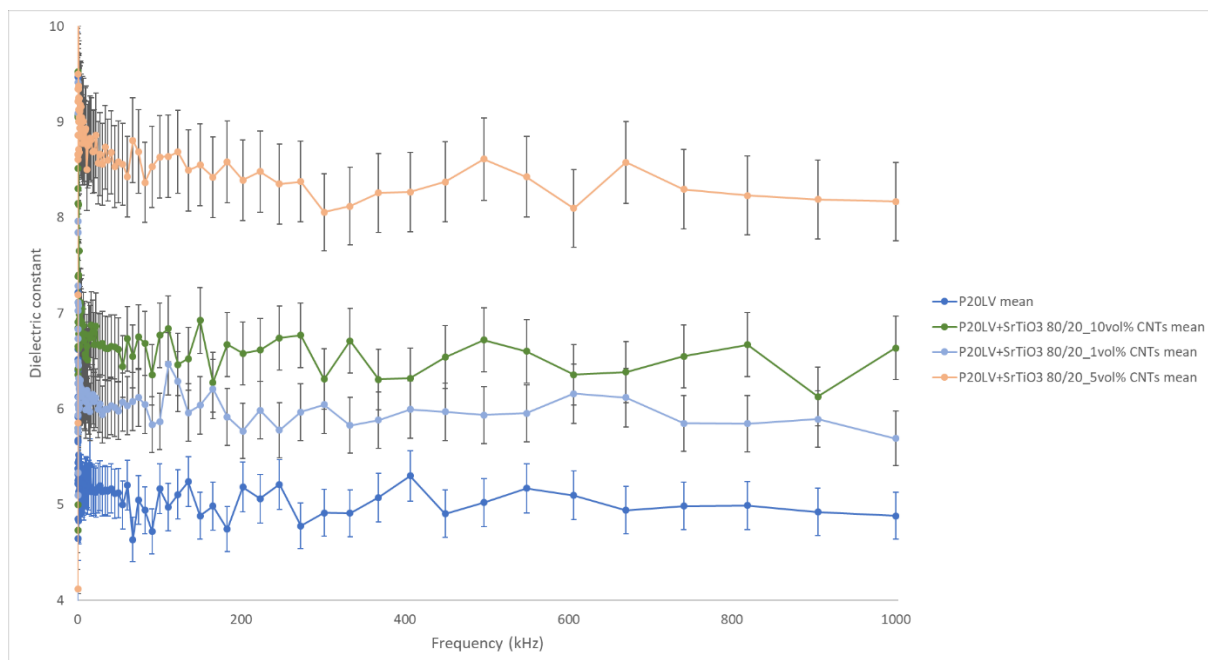


Fig. 7.6. Dielectric test measurements of nanocomposites characterised by an epoxy PRIME 20LV/strontium titanate ratio of 80:20 and cobalt plated carbon nanotube loadings of 0.7 wt.%, 2.5 wt.% and 5 wt.% (around 1 vol.%, 5 vol.% and 10 vol.%, respectively).

Initially, epoxy resin combined with strontium titanate in 80:20 ratio and blended with 0.7 wt.% of cobalt-plated nanotubes was manufactured and tested under frequencies ranging from 50 Hz to 1 MHz. The behaviour shown in this case was similar to the case of the neat epoxy resin, with an initial disturbance due to background noise. After the signal adjustment frequency range, the dielectric constant reached values, which approached 6 compared to the plateau value of 5 obtained from the neat resin sample. This indicates the effect of a relatively small addition of cobalt-plated nanotubes on the dielectric properties of the epoxy resin/strontium titanate blend.

The weight fraction of cobalt-plated nanotubes was therefore increased to 2.5 wt.%. This nanotube content was also used for previous characterisation of the cure kinetics of the resin influenced by the presence of a nano-additive.

The dielectric constant shows the same trend as the previous cases, although the increasing nanotube content does not affect the blending process efficiency. In this case, the synergistic effect of dielectric properties due to the strontium titanate and the increasing electric efficiency due to the potential generation of a conductive network between the cobalt-plated nanotubes still plays an important role. Dielectric constant values of 9 can be reached in this case. This represents a significant improvement in dielectric properties of the nanocomposite, which can still be processed. However, the nanocomposite viscosity increased if compared to the case of absence of the nanotubes. The mentioned phenomenon could be potentially exploited to implement nanotubes within adhesive systems and optimise the adhesive application onto surfaces characterised by complicated geometries.

A further increase in nanotube content was therefore attempted. In this case, the dielectric constant shows the trend already assessed in the previous case for lower nanotube loadings. However, the values of dielectric constant tend to be negatively affected. In this case, the dielectric constant approaches values of around 7.

The reduction in dielectric constant may be associated with the increasing nanotube content, which complicates the nanocomposite mixing procedure. Moreover, the generation of nanotube conductive networks can exceed the dielectric effects due to the strontium titanate introduction within the epoxy resin, causing a decrease in dielectric constant.

A comparative analysis of the dielectric constant obtained with and without the presence of cobalt-plated can be observed as follows. Results are shown in [Fig. 7.7](#).

The graph shows the comparison between the dielectric constant values of neat epoxy resin, epoxy resin with addition of 5 vol.% and 10 vol.% of strontium titanate and the combination of strontium titanate and epoxy resin with further introduction of cobalt-plated nanotubes. Loadings of 5 vol.% of strontium titanate within the epoxy resin lead to a significant increase of dielectric constant from 5 to 8. The addition of 10 vol.% of strontium titanate within the epoxy resin further enhances the dielectric constant, which reaches values of around 9.

The nanocomposite characterised by an 80:20 ratio between epoxy resin and strontium titanate and a nanotube weight fraction of 2.5 wt.%, shows dielectric constant values, which resemble the dielectric constant figures showed by the nanocomposite with the presence of 10 vol.% of strontium titanate.

The latter case can be considered more representative of the real application. Indeed, the aim of the dielectric testing was to assess a potential synergistic effect between the ceramic filler and the nanotube addition in terms of enhanced dielectric performance. The final purpose

would be the maximisation of the dielectric heating phenomena, which could be triggered remotely through kHz-MHz high frequency fields. Equation 2.5 shows that an increase of the dielectric constant for a host resin matrix by introducing dielectric additives could cause a directly proportional increase in electric conductivity of the fibre-to-fibre junction. Therefore, an increase of overall conductivity of the composite component could be obtained as described by Yarlagadda *et al.* [97]. Furthermore, induced currents could be then generated as shown in Fig. 2.29 [97]. Further numerical analysis as per Chapter 6 could help estimate the improvement in heat generation from the introduction of dielectric additives as per equation 2.5.

7.5 Case study: cure kinetics characterisation of hybrid dielectric material

Dielectric measurements investigated the most performing hybrid nanocomposite in terms of dielectric constant. Epoxy resin PRIME 20LV (blended with slow amine hardener) in a 80:20 ratio with strontium titanate and suspended with 2.5 wt.% of cobalt-plated multi-walled carbon nanotubes showed the highest dielectric constant, equal to around 8.5-9. These values could be observed throughout the entire applied frequency range, as shown in Fig. 7.8. This graph clearly shows the higher performance of the hybrid nanocomposite when compared to other strontium titanate/cobalt-plated nanotube combinations.

This nanocomposite was therefore characterised in terms of cure kinetics through mDSC. This was carried out to understand the effect of the introduction of dielectric additives within the epoxy system on the cure mechanisms involving the epoxy matrix. Furthermore, the addition of dielectric additives was studied to assess how to manipulate the cure cycle of the resin.

The temperature cycle applied *via* mDSC started with the initial temperature equilibration at 20°C and followed by temperature modulation of $\pm 1^\circ\text{C}$ every 60 s. After an isothermal period of 5 minutes, temperature was then set to raise up to 180°C with a ramp rate of 2°C/min. The low ramp rate for this test was opportunely selected to investigate the thermal phenomena with a higher level of detail.

The thermograph in Fig. 7.9 shows the total heat flow (mW) as a function of the temperature (°C) for the neat epoxy PRIME 20LV (blue curve) and the 80/20 epoxy/strontium titanate nanocomposite with 2.5 wt.% of cobalt-plated multi-walled carbon nanotubes (orange curve).

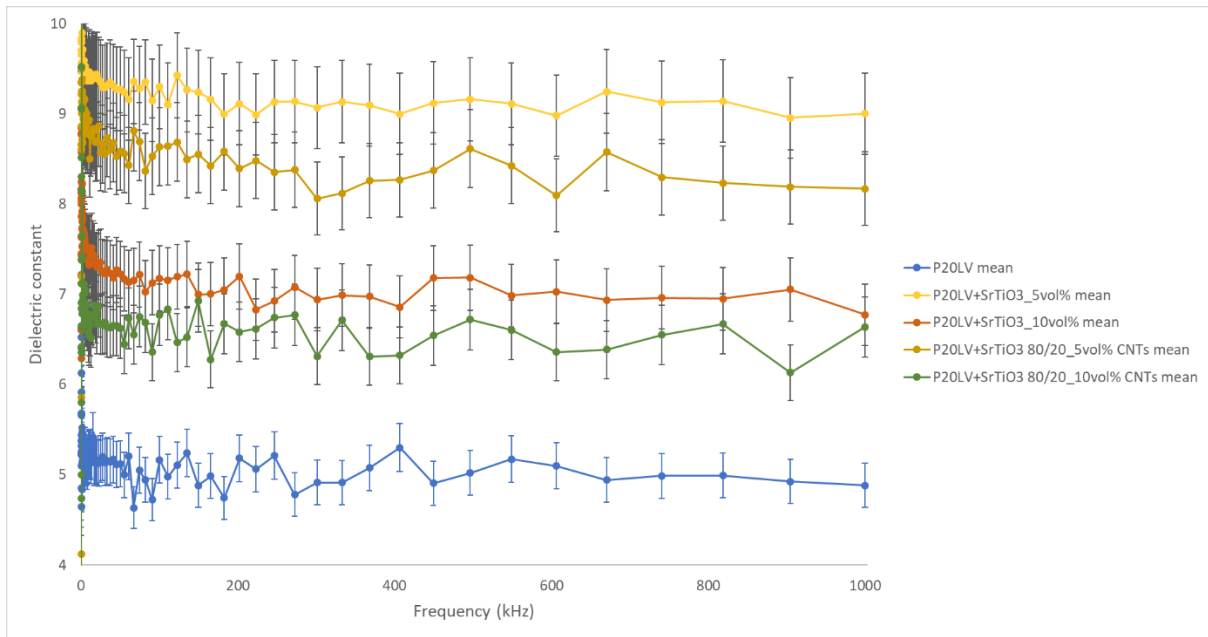


Fig. 7.7. Dielectric test measurements with epoxy PRIME 20LV/strontium titanate ratio of 80:20 and Co-CNT content of 2.5 wt.% and 5 wt.% (approximately 5 vol.% and 10 vol.%, respectively), and with strontium titanate within epoxy resin at 5 vol.% and 10 vol.%.

The behaviour of the hybrid nanocomposite (orange curve) shows a shift towards higher heat flows up to 120°C. The initial noise of the curves can be associated to sample movement within the pan due to sudden temperature changes. Moreover, a step can be observed in the case of the hybrid nanocomposite at temperatures around 45°C. The investigation of the reversing heat flow as a function of the temperature is required for a more in-depth analysis of the thermal phenomenon. This behaviour is shown in [Fig. 7.10](#).

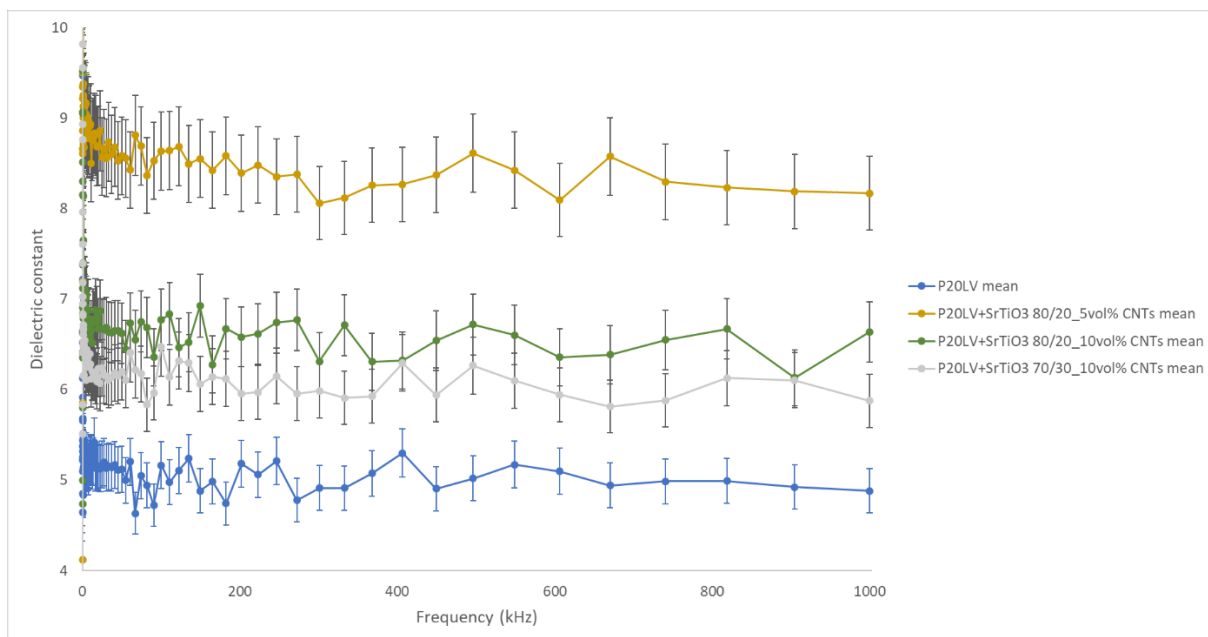


Fig. 7.8. Dielectric constant as a function of frequency (kHz) for neat epoxy resin PRIME 20LV and hybrid nanocomposites characterised by the presence of Co-plated multi-walled carbon nanotubes.

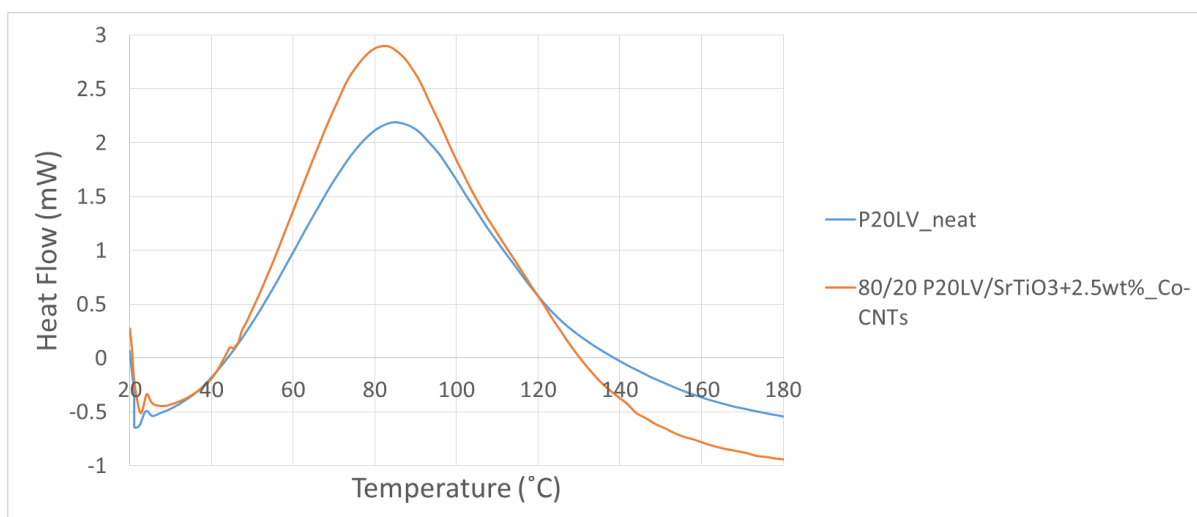


Fig. 7.9. Modulated DSC results: heat flow (mW) as a function of temperature (°C) for neat epoxy PRIME 20LV (blue curve) and the 80/20 epoxy/strontium titanate with 2.5 wt.% of cobalt-plated multi-walled carbon nanotubes.

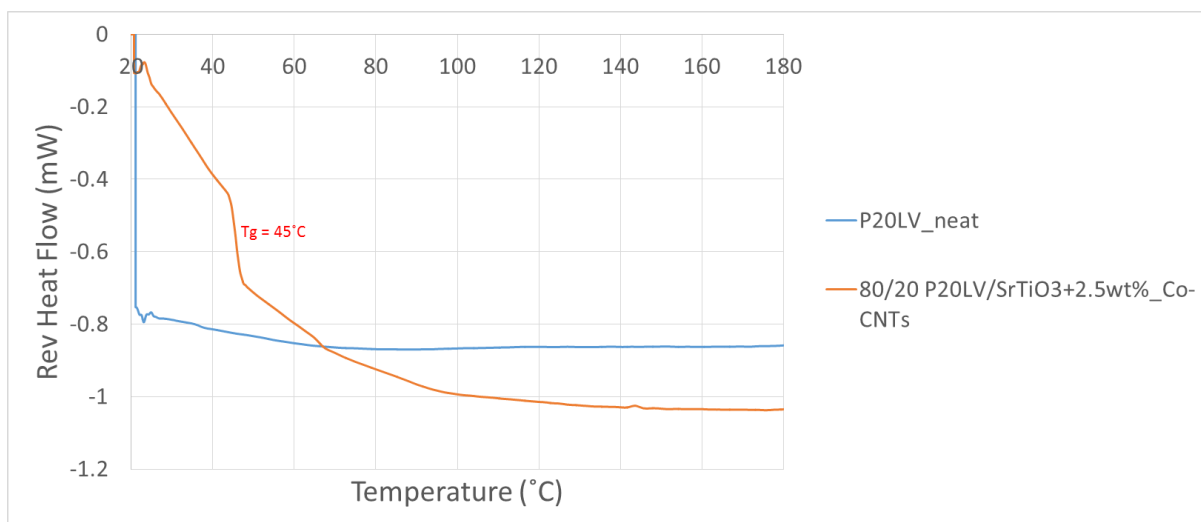


Fig. 7.10. Modulated DSC results: reversing heat flow (mW) as a function of temperature (°C) for neat epoxy PRIME 20LV (blue curve) and the 80/20 epoxy/strontium titanate with 2.5 wt.% of cobalt-plated multi-walled carbon nanotubes.

In this case, the hybrid nanocomposite shows a thermal event at around 45°C which can be related to a shift in glass transition towards lower temperatures. More precisely, the glass transition temperature shifts from the expected 70°C of the neat epoxy resin to 45°C of the hybrid nanocomposite. This clearly confirms the effect of the presence of strontium titanate and cobalt-plated nanotubes within the epoxy medium. The decrease in glass transition temperature might be associated with the fact that the strontium titanate particles and the nanotubes interfere with the radius of gyration of the polymer chains. By increasing the free volume, they also act as plasticisers. In particular, the nanoparticles and the ceramic particles might hinder the crosslinking extent in the hybrid system.

The thermal phenomenon observed at around 45°C can also be identified in the graph showing the non-reversing heat flow as a function of the temperature (orange curve in Fig. 7.11).

Similar thermal transition at 45°C is shown in the graph of Fig. 7.12 investigating the specific heat capacity (mJ/°C) as a function of the temperature (°C).

After the initial signal noise due to sample movement within the pan, the hybrid system (blue curve) shows a step at around 45°C. This specific heat change can be assumed as an indication of the thermal phenomenon already observed during the heat flow investigation. The step is then followed by a drastic reduction in specific heat capacity, associated with the gelation and crosslinking process.

Fig. 7.13 shows the reversing specific heat capacity as a function of the temperature. Likewise, the hybrid nanocomposite, following the trend of the blue curve, shows a significant transition at 45°C related to the thermal phenomenon causing the shift in glass transition temperature.

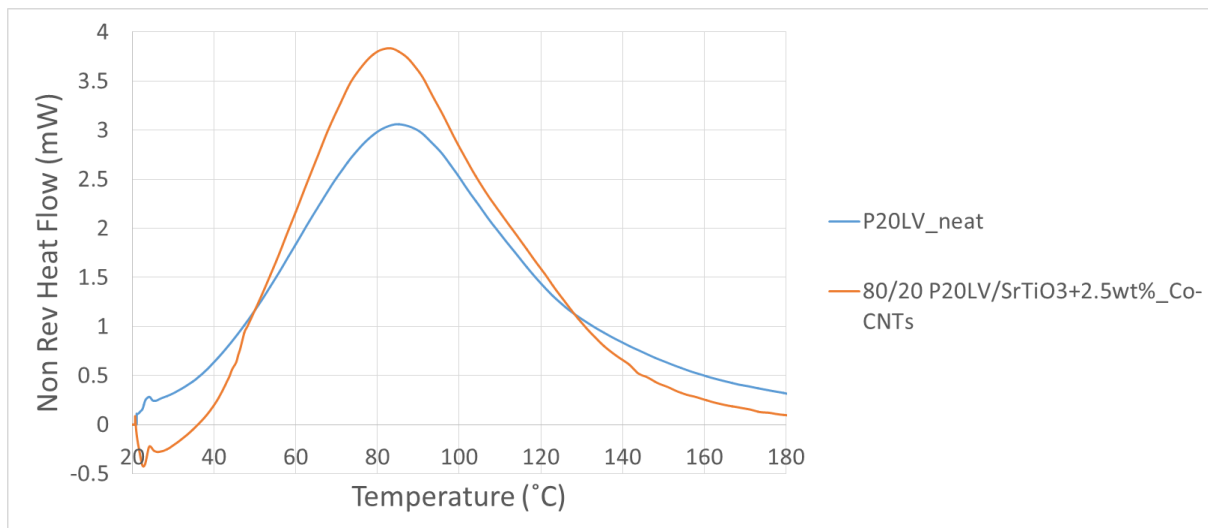


Fig. 7.11. Modulated DSC results: non-reversing heat flow (mW) as a function of temperature (°C) for neat epoxy PRIME 20LV (blue curve) and the 80/20 epoxy/strontium titanate with 2.5 wt.% of cobalt-plated multi-walled carbon nanotubes.

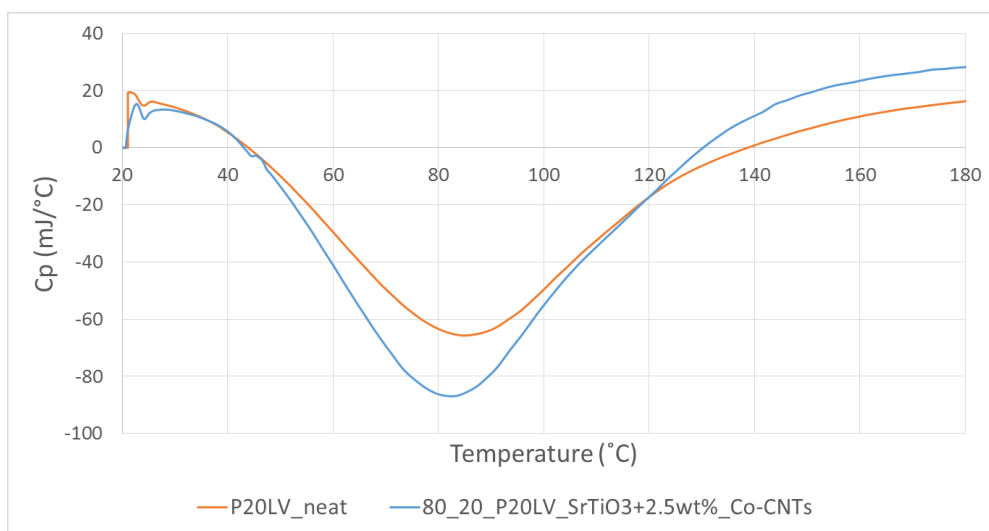


Fig. 7.12. Modulated DSC results: specific heat capacity (mJ/°C) as a function of temperature (°C) for neat epoxy PRIME 20LV (blue curve) and the 80/20 epoxy/strontium titanate with 2.5 wt.% of cobalt-plated multi-walled carbon nanotubes.

The thermal transition can be also observed at the same temperature in the graph of Fig. 7.14, showing the non-reversing heat capacity as a function of the temperature. The neat epoxy resin curves were used as a baseline for the cure kinetics tests, not showing relevant changes both in terms of heat flow and in specific heat capacity.

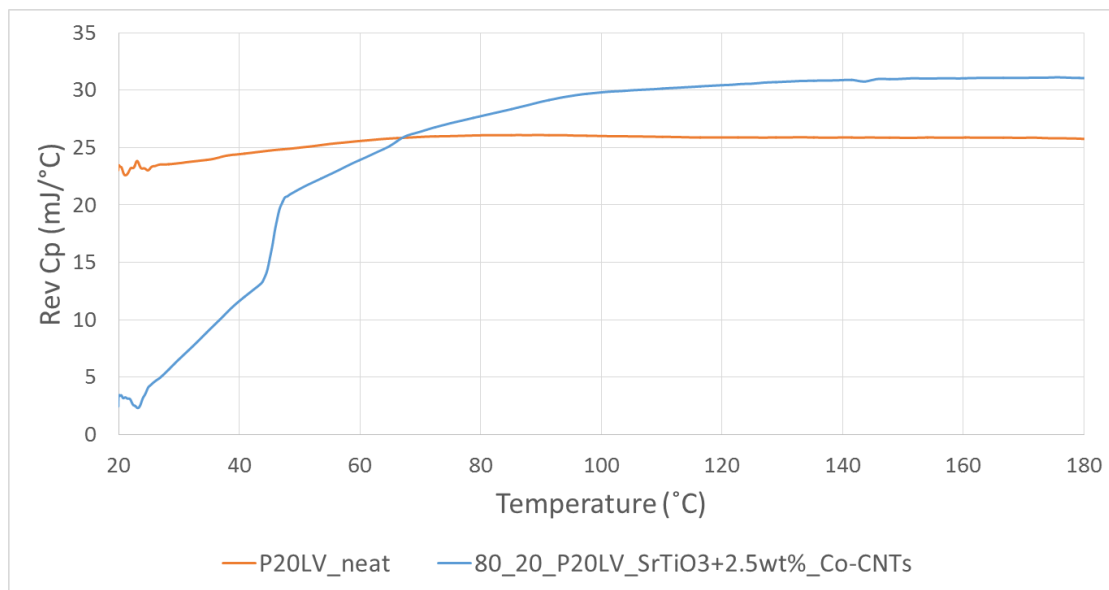


Fig. 7.13. Modulated DSC results: reversing specific heat capacity ($\text{mJ}/^{\circ}\text{C}$) as a function of temperature ($^{\circ}\text{C}$) for neat epoxy PRIME 20LV (blue curve) and the 80/20 epoxy/strontium titanate with 2.5 wt.% of cobalt-plated multi-walled carbon nanotubes.

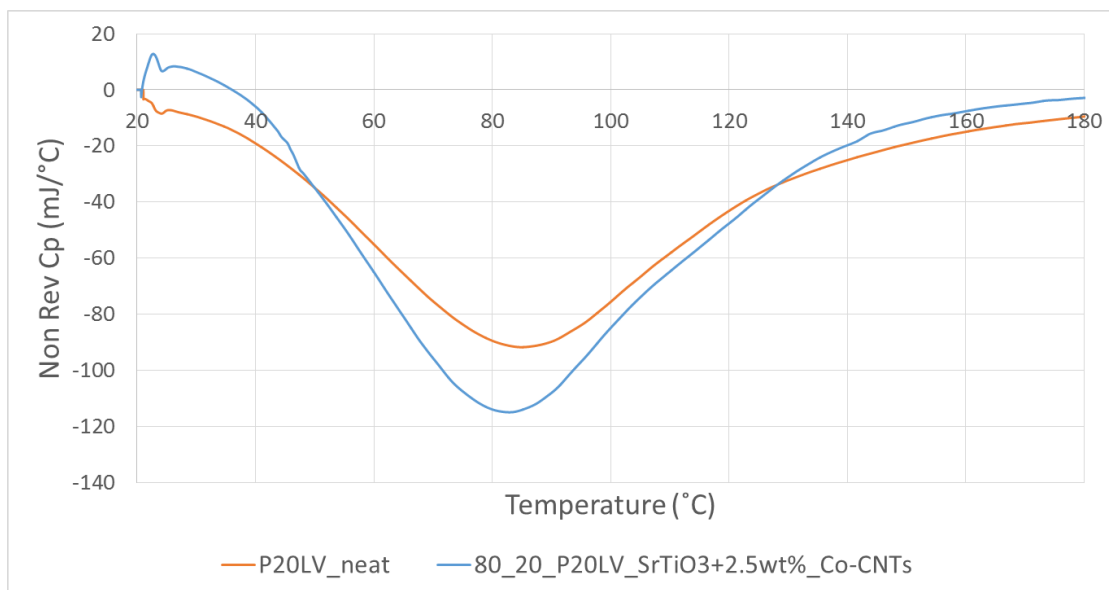


Fig. 7.14. Modulated DSC results: non-reversing specific heat capacity ($\text{mJ}/^{\circ}\text{C}$) as a function of temperature ($^{\circ}\text{C}$) for neat epoxy PRIME 20LV (blue curve) and the 80/20 epoxy/strontium titanate with 2.5 wt.% of cobalt-plated multi-walled carbon nanotubes.

7.6 Conclusions

Tests were carried out on the neat epoxy resin PRIME 20LV to evaluate the dielectric properties under the application of an AC field ranging from 50 Hz to 1 MHz. The dielectric constant for the epoxy resin PRIME 20LV reaches values around 5, which was used as baseline for the subsequent tests. The introduction of high dielectric constant ceramics was also studied. Volume fractions of 5 vol.% and 10 vol.% of strontium titanate were chosen. Specifically, the introduction of strontium titanate within PRIME 20LV caused a dielectric constant increase up to 7.5 and 9 for 5 vol.% of SrTiO_3 and 10 vol.% of SrTiO_3 , respectively. On the other hand, the introduction of another ceramic, barium titanate BaTiO_3 , inhibited the dielectric constant both with 5 vol.% and 10 vol.%. Strontium titanate was introduced as an additive within the epoxy resin system in 80:20 and 70:30 epoxy:strontium titanate proportions but equal loadings of cobalt-plated carbon nanotubes, equal to 5 wt.%.

It was found that the resin:ceramic filler proportion also plays an important role in the dielectric properties. Initially, epoxy resin combined with strontium titanate in 80:20 ratio and blended with 0.7 wt.% of cobalt-plated nanotubes was manufactured and tested under the same frequency range used previously. The dielectric constant reached values, which approached 6 compared to the plateau value of 5 obtained from the neat resin sample. The weight fraction of cobalt-plated nanotubes was therefore increased to 2.5 wt.%. In this case, the synergistic effect of dielectric properties due to the strontium titanate and the increasing electric efficiency due to the potential generation of a conductive network between the cobalt-plated nanotubes still plays an important role. Dielectric constant values of 9 can be reached in this case.

Thermal behaviour of the hybrid nanocomposite was also assessed, showing a shift towards higher heat flows up to 120°C. The hybrid nanocomposite shows a shift in glass transition temperature from the expected 70°C of the neat epoxy resin to 45°C of the hybrid nanocomposite. The decrease in glass transition temperature might be associated with the fact that the strontium titanate particles and the nanotubes interfere with the radius of gyration of the polymer chains. By increasing the free volume, they also act as plasticisers, hindering the crosslinking extent in the hybrid system. Therefore, the introduction of ceramic materials within the epoxy/CNT blend could be beneficial for the dielectric properties of the blend, leading to higher heat dissipation at high frequencies (MHz range), which could be used to optimise the temperature profile in repair applications and reduce the glass transition temperature of the nanocomposite. As discussed in the introduction to this chapter, the combination of dielectric heating from the resin modified via the introduction of dielectric

particles and the heating generated from the magnetically sensitive nano-additives *via* eddy currents, could be exploited. The synergetic effect of dielectric heating and eddy currents could enhance the overall heat dissipation of the nanocomposite and therefore aid the cure process.

8. Conclusions

Initial evaluation of the literature work was carried out to provide a strong background to the project study. Relevant work had been carried out in literature on the nanofiller alignment within viscous mediums via magnetic and electric fields, and ultrasonics. Overall mechanical, electrical and thermal properties could be improved through the creation of effective nanotube networks within the host mediums. The mechanisms involved in the process were discussed and the magnetic parameters for the generation of the alternating field required to trigger eddy currents and hysteresis losses were considered. Literature work on dielectric heating from the host matrix was also considered. The introduction of ceramic fillers within a polymer matrix could potentially increase the dielectric properties (*i.e.* dielectric constant), which is aimed in the presented project. Temperature, frequency and ceramic filler content effect on the dielectric properties were assessed as dielectric heating could be beneficial for assisting thermoset resin cure. However, the electrical conductivity enhancement through the thickness of the composite part by means of metal-plated nanotubes was not accounted for. This project mainly focused on assessing several methods to introduce and position nanotubes such as magnetic positioning and liquid resin printing. This approach has not previously been tried in repair. The potential of spatially positioning the CNTs in an accurate fashion was a focal point of this project. The method is also compatible with other methods of aligning the positioning of the CNTs such as application of static magnetic field. Local CNT positioning, and therefore potential tailoring of the heat distribution map through material high precision distribution of conductive networks, were the advantages discovered with the mentioned technique.

Initially, the feasibility of the magnetic alignment of commercially available and metal functionalised nanotubes was assessed both analytically and experimentally. An analytical model was used to evaluate the magnetic positioning of commercially available nanotubes within viscous mediums. Specifically, the minimum magnetic field required to position the nanotube at an angle spread of 20° before the cure of the viscous medium, was estimated equal to 0.5 T. This value was used as reference magnetic flux density for the experimental tests on nanotube positioning within epoxy resin and fabric. Magnetic manipulation of metal functionalised nanotubes within epoxy resin was proven *via* Computed Tomography by obtaining a magnetically induced square nanotube pattern whose geometry was due to the magnetic pole geometry (magnetic flux density edge effect studied through FEMM numerical model). Magnetic positioning of metal plated nanotubes could therefore locally place and

affect the thermal and mechanical properties of a composite part, particularly for a more efficient repair process.

Chapter 3 explored the functionalisation of CNTs and matrices. It also assessed the influence of functionalization on chemorheological and magnetic properties of a commercially available resin commonly used for composite liquid moulding. Chemical deposition was preferred over physical deposition due to the stronger adhesion obtainable for the metal coating onto the nanotube sides and walls, whereas physical functionalisation relies on physical interactions between nanotubes.

An electroless plating technique was used to deposit homogeneous, chemically-stable, metal functionalised coatings (*e.g.* nickel, cobalt, and nickel-iron) on the sides and ends of the MWCNTs. The functionalisation procedure with cobalt nanoparticles turned out to be more time consuming but potentially more efficient in terms of bond strength. TEM analyses showed that the distribution of Ni coating for commercially bought multi-walled carbon nanotubes was less uniform along the length of the CNTs if compared to the Ni coating obtained experimentally at the University of Bristol.

The metal-functionalised MWCNTs were introduced into the epoxy at different volume fractions (2.5 wt.%, 5 wt.%, 10 wt.% and 20 wt.%) within host epoxy resin PRIME™ 20LV to understand the effect of the metal-functionalised nanotube introduction on the rheological and thermal properties of the resin.

Rheological measurements on the metal-plated CNT-filled resin systems showed that the introduction of MWCNTs in the epoxy resin causes a pronounced increase in viscosity compared to neat resin. Moreover, the variation in viscosity in the range of 5-10% weight fraction of CNT and different types of CNT appears much smaller than the drop in viscosity due to shear thinning at the rates of 0.1-50 1/s.

MDSC analyses conducted on resin with Ni-plated nanotubes showed that said nanotubes can assist and facilitate the cross-linking process by decreasing the onset temperature for exothermic peak and causing an increase in exothermic peak intensity.

Magnetic characterisation through vibrating sample magnetometer (VSM) showed that Co-plated nanotubes obtained using a sonicated bath have a higher magnetic moment (around 160 $\mu\text{A}\cdot\text{m}^2$), particularly useful for nanotube magnetic manipulation within fabric preforms, potentially beneficial for application in induction heating processing of composites.

The potential of manipulating and positioning nanotubes within fabric was investigated by an unprecedented combination of liquid resin printing and magnetic positioning. The novelty of

the presented approach lies in the characterisation of the magnetically treated samples through SEM as means to detect the cobalt-plated nanotube migration away from the injection site. Magnetic field exposition was proven to affect the nanotube distribution at locations away from the injection site, with nanotube concentration increments of over 1% towards the edge of the magnetic patch. Magnetic positioning could therefore help achieve higher CNT fractions where needed. The electrical conductivity could also benefit from the nanotube magnetic positioning. The higher cobalt presence observed with the SEM study was also verified by FT-IR spectroscopy, as the furthest location from the injection point (called 'C', where the magnetic flux density showed the highest value) in the field case was characterised by a further level of cure. This effect can be linked to a higher concentration of cobalt-plated nanotubes at the outer sample locations (highest magnetic field location). Cure mechanisms could also be affected by the cobalt-plated nanotube migration, showed by glass transition temperature increases at increasing CNT contents. An extended time exposition to the magnetic field also caused an increase in glass transition temperature at locations away from the injection site, validating the higher nanotube magnetic migration and filtration in fabric performs. Potential for tailoring the mechanical properties and thermal properties of the composite perform was therefore showed.

Effective nanotube network generation at the bondline could result from the localised nanotube positioning. Ultimately, induction heating mechanisms could benefit from the magnetic positioning of the nanotubes, as detailed in Chapter 6.

The modelling study of the induction heating phenomena within a LNR (laminate with non-conductive reinforcement) and LCR (laminate with conductive reinforcement) was considered. Specifically, the magnetic patch area in the middle of the laminate was partitioned into different conductivity zones in plane and through the thickness of the laminate and assessed numerically. The heat dissipation did not change significantly when the conductivity was increased from bottom ply to top ply or vice versa. Higher values of heat dissipation were observed for the LCR case. The use of an average in-plane conductivity across the patch area caused higher heat dissipation values both for LNR and LCR. This effect could be fruitfully used for the inductive heat generation in composite repair. Further work is required to modify either the patch within the laminate or the coil geometrical properties to maximise the current density while amplifying the electric current and, ultimately, achieve the resin cure temperature through induction heating.

Dielectric tests were carried out on the neat epoxy resin PRIME 20LV to evaluate the dielectric properties under the application of an AC field with frequency from 50 Hz to 1

MHz. The dielectric constant for the epoxy resin PRIME 20LV was around 5. High dielectric constant ceramics were then introduced in the epoxy resin (5 vol.% and 10 vol.% of strontium titanate). This caused a dielectric constant increase up to 7.5 and 9 for 5 vol.% of SrTiO_3 and 10 vol.% of SrTiO_3 , respectively. Barium titanate BaTiO_3 , inhibited the dielectric constant both with 5 vol.% and 10 vol.%. Strontium titanate was embedded within the epoxy resin system in 80:20 and 70:30 epoxy:strontium titanate proportions with also equal loadings of cobalt-plated carbon nanotubes, equal to 5wt.%. The resin:ceramic filler proportion also plays an important role in the dielectric constant. Initially, epoxy resin combined with strontium titanate in 80:20 ratio and blended with 0.7 wt.% of cobalt-plated nanotubes reached values of dielectric constant around 6 compared to the plateau value of 5 obtained from the neat resin sample. Higher nanotube weight fraction (2.5 wt.%) was then used, and the synergistic effect due to the strontium titanate and the conductive network between the cobalt-plated nanotubes increased the dielectric constant up to 9.

Thermal behaviour of the hybrid nanocomposite was also assessed through DSC, showing higher heat flows up to 120°C and a decrease in glass transition temperature from the expected 70°C of the neat resin to 45°C. The decrease in glass transition temperature might be due to the plasticizing properties of strontium titanate particles and nanotubes, which increase the free volume and interfere with the polymer crosslinking.

The introduction of ceramic materials within the epoxy/CNT blend could then lead to higher heat dissipation at high frequencies (MHz range) and reduce the glass transition temperature of the nanocomposite for an easier cure processes. Furthermore, the combination of dielectric heating from the resin modified with dielectric particles and the heating generated from the magnetically sensitive nano-additives *via* eddy currents, could be used to enhance the overall heat dissipation of the nanocomposite and therefore aid the cure process. Benefits to the repair of composite parts through the suggested methodologies are evident such as more controlled cure and, therefore, more homogenous mechanical properties of the final component.

9. References

- [1] Ariu, G., Hamerton, I., Ivanov, D.S. (2017) Positioning and aligning CNTs by external magnetic field to assist localised epoxy cure. *Open Physics*. 14(1): 508-516.
- [2] Tsamasphyros, G.J., Kanderakis, G.N., Karalekas, D., Rapti, D., Gdoutos, E.E., Zacharopoulos, D., Marioli-Riga, Z.P. (2001) Study of composite patch repair by analytical and numerical methods. *Int. J. Fat. Fract. Eng. Mat. Struct.* 24: 631-636.
- [3] Composites World, (2005). *The craft of aircraft repair*. [online] Available at: <https://www.compositesworld.com/articles/the-craft-of-aircraft-repair> [18-11-2018].
- [4] Yan, X., Gu, J., Zheng, G., Guo, J., Galaska, A.M., Yu, J., Khan, M.A., Sun, L., Young, D.P., Zhang, Q., Wei, S., Guo, Z. (2016) Lowly loaded carbon nanotubes induced high electrical conductivity and giant magnetoresistance in ethylene/1-octenecopolymers. *Polymer*. 103: 315-327.
- [5] Wu, K., Xue, Y., Yang, W., Chai, S., Chen, F., Fu, Q. (2016) Largely enhanced thermal and electrical conductivity via constructing double percolated filler network in polypropylene/expanded graphite - Multi-wall carbon nanotubes ternary composites. *Composites Science and Technology*. 130: 28-35.
- [6] Lian, G., Tuan, C-C., Li, L., Jiao, S., Wang, Q., Moon, K-S., Cui, D., Wong, C-P. (2016) Vertically Aligned and Interconnected Graphene Networks for High Thermal Conductivity of Epoxy Composites with Ultralow Loading. *Chemistry of Materials*. 28: 6096-6104.
- [7] Kimura, T., Ago, H., Tobita, M., Ohshima, S., Kyotani, M., Yumura, M. (2002) Polymer Composites of Carbon Nanotubes Aligned by a Magnetic Field. *Advanced Materials*. 14(19): 1380-1383.
- [8] Erb, R.M., Libanori, R., Rothfuchs, N., Studart, A.R. (2012) Composites reinforced in three dimensions by using low magnetic fields. *Science*. 335(13): 199-204.
- [9] Choi, E.S., Brooks, J.S., Eaton, D.L. (2003) Enhancement of thermal and electrical properties of carbon nanotube polymer composites by magnetic field processing. *Journal of Applied Physics*. 94(9): 6034-6039.
- [10] Goc, K., Gaska, K., Klimczyk, K., Wujek, A., Prendota, W., Jarosinski, L., Rybak, A., Kmita, G., Kapusta, Cz. (2016) Influence of magnetic field-aided filler orientation on structure and transport properties of ferrite filled composites. *Journal of Magnetism and Magnetic Materials*. 419: 345–353.
- [11] Le Ferrand, H., Bolisetty, S., Demirörs, A.F., Libanori, R., Studart, A.R., Mezzenga, R. (2016) Magnetic assembly of transparent and conducting graphene-based functional composites. *Nature Communications*. 7: 1-9.

- [12] Mas, B., Fernández-Blázquez, J.P., Duval, J., Bunyan, H., Vilatela, J.J. (2013) Thermoset curing through Joule heating of nanocarbons for composite manufacture, repair and soldering. *Carbon*. 63: 523–529.
- [13] Bayerl, T., Duhovic, M., Mitschang, P., Bhattacharyya, D. (2014) The heating of polymer composites by electromagnetic induction - A review. *Composites Part A: Applied Science and Manufacturing*. 57: 27–40.
- [14] El-Tantawy, F., Kamada, K., Ohnabe, H. (2003) A novel way of enhancing the electrical and thermal stability of conductive epoxy resin–carbon black composites via the Joule heating effect for heating element applications. *Journal of Applied Polymer Science*. 87: 97-109.
- [15] Fink, B.K. McCullough, R.L., Gillespie Jr., J.W. (1992) A Local Theory of Heating in Cross-Ply Carbon Fiber Thermoplastic Composites by Magnetic Induction. *Polymer Engineering & Science*. 32: 357–369.
- [16] Yarlagadda, S., Kim, H.J., Gillespie Jr., J.W., Shevchenko, N.B., Fink, B.K. (2002) A study on the induction heating of conductive fiber reinforced composites. *Advanced Composite Materials*. 11(1): 71-80.
- [17] Abliz, D., Duan, Y., Steuernagel, L., Xie, L., Li, D., Ziegmann, G. (2013) Curing Methods for Advanced Polymer Composites-A Review. *Polymers & Polymer Composites*. 21(6): 341-348.
- [18] Kim, M., Kim, H., Lee, W. (2014) Repair of aircraft structures using composite patches bonded through induction heating. *Advanced Composite Materials*. 24(4): 307-323.
- [19] Mahdi, S., Gama, B.A., Yarlagadda, S., Gillespie Jr., J.W. (2003) A Comparison of Oven-cured and Induction-cured Adhesively Bonded Composite Joints. *Journal of Composite Materials* .37(6): 519-541.
- [20] Li, Q., Fan, S., Han, W., Sun, C., Liang, W. (1997) Coating of Carbon Nanotube with Nickel by Electroless Plating Method. *Japanese Journal of Applied Physics*.36(2): 501-503.
- [21] Herd, C.R., McDonald, G.C., Hees, W.M. (1992) Morphology of Carbon-Black Aggregates: Fractal Versus Euclidean Geometry. *Rubber Chemistry and Technology*. 65 (1): 107-129.
- [22] Oxfall H., Ariu, G., Gkourmpis, T., Rychwalski, R.W., Rigdahl, M. (2015) Effect of carbon black on electrical and rheological properties of graphite nanoplatelets/poly(ethylene-butyl acrylate) composites. *eXPRESS Polymer Letters*. 9(1): 66-76.

- [23] Berkowitz, B., and R. P. Ewing (1998) Percolation theory and network modeling applications in soil physics. *Surveys in Geophysics*. 19(1): 23-72
- [24] Li, J., Ma, P.C., Chow, W.S., To, C.K., Tang, B.Z., Kim, J-K. (2007) Correlations between Percolation Threshold, Dispersion State, and Aspect Ratio of Carbon Nanotubes. *Advanced Functional Materials*. 17(16) : 3207–3215.
- [25] Moisala, A., Nasibulin, A.G., Shandakov, S.D., Jiang, H., Kauppinen, E.I. (2005) On-line detection of single-walled carbon nanotube formation during aerosol synthesis methods. *Carbon*. 43(10): 2066–2074.
- [26] Yan, Q. and Wu, D. (2010) Low Percolation Threshold and High Conductivity in Carbon Black Filled Polyethylene and Polypropylene Composites. *Journal of Applied Polymer Science*. 115(6): 3527–3534.
- [27] Biercuk, M.J., Llaguno, M.C., Radosavljevic, M., Hyun, J.K., Johnson, A.T. (2002) Carbon nanotube composites for thermal management. *Appl. Phys. Lett.* 80 (15) : 2767–2769.
- [28] Banerjee, S., Hemraj-Benny, T., Wong, S.S. (2003) Covalent Surface Chemistry of Single Walled Carbon Nanotubes. *Chem. Eur. J.* 9: 1898-1908.
- [29] Chen, J., Dyer, M.J., Yu, M-F. (2001) Cyclodextrin-Mediated Soft Cutting of Single-Walled Carbon Nanotubes. *Am. Chem. Soc.* 123(5): 6201-6202.
- [30] Islam, M.F., Rojas, E., Bergey, D.M., Johnson, A.T., Yodh, A.G. (2003) High Weight Fraction Surfactant Solubilization of Single-Wall Carbon Nanotubes in Water. *Nano Lett.* 3(2): 269-273.
- [31] Matarredona, O., Rhoads, H., Li, Z., Harwell, J.H., Balzano, L., Resasco, D.E. (2003) Dispersion of Single-Walled Carbon Nanotubes in Aqueous Solutions of the Anionic Surfactant NaDDBS. *J. Phys. Chem. B.* 107(48): 13357-13367.
- [32] Bottini, M., Bruckner, S., Nika, K., Bottini, N., Bellucci, S., Magrini, A., Bergamaschi, A., Mustelin, T. (2006) Multi-walled carbon nanotubes induce T lymphocyte apoptosis. *Toxi. Lett.*, 160(2): 121-126.
- [33] Bottini, M., Tautz, L., Huynh, H., Monosov, E., Bottini, N., Dawson, M.I., Bellucci, S., Mustelin, T. (2005) Covalent decoration of multi-walled carbon nanotubes with silica nanoparticles. *Chem. Commun.* 6: 758.
- [34] Bottini, M., Balasubramanian, C., Dawson, M.I., Bergamaschi, A., Bellucci, S., Mustelin, T. (2006) Isolation and characterization of fluorescent nanoparticles from pristine and oxidized electric arc-produced single-walled carbon nanotubes. *J. Phys. Chem. B.* 110 (2): 831-836.

- [35] Bottini, M., Magrini, A., Di Venere, A., Bellucci, S., Dawson, M.I., Rosato, N., Bergamaschi, A., Mustelin, T. (2006) Synthesis and characterization of supramolecular nanostructures of carbon nanotubes and ruthenium-complex luminophores. *J Nanosci Nanotechnol.* 6: 1381–1386.
- [36] Gojny, F.H., Wichmann, M.H.G., Köpke, U., Fiedler, B., Schulte, K. (2004) Carbon nanotube-reinforced epoxy-composites: enhanced stiffness and fracture toughness at low nanotube content. *Compos. Sci. Technol.* 24 (2004), 2363–2371.
- [37] Thostenson, E.T. and Chou, T.W. (2006) Processing-structure-multi-functional property relationship in carbon nanotube/epoxy composites. *Carbon.* 44 (14): 3022–3029.
- [38] Lu, K.L., Lago, R.M., Chen, Y.K., Green, M.L.H., Harris, P.J.F., Tsang, S.C. (1996) Mechanical damage of carbon nanotubes by ultrasound. *Carbon*, 34: 814–816.
- [39] Mukhopadhyay, K., Dwivedi, C.D., Mathur, G.N. (2002) Conversion of carbon nanotubes to carbon nanofibers by sonication. *Carbon*, 40: 1373–1376.
- [40] Ma, P.C., Tang, B.Z., Kim, J-K (2008) Conversion of semiconducting behavior of carbon nanotubes using ball milling. *Chem. Phys. Lett.* 458: 166–169.
- [41] Sandler, J.K.W., Shaffer, M.S.P., Prasse, T., Bauhofer, W., Schulte, K., Windle, A.H. (1999) Development of a dispersion process for carbon nanotubes in an epoxy matrix and the resulting electrical properties. *Polymer.* 40: 5967–5971.
- [42] Schmid, C.F. and Klingenberg, D.J. (2000) Mechanical Flocculation in Flowing Fiber Suspensions. *Phys. Rev. Lett.* 84(2): 290–293.
- [43] Villmow, T., Pötschke, P., Pegel, S., Häussler, L., Kretzschmar, B., (2008) Influence of twin-screw extrusion conditions on the dispersion of multi-walled carbon nanotubes in a poly(lactic acid) matrix. *Polymer.* 49(16): 3500–3509.
- [44] Oliva H.N.P. and Avila A.F. (2017) Bonded Joints with “Nano-Stitches”: Effect of Carbon Nanotubes on Load Capacity and Failure Modes. *Lat. Am. j. solids struct.* 14(4): 674-684.
- [45] Fan, Z.H., Hsiao, K-T., Advani, S.G. (2004) Experimental investigation of dispersion during flow of multi-walled carbon nanotube/polymer suspension in fibrous porous media. *Carbon.* 42(4): 871–876.
- [46] Gojny, F.H., Wichmann, M.H.G., Fiedler, B., Bauhofer, W., Schulte, K. (2005) Influence of nano-modification on the mechanical and electrical properties of conventional fibre-reinforced composites. *Compos Part A: Appl Sci Manuf.* 36(11): 1525–1535.
- [47] Sadeghian, R., Gangireddy, S., Minaie, B., Hsiao, K-T. (2006) Manufacturing carbon nanofibers toughened polyester/glass fiber composites using vacuum assisted resin transfer

- molding for enhancing the mode-I delamination resistance. *Compos Part A: Appl Sci Manuf.* 37(10): 1787–95.
- [48] Qian, H., Bismarck, A., Greenhalgh, E.S., Shaffer, M.S.P. (2010) Carbon nanotube grafted carbon fibres: a study of wetting and fibre fragmentation. *Composites: Part A.* 41: 1107–1114.
- [49] Ivanov, D.S., Le Cahain, Y.M., Arafati, S., Dattin, A., Ivanov, S.G., Aniskevich, A. (2016) Novel method for functionalising and patterning textile composites: Liquid resin print. *Composites Part A.* 84: 175-185.
- [50] Ivanov, D.S., White, J.A.P., Hendry, W., Mahadik, Y., Minett, V., Patel, H., Ward, C. (2014) Stabilizing textile preforms by means of liquid resin print: a feasibility study. *Advanced Manufacturing: Polymer & Composites Science.* 1(1): 26-35.
- [51] Lomov, S.V., Wicks, S., Gorbatikh, L., Verpoest, I., Wardle, B. (2014) Compressibility of nanofibre-grafted alumina fabric and yarns: Aligned carbon nanotube forests. *Composites Science and Technology.* 90: 57–66.
- [52] Feng, L., Li, K-Z., Lu, J-H., Qi, L-H. (2017) Effect of Growth Temperature on Carbon Nanotube Grafting Morphology and Mechanical Behavior of Carbon Fibers and Carbon/Carbon Composites. *Journal of Materials Science & Technology.* 33(1): 65-70.
- [53] Chrissanthopoulos, A., Baskoutas, S., Bouropoulos, N., Dracopoulos, V., Tasis, D., Yannopoulos, S.N. (2007) Novel ZnO nanostructures grown on carbon nanotubes by thermal evaporation. *Thin Solid Films.* 515: 8524–8528.
- [54] Grzelczak, M., Correa-Duarte, M.A., Salgueiriño-Maceira, V., Rodríguez-González, B., Rivas, J., Liz-Marzán, L.M. (2007) Pt-Catalyzed Formation of Ni Nanoshells on Carbon Nanotubes. *Angewandte Chemie International Edition.* 46: 7156-7160.
- [55] Sun, Y.-P., Fu, K., Lin, Y., Huang, W. (2002) Functionalized Carbon Nanotubes: Properties and Applications. *Accounts of Chemical Research.* 35: 1096-1104.
- [56] Seidel, G.D., Puydupin-Jamin, A.S. (2008) Analysis of Clustering and Interphase Region Effects on the Electrical Conductivity of Carbon Nanotube-Polymer Nanocomposites via Computational Micromechanics. *ASME Proceedings [Multifunctional Materials]:* 159-165.
- [57] Ang, L-M., Andy Hor, T.S., Xu, G-Q., Tung, C., Zhao, S., Wang, J.L.S. (1999) Electroless Plating of Metals onto Carbon Nanotubes Activated by a Single-Step Activation Method. *Chem. Mater.* 11: 2115-2118.
- [58] Goel, V., Anderson, P., Hall, J., Robinson, F., Bohm, S. (2016) Electroless Plating: A Versatile Technique to Deposit Coatings on Electrical Steel. *IEEE Transactions on Magnetics.* 52(4): 42-45.

- [59] Caturla, F., Molina, F., Molina-Sabio, M., Rodríguez-Reinoso, F., Esteban, A. (1995) Electroless Plating of Graphite with Copper and Nickel. *J. Electrochem. Soc.* 142(12): 4084-4090.
- [60] Kong, F., Zhang, X.B., Xiong, W.Q., Liu, F., Huang, W.Z., Sun, Y.L., Tu, J.P., Chen, Z.W. (2002) Continuous Ni-layer on multiwall carbon nanotubes by an electroless plating method. *Surface and Coatings Technology*. 155: 33–36.
- [61] Hirsch, A. (2002) Functionalization of Single-Walled Carbon Nanotubes. *Angew. Chem. Int. Ed.* 41(11): 1853-1859.
- [62] Kelly, K.F., Chiang, I.W., Mickelson, E.T., Hauge, R.H., Margrave, J.L., Wang, X., Scuseria, G.E., Radloff, C., Halas, N.J. (1999) Insight into the mechanism of sidewall functionalization of single-walled nanotubes: an STM study. *Chem. Phys. Lett.* 313: 445-450.
- [63] Mickelson, E.T., Chiang, I.W., Zimmermann, L., Boul, P.J., Lozano, J., Liu, J., Smalley, R.E., Hauge, R.H., Margrave, J.L. (1999) Solvation of Fluorinated Single-Wall Carbon Nanotubes in Alcohol Solvents. *J. Phys. Chem. B.* 103: 4318-4322.
- [64] Chen, J., Hamon, M.A., Chen, Y., Rao, A.M., Eklund, P.C., Haddon, R.C. (1998) Solution properties of single-walled carbon nanotubes. *Science*. 282: 95-98.
- [65] Holzinger, M., Vostrowsky, O., Hirsch, A., Hennrich, F., Kappes, M., Weiss, R., Jellen, F. (2001) Sidewall Functionalization of Carbon Nanotubes. *Angew. Chem. Angew. Chem.* 40 (21): 4002-4005.
- [66] Georgakilas, V., Kordatos, K., Prato, M., Guldi, D.M., Holzinger, M., Hirsch, A. (2002) Organic Functionalization of Carbon Nanotubes. *J. Am. Chem. Soc.* 124: 760-761.
- [67] Wang, M-W. (2008) ASME 2008 First International Conference on Micro/Nanoscale Heat Transfer, Parts A and B. 1185–1189.
- [68] Prasse, T., Cavaillé, J-Y., Bauhofer, W. (2003) Electric anisotropy of carbon nanofibre/epoxy resin composites due to electric field induced alignment. *Composite Science and Technology*. 63 (13): 1835-1841.
- [69] Lim, W.P., Yao, K., Chen, Y. (2007) Alignment of Carbon Nanotubes by Acoustic Manipulation in a Fluidic Medium. *J. Phys. Chem.* 111(45): 16802-16807.
- [70] Martin, C.A., Sandler, J.K.W., Windle, A.H., Schwarz, M.K., Bauhofer, W., Schulte, K., Shaffer, M.S.P. (2005) Electric field-induced aligned multi-wall carbon nanotube networks in epoxy composites. *Polymer*. 46 (3): 877-886.
- [71] Park, C., Wilkinson, J., Banda, S., Ounaies, Z., Wise, K.E., Godfrey, S., Lillehei, P.T., Harrison, J.S. (2006) Aligned single-wall carbon nanotube polymer composites using an electric field. *Journal of Polymer Science: part B. Polymer physics*. 44(12): 1751-1762.

- [72] Remillard, E.M., Zhang, Q., Sonina, S., Branson, Z., Dasgupta, T., Vecitis, C.D. (2016) Electric-field alignment of aqueous multi-walled carbon nanotubes on microporous substrates. *Carbon*. 100: 578-589.
- [73] Ahmed, T.J., Stavrov, D., Bersee, H.E.N., Beukers, A. (2006) Induction welding of thermoplastic composites—an overview. *Composites Part A: Applied Science and Manufacturing*, 37 (10): 1638-1651.
- [74] Ogden, J.E. (1991) US Patent 07/350,063.
- [75] Holmstrom, G. (1991) US Patent 07/476,738.
- [76] Yousefpour, A., Hojjati, M., Immarigeon, J-P. (2004) Fusion Bonding/Welding of Thermoplastic Composites. *Journal of THERMOPLASTIC COMPOSITE MATERIALS*. 17: 303-341.
- [77] Miller, A.K. (1993) US Patent 07/579,379.
- [78] Guiles, M.A., Ross, H., Anant, S., Rochelle, L. (2000) US Patent 09/090,865.
- [79] Tsamasphyros, G. and Christopoulos, A. On the induction heating of particle reinforced polymer matrix composites. *Recent Advances in Mechanical Engineering and Mechanics*. 65-72.
- [80] Rudolf, R., Mitschang, P., Neitzel, M. (2000) Induction heating of continuous carbon-fibre-reinforced thermoplastics. *Composites: Part A*. 31: 1191–1202.
- [81] Miller, A.K., Chang, C., Payne, A., Gur, M., Menzel, E., Peled, A. (1990) The Nature of Induction Heating in Graphite– fiber, Polymer–matrix Composite Materials. *SAMPE Journal*. 26(4): 37–54.
- [82] Koblinski, P., Cahill, D.G., Bodapati, A., Sullivan, C.R., Taton, T.A. (2006) Limits of localized heating by electromagnetically excited nanoparticles. *Journal of Applied Physics*. 100: 054305.
- [83] Mohr, R., Kratz, K., Weigel, T., Lucka-Gabor, M., Moneke, M., Lendlein, A. (2006) Initiation of shape-memory effect by inductive heating of magnetic nanoparticles in thermoplastic polymers. *PNAS*. 103(10): 3540–3545.
- [84] Menana, H. and Feliachi, M. (2009) 3-D Eddy Current Computation in Carbon-Fiber Reinforced Composites. *IEEE Transactions on Magnetics*. 3(45): 1008-1011.
- [85] Hergt, R., Andra, W., d'Ambly, C.G., Hilger, I., Kaiser, W.A., Richter, U., Schmidt, H.G. (1998) Physical Limits of Hyperthermia Using Magnetite Fine Particles. *IEEE TRANSACTIONS ON MAGNETICS*. 34(5): 3745-3754.
- [86] Wang, L. and Dang, Z-M. (2005) Carbon nanotube composites with high dielectric constant at low percolation threshold. *Appl. Phys. Lett.* 87: 042903.

- [87] Arlt, G., Hennings, D., de With, G. (1985) Dielectric properties of fine-grained barium titanate ceramics. *J. Appl. Phys.* 58(4): 1619-1625.
- [88] Kinoshita, K. and Yamaji, A. (1976) Grain-size effects on dielectric properties in barium titanate ceramics. *Journal of Applied Physics*. 47: 371-373.
- [89] Rao, Y. and Wong, C.P. (2004) Material characterization of a high-dielectric-constant polymer–ceramic composite for embedded capacitor for RF applications. *Journal of Applied Polymer Science*. 92: 2228–2231.
- [90] Rao, Y., Ogitani, S., Kohl, P., Wong, C.P. (2002) Novel polymer–ceramic nanocomposite based on high dielectric constant epoxy formula for embedded capacitor application. *Journal of Applied Polymer Science*. 83(5): 1084–1090.
- [91] Liang, S., Chong, S.R., Giannelis, E.P. (1998) Barium titanate/epoxy composite dielectric materials for integrated thin film capacitors. *Electronic Components and Technology Conference*. 171-175.
- [92] Hadik, N., Outzourhit, A., Elmansouri, A., Abouelaoualim, A., Oueriagli, A., Ameziane, E.L. (2009) Dielectric Behavior of Ceramic (BST)/Epoxy Thick Films. *Active and Passive Electronic Components*. 1-6.
- [93] Ramjo, L. M. R. and Castro M. (2005) Dielectric response and relaxation phenomena in composites of epoxy resin with BaTiO₃ particles. *Composites A*. 36: 1267–1274.
- [94] Psarras, G., Manolakaki, E., Tsangaris, G.M. (2002) Electrical relaxations in polymeric particulate composites of epoxy resin and metal particles. *Composites A*. 33(3): 375–384.
- [95] Cheng, K-C., Lin, C-M., Wang, S-F., Lin, S-T., Yang, C-F. (2007) Dielectric properties of epoxy resin-barium titanate composites at high frequency. *Materials Letters*. 61: 757–760.
- [96] Dang, ZM., Xie, D., Shi, C-Y. (2007) Theoretical prediction and experimental study of dielectric properties in poly(vinylidene fluoride) matrix composites with micron-size BaTiO₃ filler. *Applied Physics Letters*, 91(22): 222902.
- [97] Yarlagadda, S., Kim, H.J., Gillespie Jr., J.W., Shevchenko, N.B., Fink, B.K. (2002) A study on the induction heating of conductive fiber reinforced composites. *Journal of Composite Materials*. 36(4): 401-421.
- [98] Radhakrishnan, A. (2016) Functionalising glass preforms with carbon nanotube filled heterogeneous solution using liquid resin printing (LRP). Preprint submitted to *Composite: Part A. Property of the University of Bristol*.
- [99] Ozawa, T. (2000) Thermal analysis—review and prospect. *Thermochimica Acta*. 355(1-2): 35-42.

- [100] Foner, S. (1996) The vibrating sample magnetometer: Experiences of a volunteer (invited). *Journal of Applied Physics*. 79(8): 4740-4745.
- [101] Kimura, T., Umehara, Y., Kimura, F. (2012) Magnetic field responsive silicone elastomer loaded with short steel wires having orientation distribution. *Soft Matter*. 8(23): 6206.
- [102] Ciambella, J., Stanier, D.C., Rahatekar, S.S. (2017) Magnetic alignment of short carbon fibres in curing composites. *Composites Part B*. 109: 129-137.
- [103] Bay, F., Labbe, V., Favennec, Y., Chenot, J.L. (2003) A numerical model for induction heating processes coupling electromagnetism and thermomechanics. *International Journal for Numerical Methods in Engineering*. 58: 839-867.
- [104] The University of Texas at Austin, (2007). *Maxwell's Equations*. [online] Available at: <http://farside.ph.utexas.edu/teaching/302/lectures/node116.html> [22-08-2018].
- [105] Turna, K. (2018) Towards uniform curing of fiber reinforced composites by grading material properties. *Property of the University of Bristol*. 1-12.
- [106] Rehbein, J., Wierach, P., Gries, T., Wiedemann, M. (2017) Improved electrical conductivity of NCF-reinforced CFRP for higher damage resistance to lightning strike. *Composites: Part A*. 100: 352–360.
- [107] Fiberglass Supply - Carbon Fiber and Composite Supplies for the 21st Century, (2016). *Carbon and Kevlar Fabrics*. [online] Available at: http://www.fiberglasssupply.com/Product_Catalog/Reinforcements/Carbon_and_Kevlar/carbon_and_kevlar.html [18-08-2018].
- [108] Engineering ToolBox, (2003). *Specific Heat of Solids*. [online] Available at: https://www.engineeringtoolbox.com/specific-heat-solids-d_154.html [18-08-2018].
- [109] Wasselynck, G., Trichet, D., Ramdane, B., Fouladgar, J. (2011) Microscopic and Macroscopic Electromagnetic and Thermal Modeling of Carbon Fiber Reinforced Polymer Composites. *IEE Transactions on Magnetics*. 5(47): 1114-1117.
- [110] Engineers Edge (2018). [online] Available at: https://www.engineersedge.com/copper_wire.htm [12-09-2018].
- [111] Abaqus 2016 Documentation (2016). [online] Available at: <http://130.149.89.49:2080/v2016/index.html> [18-08-2018].

APPENDIX A - Induction heating experimental analysis

The effect of an AC magnetic field on the heat dissipation through eddy current generation within a composite laminate (GFRP and CFRP) was investigated. The feasibility of using an external AC magnetic field to aid repair within a perform patch was assessed via an AC magnetic setup, shown in Fig. A.1.

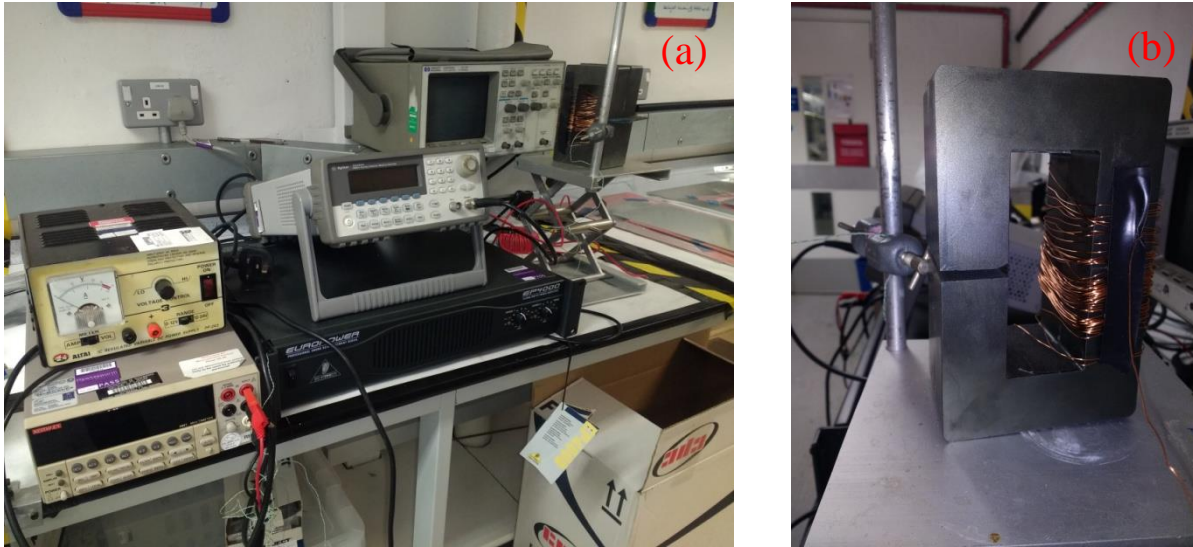


Fig. A.1. AC magnetic setup (a) and detail of the ferrite horseshoe core (b).

The magnetic setup was characterised by a horseshoe core wrapped with 50 turns of copper wire. The copper wire was connected to an AC amplifier, as shown in Fig. A.1. A voltmeter/amperometer was connected to the setup to monitor the voltage and the current intensity during the experiment and therefore retrieve the magnetic flux density.

Samples were located on the bottom side of the magnetic core and connected to a thermocouple to monitor the temperature developments during the application of the AC field.

A.1 Samples

Glass fibre reinforced polymer (GFRP) and carbon fibre reinforced polymer (CFRP) samples were tested with the AC magnetic setup.

A.2 GFRP sample preparation

GFRP laminates were characterised by four plies of woven glass fabric injected with liquid resin printing through the procedure explained in Section 5.2.

Two samples with concentrations of 0.75 wt.% (shown in Fig. A.2 [104]) and 3.75 wt.% of as received carbon nanotubes (CNTs), were manufactured by introducing the blend of CNTs and epoxy resin PRIME 20 LV through liquid resin printing. Multiple injections were carried out through the thickness of the laminate to distribute the epoxy/CNT blend homogeneously from the bottom to the top ply of the samples. After liquid resin printing, the samples were compacted by means of a hot press as detailed in Section 5.6.4.

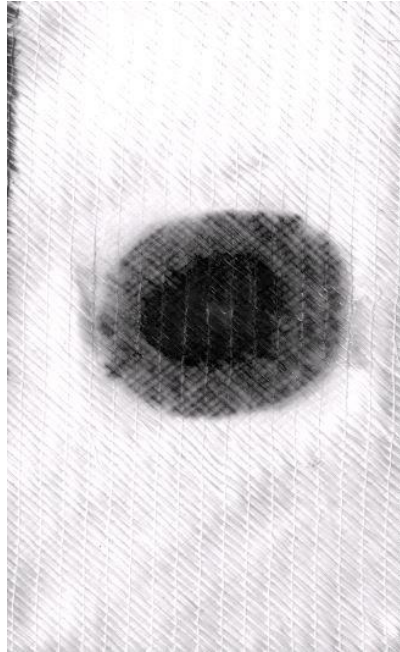


Fig. A.2. GFRP induction heating samples with 0.75 wt.% CNTs [98].

A.3 CFRP sample preparation

CFRP samples were manufactured through resin transfer moulding of carbon fibre laminate in a quasi-isotropic layup. Infused panels were then machined to size to obtain samples characterised by a length of 125 mm and a width of 32 mm.

The samples were machined at the National Composites Centre in Emersons Green, Bristol. The panels were labelled before machining. This was carried out to discretise between panels obtained with CNT-filled resin printing and without magnetic patch introduction.

Scarf joint samples were aimed to be manufactured from the samples obtained after preliminary machining.

The samples were obtained after room temperature cure with the consolidation relying on the vacuum applied during the infusion process. This introduced thickness changes within the partially cured samples, which resulted in thickness variability. The sample shown in Fig. 8.5 was subjected to preliminary scarf procedure to assess the feasibility of the scarf machining process. This was carried out by placing the sample onto a vacuum bed provided with a side groove, which imposed the scarf angle to the machining head.

However, the sample failed at the scarf edge due to the reduced thickness and the laminate architecture characterised by individual tows separated by considerable resin interlayers, as shown in Fig. A.3.



Fig. A.3. Scarf sample after unsuccessful machining process.

The scarf machining process was modified accordingly to provide the scarf edge with higher thickness and, therefore, enhanced structural stability. The outcome of the machining process on the sample is shown in Fig. A.4.

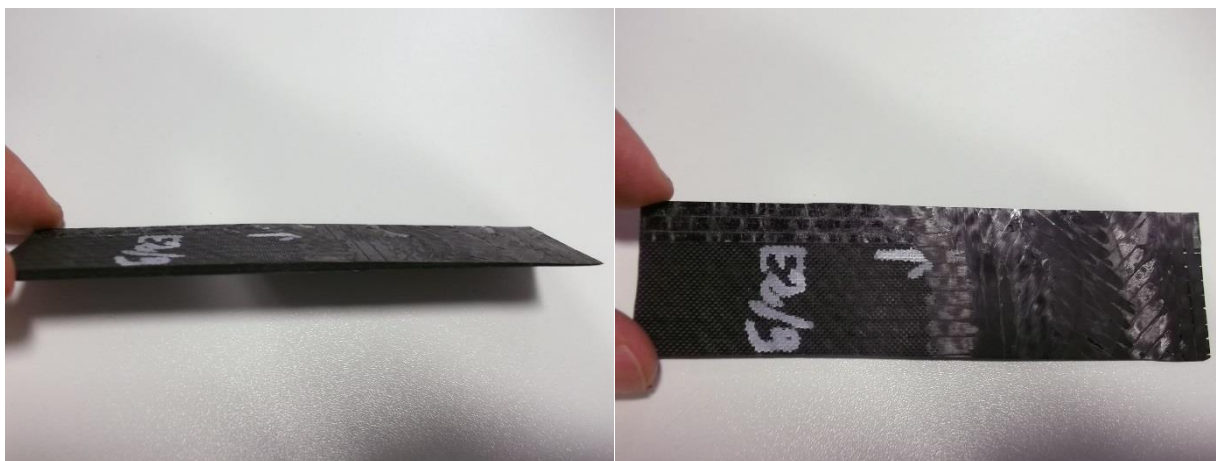


Fig. A.4. Scarf sample after machining process.

The samples obtained from the final machining supposedly served as half sample of a tensile coupon. These would be connected to the counterpart scarf joint half sample through the application of an adhesive characterised by fast cure resin system Huntsman Araldite® LY 3585 blended with a hardener Aradur® 3475 in a weight ratio 100:21. The adhesive would be enriched with the presence of 2.5 wt.% of cobalt-plated carbon nanotubes. Owing to time constraints, the samples were only tested for induction heating through application of an external AC magnetic field.

Samples were therefore exposed to an alternated current magnetic field. The purpose of the field application was the internal heat generation due to hysteresis losses from the metal plated multi-walled carbon nanotubes. This was aimed to ensure the homogenisation of the temperature profile in the adhesive located at the bondline between the preformed patch implemented with the introduction of magnetic patches, and the original undamaged composite component. In this case, the half sample characterised by the presence of the printed magnetic patch represented the preformed patch, whereas the resin infused counterpart without magnetic patch served as original undamaged component.

A schematic of the CFRP induction heating test coupon is presented in [Fig. A.5](#). As shown in the schematics below, the adhesive layer between the laminates consists of fast curing resin with embedded cobalt-plated multi-walled carbon nanotubes. The tensile testing aimed to verify the contribution of the inductive heating from the magnetic patch and the nanotubes embedded within the adhesive layer to the homogenisation of the temperature profile at the bondline between the two sample halves. This configuration replicates the bondline between

an undamaged in-service component and the preform patch used to replace a damaged composite region of the overall part.

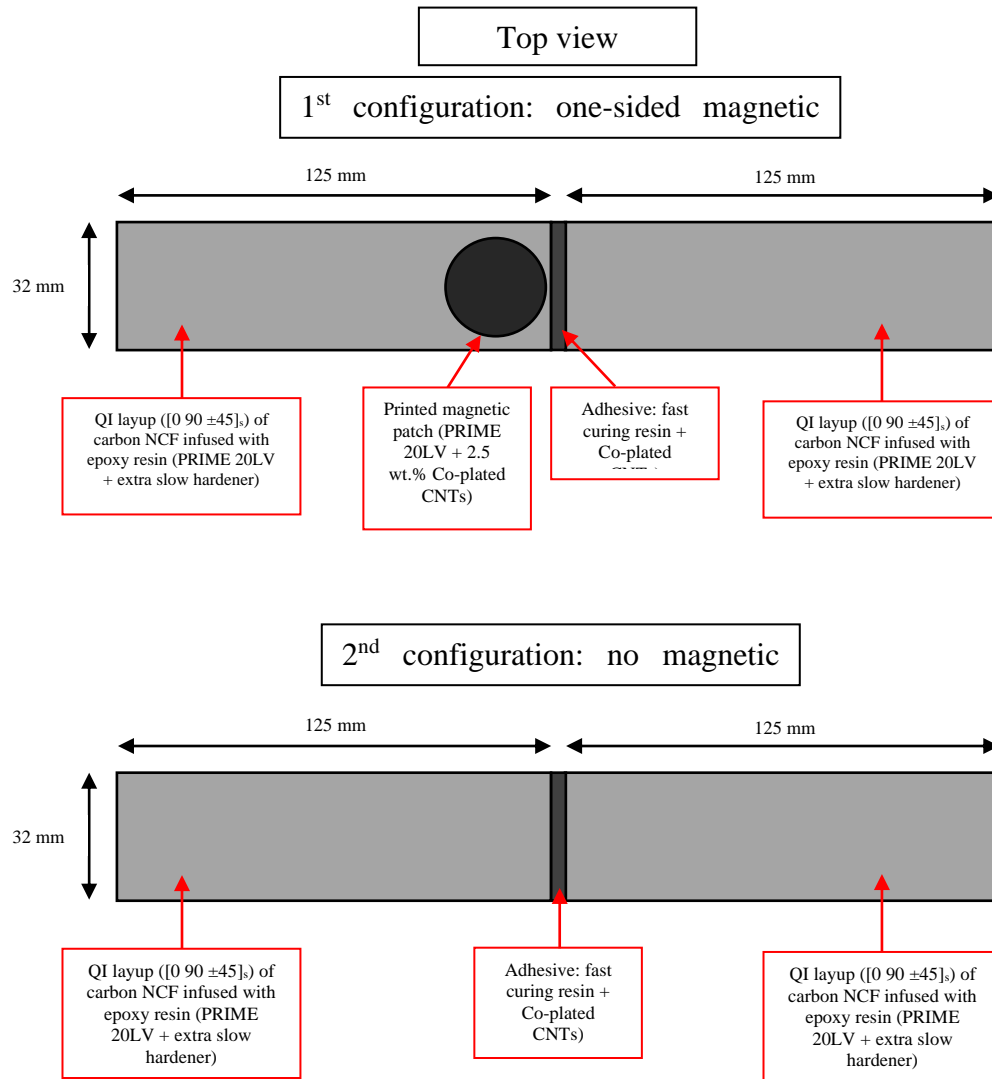


Fig. A.5. Top view of the two coupon configurations: one-sided magnetic patch and no magnetic patch within the coupons.

CFRP induction heating test coupons were therefore composed of two halves with length of 125 mm and width of 32 mm. Sample thickness was 2 mm. The samples were machined according to a scarf angle of 2° to simulate more realistic in-service conditions.

Adhesive thickness was chosen and set to 1.5 mm. The sample side view of Fig. A.6 shows the presence of the scarf angle α .

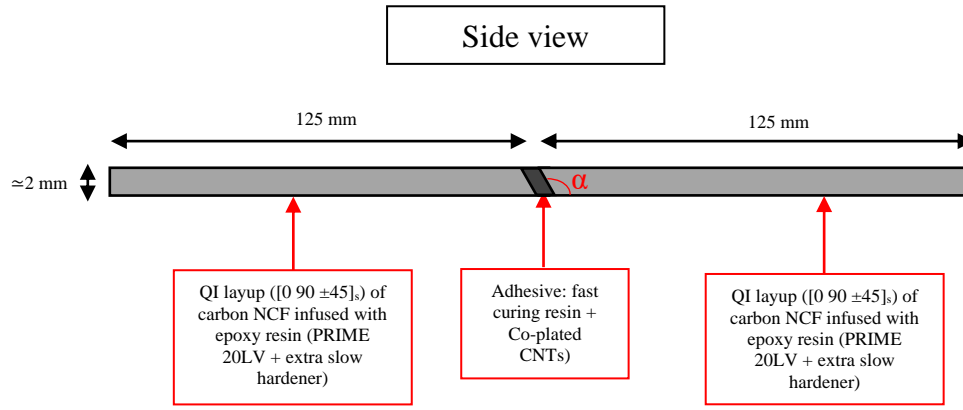


Fig. A.6. Side view of the coupons, showing the presence of the scarf angle α .

A.4 Results and conclusions

The samples were tested with two types of magnetic core, a steel core and a ferrite core. Frequencies levels of around 10 kHz were applied as only permissible by the magnetic setup and the amplifier capacity. In both instances and for both GFRP and CFRP samples, the results were unsatisfactory. Specifically, no noticeable temperature increase was recorded for both steel and ferrite cores. This is due to the limited capability of the amplifier used for the experiments, which could only allow for 4 kW of power outcome. Moreover, thermal insulation from the external environment was absent, leading to temperature fluctuations in the air domain surrounding the magnetic core and samples. Therefore, a more effective thermal insulation as a controlled chamber could help isolate the setup from the external environment, removing the influence of temperature fluctuations. Moreover, higher concentrations of CNTs in the epoxy resin injected through liquid resin printing within the laminate, both GFRP and CFRP, could be used to create a more efficient conductive network between the laminate plies. This could help the generation of eddy currents, therefore leading to higher values of heat dissipation, which can assist the resin cure mechanisms.

APPENDIX B – Materials Technical Data Sheets (MTDS)

B.1 COOH- functionalised Multi-Walled Carbon Nanotubes (Sigma Aldrich)

SIGMA-ALDRICH

sigma-aldrich.com

3050 Spruce Street, Saint Louis, MO 63103, USA

Website: www.sigmaaldrich.com

Email USA: techserv@sial.com

Outside USA: eurtechserv@sial.com

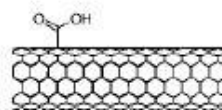
Product Specification

Product Name:

Carbon nanotube, multi-walled - carboxylic acid functionalized, thin, extent of labeling: >8% carboxylic acid functionalized, avg. diam. \times L 9.5 nm \times 1.5 μ m

Product Number: 755125

Formula: C



TEST	Specification
Appearance (Color)	Black
Appearance (Form)	Powder
Carbon	> 80 %
Content (TGA)	
Miscellaneous Assay	> 8
-COOH Functionalization (XPS)	
Product of Supplier	Confirmed
Nanocyl Inc	

Specification: PRD.1.ZQ5.10000028402

Sigma-Aldrich warrants, that at the time of the quality release or subsequent retest date this product conformed to the information contained in this publication. The current Specification sheet may be available at Sigma-Aldrich.com. For further inquiries, please contact Technical Service. Purchaser must determine the suitability of the product for its particular use. See reverse side of invoice or packing slip for additional terms and conditions of sale.

1 of 1

B.2 Nickel-Coated Multi-Walled Carbon Nanotubes (US Research Nanomaterials)

* Nickel-Coated Multi-Walled Carbon Nanotubes (Nickel-Coated MWNTs, >98%, OD: 5-15nm)

Stock#: US4430

Please click [here](#) for price information.

Details:

Nickel-Coated Multi-Walled Carbon Nanotubes (MWNTs)

Purity: > 98 wt% (from TGA & TEM)

Content of Nickel: >60 wt% (XPS & Titration)

Content of CNTs: >38 wt% (XPS & Titration)

Outside diameter: 5-15 nm (from HRTEM, Raman)

Inside diameter: 3-5 nm

Length: ~50 um (TEM)

Color: Black

Tap density: 0.27 g/cm³

Manufacturing method: CVD

Flammable Hazards, UN3089

Application

Potential applications of carbon nanotubes are: (1) additives in polymers; (2) catalysts; (3) electron field emitters for cathode ray lighting elements; (4) flat panel display; (5) gas-discharge tubes in telecom networks; (6) electromagnetic-wave absorption and shielding; (7) energy conversion; (8) lithium-battery anodes; (9) hydrogen storage; (10) nanotube composites (by filling or coating); (11) nanoprobe for STM, AFM, and EFM tips; (12) nanolithography; (13) nanoelectrodes; (14) drug delivery; (15) sensors; (16) reinforcements in composites; (17) supercapacitor.



[Certificate of Analysis](#)
[MSDS](#)

US Research Nanomaterials, Inc.

3302 Twig Leaf Lane, Houston, TX 77084, USA

Phone: (Sales) 832-460-3661; (Shipping) 832-350-7887 Fax: 281-492-8628

E-mail: Service@us-nano.com; Tech@us-nano.com

B.3 Epoxy Infusion System PRIME™ 20LV (Gurit)



PRIME™ 20LV EPOXY INFUSION SYSTEM

- **Very low viscosity**
- **Variable infusion times**
- **Very low exotherm even in thick sections**
- **Suitable for infusing very large structures**
- **GL and Lloyds approved***

INTRODUCTION

PRIME™ 20LV is the next generation of PRIME™ 20 epoxy infusion system, which is specifically designed for use in a variety of resin infusion processes including RTM (resin transfer moulding), SCRIMP™ and RIFT (resin infusion under flexible tooling).

PRIME™ 20LV has a much reduced viscosity resin and longer working time, which makes it ideal for infusing very large parts with complex reinforcements in one operation. It maintains the exceptionally low exotherm characteristic, which allows thick sections to be manufactured without risk of premature gelation due to the heat of exothermic reaction. This low exotherm will also help to extend the life of mould tools.

PRIME™ 20LV has been used successfully for the single-operation moulding of components ranging from narrow carbon yacht masts, up to 80' yacht hulls and wind turbine blades. It achieves excellent mechanical and physical properties from a moderate (50°C) postcure, offering the finished laminate properties that lie between hand lamination and low-temperature cure prepreg processes.

The PRIME™ 20LV system is available with four hardeners, offering a range of working times and cure speeds. This enables the geltime of the resin to be more closely matched to the required infusion time for any particular size of moulded part. The high Tg hardener is ideal for applications requiring 100°C plus thermal capability, whilst maintaining all the other properties of the system.

Extensive tests at Gurit have shown that PRIME™ 20LV with Slow and Extra Slow Hardeners provide an excellent bond to certain types of vinylester resin. This permits production boat builders to use existing polyester gelcoat products with high performance epoxy infusion systems by using a vinylester tie-coat interface. This delivers significant benefits to the production boat builder, in terms of improved durability and performance of hulls/decks whilst retaining the high gloss and ease of gelcoat repair associated with polyester systems.

For further advice and comprehensive processing notes please contact Gurit Technical Support.

*High Tg Hardener excluded

Table 1. Component Properties

	LV Resin	Hardener			
		Fast	Slow	Extra Slow	High Tg
Mix Ratio by Weight	100	26	26	26	24
Mix Ratio by Volume	100	31.4	31.4	31.4	29.1
Viscosity @20°C (cP)	1010-1070	25-27	22-24	16-18	29-31
Viscosity @25°C (cP)	600-640	20-22	15-17	13-15	25-27
Viscosity @30°C (cP)	390-410	16-18	12-14	10-12	21-23
Shelf Life (months)	12	12	12	12	12
Colour (Gardener)	1	7	Clear	1	Clear
Mixed Colour (Gardener)	-	3	1	1	1
Density (g/cm ³)	1.123	0.983	0.936	0.931	0.926
Mixed Density	-	1.089	1.084	1.083	1.078

MIXING AND HANDLING

PRIME™ 20LV resin must be mixed with PRIME™ hardener in the following ratio:

**PRIME™ 20LV resin: PRIME™ hardener
(Fast, Slow or Extra Slow)**

100 : 26 (by weight)

100 : 31.4 (by volume)

PRIME™ 20LV resin: PRIME™ High Tg Hardener

100 : 24 (by weight)

100 : 29.1 (by volume)

The fast hardener is not usually used alone with the resin - although it can be used in this way, it is more often premixed with another PRIME™ hardener to achieve shorter gel times than would otherwise be obtained with the use of Slow or Extra Slow hardener alone. The premixed hardener combination (Fast + Slow, or Fast + Extra Slow) is still mixed with resin at 100 : 26 by weight. High Tg hardener should be used as a stand alone hardener

Accurate measurement and thorough mixing are essential when using this system, and any deviation from the prescribed mixing ratios will seriously degrade the physical properties of the cured system. The resin and hardener must be well stirred for two minutes or more, with particular attention being paid to the sides and bottom of the container. As soon as the material is mixed the reaction begins. This reaction produces heat (exothermic), which will in turn accelerate the reaction. If this mixed material is left in a confined mixing vessel the heat cannot disperse, and the reaction will become uncontrollable. See "Working Properties" for details

APPLICATION

PRIME™ 20LV system is intended for use in any established resin infusion process. The information provided in the tables in this datasheet should allow the user to achieve a successful result with PRIME™ 20LV system. However, if further information is required, please contact Technical Services.

CURE SCHEDULE

To generate optimum mechanical properties for this system an elevated temperature cure is required. The recommended minimum cure schedule is 7 hours at 65°C or 16 hours at 50°C. Ambient temperature (15-25°C) cure of this system will not generate adequate properties and is therefore not recommended.

Parts can be 'pre-cured' in the mould at temperatures just above ambient (e.g. 35-45°C) to give the part sufficient strength and stiffness to allow earlier demoulding. Such parts should still be post cured at the minimum recommended time/temperature indicated above. Contact Technical Services for 'pre-cure' time/temperature recommendations.

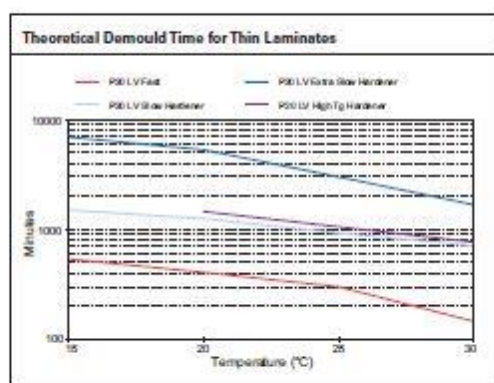
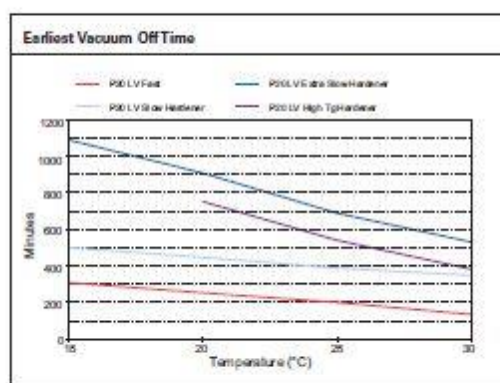
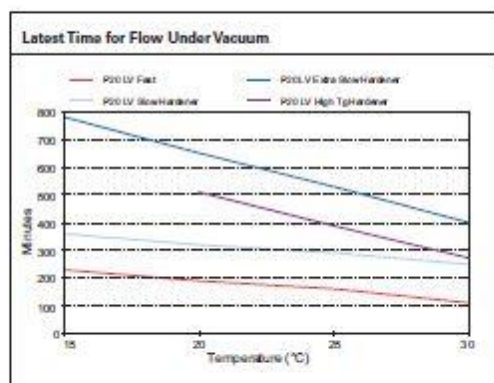
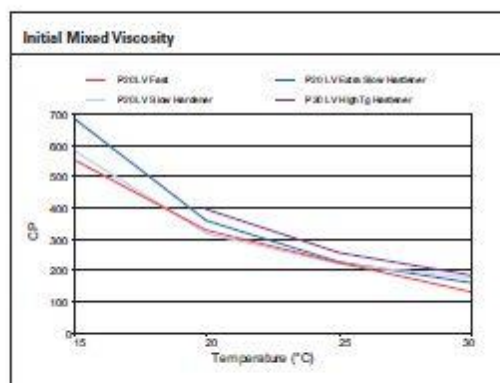
To get the maximum benefit from the High Tg hardener a further elevated post cure is required. For specific requirement contact Technical Services Department.

Table 2. Working Properties

	Fast Hardener				Slow Hardener				Extra Slow Hardener				High Tg Hardener		
	15°C	20°C	25°C	30°C	15°C	20°C	25°C	30°C	15°C	20°C	25°C	30°C	20°C	25°C	30°C
Initial Mixed Viscosity (cP)	535-568	318-338	219-232	127-134	564-598	308-328	214-228	172-182	662-702	347-369	220-234	155-165	397	265	181
Geltime – Tecam 150g in water (hr : min)	1:30	1:09	0:30	0:17	6:20	5:00	3:20	2:20	13:30	10:20	9:00	6:15	7:45	6:30	4:08
Pot life 500g in air (hr : min)	0:35	0:28	0:23	0:16	1:30	1:15	1:00	0:45	7:55	6:00	4:05	2:10	3:20	2:10	1:10
Latest flow under vacuum (theoretical, thin film, hr : min)	3:50	3:10	2:40	1:50	6:00	5:20	4:50	4:10	13:00	10:50	8:50	6:40	8:25	6:30	4:40
Earliest vacuum off time (theoretical thin film) (hr : min)	5:10	4:15	3:20	2:15	8:20	7:30	6:30	5:50	18:10	15:10	11:30	8:50	12:30	9:00	6:30
Demould time (hr : min)	9:00	6:45	5:00	2:30	25:00*	21:00*	15:30*	11:50*	115:00*	88:00*	50:00*	28:00*	24:30*	18:45*	13:00*

Notes: All figures quoted are indicative of the properties of the product concerned. Some batch to batch variation may occur.

*Demoulding components made with Slow, Extra Slow or High Tg Hardener should only be carried out after the part has received an elevated temperature cure in the mould.



CURED PROPERTIES

CURED SYSTEM THERMAL PROPERTIES

The thermal properties of PRIME™ 20LV system, as determined by Differential Scanning Calorimeter (Mettler Toledo DSC821E), and Dynamic Mechanical Thermal Analysis (Rheodyne Thermal Analyser MkIII) are presented in Table 3.

Table 3. Cured System Thermal Properties

Hardener used	Fast	Slow	Extra Slow	High Tg
Cure Schedule	16hrs 50°C	16hrs 50°C	16hrs 50°C	16hrs 50°C
Tg (DMTA - peak tan δ)	82.8	82.6	82.9	87
TgUlt (DMTA)	74-76	87-89	90-92	112-115
Tg1 (DMTA)	68-70	68-70	69-71	72-74
ΔH - DSC (J/g)	1.54	7.3	0.00	0.00
Estimated HDT	67	68	67	72

CURED SYSTEM MECHANICAL PROPERTIES (MATRIX PROPERTIES)

The mechanical properties of the matrix system are presented in Table 4.

Table 4. Cured System Mechanical Properties

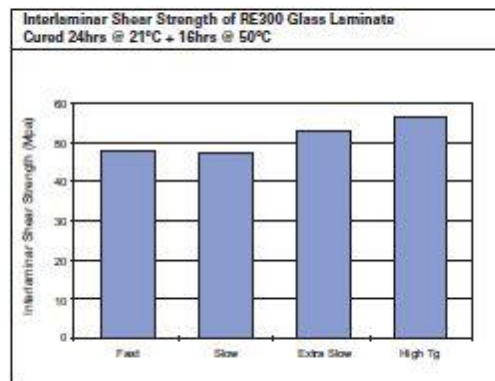
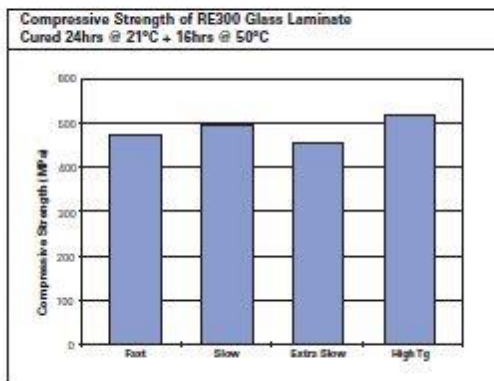
Hardener used	Fast	Slow	Extra Slow	High Tg
Cure Schedule	16hrs 50°C	16hrs 50°C	16hrs 50°C	16hrs 50°C
Tensile Strength (MPa)	75	73	69	69.7
Tensile Modulus (GPa)	3.2	3.5	3.5	3.2
Strain to failure (%)	4.1	3.5	3.1	3
Moisture Absorption (%)	tba	tba	tba	tba
Cured density (g/cm ³)	1.153	1.144	1.132	1.13
Linear Shrinkage (%)	1.830	1.765	1.541	1.747
Barcol Hardness	21	27	25	34.1

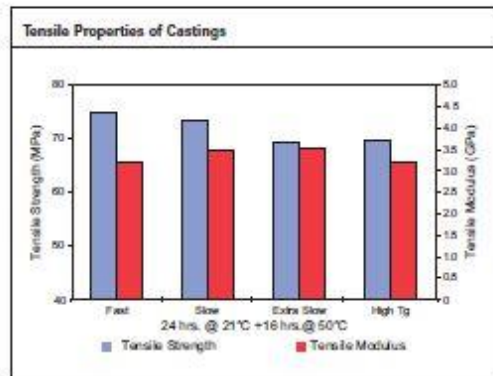
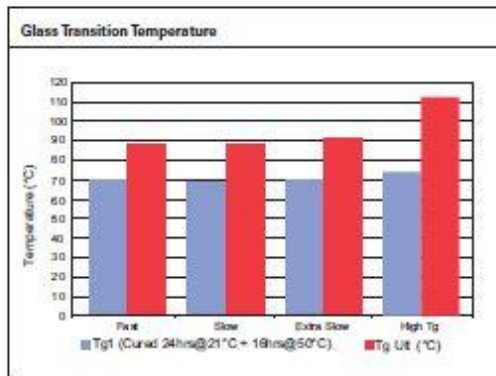
CURED LAMINATE PROPERTIES

The cured laminate properties are presented in Table 5. The laminate is constructed using RE301 8 harness satin weave glass and PRIME™ 20LV/Extra-Slow.

Table 5. Cured Laminate Properties

Hardener used	Fast	Slow	Extra Slow	High Tg
Cure Schedule	16hrs 50°C	16hrs 50°C	16hrs 50°C	16hrs 50°C
Compr. Strength (MPa)	473	492	456	519
ILSS (MPa)	476	470	52.8	56.9
ILSS wet retention (%)	tba	tba	95	tba





HEALTH AND SAFETY

PRIME™ 20LV SYSTEM

PRIME™ 20LV resin and hardeners have been designed for use in closed-mould processes. This includes the mixing phase, which should ideally be carried out by automated mixing machines.* It is not suitable for open-mould processing and strict adherence to the health and safety procedures stated in the product SDS is essential.

Users should ensure that some elevated temperature-cure is applied to the component before trying to machine it. In a component made from PRIME™ 20LV which has seen no heat, there will be only a partial cure. Therefore the sanding dust will be more irritating than dust from a laminate cured at elevated temperature, in which there will be more thorough cross linking.

Gurit produces a separate full Safety Data Sheet (SDS) for each component of this system. Please ensure that you have the correct SDS to hand for the materials you are using before commencing work. A more detailed guide for the safe use of Gurit resin systems is also available from Gurit, and can be found on our website at www.gurit.com

Any accidental spillage should be soaked up with sand, sawdust, cotton waste or any other absorbent material. The area should then be washed clean (see appropriate Safety Data Sheet).

The following points must be considered:

1. Skin contact must be avoided by wearing protective gloves. Gurit recommends the use of disposable nitrile gloves for most applications. The use of barrier creams is not recommended, but to preserve skin condition a moisturising cream should be used after washing.
2. Overalls or other protective clothing should be worn when mixing, laminating or sanding. Contaminated work clothes should be thoroughly cleaned before re-use.
3. Eye protection should be worn if there is a risk of resin, hardener, solvent or dust entering the eyes. If this occurs flush the eye with water for 15 minutes, holding the eyelid open, and seek medical attention.

4. Ensure adequate ventilation in work areas. Respiratory protection should be worn if there is insufficient ventilation. Solvent vapours should not be inhaled as they can cause dizziness, headaches, loss of consciousness and can have long term health effects.

5. If the skin becomes contaminated, then the area must be immediately cleansed. The use of resin-removing cleansers is recommended. To finish, wash with soap and warm water. The use of solvents on the skin to remove resins etc must be avoided.

Washing should be part of routine practice:

- before eating or drinking
 - before smoking
 - before using the lavatory
 - after finishing work
6. The inhalation of sanding dust should be avoided and if it settles on the skin then it should be washed off. After more extensive sanding operations a shower/bath and hair wash is advised.

APPLICABLE RISK & SAFETY PHRASES

Please refer to product SDS for up to date information specific to this product.

* Other mixing methods can be used.



TRANSPORT & STORAGE

The system should be kept in securely closed containers during transport and storage. Storage should be in a dry place out of direct sunlight. The temperature should be between 18°C and 25°C. Containers should be firmly closed. The hardeners, in particular, will suffer serious degradation if left exposed to air.

SHELF LIFE

Adequate long-term storage conditions for both materials will result in a shelf life of one year for both the resin and hardeners.

NOTICE

All advice, instruction or recommendation is given in good faith but Gurit AG (the company) only warrants that advice in writing is given with reasonable skill and care. No further duty or responsibility is accepted by the Company. All advice is given subject to the terms and conditions of sale (the Conditions) which are available on request from the Company or may be viewed at the Company's Website: <http://www.gurit.com/terms-and-conditions.aspx>

The Company strongly recommends that Customers make test panels and conduct appropriate testing of any goods or materials supplied by the Company to ensure that they are suitable for the Customer's planned application. Such testing should include testing under conditions as close as possible to those to which the final component may be subjected. The Company specifically excludes any warranty of fitness for purpose of the goods other than as set out in writing by the Company. The Company reserves the right to change specifications and prices without notice and Customers should satisfy themselves that information relied on by the Customer is that which is currently published by the Company on its website. Any queries may be addressed to the Technical Services Department.

Gurit are continuously reviewing and updating literature. Please ensure that you have the current version, by contacting Gurit Marketing Communications or your sales contact and quoting the revision number in the bottom right-hand corner of this page.

E gurit@gurit.com
W www.gurit.com

B.4 EPON™ Resin 828 (Hexion)



Technical Data Sheet

Re-issued September 2005

EPON™ Resin 828

Product Description

EPON™ Resin 828 is an undiluted clear difunctional bisphenol A/epichlorohydrin derived liquid epoxy resin. When cross-linked or hardened with appropriate curing agents, very good mechanical, adhesive, dielectric and chemical resistance properties are obtained. Because of this versatility, EPON Resin 828 has become a standard epoxy resin used in formulation, fabrication and fusion technology.

Benefits

- Fiber reinforced pipes, tanks and composites
- Tooling, casting and molding compounds
- Construction, electrical and aerospace adhesives
- High solids/low VOC maintenance and marine coatings
- Electrical encapsulations and laminates
- Chemical resistant tank linings, flooring and grouts
- Base resin for epoxy fusion technology

Sales Specification

Property	Units	Value	Test Method/Standard
Weight per Epoxide	g/eq	185 – 192	ASTM D1652
Viscosity at 25°C	P	110 – 150	ASTM D445
Color	Gardner	1 max.	ASTM D1544

Typical Properties

Property	Units	Value	Test Method/Standard
Density at 25°C	lb/gal	9.7	ASTM D1475
Density at 25°C	g/ml	1.16	
Vapor pressure @ 25°C (77° F)	mm Hg	0.03	
Refractive index @ 25°C (77° F)		1.573	
Specific heat	BTU/lb°F	0.5	

Processing/How to use**General Information**

The low viscosity and cure properties of EPON Resin 828 allow its use under various application and fabrication techniques including:

• Spraying and brushing	• Pultrusion
• Filament winding	• Casting
• Pressure laminating	• Molding
• Vacuum bag laminating	• Toweling

Curing Agents

EPON Resin 828 can be cured or cross-linked with a variety of curing agents depending on properties desired in the finished product and the processing conditions employed. Some commonly used curing agents, recommended concentrations, typical cure schedules employed in major end-use applications, plus sources for these curing agents are displayed in Table 1.

Performance Properties**Performance Characteristics of Cured EPON Resin 828****Mechanical Properties**

High performance, high strength materials are obtained when this resin is cured with a variety of curing agents. Unfilled systems in common use have tensile values greater than 10,000 psi (69 MPa) with modulus values greater than 400,000 psi (2750 MPa). Such systems are normally very rigid. If greater flexibility is needed systems can be formulated to provide up to 300% elongation.

Adhesive Properties

One of the most widely recognized properties of cured EPON Resin 828 is strong adhesion to a broad range of substrates. Such systems exhibit shear strength of up to 6,000 psi (41 Mpa). One factor which contributes to this property is the low shrinkage shown by these systems during cure. Compared to other polymers, epoxy resins have low internal stresses resulting in strong and durable finished products.

Electrical Properties

EPON Resin 828 cured systems have very good electrical insulating characteristics and dielectric properties. For example, systems can be obtained with anhydride and amine curing agents having volume resistivities up to 1×10^{16} ohm-cm, dielectric constants of 3-5 and dissipation factors of 0.002 to 0.020 at ambient conditions. Electrical encapsulations, laminates and molding compounds are frequently based on EPON Resin 828.

Chemical Resistance

Cured EPON Resin 828 is highly resistant to a broad range of chemicals, including caustic, acids, fuels and solvents. Chemically resistant reinforced structures and linings or coatings over metal can be formulated with EPON Resin 828.

Formulating Techniques

The primary components of a thermosetting resin formula are the epoxy resin and the hardener or curing

agent. However, in practice other materials are normally incorporated to achieve special properties. For example, inert fillers such as silicas, talcs, calcium silicates, micas, clays and calcium carbonate can be added to further reduce shrinkage and improve dimensional stability. Also, reactive diluents can be added to EPON Resin 828 to reduce viscosity. The effect on viscosity by adding such materials is shown in Figure 1.

Table 1 / Curing Agents for EPON™ 828

<u>Curing Agent</u> ¹	<u>Physical State</u>	<u>Recommended Concentration Range, phr²</u>	<u>Typical Cure Schedule Time °C (°F)</u>	<u>Deflection Temperature °C (°F)</u>	<u>Applications</u> ⁴	<u>Suppliers</u> ⁵
Aliphatic Amines						
EPIKURE™ 3223 (DETA)	Liquid	12	7d, 25 (77)	120(250)	ABCDEFHI	5
EPIKURE 3234 (TETA)	Liquid	13	7d, 25 (77)	120(250)	ABCDEFHI	5
EPIKURE 3200 (AEP)	Liquid	22	24h, 25 (77) & 1h, 150 (300)	120(250)	BCEFGH	5
EPIKURE 3270	Liquid	75	14d, 25 (77)	56(133)	ABCDEFHI	5
EPIKURE 3271	Liquid	18	14d, 25 (77)	66(151)	ABCDEFHI	5
EPIKURE 3274	Liquid	40	14d, 25 (77)	—	ABCDEFHI	5
EPIKURE 3230	Liquid	35	7d, 25 (77)	68(155)	ABCDEFHI	1
D-400 Type PEA	Liquid	55	30 min, 115(240)	31(88)	ABCEFH	1
Cycloaliphatic Amines						
EPIKURE 3370	Liquid	38	7d, 25 (77)	56(133)	ABCDEFHI	5
EPIKURE 3382	Liquid	63	7d, 25 (77)	63(145)	ABCDEFHI	5
EPIKURE 3383	Liquid	60	24h, 25 (77) & 2h, 100 (212)	54(129)	ABCDEFHI	5

EPON Resin 828

Polyamides

EPIKURE 3115	Liquid	120	1h, 100 (212)	85(185)	AB	5
EPIKURE 3125	Liquid	90	7d, 25 (77)	90(195)	ABCEFH	5
EPIKURE 3140	Liquid	75	7d, 25 (77)	115(240)	ABCEFH	5

Amidoamines

EPIKURE 3015	Liquid	50	16h, 25 (77) & 2h, 93 (200)	—	ABCDEFGHI	5
EPIKURE 3055	Liquid	50	16h, 25 (77) & 2h, 93 (200)	67(153)	ABCDEFGHI	5
EPIKURE 3072	Liquid	35	14d, 25 (77)	59(138)	ABCDEFGHI	5

Aromatic Amines

EPIKURE W	Liquid					5
Metaphenylenediamine (MPDA)	Solid	14	2h, 80 (175) & 2h, 150 (300)	150(300)	BCDGH I	3
Methylene dianiline (MDA)	Solid	27	2h, 80 (175) & 2h, 150 (300)	160(320)	BCDEGH I	13
Diaminodiphenyl Sulfone (DADS)	Solid	25	5h, 125 (257) & 1h, 200 (392)	170(350)	BCDGH I	2, 13

Table 1 / Curing Agents for EPON™ 828, cont.

<u>Curing Agent</u> ¹	<u>Physical State</u>	<u>Recommended Concentration Range, phr²</u>	<u>Typical Cure Schedule Time</u>	<u>Deflection Temperature °C (°F)</u>	<u>Applications</u> ⁴	<u>Suppliers</u> ⁵
----------------------------------	-----------------------	---	---	---	----------------------------------	-------------------------------

°C (°F)						
Anhydrides						
Methyl tetrahydrophthalic Anhydride (MTHPA)	Liquid	80	2h, 120 (250) & 2h, 150 (300)	130(266)	BCDGH I	9, 11, 14
NADIC Methyl Anhydride (NMA)	Liquid	90	1h, 120 (250) & 2-24h, 260(500)	180(356)	BCDGH I	9, 14
Hexahydrophthalic Anhydride (HHPA)	Solid	80	1h, 80 (175) & 2h, 150 (300)	130(265)	BCDGH I	8, 12, 14
Catalysts and Miscellaneous						
2-Ethyl- 4-Methyl Imidazole (EMI-24)	Metastable Liquid	3	4h, 50 (122) & 2h, 170 (340)	170(340)	BCDGH I	15, 16
BF ₃ -Monoethylamine (BF ₃ -MEA)	Liquid	3	1h, 120 (250) & 2h, 170 (340)	170(340)	BCDGH I	17
Diethylaminopropylamine ⁶	Solid	6	30 min, 115(240)	100(212)	ABC	6
Dicyandiamide	Solid	4	1h, 177 (350)	150(300)	BCDGH I	18, 19

¹ Cures can be effected with these curing agents over a wide range of temperatures. Higher temperatures yield shorter cure times and highest Tg.

² Parts of curing agent per 100 parts of resin.

³ Systems cured at room temperature were post cured at elevated temperature to achieve deflection values.

⁴ Application codes: A - Coatings; B - Adhesives; C - Castings; D - Moldings; E - Flooring; F - Paving; G - Electrical Laminates; H - Structural Laminates; I-Filament Winding.

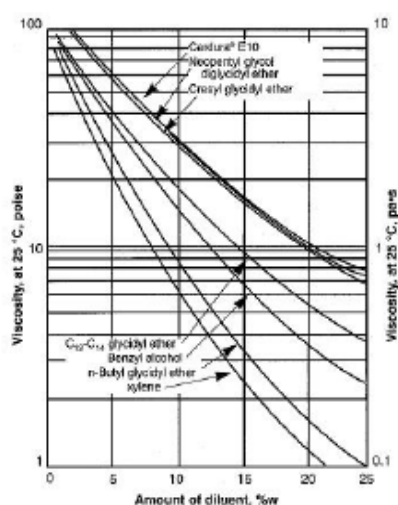
⁵ Supplier Code:

1. Huntsman Chemical
2. RSA Corporation
3. E.I. DuPont de Nemours & Co., Chemicals & Pigments Dept.
4. Harshaw Chemical Company
5. Hexion Specialty Chemical
6. BASF Corporation
7. American Cyanamid - Industrial Chemical Div.
8. Milliken & Company

9. Lindau Chemicals, Inc.
10. Anhydrides and Chemicals, Inc.
11. Dixie Chemical Co., Inc.
12. Buffalo Color Corp.
13. Air Products and Chemicals, Inc.
14. Lonza
15. Interchem
16. Polyorganix
17. Atotech
18. SKW Trotsbery
19. Ashland Chemical

⁶ Dimethylamino propylamine may be substituted at expense of slightly reduced pot life. Sources are 2 and 16.

Figure 1 / Viscosity at 25 °C of EPON™ Resin 828 blends with various diluents



Fusion Technology

EPON Resin 828 is the product of choice for a resin chemist using a specific fusion catalyst when processing proprietary solid epoxy resins or epoxy esters. Upon request, Hexion can provide EPON Resin 828 exhibiting extremely low hydrolyzable and total chlorine, two end groups that may be deleterious to resin curing and long term performance in electrical uses.

FDA Status

Provisions are made in the FDA regulations for the use of EPON Resin 828, when properly formulated, applied and cured, for food contact applications under Title 21 Code of Federal Regulations 175.300. The regulations should be consulted for complete details. In particular, we direct your attention to subparagraph (b) of 21 CFR 174.5 and the general provisions applicable to indirect food additives listed there.

Identification and Classification

EPON Resin 828

Chemical Abstract Service Registry Number: 25088-38-8 (EPA/TSCA inventory designation)

Generic name: Liquid Bisphenol A Epichlorohydrin based epoxy resin.

Chemical designation: Phenol, 4,4O - (1-methylethylidene) bis-polymer with (chloromethyl) oxirane.

Figure 2 / Viscosity - temperature profile for EPON™ Resin 828

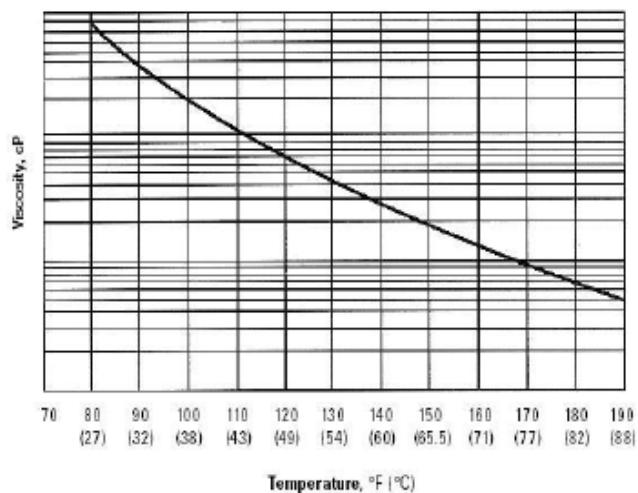
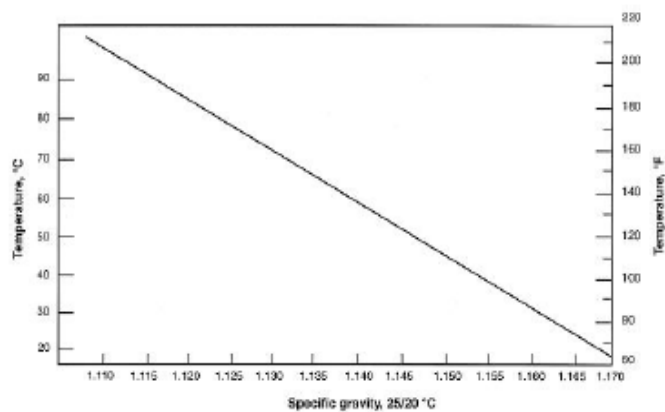


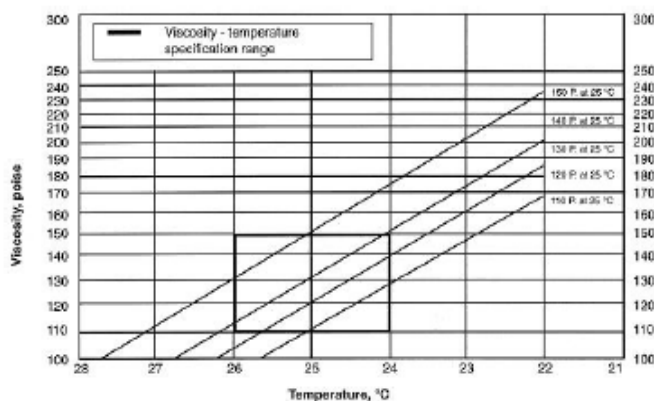
Figure 3 / Specific gravity - temperature profile for EPON™ Resin 828



Formulation and Application Information

For additional performance characteristics information covering adhesives, laminating, casting and molding applications, consult bulletin SC:67, entitled "EPON Resin Structural Reference Manual." For epoxy resin amine-cured coatings, consult bulletin SC:193, entitled "Formulating Amine-Cured Coatings with EPON Resin."

Figure 4 / Viscosity - temperature profile (for 5 samples of EPON™ Resin 828 ranging in viscosity from 110-150 poise)



Safety, Storage & Handling

Please refer to the MSDS for the most current Safety and Handling information.

Please refer to the Hexion web site for Shelf Life and recommended Storage information.

EPON Resin 828 is an undiluted liquid epoxy resin that is available in tank cars, tank trucks and 500 pound net closed head drums. EPON Resin 828 is normally shipped in bulk from 150 °F (66 °C) to 180 °F (82 °C) and can be stored at 120-140 °F (49-60 °C) for ease of handling. The viscosity/temperature profile and the specific gravity/temperature profile for EPON Resin 828 are displayed in Figures 2 and 3 respectively for your guidance.

NOTE OF CAUTION: When checking viscosity of EPON Resin 828 incoming samples, we caution you to make certain that the product is maintained at 25 +/- 0.01 °C before testing. You will note in Figure 4 that EPON Resin 828 can vary in viscosity by 10-15 poise for each degree in temperature the product varies from 25 °C.

Exposure to these materials should be minimized and avoided, if feasible, through the observance of proper precautions, use of appropriate engineering controls and proper personal protective clothing and equipment, and adherence to proper handling procedures. **None of these materials should be used, stored, or transported until the handling precautions and recommendations as stated in the Material Safety Data Sheet (MSDS) for these and all other products being used are understood by all persons who will work with them.** Questions and requests for information on Hexion Inc. ("Hexion")

EPON Resin 828

products should be directed to your Hexion sales representative, or the nearest Hexion sales office. Information and MSDSs on non-Hexion products should be obtained from the respective manufacturer.

Packaging

Available in bulk and drum quantities.

Contact Information

For product prices, availability, or order placement, call our toll-free customer service number at: 1-877-859-2800

For literature and technical assistance, visit our website at: www.hexion.com

® and ™ Licensed trademarks of Hexion Inc.

DISCLAIMER

The information provided herein was believed by Hexion Inc. ("Hexion") to be accurate at the time of preparation or prepared from sources believed to be reliable, but it is the responsibility of the user to investigate and understand other pertinent sources of information, to comply with all laws and procedures applicable to the safe handling and use of the product and to determine the suitability of the product for its intended use. All products supplied by Hexion are subject to Hexion's terms and conditions of sale. HEXION MAKES NO WARRANTY, EXPRESS OR IMPLIED, CONCERNING THE PRODUCT OR THE MERCHANTABILITY OR FITNESS THEREOF FOR ANY PURPOSE OR CONCERNING THE ACCURACY OF ANY INFORMATION PROVIDED BY HEXION, except that the product shall conform to Hexion's specifications. Nothing contained herein constitutes an offer for the sale of any product.

PDS-3942- (Rev.3/6/2015 11:22:27 AM)

B.5 Benzoxazine 35600 (Araldite®, Huntsman)



Advanced Materials

Araldite® MT 35600 Benzoxazine Resin

Bisphenol-A based Benzoxazine

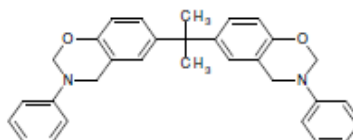
Key properties

- High temperature resistance
- Good electrical properties
- Low water absorption
- Dimensional stability
- High modulus properties

Description

Araldite® MT 35600 is a bisphenol-A based benzoxazine thermoset resin which can be homopolymerized or co-react with an epoxy or phenol resin resulting in polymers with extremely good thermal and mechanical properties.

Chemical Structure



Processing

Pultrusion, Pre-preg, Pressure Molding, Resin Transfer Molding (RTM)

Applications

Advanced composites, Structural adhesives, Laminates for printed wiring boards, Encapsulates, High performance coatings, Molding compounds.

Product data

	Araldite® MT 35600
Visual Appearance	Yellow solid
Viscosity at 125°C, cP	50 – 500
Gel time at 220°C, sec.	250 – 550
Melting Point, °C (°F)	58 – 70 (136 – 158)

* Product data are based on Huntsman's test methods. Copies are available upon request.

Typical Cured Properties

Unless otherwise stated, the data were determined with typical production batches using standard testing methods. They are provided solely as technical information and do not constitute a product specification.

Mechanical Properties

Cure schedule: 2h at 180°C + 2h at 200°C

Flexural test ¹	
Flexural Modulus, MPa	5,452
Flexural Strength, MPa	122
Tensile test ²	
Tensile Modulus, MPa	6,694
Tensile Strength, MPa	59
Ultimate Elongation, %	0.9
Toughness test ³	
K1c, MPa√m	0.69
G1c, J/m ²	80.5

Thermal Properties

Cure schedule: 2h at 180°C + 2h to 4h at 200°C

Glass transition (Tg)	
DSC ⁴ , °C	160 – 170
DMA ⁵ , °C	170 – 180
Weight loss ⁶	
@ 300 °C, %	0.84
@ 350 °C, %	1.34
@ 400 °C, %	6.65

Electrical Properties⁷

Dk	3.1 – 3.6
Df	0.006 – 0.030

¹ ISO 178/01

² ISO 5272/93

³ Bend Notch test ISO 13586/03

⁴ DSC: TA Q2000 / ramp @ 10 °C / 30 °C – 300 °C / nitrogen

⁵ DMA: TA Q800 / ramp @ 10 °C / 30 °C – 300 °C / nitrogen

⁶ TGA: TA 2950 / ramp @ 10 °C / 30 °C – 800 °C / air

⁷ Test range 10 MHz – 1.0 GHz, HP Impedance Analyzer, samples thickness 2.0 – 2.5 mm

Cast Procedure

Weigh benzoxazine material in an appropriate kettle equipped with heating capability, mechanical stirrer and temperature recording device. Heat with continuous stirring to 120-140°C until a clear homogeneous solution is obtained. Additional heating dictates the pot life of the resultant prepolymer. For clear casting, degas the resultant mixture, while maintained at 120°C - 140°C, at 26+ inches of vacuum for 15 minutes; or until foaming has stopped. This indicates that the product has been purged of any volatiles. Hot degassed melt can be poured into preheated molds; and cured at the desired conditions.

Formulations

Araldite® MT 35600 can be homopolymerized or formulate with epoxy resins, catalysts and toughener agents to improve performance. While formulating the Benzoxazine must be melted below their onset temperature of reaction by 30°C. Degassing time of the components in a vacuum oven should not exceed 50% of the gel time at temperature at least 30°C below the onset temperature of reaction. Once degassed cured as recommended cure schedule.

Formulations with epoxy resins

Formulation No.	1	2	3
Araldite® MT 35600 Benzoxazine Resin	75	75	75
Araldite® CY 179 Epoxy Resin ^a	25		
Araldite® MY 0500 Epoxy Resin ^b		25	
Araldite® GY 6010 Epoxy Resin ^c			25
Gel time at 200°C, min.	47	41	40
Mechanical Properties			
Cure schedule: 2h at 180°C + 2h at 200°C			
Flexural test ¹			
Flexural Modulus, MPa	4,478	4,608	4,360
Flexural Strength, MPa	86	93	111
Ultimate Elongation	1.7	1.8	2.3
Tensile test ²			
Tensile Modulus, MPa	4,524	4,690	4,429
Tensile Strength, MPa	37	35	36
Ultimate Elongation, %	0.8	0.8	0.8
Toughness test ³			
K1c, MPa√m	0.52	0.47	0.56
G1c, J/m ²	52	41	61
Thermal Properties			
Cure schedule: 2h at 180°C + 2h at 200°C			
Tg DSC ⁴ , °C	198	196	168
DMA ⁵			
Storage Modulus, °C	192	167	149
Loss Modulus, °C	222	200	177
Tangent Delta, °C	238	219	195
Weight loss ⁶			
@ 300°C, %	1.31	0.98	1.15
@ 350°C, %	4.12	2.40	3.61

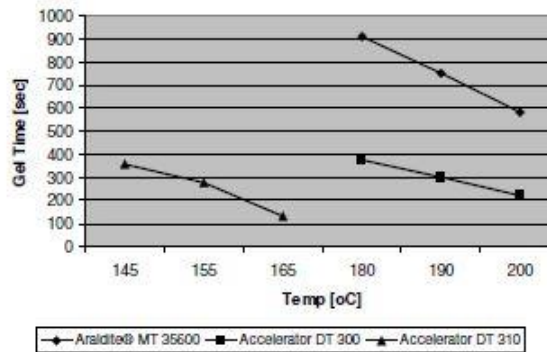
^a Liquid cycloaliphatic epoxy resin (epoxy equivalent weight: 131 – 143)

^b Low viscosity trifunctional liquid epoxy resin (epoxy equivalent weight: 105 - 115)

^c Standard bisphenol-A liquid epoxy resin (epoxy equivalent weight: 182 - 192)

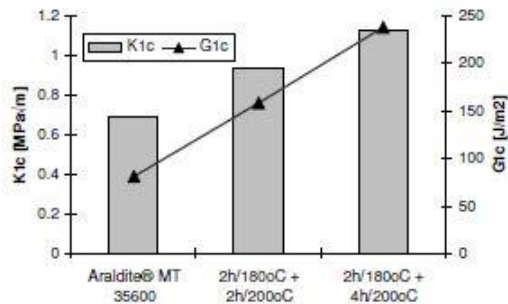
Catalysts for Benzoxazine Formulations

Catalysts such as Accelerator DT 300 and Accelerator DT 310 can be used to improve reactivity for both benzoxazine homopolymerization and benzoxazine/epoxy combinations. The type of catalyst selected and its loading level in a formula depend on factors such as cure time/temperature, epoxy content and other additives being incorporated. The graph below shows how reactivity is affected by the addition of 10phr of catalyst to Araldite® MT 35600.



Toughener Agent for Benzoxazine Formulations

The addition of Araldite® LT 1522 epoxy toughener can further improve the fracture resistance of benzoxazine based formulations. The loading level of toughener and resin cure schedule will affect toughening performance. The graph below shows results of Bend Notch Test after 10phr of Araldite® LT 1522 toughening agent is added using two different cure schedules.



Storage	Araldite® MT35600 benzoxazine resin may be stored for up to 3 years from date of manufacture at temperature around 25°C provided the product is stored in sealed container.
Handling precautions	<p>Caution</p> <p>Do not use this product until the MSDS have been read and understood. To protect against any potential health risks presented by our products, the use of proper personal protective equipment (PPE) is recommended. Eye and skin protection is normally advised. Respiratory protection may be needed if mechanical ventilation is not available or is insufficient to remove vapors. For detailed PPE recommendations and exposure control options consult the product MSDS or a Huntsman EHS representative.</p>

Huntsman Advanced Materials
(Switzerland) GmbH
Klybeckstrasse 200
4057 Basel
Switzerland

Tel: +41 (0)61 299 11 11
Fax: +41 (0)61 299 11 12

www.huntsman.com/advanced_materials
Email: advanced_materials@huntsman.com



Huntsman Advanced Materials warrants only that its products meet the specifications agreed with the buyer. Typical properties, where stated, are to be considered as representative of current production and should not be treated as specifications.

The manufacture of materials is the subject of granted patents and patent applications; freedom to operate patented processes is not implied by this publication.

While all the information and recommendations in this publication are, to the best of our knowledge, information and belief, accurate at the date of publication, NOTHING HEREIN IS TO BE CONSTRUED AS A WARRANTY, EXPRESS OR OTHERWISE.

IN ALL CASES, IT IS THE RESPONSIBILITY OF THE USER TO DETERMINE THE APPLICABILITY OF SUCH INFORMATION AND RECOMMENDATIONS AND THE SUITABILITY OF ANY PRODUCT FOR ITS OWN PARTICULAR PURPOSE.

The behaviour of the products referred to in this publication in manufacturing processes and their suitability in any given end-use environment are dependant upon various conditions such as chemical compatibility, temperature, and other variables, which are not known to Huntsman Advanced Materials. It is the responsibility of the user to evaluate the manufacturing circumstances and the final product under actual end-use requirements and to adequately advise and warn purchasers and users thereof.

Products may be toxic and require special precautions in handling. The user should obtain Safety Data Sheets from Huntsman Advanced Materials containing detailed information on toxicity, together with proper shipping, handling and storage procedures, and should comply with all applicable safety and environmental standards.

Hazards, toxicity and behaviour of the products may differ when used with other materials and are dependent on manufacturing circumstances or other processes. Such hazards, toxicity and behaviour should be determined by the user and made known to handlers, processors and end users.

Except where explicitly agreed otherwise, the sale of products referred to in this publication is subject to the general terms and conditions of sale of Huntsman Advanced Materials LLC or of its affiliated companies including without limitation, Huntsman Advanced Materials (Europe) BVBA, Huntsman Advanced Materials Americas Inc., and Huntsman Advanced Materials (Hong Kong) Ltd.

Huntsman Advanced Materials is an international business unit of Huntsman Corporation. Huntsman Advanced Materials trades through Huntsman affiliated companies in different countries including but not limited to Huntsman Advanced Materials LLC in the USA and Huntsman Advanced Materials (Europe) BVBA in Europe.

[] is a registered trademark of Huntsman Corporation or an affiliate thereof.

Copyright © 2009 Huntsman Corporation or an affiliate thereof. All rights reserved.

B.6 Cyanate ester resin PT-30 (Primaset™, Lonza)

Materials Science

Primaset™ Cyanate Ester Resins
Leading Edge High Performance Thermoset Resins



Primaset™ Cyanate Ester Resins for high-end electronic, aerospace, and industrial applications

Lonza

Introduction

Cyanates are a novel class of high performance thermoset resins. They are characterized by glass temperatures up to 400°C resp. 800°F, excellent dielectric and mechanical properties and an epoxy like processing. Areas of use are electronics, aerospace, automotive and industrial composites and compounds.

Switzerland
Lonza Ltd
Muenchensteinerstrasse 38
4002 Basel
Tel +41 61 316 81 11
hpm@lonza.com

USA
Lonza Inc.
90 Boroline Road
Allendale, NJ 07401
Tel +1 201 316 9200
contact.allendale@lonza.com

Product grade	Resin content %	Appearance	Viscosity at temperature		T _g * °C
			mPa × s	°C	
Primaset™ BA 230 S	75	liquid	450	25	320
Primaset™ BA 3000	100	semisolid	12 000	70	> 300
Primaset™ BA 3000 S	75	liquid	250	25	> 310
Primaset™ BTP 6020 S	65	liquid	150	25	260
Primaset™ DT 4000	100	semisolid	3500	70	285
Primaset™ DT 7000	100	liquid	12 000	70	280
Primaset™ LECy	100	liquid	< 10	80	305
Primaset™ PT 1 S	100	liquid	30	80	> 325
Primaset™ PT 30	100	viscous liquid	400	80	> 400
Primaset™ PT 30 S	80	liquid	300	20	> 400
Primaset™ PT 60	100	viscous liquid	10 000	90	> 400
Primaset™ PT 60 S	75	liquid	225	25	> 400
Primaset™ PTC 2500	100	semisolid	1600	80	> 300

*: T_g [°C] run by DMA

www.lonza.com
www.high-performance-materials.com

The information contained herein is believed to be correct and corresponds to the latest state of scientific and technical knowledge. However, no warranty is made, either express or implied, regarding its accuracy or the results to be obtained from the use of such information. No statement is intended or should be construed as a recommendation to infringe any existing patent.

© 2012 Lonza Ltd

B.7 Strontium titanate (SrTiO₃, Sigma Aldrich)

SIGMA-ALDRICH

sigma-aldrich.com

3050 Spruce Street, Saint Louis, MO 63103, USA

Website: www.sigmaaldrich.com

Email USA: techserv@sial.com

Outside USA: eurtechserv@sial.com

Product Specification

Product Name:
Strontium titanate – nanopowder, <100 nm particle size, 99% trace metals basis

Product Number: 517011
CAS Number: 12060-59-2
MDL: MFCD00049554
Formula: O₃SrTi
Formula Weight: 183.49 g/mol



TEST	Specification
Appearance (Color)	White to Off-White
Appearance (Form)	Powder
X-Ray Diffraction	Conforms to Structure
Loss on Ignition 1 Hour at 1000 Degrees Celsius	
Size	≤ 100 nm
ICP Major Analysis Confirms Ti and Sr Components	Confirmed
Purity 99% Based On Trace Metals Analysis	Conforms
Trace Metal Analysis	≤ 15000.0 ppm

Specification: PRD.1.ZQ5.10000024725

Sigma-Aldrich warrants, that at the time of the quality release or subsequent retest date this product conformed to the information contained in this publication. The current Specification sheet may be available at Sigma-Aldrich.com. For further inquiries, please contact Technical Service. Purchaser must determine the suitability of the product for its particular use. See reverse side of invoice or packing slip for additional terms and conditions of sale.

1 of 1

B.8 Barium titanate (BaTiO₃, Sigma Aldrich)

SIGMA-ALDRICH®

sigma-aldrich.com

3050 Spruce Street, Saint Louis, MO 63103, USA

Website: www.sigmaaldrich.com

Email USA: techserv@sial.com

Outside USA: eurtechserv@sial.com

Product Specification

Product Name:
Barium titanate(IV) – nanopowder (cubic), 50 nm (SEM), 99.9% trace metals basis

Product Number: 745952
CAS Number: 12047-27-7



Formula: BaO₃Ti
Formula Weight: 233.19 g/mol

TEST	Specification
Appearance (Color)	White to Off White
Appearance (Form)	Powder
X-Ray Diffraction	Conforms to Structure
Size	Conforms
50 nm (SEM)	
Purity	Meets Requirements
99.9% Based On Trace Metals Analysis	
Trace Metal Analysis	≤ 1500 ppm

Specification: PRD.1.ZQ5.10000041537

Sigma-Aldrich warrants, that at the time of the quality release or subsequent retest date this product conformed to the information contained in this publication. The current Specification sheet may be available at Sigma-Aldrich.com. For further inquiries, please contact Technical Service. Purchaser must determine the suitability of the product for its particular use. See reverse side of invoice or packing slip for additional terms and conditions of sale.

1 of 1